ORGANIC AND ORGANOMETALLIC PHOTOSENSITIZERS FOR ELECTRON TRANSFER REACTIONS

DISSERTATION

Athul Krishna

General Information

The experimental investigations of this thesis were performed between April 2019 and November 2025 in the research group of Prof. Dr. Matthias Bauer.

Chairman: Prof. Dr. Thorsten Gutmann

First Reviewer: Prof. Dr. Matthias Bauer

Second Reviewer: Jun. Prof. Dr. Felix Fischer

Third Reviewer: PD Dr. Hans Egold

Declaration

I hereby accept the regulations to achieve a doctoral degree of the faculty of natural sciences of the Paderborn University dated March 31, 2021. Issued by Paderborn University based on Section §2 Section 4 and §67 Section 3 of the Higher Education Act of the State of North Rhine-Westphalia (Higher Education Act - HG) of September 16, 2014 (GV.NRW. p. 547), last amended by Article 1 of the Act of December 1, 2020 (GV. NRW. p. 1110).

Paderborn, ...

Athul Krishna

I hereby certify that I have written this thesis independently and that I have only used the the sources and aids listed here. The ideas directly or indirectly from external sources are identified as such. I have not applied for the opening of the doctoral procedure at any other place, and this dissertation has not been rejected by any other department or faculty.

Paderborn, ...

Athul Krishna

Acknowledgements

This dissertation would not have been possible without the support and encouragement of many people. Their contributions, whether through academic guidance, thoughtful discussions, practical assistance, or personal kindness, have helped to bring this work to life. I am deeply grateful to all those who have accompanied me throughout this process, and the following acknowledgements aim to express my sincere appreciation for their presence and support.

I would like to thank **Prof. Dr. Matthias Bauer** for his supervision of this project. His trust in my ability to pursue the scientific questions that inspired me, and his openness in allowing me to explore my own research interests, created an environment in which my curiosity could truly thrive. I am equally grateful for the funding and institutional backing he provided, which offered the stability necessary to complete this dissertation. His guidance and confidence in my work have been invaluable throughout this journey.

My sincere thanks go to **Jun.-Prof. Dr. Felix Fischer**, **Dr. Jakob Steube**, **Dr. Michał Nowakowski** and **Dr. Roland Schoch** for their continuous support and their help in strengthening my scientific writing. Their constructive feedback and willingness to offer guidance contributed greatly to the quality of this work. I would like to extend special thanks to **Jakob Steube** for the countless hours of insightful scientific discussions we shared. His ability to challenge and refine my thinking played an important role in shaping the ideas presented in this dissertation.

I am grateful to **Dr. Hans Egold** for generously sharing his expertise in NMR spectroscopy and for the valuable insights he offered throughout my research. His guidance was particularly instrumental in helping me formulate the central hypothesis for my final project. I deeply appreciate his time and his readiness to support my work whenever needed.

My heartfelt thanks go to my friends — **Iréne, Viktorija**, **Lennart, Simón, Seb, Zofia, Saad, Anke, Nacho, Nicole, and Sabith**. Their presence, encouragement and willingness to lift me up during demanding moments were essential to my well-being and perseverance. I am truly grateful for the sense of community and friendship they brought into my daily

life. I would also like to thank all my students — **Maximilian Henning, Franziska Lux, Marcus Reese** and **Michal Rout** for all their support.

I would also like to thank **Dr. Steffen Schlicher** and **Dr. Fabian Watt** for helping me find my footing in Germany. Their guidance during this period of transition made a profound difference and allowed me to settle into both my work and daily life with confidence.

My gratitude extends to **Prof. Dr. Stephan Hohloch**, whose invitation to join the University of Paderborn provided an important foundation for my academic development throughout my PhD.

I am deeply thankful to my friends around the world — **Adithya, Ananthu, Sreehari, and Arun** — who provided a much-needed source of balance and relief throughout my PhD. Our time spent gaming together helped me take my mind off the pressures of research and offered moments of genuine joy and relaxation. Their friendship has been an important anchor.

Finally, I would like to express my appreciation to **Nina** as well as my family who has supported me, in ways both large and small, throughout the completion of this dissertation. Each contribution has shaped this work and helped me grow, both personally and academically. To all of you, thank you.

List of Publications

1. Low Temperature emissive cyclometalated cobalt (III) complexes:
Athul Krishna, Lorena Fritsch, Jakob Steube, Miguel A. Argüello Cordero, Roland Schoch, Adam Neuba, Stefan Lochbrunner, Matthias Bauer*, Inorganic Chemistry, 2025
https://doi.org/10.1021/acs.inorgchem.4c04479

2. Emissive oxygen bridged pyridine phenolate complex:
Athul Krishna, Jannik Lösecke, Jakob Steube, Lorena Fritsch, Michal Nowakowski, Roland Schoch, Stephan Hohloch, Matthias Bauer, Felix Fischer*, Chemistry (Wiley), 2026
manuscript submitted

3. Photogeneration of cobalt stabilized aminium radical:
Athul Krishna, Timur Biktagirov, Daniel Leitner, Ayla Kruse, Hamada Rezk, Fridolin Hennhoefer, Jannik Löseke, Michal Nowakowski, Lorena Fritsch, Jakob Steube, Anke Schoch, Hossam Elgabarty, Olga Bokareva, Adam Neuba, Hans Egold, Roland Schoch, Katharina Lorena Franzke, Uwe Gerstmann, Stephan Hohloch, Oliver Kühn, Biprajith Sarkar, Stefan Lochbrunner, Wolf Gero Schmidt, Matthias Bauer*, Journal of American Chemical Society (JACS), 2026
manuscript submitted

4. Janus-type emission from a cyclometalated iron(III) complex:
Jakob Steube, Ayla Kruse, Olga Bokareva, Thomas Reuter, Serhiy Demeshko, **Athul Krishna** Roland Schoch, Stephan Hohloch, Franc Meyer, Katja Heinze, Stefan Lochbrunner, Matthias Bauer*, Nature Chemistry, 2023
https://doi.org/10.1038/s41557-023-01137-w

5. Monoanionic Anilidophosphine Ligand in Lanthanide Chemistry: Scope, Reactivity, and Electrochemistry:
Fabian A. Watt, **Athul Krishna**, Grigoriy Golovanov, Holger Ott, Roland Schoch, Christoph Wölper, Adam G. Neuba, Stephan Hohloch*, Inorganic chemistry, 2020 https://doi.org/10.1021/acs.inorgchem.9b03071

List of Talks and Posters

Talks,

1. **Cobalt (II), Cobalt (III) and NO inserted Cobalt (III) Complexes**
   Athul Krishna, Matthias Bauer,
   Koordination Chemie Treffen (KCT), Jena, Germany, 2022
2. **Tuning the Emission and Reactivity in Cobalt(III) Complexes by Amino Groups,**
   Athul Krishna, Lorena Fritsch, Miguel Cordero, Stefan Lochbrunner, Matthias Bauer
   International Conference on Photochemistry (ICP), Sapporo, Japan 2023

Posters

1. **Low and Room Temperature Emissive Cobalt Complexes,**
   Athul Krishna, Matthias Bauer,
   PHOTOIUPAC, Amsterdam, Netherlands, 2022
2. **Low and Room Temperature Emissive Cobalt Complexes,**
   Athul Krishna, Matthias Bauer,
   Bring Your Own Poster Session by JCF, Paderborn, Germany, 2022
   Won the best poster award
3. **Light Induced Cobalt Stabilized Highly Delocalized Radical for Hydrogen Production,**
   Athul Krishna, Timur Biktagirov, Daniel Leitner, Ayla Kruse, Hamada Rezk, Fridolin Hennhoefer, Jannik Löseke, Michal Nowakowski, Lorena Fritsch, Jakob Steube, Anke Schoch, Hossam Elgabarty, Olga Bokareva, Adam Neuba, Hans Egold, Roland Schoch, Katharina Lorena Franzke, Uwe Gerstmann, Stephan Hohloch, Oliver Kühn, Biprajith Sarkar, Stefan Lochbrunner, Wolf Gero Schmidt, Matthias Bauer
   SPP, Stuttgart, Germany, 2023
4. **Light Induced Cobalt Stabilized Highly Delocalized Radical for Hydrogen Production,**
   Athul Krishna, Timur Biktagirov, Daniel Leitner, Ayla Kruse, Hamada Rezk, Fridolin Hennhoefer, Jannik Löseke, Michal Nowakowski, Lorena Fritsch, Jakob Steube, Anke Schoch, Hossam Elgabarty, Olga Bokareva, Adam Neuba, Hans Egold, Roland Schoch, Katharina Lorena Franzke, Uwe Gerstmann, Stephan Hohloch, Oliver Kühn, Biprajith Sarkar, Stefan Lochbrunner, Wolf Gero Schmidt, Matthias Bauer
   Lecture Conference in Photochemistry (LCP) Mainz, Germany, 2024
5. **Light Induced Cobalt Stabilized Highly Delocalized Radical for Hydrogen Production,**
   Athul Krishna, Timur Biktagirov, Daniel Leitner, Ayla Kruse, Hamada Rezk, Fridolin

Hennhoefer, Jannik Löseke, Michal Nowakowski, Lorena Fritsch, Jakob Steube, Anke Schoch, Hossam Elgabarty, Olga Bokareva, Adam Neuba, Hans Egold, Roland Schoch, Katharina Lorena Franzke, Uwe Gerstmann, Stephan Hohloch, Oliver Kühn, Biprajith Sarkar, Stefan Lochbrunner, Wolf Gero Schmidt, Matthias Bauer SPP Mainz , Germany, 2024

6. **Light Induced Cobalt Stabilized Redox Active Highly Delocalized Radical,** **Athul Krishna**, Timur Biktagirov, Daniel Leitner, Ayla Kruse, Hamada Rezk, Fridolin Hennhoefer, Jannik Löseke, Michal Nowakowski, Lorena Fritsch, Jakob Steube, Anke Schoch, Hossam Elgabarty, Olga Bokareva, Adam Neuba, Hans Egold, Roland Schoch, Katharina Lorena Franzke, Uwe Gerstmann, Stephan Hohloch, Oliver Kühn, Biprajith Sarkar, Stefan Lochbrunner, Wolf Gero Schmidt, Matthias Bauer Koordination Chemie Treffen (KCT) Munster, Germany, 2025
7. **Light Induced Cobalt Stabilized Redox Active Highly Delocalized Radical,** **Athul Krishna**, Timur Biktagirov, Daniel Leitner, Ayla Kruse, Hamada Rezk, Fridolin Hennhoefer, Jannik Löseke, Michal Nowakowski, Lorena Fritsch, Jakob Steube, Anke Schoch, Hossam Elgabarty, Olga Bokareva, Adam Neuba, Hans Egold, Roland Schoch, Katharina Lorena Franzke, Uwe Gerstmann, Stephan Hohloch, Oliver Kühn, Biprajith Sarkar, Stefan Lochbrunner, Wolf Gero Schmidt, Matthias Bauer ISPPCC Milazzo, Italy, 2025

Abstract

The accelerating depletion of fossil-fuel resources underscores the urgency of transitioning toward renewable energy technologies. Among these, the photochemical conversion of solar energy into chemical reactions particularly towards the generation of hydrogen, offers a sustainable pathway for long-term energy storage. Achieving this requires efficient photoactive materials capable of harvesting sunlight and driving otherwise unfavorable chemical transformations.

This thesis contributes to the goal by developing and characterizing organic boron-based photoactive complexes as sustainable alternatives to precious-metal chromophores which have been employed in photocatalysis. Rigid O- and N-donor ligand frameworks, including oxygen-bridged architectures, are shown to support strong absorption features, enhanced conjugation, and well-defined charge-transfer transitions. These structural elements enable boron chromophores to access long-lived emissive states and exhibit high photostability, highlighting their potential in light-harvesting and photochemical applications.

Complementary studies focus on first-row transition-metal photophysics, particularly cobalt (III) complexes. Although Co^{III} typically suffers from ultrafast non-radiative decay, it is demonstrated in this thesis that strategic ligand design can stabilize higher-energy charge-transfer excited states, yielding Co^{III} complexes with observable low-temperature emission and distinct excited-state manifolds. These results provide new insight into how ligand field strength and coordination rigidity modulate 3d-metal photophysics.

Since the low temperature emissive complexes pose a serious concern of practical applicability, a further component of this work examines light-induced ligand-centered radicals in cobalt systems. Through combined spectroscopic, electrochemical, and computational analysis, the formation of a cobalt-stabilized aminyl radical is revealed, a rare example of a photochemically accessible ligand radical in a first-row metal complex. This pathway demonstrates how tailored coordination environments can redirect photoexcitation away from metal-centered decay toward productive ligand-localized redox chemistry.

Collectively, the boron chromophores, emissive Co^{III} complexes, and photogenerated ligand radicals presented in this thesis showcase how rational ligand and structural design can overcome inherent limitations of first-row elements. The resulting insights offer new strategies for developing sustainable, efficient photoactive systems for solar-energy conversion and photochemical reactivity.

Kurzzusammenfassung

Die fortschreitende Erschöpfung fossiler Energieressourcen verdeutlicht die Dringlichkeit eines Übergangs zu erneuerbaren Energiequellen. Unter diesen bietet die photochemische Umwandlung von Sonnenenergie in chemische Reaktionen, insbesondere zur Erzeugung von Wasserstoff, einen vielversprechenden Ansatz für eine langfristige Energiespeicherung. Dies erfordert hocheffiziente photoaktive Materialien, die in der Lage sind, Sonnenlicht zu absorbieren und energetisch ungünstige chemische Umwandlungen anzutreiben.

Diese Arbeit trägt zu diesem Ziel bei, indem organische, bor-basierte photoaktive Komplexe als nachhaltige Alternativen zu edelmetallhaltigen Chromophoren entwickelt und charakterisiert werden, die bisher in der Photokatalyse eingesetzt wurden. Starre O- und N-Donor-Ligandengerüste, einschließlich sauerstoffverbrückter Architekturen, zeigen ausgeprägte Absorptionsbanden, erweiterte Konjugation und klar definierte Ladungstransferübergänge. Diese strukturellen Merkmale ermöglichen den Bor-Chromophoren den Zugang zu langlebigen emissiven Zuständen bei gleichzeitig hoher Photostabilität und unterstreichen ihr Potenzial für Lichternte- und photochemische Anwendungen.

Komplementäre Studien konzentrieren sich auf die Photophysik von Übergangsmetallkomplexen der ersten Reihe, insbesondere Co^{III}-Systemen. Obwohl Co^{III}-Komplexe typischerweise unter ultraschneller nicht-radiativer Desaktivierung leiden, wird in dieser Arbeit gezeigt, dass durch gezielte Ligandgestaltung höherenergetische Ladungstransferzustände stabilisiert werden können, wodurch Co^{III}-Komplexe mit nachweisbarer Emission bei tiefen Temperaturen und klar abgegrenzten angeregten Zuständen zugänglich werden. Diese Ergebnisse liefern neue Einblicke, wie Ligandenfeldstärke und Koordinationsrigidität die Photophysik von 3d-Metallen beeinflussen.

Da die Tieftemperatur-Emission die praktische Anwendbarkeit einschränkt, widmet sich ein weiterer Teil dieser Arbeit lichtinduzierten ligandenzentrierten Radikalen in Cobaltsystemen. Kombinierte spektroskopische, elektrochemische und computergestützte Analysen belegen die Bildung eines cobaltstabilisierten Aminylradikals, ein seltenes Beispiel für ein photochemisch zugängliches Ligandenradikal in einem Übergangsmetallkomplex der ersten Reihe. Dieser Reaktionsweg zeigt, wie maßgeschneiderte Koordinationsumgebungen Photoanregung von metallzentrierter Desaktivierung hin zu ligandlokalisierter Redoxchemie umlenken können.

Insgesamt verdeutlichen die untersuchten Bor-Chromophore, emissiven Co^{III}-Komplexe und lichtinduzierten Ligandenradikale, wie rationales Liganden- und Strukturdesign inhärente Einschränkungen von Elementen der ersten Reihe überwinden kann. Die gewonnenen Erkenntnisse eröffnen neue Strategien für die Entwicklung nachhaltiger und effizienter photoaktiver Systeme zur solaren Energieumwandlung und photochemischen Reaktivität.

Contents

List of Abbreviations

Å	Angstrom
bimp	2,6-bis(imidazole-2-ylidene)pyridine
bpy	2,2'-biypridine
bpz	2,2'-bipyrazine
B	Racah parameter
Bu	Butyl
CSP	Concentrated solar power plants
CT	Charge-transfer
CtC-XES	Core-to-Core X-ray emission spectroscopy
dcpp	2,6-bis(2-carboxypyridyl)pyridine
dppy	2,2'-(pyridine-2,6-diyl)diphenolate
DFT	Density functional theory
Dq	Ligand-field strength
DIPEA	Diisopropylethylamine
DMF	Dimethylformamide
DSSC	Dye-sensitized solar-cell
EPR	Electron Paramagnetic Resonance
EnT	Energy-transfer
ES	Excited State
ESI-MS	Electron-spray ionization mass spectrometry
GS	Ground state
HAT	Hydrogen atom transfer
HER	Hydrogen evolution reaction
H^{Me}ImP	1,1'-(1,3-phenylene)bis(3-methyl-1-imidazol-2-ylidene)
IC	Internal conversion

ISC	Intersystem crossing
LC	Ligand centered
LMCT	Ligand-to-metal charge-transfer
MC	Metal-centered
Me	Methyl
Et	Ethyl
***i*-pr**	isopropyl
MeCN	Acetonitrile
MECP	Minimum energy crossing point
MLCT	Metal-to-ligand charge-transfer
MO	Molecular orbital
NHC	*N*-Heterocyclic carbene
NIR	Near infrared
NMR	Nuclear magnetic resonance
PET	Photoinduced electron-transfer
PGM	Platinum metal group
phtmeimb	phenyl(tris(3-methylimidazol-1-ylidene))borate
PH	Phosphorescence
PS	Photosensitizer
RP-ISC	Radical-Pair Intersystem crossing
R	Relay
S	Substrate
SCE	Saturated calomel electrode
SCXRD	Single crystal X-ray diffraction
SOCT	Spin-orbit charge transfer intersystem crossing
TA	Transient absorption
TW	Terawatt

tBu	tert-butyl
TCSPC	Time-correlated single-photon counting
TDDFT	Time-dependant density functional theory
TEOA	Triethanolamine
THF	Tetrahydrofuran
TMP	2,2,6,6-Tetramethylpiperidine
TPT	2,4,6- Triphenylpyrylium tetrafluoroborate (TPT)
TW	Terawatt
tpy	2,2;6,2-Terpyridine

“Rise and Rise Until ,,,,,,

,,,,,,Lambs Become Lions”

Chapter 1: Introduction

Motivation

Over the past several centuries, humanity has become increasingly dependent on fossil fuels as its primary energy source. This sustained and intensive reliance has been accompanied by far-reaching consequences. Fossil fuels when burnt emit greenhouse gases like CO_2. These can trap heat in the atmosphere which leads to increased surface temperatures. Recent research provides compelling evidence that anthropogenic climate change is intensifying extreme weather events across the globe, with particularly severe impacts in vulnerable regions. Variability and long-term shifts in Arctic climate strongly influence extreme winter weather patterns in mid-latitude regions such as the United States, challenging the misconception that warming solely reduces cold extremes.[1] Complementarily, clear upward trends in the frequency, duration, and severity of regional heatwaves, a finding consistent with global-scale observational datasets has also been reported in the recent years.[2]

Several studies highlight the increasing persistence and extremity of summertime weather regimes. Pfleiderer et al. reported in 2019 that in a 2 °C warmer world, summer weather patterns tend to lock into prolonged states, amplifying the risk of heatwaves and droughts.[3] Similarly, Fischer and Knutti quantified in 2015, the anthropogenic contribution to the growing occurrence of both heavy-precipitation and high-temperature extremes, demonstrating that human influence is now detectable in a wide range of climate anomalies.[4] The spatial distribution and underlying drivers of extreme precipitation changes are examined by Pfahl et al., who attribute regional heterogeneity to thermodynamic and dynamic factors that shape future rainfall intensification.[5] This is further supported by the recent work of Liu et al., showing that the global warming amplifies day-to-day temperature variability in mid- to low-latitude regions, making climatic conditions more volatile and less predictable.[6]

Beyond global patterns, regional analyses reveal severe socio-economic consequences of climate extremes. Ayugi et al. review the history and impacts of meteorological droughts across Africa, documenting rising frequency, widespread agricultural losses, and increasing human vulnerability.[7] The situation is acute in South Asia, where rapidly intensifying climate-driven disasters have been reported. Khan and Liu (2025) emphasize the need for coordinated action in Pakistan as the country faces recurrent floods and climate-induced hazards,[6] while reports from Waqas argues that Pakistan's catastrophic floods are rooted in broader climate injustice, with disproportionate burdens falling on low-emission countries.[6,8,9]

Together, these studies form a consistent scientific consensus that the climate change is increasing the frequency, intensity, and persistence of extreme weather events, with the most severe consequences occurring in tropical and developing regions. This growing instability underscores the urgent need for sustainable energy technologies, resilient materials, and low-carbon solutions such as wind, solar, hydro, geothermal and biomass. Hydrogen as a fuel should be considered as a green alternative to the existing fossil fuel-based industry as it only forms water as a by product upon combustion.

Hydrogen as a fuel

Hydrogen is the most abundant element in the entire Universe comprising of about 90 percent but this stellar fuel is only available on Earth for about 0.75 percent of the mass fraction.[10] This creates an industrial bottleneck as it is one of the building blocks for the synthesis of basic chemicals like ammonia and methanol. From an energetic point of view, hydrogen also has the highest gravimetric heating value of 119 MJ/kg which generates further interest in it as a fuel.[11,12] Coupling this with zero emission of green house gases makes it the ideal source for all energy demands but the problem lies in the scarcity of hydrogen in its purest form on Earth.[13] It is mainly found on either as water, or as hydrocarbons and the extraction process from these resources raises the question of sustainability once more. Accordingly, the sustainability of hydrogen is determined by its primary energy source and the method used for its production. Current classifications distinguish between grey hydrogen, generated from fossil hydrocarbons; blue hydrogen, also derived from fossil fuels but coupled with carbon-capture and storage technologies; turquoise hydrogen, produced via thermal methane splitting; and green hydrogen, obtained through water electrolysis or other processes powered by renewable energy sources.[14] As of 2025, more classifications of hydrogen has been available as noted in table 1.[15]

Table 1. Classification of sustainability of hydrogen by colors.[15]

	Color	Hydrogen produced from
Overall common understanding	Green	Solar, wind and water power[16–21]
	Grey	Steam reforming of natural gas with CO_2 emissions[20,22]
	Blue	Steam reforming of natural gas with preventing measure for emissions[23,24]
	Turquoise	Pyrolysis of natural gas[17,25]
Coal based hydrogen	Brown	Gasification of lignite[19]
	Black	Gasificiation of black coal[19]

Nuclear Powered hydrogen	Pink	Electrolysis using energy from power plants[19,22,26]
	Purple	Combined chemothermal energy from power plants[19,22,26]
	Red	High temperature catalytic splitting of water based on nuclear power[19,22,26]
Other introduced colors	Yellow	Electrolysis using mixed carbon electrical grid[27,28]
	White	Naturally occurring hydrogen[19,26]
	Orange	Conversion of biomass[29]

Although green hydrogen yields no greenhouse gas emissions and provides cleanest generation of hydrogen, grey hydrogen still dominates around 90 percent of the share of the overall hydrogen production.[20,22] A possible green source of hydrogen production was proposed via photocatalytic reactions where light is used to reduce protons.[12]

Solar Energy

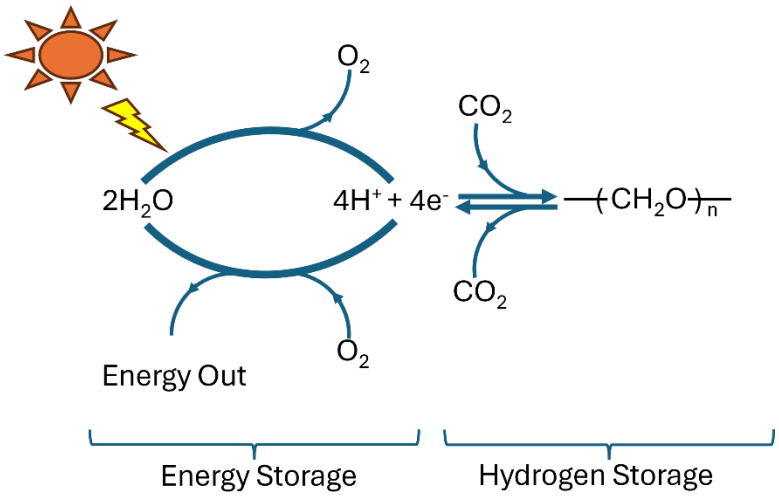

Figure 1. Sunlight powers the splitting of water into O_2, H^+, and e^-, which are then used to reduce CO_2 to carbohydrates.[30,31]

Sorting available energy resources by abundancy, solar energy is the most abundant as Earth receives it at a rate of approximately 100,000 TW (terawatt) while we use only approximately 15 TW.[30,32–34] Developing effective ways to harness and store this immense energy flux for practical use remains one of the defining scientific challenges of our time. It is widely recognized that no single technology can meet future global energy demands; instead, a diversified portfolio of sustainable solutions will be necessary, one of them being photovoltaics.[35] The major challenges for large scale deployment of these include storage, availability and accessibility.[36] Concentrated solar power plants (CSP) are

quite efficient but are prone to varying solar radiation flux. CSP plants rely solely on direct normal irradiance, their design and evaluation demand clear-sky irradiation models.[37] Another approach is to capture solar energy using tailored photochemical reactions, enabled by newly designed compounds that replicate the sophisticated light-driven processes long perfected by plants.[38] During photosynthesis, solar energy is captured and used to extract four electrons and four protons from water, releasing oxygen. These photochemically generated redox equivalents enable the subsequent reduction of CO_2 into carbohydrate products. The process can be viewed as form of hydrogen storage through synthesis of organic molecules which store solar energy in their chemical bonds (Figure. 1). [30,31] Photochemical systems can drive inherently endergonic transformations, most notably water oxidation and proton reduction by using photon energy to generate high-energy charge-separated states ultimately leading to green hydrogen production.[30,33,39,40]

Photocatalytic Water-Splitting

Building on this natural blueprint, artificial photocatalytic systems seek to emulate the core principles of the photosynthesis, using light-driven charge separation to promote energy-intensive redox reactions. Among these, the photocatalytic splitting of water into hydrogen and oxygen has emerged as a central benchmark, offering a direct route to solar-to-chemical energy conversion through the green hydrogen production.[11,41–48] This can be done with homogenous as well as heterogeneous systems, which involves the formation of electron-hole pairs through direct excitation or photosensitization of semiconductor.[49] Most of the homogeneous systems use a multimolecular approach involving a photosensitizer (PS), an electron relay (R), a sacrificial electron donor (D) and a water reduction catalyst (WRC). The PS after the absorption of light can either convert the absorbed energy into light by photoluminescence (k_{nr}) or the energy can be used for photoreactions before being converted into photoluminescence (Figure. 2). From this excited state it can either undergo an energy transfer or an electron transfer to the substrate (S).

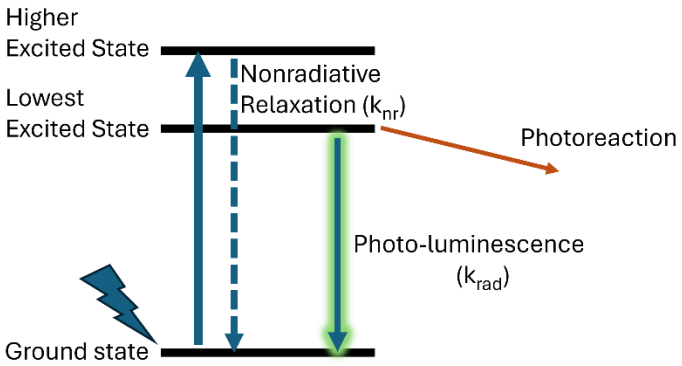

Figure 2: Schematic Representation Of The Energy-Level Landscape Highlighting Radiative Emission, Nonradiative Relaxation, And Photochemical Reactivity From An Electronically Excited State

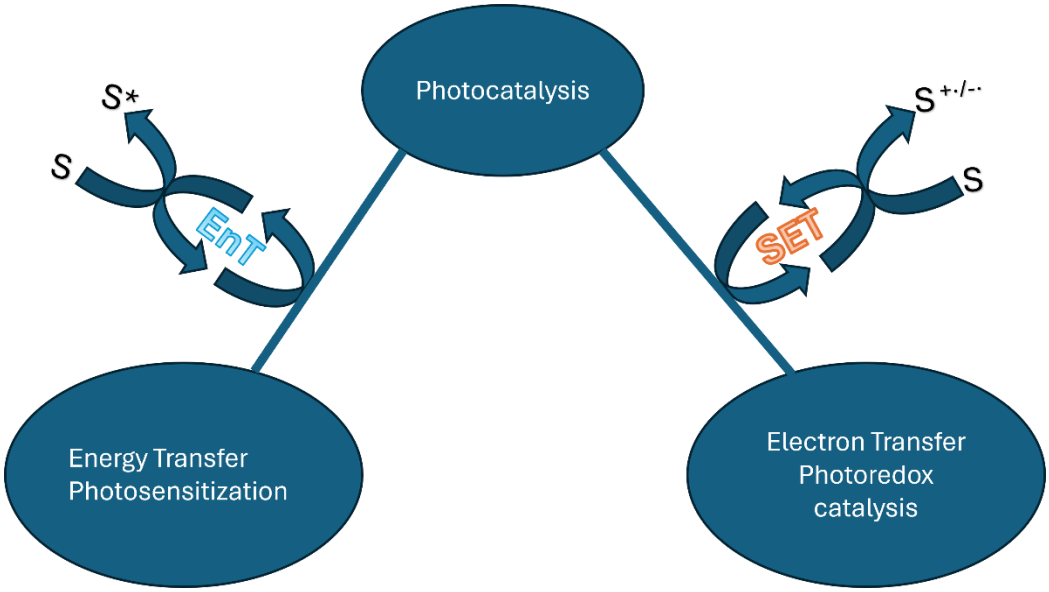

Figure 3: Schematic representation of the two pathways of photocatalysis.

The latter can happen via two reaction pathways, either the reductive or the oxidative quenching pathway. In the oxidative quenching pathway, the excited photosensitizer (PS*) first transfers an electron to the water-reduction catalyst (WRC), after which it is regenerated by accepting an electron from the electron donor (ED). In contrast, in the reductive quenching pathway, the excited PS* is initially reduced by the ED and then delivers this electron to the WRC. Ruthenium tris bipyridine $[Ru(bpy)_3]^{2+}$, even from the onset of the topic and remains to this day the most investigated PS and is mostly associated with the oxidative quenching mechanism.[50,51] Ruthenium tris bipyrazine $[Ru(bpz)_3]^{2+}$ on the other hand was reported as a good candidate for the reductive mechanism.[52,53] The key factor in determining the effectiveness of the PS is its excited

state lifetime. If the excited state does not survive long enough before the collision with the substrates, no reaction can be expected to take place as no electron transfer is expected. Other than lifetime PS depends on how quickly it can encounter the substrate and since these encounters occur by random motion in solution, the diffusion constant (D) becomes a key kinetic parameter.[54] Diffusion is strongly depends on the viscosity (η) of the solvent according to the Stokes-Einstein-Sutherland equation for laminar solvents:

$$D = \frac{k_B T}{6\pi\eta r} \qquad \text{Eq 1.1}$$

Where $k_B$is the Boltzmann constant, T is temperature, η is the solvent viscosity, r is the hydrodynamic radius of the diffusing species. The factors in this equation can be used to fine tune the performance of the catalytic systems. Since most of these factors are well within experimental control the focus is on the PS and lifetimes.

Photosensitizers

The design and selection of an effective photosensitizer become critical, as its photophysical properties control the very core of modern photochemistry and water splitting reactions. The first model systems were available since 1977, making use of acridine yellow as the photosensitizer.[55] They were soon followed by transition metal photosensitisers based on ruthenium, chromium, rhodium, osmium, metallo porphyrins and metallophthalocyanines which showed remarkable visible light absorption, excited state properties, kinetic requirements and redox potentials.[51,56–58] Organic photosensitizers like 2,4,6- triphenylpyrylium tetrafluoroborate (TPT) were used for photo-induced electron transfer reactions where its strong oxidizing power in both excited singlet and triplet states allowed for the easy generation of radical cations even from substrates with high oxidation potentials.[59] Organometallic compounds due to their high photostability and flexible range of excited-state redox potentials became more popular. In this thesis, a compact review on organic photosenisitizers will be followed on by a review on organometallic photosensitizers.

Organic photosensitizers

Organic dyes offer several inherent advantages including structural tunability, high molar extinction coefficients, and metal free composition, which adds to their economic benefits. However, critical limitations of most organic chromophores are very weak spin-orbit coupling, dominant singlet excited state behaviour and inefficient population of triplet states. Triplet states are generally preferred for photochemistry due to their longer lifetimes. Consequently, a major focus in the design of organic photosensitizers has been on the enhancement of triplet state population to enable effective charge transfer reactions in photocatalytic systems.[60]

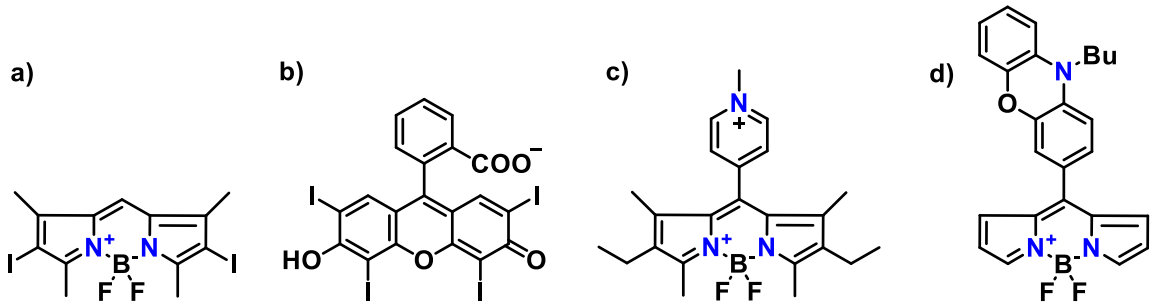

Figure 4: Selected examples of triplet-state sensitizers modified via halogenation (a,b) and charge-recombination donor-acceptor dyad (c,d).[60]

Several synthetic strategies were used to address this challenge. One widely used approach is the "heavy atom" effect, where heavier halogens are applied to increase the spin-orbit coupling and promote intersystem crossing (ISC). This strategy has been successfully used in Xanthene based dyes as well as BODIPY derivatives.[60–62] Although this strategy reduces the fluorescence quantum yields, the complexes are turned into efficient triplet photosensitizers capable of driving photocatalytic reactions. Xanthene based dyes such eosin Y and rose Bengal are among the most widely studied systems for photocatalytic hydrogen evolution reaction (HER) and are often combined with cobaloxime or nickel as catalysts in presence of sacrificial donors.[60,63–69] One downside to this strategy is the reduced photostability.[60,70,71]

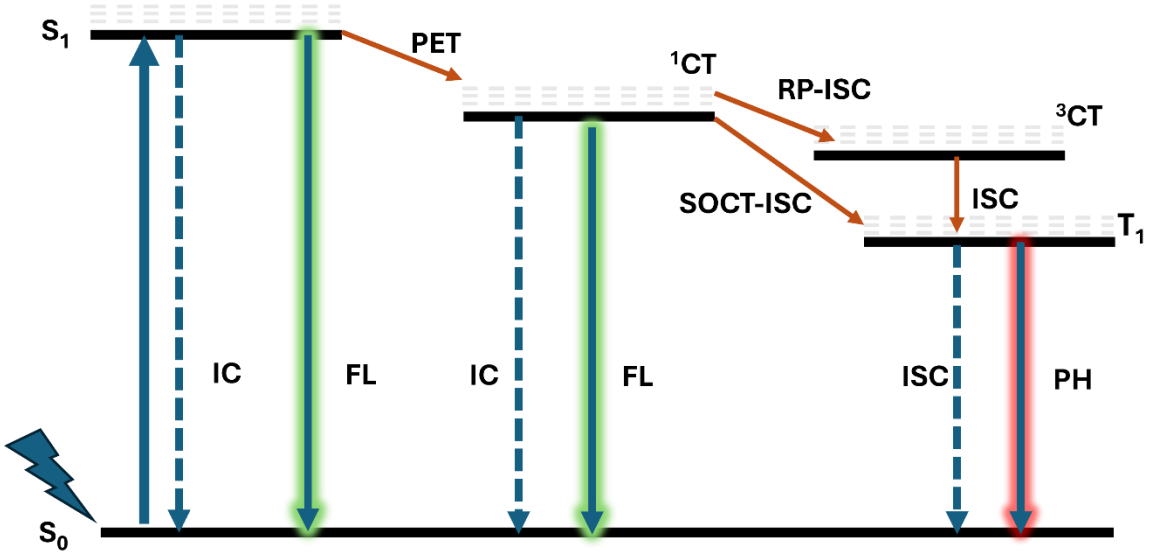

Figure 5: Energy diagram for triplet excited state formation (T_1) initiated by photo-induced electron transfer (PET) and mediated by charge recombination by either radical-pair intersystem crossing (RP-ISC) or spin-orbit charge transfer intersystem crossing (SOCT-ISC) to undergo phosphorescence (PH) (FL-fluoresecence, IC-internal conversion).[60]

An alternative strategy involves donor-acceptor architectures that generate triplet states through charge-recombination pathways. In these systems, photoexcitation produces a charge-transfer state that undergoes radical-pair intersystem crossing or spin-orbit charge transfer ISC, eventually leading to triplet state formation even in the absence of the heavy halogens (Figure. 5).[60] Therefore, heavy-atom-free cationic organic dyes were examined as photosensitizers, a typical example being the class of acridinium dyes.[72–76] BODIPY based dyads and phenoxazine containing chromophores also use the same strategy to exhibit long lived triplet states and highly reducing excited state potentials.[77–79] These designs avoid reliance on heavy elements while maintaining strong photoredox activity.

Despite these advances, many organic photosensitizers exhibit limited water solubility and rely on sacrificial electron donors which restricts practical applicability. Additionally, most systems still require relatively high-energy visible or UV light to access sufficiently energetic excited states. On the other hand, organometallic photosensitizers mostly have a significant absorption profile lying in the visible region. This is where organometallic sensitizers have an advantage over the organic photosensitizers.

Organometallic photosensitizers

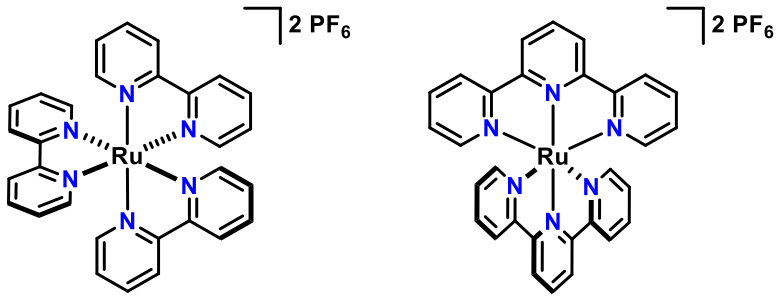

Figure 6: Ruthenium based photosensitizers.[80]

To examine the photophysical properties of organometallic photosensitizers in greater detail, the discussion begins with using ruthenium polypyridyl complexes as model photosensitizers. The complexes upon excitation by light, an electron from its ground state (GS) is excited to a singlet metal- to-ligand charge transfer (^{1}MLCT) state. Once this charge separated state is formed, an electron transfer from the filled t_{2g}-based d- orbital of the metal gets transferred into the empty π^*- orbitals of the ligands. This is followed by a fast intersystem crossing (ISC, spin change involved) to a triplet metal -to-ligand charge transfer (^{3}MLCT) state in the case of most transition metal complexes.[81] From this point it can either relax into the ground state non radiatively (k_{nr}) via internal conversion (IC, no spin change involved) to a metal centered (MC) state or radiatively (k_r) via spin - allowed fluorescence. As the internal conversion from the ^{3}MLCT to the ^{1}GS is a spin forbidden transition, these states usually exhibit long lifetimes which could be exploited for energy transfer or electron transfer reactions. If not exploited for its reactivity, this state can relax back into the ground state through phosphorescence.

The possibilities discussed above, that is the two relaxation pathways, either involving long lived phosphorescence or relaxation into the MC states can be observed in different ruthenium polypyidyl complexes. The first can be experimentally observed in $[Ru(bpy)_3]^{2+}$ whereas the relaxation pathway involving the internal conversion from ^{3}MLCT to ^{3}MC is found in the $[Ru(tpy)_2]^{2+}$ (Figure 7).[82,83] $[Ru(bpy)_3]^{2+}$ upon 455 nm excitation exhibits phosphorescence in solution at a wavelength of 620 nm. It also displays an emission quantum yield (Φ_{em}) of 0.018 under aerated conditions at room temperature. Much of the emission here is assumed to be quenched by oxygen as the deaerated solution displays a Φ_{em} of 0.095 in acetonitrile.[80,82] Emission lifetime investigations through time correlated single photon count (TCSPC) at room temperature

(r.t.) (850 ns) and at 77 K (5 µs) show significant differences indicating that a thermally activated non-radiative deactivation plays a significant role.[80,82,83]

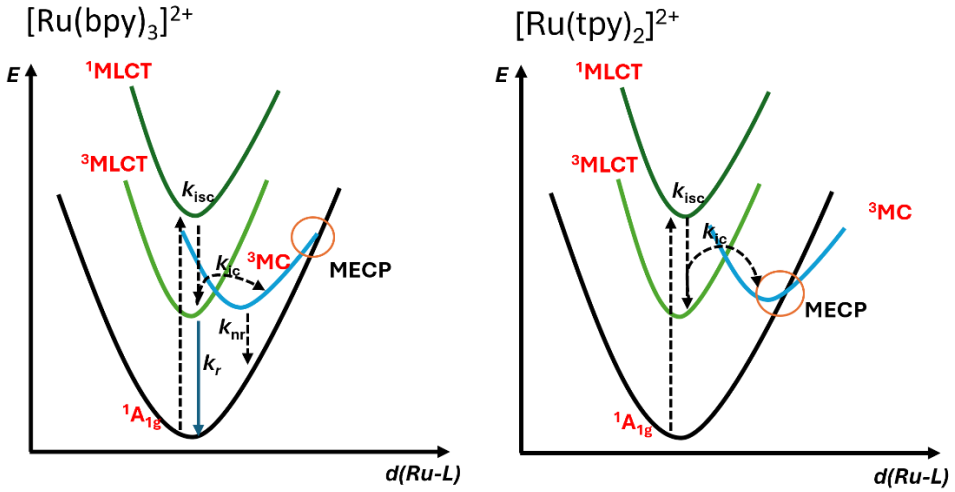

Figure 7: Excited state dynamics of tris(2,2'- bipyridine)ruthenium(II) $[Ru(bpy)3]^{2+}$ (left) and bis(2,2':6',2''-terpyridine) ruthenium(II) $[Ru(tpy2)]^{2+}$ (right).[80]

The potential energy surface of the ^{3}MC state is significantly displaced along the Ru-N bond length coordinate, accounting for its large nonradiative decay rate. This displacement arises from population of σ-antibonding e_g* orbitals, which leads to elongation of the Ru-N bonds (Figure 7). As a consequence, the ^{3}MC state is substitutionally labile. Moreover, ^{3}MC surface intersects with GS surface at a minimum-energy crossing point (MECP), providing an additional efficient pathway for nonradiative deactivation. Hence, a horizontal shift toward larger geometric distortions or a vertical shift towards lower energies will reduce the activation barrier, thereby facilitating deactivation of the ^{3}MC state via the MECP towards the GS. This mechanism is particularly pronounced in the related complex $[Ru(tpy_2)]^{2+}$ (tpy = 2,2':6',2''-terpyridine). The main difference between the two complexes is the strength of the ligand field of the repective ligands. $[Ru(tpy_2)]^{2+}$ possesses a weaker ligand field and correspondingly lower-lying ^{3}MC states. As a result, thermal population of the ^{3}MC state is facile, enabling efficient

nonradiative decay through the MECP. Consequently, $[Ru(tpy)_2]^{2+}$ exhibits significant phosphorescence only at low temperatures.[80,83,84]

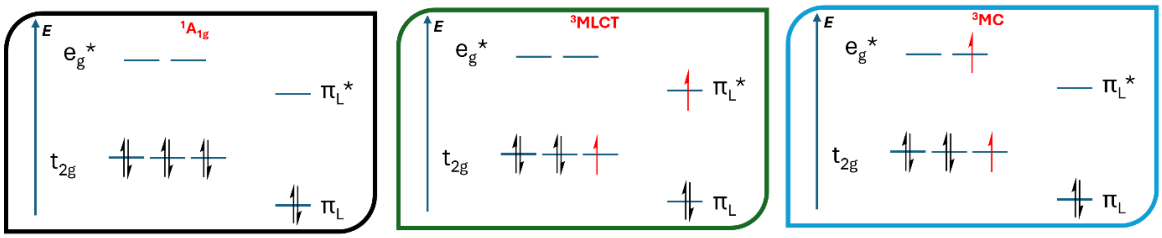

Figure 8: Microstate schemes for ground state, ^{3}MLCT and ^{3}MC for $[Ru(bpy)_3]^{2+}$.[80]

The same tris(bipyridine) ligand when complexated with lighter 3d transition metals exhibits further deterioration of the above condition, not due to the geometric distortion and associated metal-ligand bond elongation, but rather because of the intrinsically weaker ligand field splitting of 3d-metals. Tris (2,2'- bipyridine)iron(II) ($[Fe(bpy)_3]^{2+}$) for example, displays similar excited state dynamics until the transition to the ^{3}MLCT state, but later relaxes into the ^{3}MC and then further into the ^{5}MC pathways as compared to the ruthenium polypyridyl complexes.[85–87] This behaviour arises from the weaker ligand field splitting imposed by Fe^{2+}, which places the metal e_g* orbitals below the π_L* of the ligand, thereby providing an efficient non-radiative decay for the ^{3}MLCT state (Figure 9). The weaker ligand field splitting by the 3d transition metal is a consequence of the primogenic effect.[85,88] When moving from the 3d to 4d and 5d transition metals, the metal d orbitals are more spatially extended and more covalent in character. Since the ^{3}MC orbitals are metal centered, their energies are increased significantly and at the same time destabilize e_g* orbitals higher as well placing them above the energies of ligand π* orbitals.

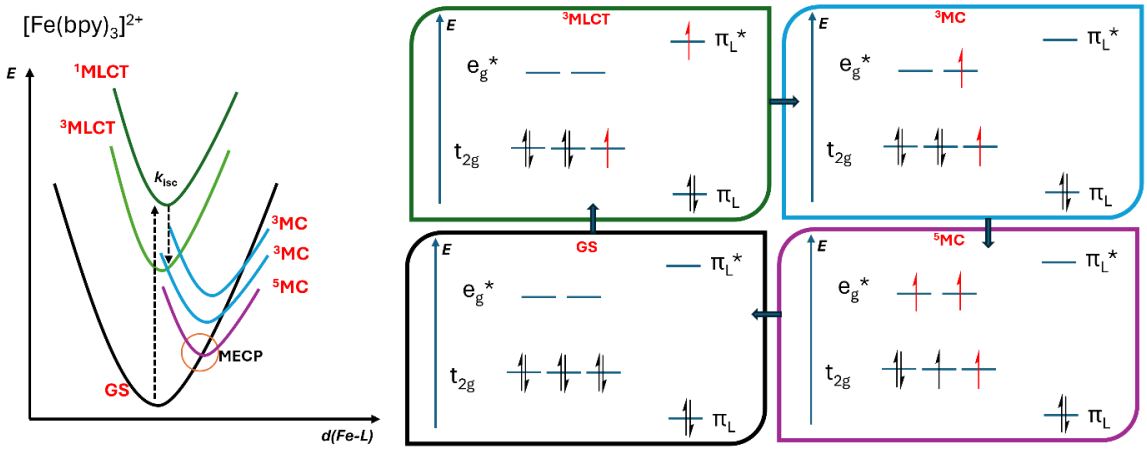

Figure 9: Excited state dynamics for $[Fe(bpy)_3]^{2+}$ (left) and microstate scheme for its ground state, ^{3}MLCT, ^{3}MC and ^{5}MC.[80,85–87]

The consequences of all the above-mentioned effects can be experimentally observed in $[Fe(bpy)_3]^{2+}$, where the ^{3}MLCT state is very short lived (≈ 50 fs) at room temperature in

solution.[86] This comparison underscores the intrinsic difficulty of realizing luminescent 3d metal complexes due to low-energy, distorted and non-emissive metal-centered states.[85,86,89]

The energies of the ^{3}MC and the ^{5}MC increase with an increasing ratio between ligand-field strength (Dq) to the Racah-parameter (B). The energy of the ^{5}MC state is more affected as it involves two electrons being placed in e_g* orbitals, and this causes further displacement of ^{5}MC energy well along the horizontal axis of nuclear coordinates. Hence, altering the ligand field strength can be a key strategy for achieving room-temperature emission in 3d transition metals from ^{3}MLCT states.[86] This can be achieved via multiple methods. McCusker and coworkers employed ligands that improved the coordination symmetry by using a homoleptic iron (II) complex ($[Fe(dcpp)]^{2+}$) with 2,6-bis(2-carboxypyridyl)pyridine as the ligand. The bridging carboxy groups helped in achieving a near perfect octahedral geometry.[90] The electron withdrawing effect of the carboxy groups added to the increased π -accepting properties as well. Heinze and coworkers tried to introduce a push pull system to decrease the $^{1/3}$MLCT manifold while simultaneously increasing the ^{3}MC and ^{5}MC energies facilitated by the improved bite angles.[91] Computational work which followed these works suggested the replacement of the pyridine units with cyclometalating phenyl unit or NHC would prove helpful in imposing a stronger ligand field.[92]

NHC and cyclometalating ligands

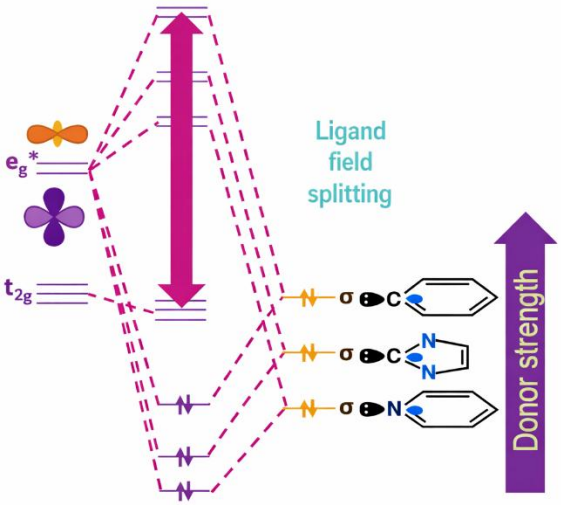

Figure 10: Effects of increasing donor strength on the ligand field splitting.[93]

As the use of strong π -acceptors increases the stability of the t_{2g} orbitals, the other option would be to destabilize the e_g* orbitals with strong σ-donating ligands like imidazolylidenes. The interaction between a carbene ligand and a metal center can

generally be described in terms of σ- and π-contributions. The σ-interaction arises from the overlap of the ligand σ-orbital with metal-centered orbitals. Owing to symmetry considerations, this interaction is restricted to the antibonding e_g* orbitals (Figure 10), resulting in the formation of σ-bonds between the metal and the ligand. Like pyridine units commonly employed in photoactive complexes, N-heterocyclic carbenes (NHCs) act as neutral two-electron donor ligands. However, because carbon is less electronegative than nitrogen, the carbene lone pair has higher energy, leading to increased metal-ligand covalency for C-donor ligands compared to N-donors.[94] This enhanced σ-donation destabilizes the e_g* orbitals and consequently raises the energy of metal-centered (MC) excited states. This idea was first put into use by Wärnmark and coworkers obtaining long-lived ^{3}MLCT excited states and inspired many to follow.[95–99] C_{NHC}-$N_{pyridine}$-C_{NHC} manifold provides strong σ-donating properties but their π -accepting properties remain modest. This was further improved by introducing benzimidazolylidene and replacing the imidazolylidene moieties.[100] Iron NHC complexes have also been evaluated as photocatalysts for proton reduction, achieving turnover numbers of upto 10, in comparison to approximately 30 for analogous noble-metal photosensitizers.[101] Further increase of the number of carbene units had also resulted in increased lifetimes.[98] All six coordinations with carbenes provided the best results with lifetimes of up-to 0.5 ns.[102] π -Interactions play a comparatively minor role in NHC-metal bonding but are nonetheless noteworthy. Electron density from the nitrogen lone pairs within the NHC framework is donated into the empty p_z orbital of the carbene carbon (Figure 10), generating a partially occupied π-orbital that can weakly interact with the metal center. Despite this minor π -donating contribution, back-donation from the metal into the vacant π-acceptor orbitals of the carbene dominates, resulting in an overall π-accepting character of NHC ligands.[103] While discussing the π-acceptor properties, its also important to consider the π - donating contributions of the cyclometalating ligands. These complexes feature anionic carbon atoms bound to the metal center. Compared to the neutral charged carbene donors, the lone pairs on the anionic carbon atoms are higher in energy resulting in a more pronounced metal-carbon covalent bond. This further destabilizes the e_g* orbitals (Figure 10).[104] In ruthenium and iridium cyclometalated complexes with N^C^N and N^N^N ligand systems , it was also observed that the t_{2g} ground state was destabilized by the phenyl π orbital interaction with the t_{2g} orbital.[105–107] However, this was not the case in 3d transition metals, namely iron when both the central coordinating moieties were phenyl groups. This is due to the higher electron density along the central metal atom and the σ- donating phenyl carbon axis which causes the elongation of the metal-carbon bonds enabling low lying MC states to come into effect once more.[108] A simple solution to this problem would be to exchange the position of the central phenyl to the peripheral coordination spots on one of the ligands while keeping the other same.[108] This resulted in one of the first long-lived MLCT emission lifetimes reported for $3d^6$ transition metals at 2.4 ns in the NIR

region.[109] With these considerable advancements that had been availed in iron(II) complexes, it would be noteworthy to take a look into the photophysics of cobalt(III) complexes as they also have a d^6 electron configuration.

Cobalt based photosensitizers

Focus of photochemical research has slowly shifted to lighter transition metals in the recent years.[80,110,111] This is mostly motivated by the low cost and high abundance of such materials as compared to the precious metals.[112] Aside from the economic benefits these complexes offer much more in terms of fundamental understanding of photophysics in transition metals.[113–118] Much of the photophysical research on transition metals with d^6 configuration has been concentrated on Ru^{II}, Ir^{III} and Fe^{II} while isoelectronic Co^{III} still remains underexplored.

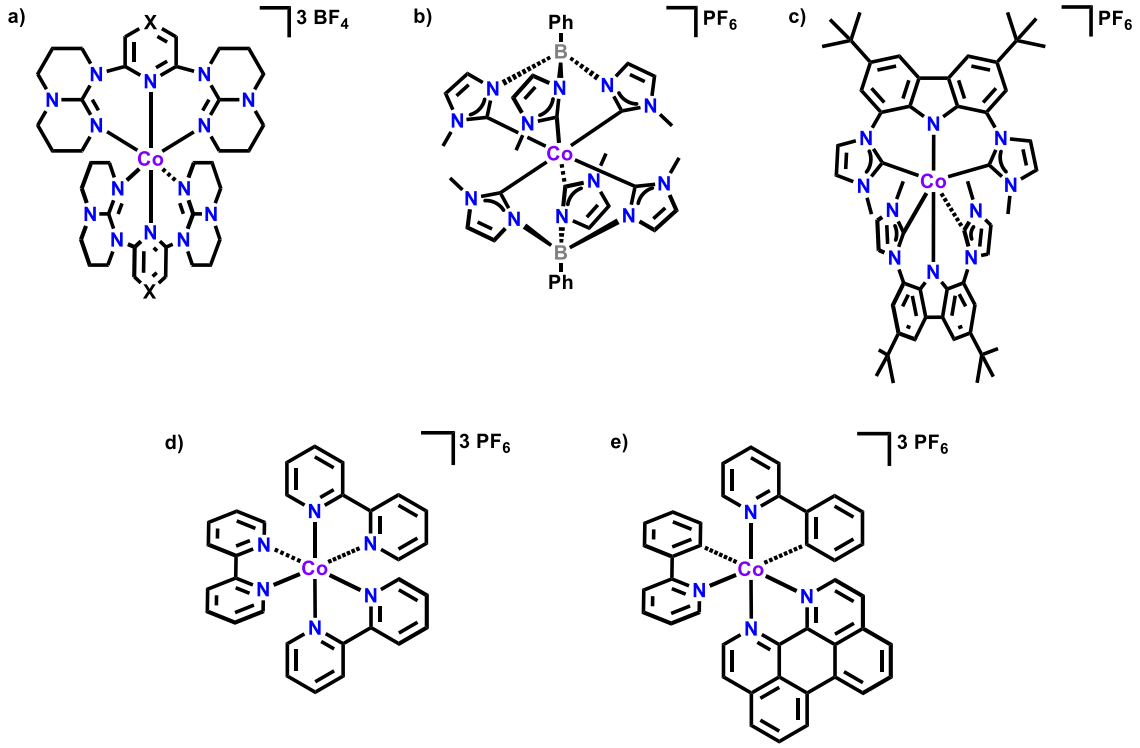

Figure 11: Molecular structures of previously investigated pertinent cobalt complexes.[118–123]

Until now there are only five known examples of Co^{III} complexes which are known to display photoactive behaviour and has been employed in photochemical applications (Figure 11).[119–123] Several studies have demonstrated that Co^{III} complexes can exhibit unexpected emissive behaviour. For example, Zysman-Colman and co-workers (Figure 10a) identified blue emission associated with ligand-to-metal charge-transfer (LMCT)

excited states, while Persson and co-workers reported markedly red-shifted emission originating from a ^{3}MC state (Figure 11b).[120,122] These observations are striking in light of the generally short-lived excited states typical of first-row transition-metal complexes, as the cobalt systems display excited-state lifetimes extending into the nanosecond and even microsecond regime. Although emissive metal-to-ligand charge-transfer (MLCT) states comparable to those found in Ru^{II} and Ir^{III} complexes have not yet been realized for Co^{III}, the unusually long-lived excited states of these complexes have already been harnessed for photoinduced electron-transfer (PET) processes (Figure 11c), as shown in subsequent studies by Wenger and co-workers.[121] Similar observations for PET have been observed in cyclometallated Co^{III} complexes by using just visible green light as well (Figure 11d).[123] This new type of photoreactivity has been suggested and proved for Co^{III} complexes by McCusker and co-workers by making use of inverted Marcus theory.[119] The relationship between ligand-field strength and excited-state lifetime can be rationalized using concepts derived from Marcus theory. It is most commonly applied to electron transfer processes but can also constitute a particular case of nonradiative decay theory within it and hence applicable to wider class of processes governing excited-state relaxation. [124] Eq1.2 describe the general correlation between, activation energy ($\Delta G^{\ddagger}$), reorganization energy (λ) and ground state recovery (ΔG^{o}). [125–127] An interesting output of this equation is that ($\lambda + \Delta G^{o}$) is quadratic in nature, which means that if ΔG^{o} is lesser than $-\lambda$, $\Delta G^{\ddagger}$ increases again. This region where $\Delta G^{\ddagger}$ increases again is termed as the Marcus inverted region as it behaves opposite to intuition.

$$\Delta G^{\ddagger} = \frac{(\lambda + \Delta G^{o})^2}{4\lambda} \qquad \text{Eq 1.2}$$

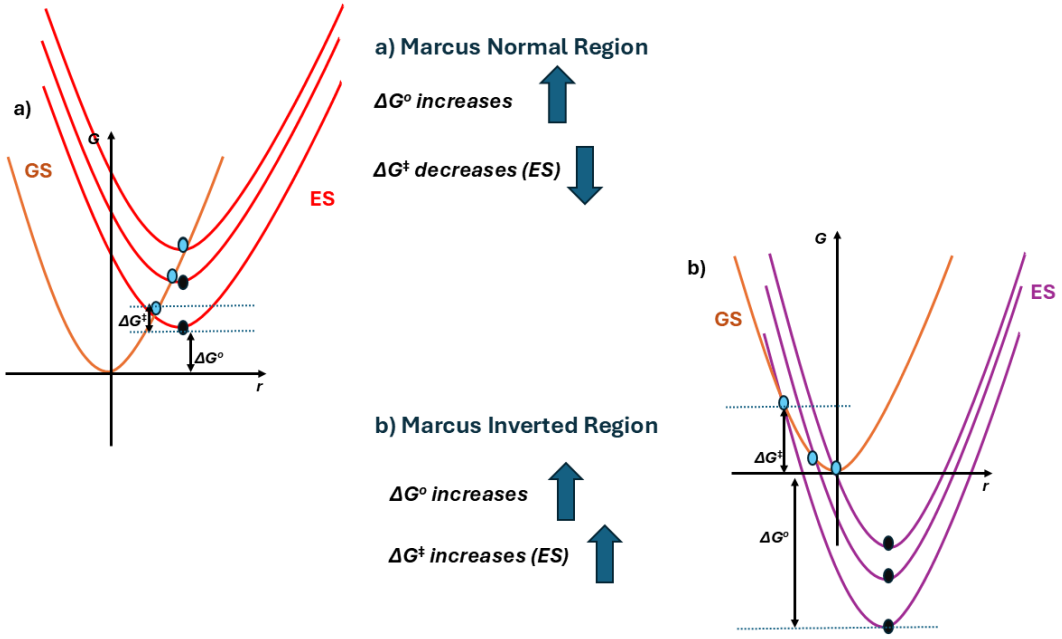

Figure 12: Potential energy wells of a) Marcus normal region and b) Marcus inverted region.[119]

Applying this theory to excited state mechanics yields the conclusion that increasing the ligand field leads to the fast excited state relaxation times in the Marcus normal region (Figure 12a). While stronger ligand fields are needed to access highly energetic excited states for demanding photocatalytic reactions, they simultaneously tend to shorten excited state lifetimes due to the inverse relationship between driving force and lifetime. Studies of ligand field strength of cobalt complexes cites that $[Co(en)_3]^{3+}$ has field strength that is 0.6 V higher than that of $Co(acac)_3$, and also experiences a lifetime that is almost 100 times higher than $Co(acac)_3$.[128,129] Hence it was hypothesized that photophysics of Co^{III} complexes would be occuring in the Marcus inverted region. $[Co(bpy)_3]^{3+}$ exhibits excited state lifetimes of 5.0 ns and was henceforth tested in catalyzing oxidative $C(sp^2)$–N coupling of aryl amides with challenging sterically hindered aryl boronic acids.[119] These new advances are quite remarkable but still the need for more easily accessible systems based on Earth-abundant metals need to be prioritized. Light induced radical reactions is a very well researched field but once again the research is heavily based on organic substrates which require high energy for their activation. Hence, once again the alternative would be to look into organometallic complexes which are capable of generating radicals.[130]

Organometallic radicals

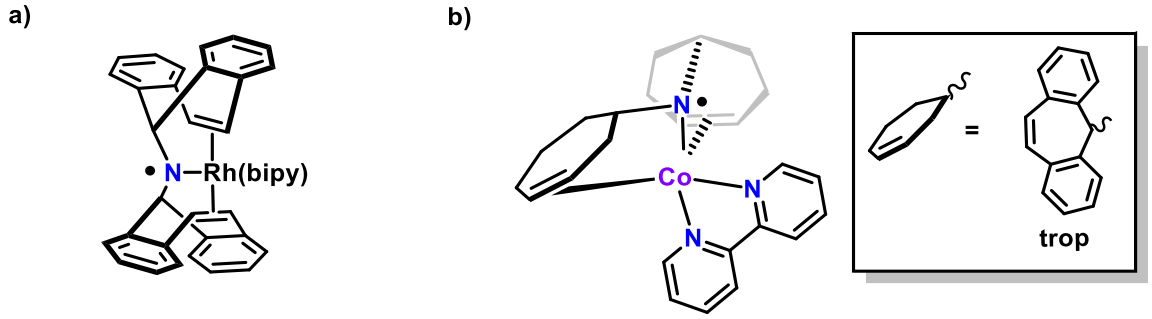

Figure 13: Stable aminyls radicals based on rhodium (a) and cobalt (b).[131,132]

In most transition-metal complexes that contain unpaired electrons, the spin density is largely localized on the d orbitals of the metal center with only limited extension on to the surrounding ligands. The cases where the radical instead resides on the ligands are much rarer. Semiquinone and phenoxyl based systems are known to form π-delocalized radicals that coordinate to metals through oxygen atoms and play significant roles in biological and chemical processes.[133,134] Another important class is the nitrogen based aminyl radical complexes. Aminyl radicals are normally short lived and very unstable species.[135] The first metal stabilized aminyl radical was reported by Grützmacher and co-workers in 2005 (Figure 13a).[131] These were used in hydride abstraction reactions featuring their ability to attack only selected substrates despite being a radical species. Spin density calculations attributed 54 % on the nitrogen atom and only about 30 % on the metal center. Similar complexes bearing on $trop_2NH$ ligand ([bis(5-H-dibenzo[a,d]cyclohepten-5-yl)-amine]) were also investigated on rhodium and iridum as metal centers.[136] More recently in 2017, Grützmacher and co-workers were able to translate this work onto cobalt as well (Figure 13b).[132]

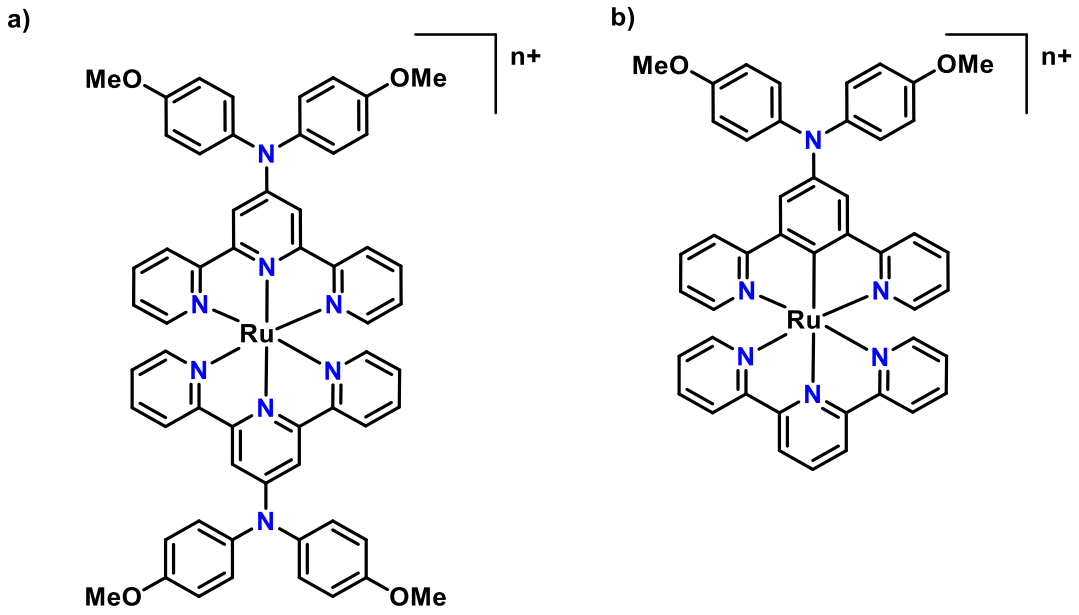

Figure 14: Structures of ruthenium based mixed valence complexes.[137,138]

Mixed valence complexes are another class of complexes which upon oxidation could generate different radical states based on the redox activity of the metal center. Bis(terpyridine)ruthenium(II) complexes were modified with di-*p*-anisylamino group to unlock these mixed valence complexes (Figure 14a).[138–140]Assymetric complexes of ruthenium with cyclometalation on one side and further modified with the di-*p*-anisylamino group were also inspected.[137] The influence of cyclometalation resulted in reduced redox potentials as compared to the former set of complexes[137,141]. These complexes have found a lot of applications in molecular electronics.[142] However, most of them require harsh oxidative conditions to function. Consequently, the photogeneration of such a radical state would give these complexes much better practical applicability. Furthermore, the economic aspects would benefit if these complexes could be synthesized out of Earth-abundant metals. As from previously discussed $Co(trop_2N)(PF_6)$ complexes, it is possible for cobalt to stabilize radicals and use them for chemical applications. Combining these two ideas to synthesize a light induced radical system stabilized by cobalt as the metal center was the last objective of this dissertation and is further discussed in chapter 4.

Aim Of This Work

Climate change is driven primarily by greenhouse gas emissions from the combustion of fossil fuels, represents one of the most pressing global challenges of the 21st century. The continued reliance on coal, oil and natural gas not only accelerate global warming but also increases air pollution, ecosystem degradation and depletion of resources. In response, the transition toward renewable energy resources has become a central scientific and technological priority. Renewable resources such as solar, wind and hydropower offer the possibility of drastically reducing carbon emission while providing a sustainable and virtually inexhaustible energy supply. Consequently, the development of efficient technologies for harvesting, converting and storing renewable energy is essential for achieving climate change targets and enabling a sustainable energy future. Therefore, in this thesis, the focus is on finding new alternatives for utilizing and converting sunlight into a usable driving force for electron transfer reactions.

Much of the photochemistry that has been done is based on organometallic complexes based on precious metals like ruthenium, iridium and platinum. These form a very small percentage on the Earth's crust and their extraction and refinement are equally challenging. However, photochemistry can still be done from Earth-abundant metals like iron and cobalt as well as purely organic substrates. Organic complexes are far cheaper to synthesize as compared to the precious metals and offer exceptional emissive properties that has been used in a lot of applications. However, they suffer some photodegradation under continuous use. Hence, one of the objectives of this thesis is to design and synthesize an organic photosensitizer that displays improved stability when compared to the already existing ones.

Increasing the photostability alone does not cover the difference in performance when compared to the heavier transition metal-based photosensitizers. Most of these photosensitizers show significant absorptions in the visible range while organic photosensitizers most often require high energy UV radiation to initiate their photochemistry. They are also much more photostable when compared to the organic photosensitizers. Therefore, for the later chapters of this thesis, the focus shifts to uncovering the excited state dynamics of complexes based on cobalt, a reasonably abundant metal in Earth’s crust.

Chapter 2: Emissive Oxygen Bridged Pyridine Phenolate Boron Complex

This chapter focuses on the synthesis, structural elucidation, and photophysical characterization of a novel oxygen-bridged diboron complex (BOB) supported by a rigid O^N^O ligand framework, together with its fluorinated monomeric analogue (BF) which is very similar to the already well documented 2,2'-(pyridine-2,6-diyl)diphenolate (dppy) systems. These two systems provide an instructive platform for examining how bridging versus monomeric coordination at boron influences molecular geometry, electronic structure, and excited-state behavior. The incorporation of an intramolecular oxygen bridge between two boron centers represents a comparably rare architectural motif.

Single-crystal X-ray diffraction reveals pronounced geometric differences between the two architectures. The fluorinated monomer BF adopts a nearly ideal tetrahedral coordination environment at the boron center, with narrow angular distributions and bond lengths consistent with previously reported O^N^O-supported boron complexes, including closely related (dppy) systems. In contrast, the oxygen-bridged diboron complex BOB exhibits significantly distorted tetrahedral geometries at both boron centers. These distortions manifest as broader angular dispersions and slightly elongated bond lengths, arising from the geometric constraints imposed by the oxygen bridge. Electrochemical investigations further highlight the robustness of the oxygen-bridged framework. The BOB complex displays high stability over a wide electrochemical window and undergoes a quasi-reversible oxidation at +1.20 V versus Fc/Fc^{+}. Photophysical studies reveal clear consequences of oxygen bridging on the optical properties. The diboron complex BOB exhibits bathochromically shifted and more intense absorption bands relative to BF, with prominent features observed at 400, 357, and 306 nm, compared to absorption maxima at 383 and 330 nm for the monomer. Both complexes emit in the visible region, with emission maxima at 483 nm for BOB and 474 nm for BF. Time-resolved emission spectroscopy demonstrates comparable excited-state lifetimes on the nanosecond timescale (3.57 ns for BOB and 3.89 ns for BF), accompanied by moderate photoluminescence quantum yields of 0.15 and 0.18, respectively.

Overall, the results presented in this chapter establish oxygen-bridged diboron complexes as structurally distinctive yet underexplored photosensitizers. By directly comparing bridged and monomeric O^N^O-supported boron systems, this work provides fundamental insight into how framework connectivity and geometric constraint influence electronic structure and emissive behaviour. These findings lay the groundwork for future ligand design strategies aimed at optimizing boron-based chromophores for light-harvesting, sensing, and photonic applications

Participations in this project:

Athul Krishna: Design and synthesis of the title molecule, its standard characterization (NMR, MS, IR), cyclic voltammetry, UV-Vis spectroscopy, emission spectroscopy, interpretation of the data, manuscript writing- Institute for Inorganic Chemistry and Center for Sustainable Systems Design (CSSD), Paderborn University, Paderborn 33098, Germany

Jannik Lösecke: TD-DFT calculations − Institute for Inorganic Chemistry and Center for Sustainable Systems Design (CSSD), Paderborn University, Paderborn 33098, Germany

Dr. Lorena Fritsch: TD-DFT calculations − Institute for Inorganic Chemistry and Center for Sustainable Systems Design (CSSD), Paderborn University, Paderborn 33098, Germany

Dr. Michal Nowakowski: TD-DFT calculations − Institute for Inorganic Chemistry and Center for Sustainable Systems Design (CSSD), Paderborn University, Paderborn 33098, Germany

Dr. Jakob Steube: Interpretation of the data, insightful discussions and review of the manuscript - Institute for Inorganic Chemistry and Center for Sustainable Systems Design (CSSD), Paderborn University, Paderborn 33098, Germany

Dr. Roland Schoch: X-ray diffraction measurements - Institute for Inorganic Chemistry and Center for Sustainable Systems Design (CSSD), Paderborn University, Paderborn 33098, Germany

Jun. Prof. Dr. Felix Fischer: Review of the manuscript- Institute for Inorganic Chemistry and Center for Sustainable Systems Design (CSSD), Paderborn University, Paderborn 33098, Germany

Prof. Dr. Matthias Bauer: Project Supervisor - Institute for Inorganic Chemistry and Center for Sustainable Systems Design (CSSD), Paderborn University, Paderborn 33098, Germany

Emissive Oxygen Bridged Pyridine Phenolate Boron Complex

Athul Krishna*[a], Jannik Lösecke[a], Jakob Steube[a], Lorena Fritsch[a], Michal Nowakowski[a], Roland Schoch[a], Stephan Hohloch[b], Matthias Bauer[a], Felix R. Fischer*[a]

[a] A. Krishna, J. Lösecke, Dr. J. Steube, Dr. L. Fritsch, Dr. M. Nowakowski, Dr. R. Schoch, Jun. Prof. Dr. F. R. Fischer, Prof. Dr. M. Bauer
Institute of Inorganic Chemistry and Center for Sustainable Systems Design (CSSD)
Paderborn University
Warburger Str. 100, 33098- Paderborn, Germany
E-mail: matthias.bauer@upb.de

[b] assoz. Prof. Dr. S. Hohloch,
Department of General, Inorganic and Theoretical Chemistry
University of Innsbruck
Innrain 80-82
A-6020 Innsbruck, Austria

Supporting information for this article is given via a link at the end of the document.

Abstract: The exploration of new boron-based luminescent materials offers opportunities for advancing optoelectronic, sensing, and photonic applications. In this study, we describe the synthesis, structural analysis, and photophysical characterization of an oxygen-bridged diboron complex (BOB) supported by an O^N^O ligand framework, together with its fluorinated monomeric analogue (BF). Single-crystal X-ray diffraction revealed that BF adopts a nearly ideal tetrahedral environment at boron central atom, whereas BOB exhibits significantly distorted tetrahedral geometries, characterized by broader angular dispersions and elongated B-X bond lengths induced by the oxygen bridge. Electrochemical investigations demonstrated high stability across a wide potential window, with BOB undergoing a quasi-reversible oxidation at +1.20 V vs. Fc/Fc^+. Fluorinated monomeric species (BF) being very similar to the already reported 2,2′-(pyridine-2,6-diyl)diphenolate (dppy) systems were obtained after reaction with $NOPF_6$. Photophysical studies revealed that BOB displays red-shifted and more intense absorption features (400, 357, 306 nm) compared to BF (383, 330 nm). Both complexes emit in the visible region, with maximum intensity at 483 nm (BOB) and 474 nm (BF). Time-resolved spectroscopy proved similar excited-state lifetimes (3.57 and 3.89 ns, respectively) and moderate quantum yields (Φ = 0.15 and 0.18). These results identify oxygen-bridged diboron systems as structurally distinctive yet underexplored scaffolds, offering new opportunities for tailoring emissive boron chromophores through ligand and framework design.

Introduction

The development of novel luminescent compounds remains a central focus of modern materials chemistry, as their utility spans from optoelectronics to energy conversion, sensing, and biomedical imaging.[1] The demand is particularly high for organic luminescent compounds, which combine synthetic tunability, solution processability, and versatile photophysical behavior.[2] Their use as fluorescent probes, laser dyes, indicator dyes, and emissive components in organic light-emitting diodes (OLEDs) has already revolutionized multiple fields of science and technology.[3] Within this broad class of chromophores, boron-containing luminescent materials have attracted exceptional attention due to their distinctive structural and optical features.[4] Boron complexes often exhibit high fluorescence quantum yields, sharp and tunable emission bands, and significant stability under ambient conditions.[5] Boron-based chromophores derive their advantages from the electron-deficient nature of boron and its capacity to stabilize delocalized

π-systems through coordination. This is particularly evident in B-N compounds, whose luminescent efficacy stems from their unique electronic structures and aromatic stabilization.[6] The coordination often rigidifies the molecular framework, thereby suppressing non-radiative decay pathways by limiting vibrational and rotational freedom.[7] Moreover, through purposeful design of boron incorporation, such as in multiple-resonance coordination motifs, the electronic transitions of these systems can be finely tuned, achieving narrow emission, high quantum efficiency, and adjustable photophysical behavior.[8]

Among boron-based fluorophores, BODIPY (boron-dipyrromethene) dyes have achieved a dominant role due to their outstanding photophysical properties, including narrow absorption and emission profiles, high molar extinction coefficients, and photostability.[2] They have been widely exploited in biological imaging, photodynamic therapy, solar energy harvesting, and as laser dyes.[9] Structural modification of BODIPYs, such as through π-extension, introduction of electron-withdrawing substituents, or replacement of heteroatoms, has expanded their emission range from visible light into the near-infrared range, further broadening their applicability.[10] One commonly noted limitation of BODIPY dyes is their susceptibility to photodegradation or solvent-induced instability, which arises from the sensitivity of the B-F bonds to polar environments.[11] One effective approach to addressing this limitation is to replace the fluorine atoms with aryl or alkynyl substituents. The resulting organoboron derivatives typically exhibit enhanced stability and improved photophysical properties with bis(alkynyl)-borane systems being particularly successful examples.[12] Beyond BODIPYs, a wide range of boron-based luminescent materials has emerged, which are decorated by versatile ligand scaffolds. For instance, triarylboranes with strong electron-accepting boron centers have been investigated as efficient electron-transporting materials and luminescent building blocks for OLEDs and sensors.[5b,8,13] Boron complexes with N^O-type ligands, particularly phenolic and salicylaldimine frameworks, have also been extensively studied, showing their promise in OLED applications due to their strong absorption and emission in the visible light region.[14]

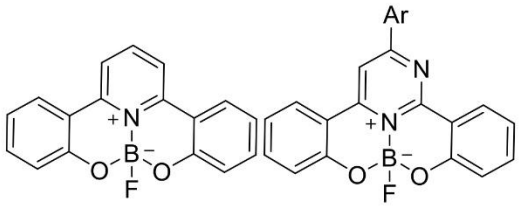

Scheme 1. Similar four-coordinate boron complexes reported in literature.[15]

More recently, four-coordinate boron complexes have garnered increasing attention once more as highly robust luminescent systems for electroluminescent applications.[16] 2,2′-(pyridine-2,6-diyl)diphenolate (dppy) (A) is a well-established tridentate ligand known to reliably generate tetracoordinate boron complexes.[15a,17] 6-aryl-2,4-bis(2′-hydroxyphenyl)pyrimidine ligands and their boron fluoride complexes (B) have also been recently reported which display tetracoordinate boron complexes.[15b] Their ability to enforce rigid ligand geometries enhances emission efficiency, while their structural modularity permits precise tuning of electronic and photophysical properties[14a]. For example, incorporation of boron into donor-acceptor systems enables intramolecular charge transfer, yielding compounds with broad and tunable emission ranges.[18] The introduction of heavy atoms or fluorinated substituents has further expanded their photophysical versatility by promoting intersystem crossing and enabling phosphorescent or delayed fluorescence pathways.[14a,19] A particularly exciting advance is the development of boron-based emitters capable of thermally activated delayed fluorescence (TADF), which hold promise for next-generation OLEDs. TADF-active boron complexes have been reported by Yam and co-workers, who introduced four-coordinate fluoro-boron complexes supported by O^N^O-type ligands, achieving efficient emission through a small singlet-triplet energy gap.[20] This approach highlights the potential of ligand design and boron

coordination to control excited-state dynamics in ways previously reserved for purely organic donor-acceptor systems.[21] In parallel, boron-containing luminescent compounds are being explored beyond OLEDs. Their excellent optical properties and modularity have positioned them as promising candidates for chemosensors, nonlinear optical materials, and light-harvesting assemblies.[3,4c] In bioimaging, the biocompatibility and tunability of boron complexes are leveraged for designing near-infrared dyes with deep tissue penetration.[5b] These diverse applications underscore the multifunctional nature of boron-based luminescent systems and the critical role of structural design in tailoring their properties.

Despite this impressive progress, the scope of boron luminescent compounds remains far from fully explored. New ligand architectures that enforce rigidity while allowing electronic modulation are needed to achieve high efficiency and stability across applications. Oxygen-bridged diboron complexes, for example, remain relatively underexplored, despite their potential to combine strong B-O coordination with extended conjugation. Similarly, fluorinated analogues of boron complexes represent an emerging class with unique electronic effects that could be harnessed for tuning excited-state dynamics.[16a] In this study, we report the synthesis, crystal structures, and optoelectronic properties of a new oxygen-bridged diboron complex based on an O^N^O ligand system, along with a fluorinated monomeric analogue. By comparing their structural and photophysical characteristics, we provide new insights into the design of luminescent boron-based materials, thereby expanding the growing family of emissive boron complexes for advanced optoelectronic applications.

Results and Discussion

Synthesis and Characterisation

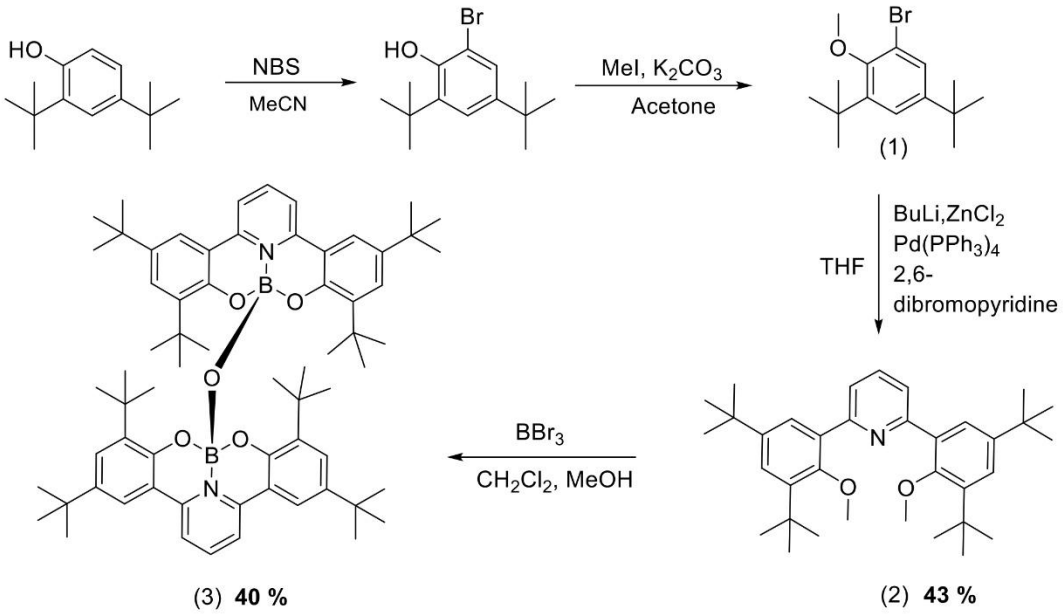

Scheme 2. Four-step synthesis of BOB-complex (3) starting from 2,4-di-tert-butylphenol.

Initial synthesis was done by targeting the phenolate-pyridine-phenolate (**O^N^O**) ligand starting from 2,4-di-tert-butylphenol as precursor. It was brominated using N-bromosuccinimide. The hydroxyl group was then methylated using a procedure reported earlier by deprotonating first with potassium carbonate in acetone and followed by the addition of methyl iodide.[22] This was followed by coupling two equivalents of 1 with 2,6- dibromopyridine under Negishi reaction conditions.[23] Boron tribromide was finally used as the boronating agent and transforming the dimethylated species 2 into the desired oxygen bridged dimeric pyridine bis phenolate boron complex - BOB (3). Borylation was confirmed using ^{11}B NMR which showed a single peak at 2.38 ppm. (cf. Figure S9). The small difference relative to the literature-known pyrimidine diphenolate boron fluoride complexes (δ ≈ 1.65 ppm) reflects the different coordination environments and presence of B-F bonds in the latter.[15b] Single crystal X-ray diffraction of crystals grown out of toluene evaporation gave evidence of the formation of oxygen bridged diboron complex (Figure 2).

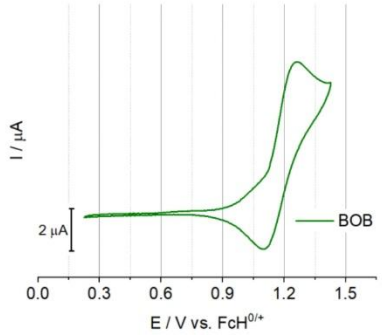

Figure 1. Cyclic voltammetry spectrum of BOB-complex (1 mM solution in MeCN) with (nBu$_4$N)(PF$_6$) as the electrolyte at 0.1 V/s.

Cyclic voltammetry provided valuable insights into the stability of the complex across a broad potential window. A quasi-reversible oxidation was observed at 1.20 V vs. Fc/Fc$^+$, while no reductive events occurred prior to solvent reduction (Figure 1). The relatively high stability under both oxidative and reductive conditions suggests that the complex is well suited for solution-phase applications under variable electrochemical environments. Additionally, to probe the stability of the BOB-compound against chemical oxidation conditions, this complex was dissolved in dichloromethane together with nitrosonium hexafluorophosphate.[24] The choice of this oxidant ensured minimal byproducts, as the nitrogen oxides formed are gaseous and can be readily removed. ^{1}H NMR analysis of the product showed that all signals

4

were retained, though small shifts were observed, most notably in the aromatic region, supporting the formation of a new product.

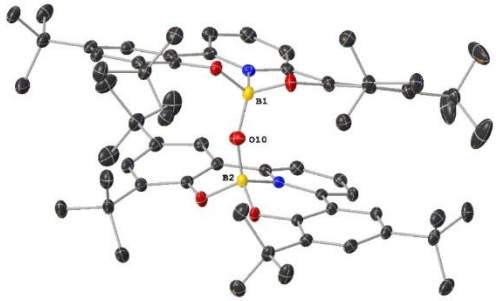

Figure 2. Single crystal structure of BOB with relevant atoms marked. (Anisotropic displacement parameters drawn on a 50% probability level, H atoms omitted for clarity).

A fluorinated monomeric version (BF) of the BOB complex was obtained by treating the BOB complex with $NOPF_6$ in dichloromethane. Single crystals suitable for X-ray diffraction were subsequently obtained from toluene solution evaporation. Structural analysis revealed a monomeric species in which fluorination occurred at the boron center. This was further underlined by ^{19}F NMR investigation showing a fluorine peak at -145 ppm. A fluorine peak at -136 ppm was reported for the pyrimidine based boronate complex.[15b] Pyrimidine ligands are stronger π-accepting and therefore electron-withdrawing moieties, which deshields the boron center to a higher extend than in this pyridine-based BF-complex, shifting the fluorine resonance downfield. Cyclic voltammetry of the newly formed product reveals a redox event at +0.60 V vs Fc/Fc^+ (c.f. Figure S13). In contrast, the parent BOB complex exhibits an oxidation at +1.20 V vs Fc/Fc^+, representing a pronounced anodic shift relative to the corresponding redox process. Given the similar electronic structures of the product species, this shift indicates increased ground state stabilization within the BOB framework. This behavior may further be influenced by the steric demand of the tert-butyl substituents, which likely enforces a more rigid coordination environment.

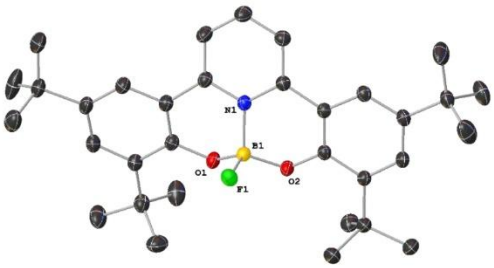

Figure 3. Single crystal structure of BF with relevant atoms marked. (H atoms omitted for clarity).

The monomeric BF complex exhibits a nearly ideal tetrahedral geometry at the boron center, with six X-B-X angles giving a mean value of 109.47° (range 106.5-112.1°), a mean angular deviation (MAD) from 109.5° of 1.79°, and a maximum deviation of only 3.0°. By contrast, the dimeric BOB complex contains two boron centers (B1 and B2) that display significantly more distorted tetrahedral environments. The combined analysis yields an averaged mean angle of 109.34° with a broader range of 102.3-116.6°, corresponding to an average MAD of 4.07° and a maximum deviation of 7.2°. Although the mean values remain close to the ideal tetrahedral angle, the angular dispersion is approximately twice as large in the dimer compared

to the monomer, clearly indicating greater deviation from ideal sp^3 geometry. This enhanced distortion can be attributed to the bridging/chelating constraints. In contrast, the monomer with its single boron site, maintains a more isotropic and rigid coordination sphere. Consistent with this increased strain, the B-X bond lengths in the dimer are elongated relative to those in the monomer, most notably the N1-B1 bond, which extends to 1.618(8) Å in the BOB complex compared to 1.580(2) Å in the BF compound. Similar observations were noted in the dppy borane complexes.[17] The observed averaged bond lengths are slightly longer than those observed in F-BODIPY[25] but these bond lengths around the boron atom are in agreement with literature reported values of borane compounds with a N,O-coordinating and N,N-coordinating ligand.[12b,26] Furthermore, the steric influence of the tert-butyl substituents on the phenyl rings directs them into the intermolecular voids, thereby preventing potential π-π stacking interactions and results in the bridging angle (B1-010-B2) of 152.8°.

Table 1. Relevant bond angles and bond lengths for BOB and BF obtained by single crystal X-ray diffraction.

Bond angle and length	BOB	BF
N1-B1-O1	106.0(5)°	108.8(12)°
N1-B1-O2	106.4(5)°	110.4(12)°
N1-B1-(O10/F1)	110.9(5)°	106.5(12)°
O2-B1-(O10/F1)	116.6(6)°	111.3(12)°
O1-B1-(O10/F1)	112.3(5)°	112.1(12)°
O1-B1-O2	103.8(5)°	107.7(13)°
N1-B1	1.618 (9) Å	1.580 (2) Å

6

O2-B1	1.448 Å	(8)	1.428(18) Å
O1-B1	1.460 Å	(8)	1.438(19) Å

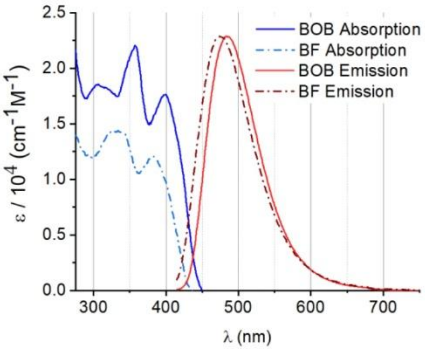

Figure 4. Absorption and normalized emission spectra of BOB and BF in dichloromethane [10 mM]. Emission spectra were recorded after excitation at 340 nm.

The UV/Vis absorption spectrum of the BOB complex exhibits three distinct absorption bands with maxima at 400, 357, and 306 nm (Figure 4). In comparison, the BF monomer displays two principal absorption bands that are blue shifted, with maxima at approximately 383 and 330 nm (Figure 4). Time-dependent DFT (TD-DFT) calculations confirm almost purely ligand centered ($\pi \rightarrow \pi^*$) transition characters for all features in both molecules (Figure 5). Additionally, TD-DFT calculation showed that analogous transitions are responsible for the 400 nm absorption feature in BOB and the 383 nm absorption feature in BF as well as for the 357 nm (BOB) and 330 nm (BF) (Figure 5, cf. Table S1-S3). Notably, the BOB complex also shows significantly higher molar extinction coefficients than the monomer. For BOB, the absorptions at 400 and 357 nm correspond to $\varepsilon = 1.76 \times 10^4$ and 2.20×10^4 M^{-1} cm^{-1}, respectively, while for BF the corresponding values at 383 and 330 nm are $\varepsilon = 1.20 \times 10^4$ and 1.42×10^4 M^{-1} cm^{-1}. The bathochromic shift and increased intensity observed for BOB are consistent with an extended conjugation pathway and stronger electronic transitions induced by the oxygen-bridged diboron framework.[26a]

7

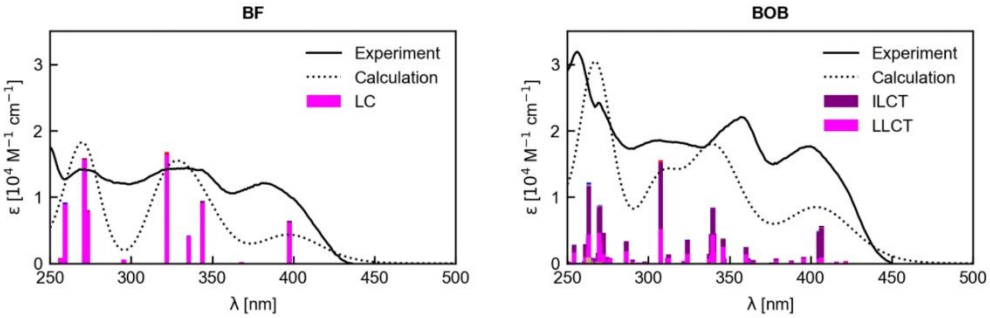

Figure 5. Comparison between TD-DFT calculated and experimentally measured absorption spectra of BF- and BOB-complexes. TD-DFT calculated vertical transitions are shown as sticks reflecting the oscillator strength and shown as a spectrum with a broadening (fwhm) of 2825. 75 cm^{-1} as a dotted line in comparison to the experimental spectrum as a black solid line. The colors indicate different transition characters. (LC- ligand centered, ILCT- intraligand charge transfer, LLCT- ligand to ligand charge transfer) For simplicity only characters with significant contribution are listed in the figure. For more details review Figure S11.

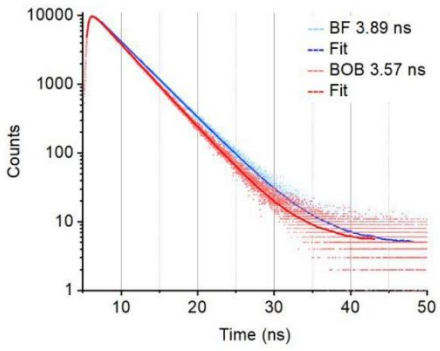

Figure 6. Time-corelated single-photon count (TCSPC) of BOB and BF in dichloromethane

Similarly, in the emission spectra the BOB complex displays a fluorescence maximum at 483 nm, while the BF monomer exhibits a blue-shifted emission maximum at 474 nm. Excitation spectra of both emissions reciprocated the absorption spectra (cf. Figure S12). The red-shifted and more intense emission of BOB relative to BF mirrors the absorption trends, reflecting enhanced conjugation and stabilization of the excited state.[2,3,26a,27] The emissions are slightly red shifted compared to the previously reported (dppy)BF which exhibits strong blue emission at 445 nm.[15a] Strong intermolecular π-π interactions were expected in (dppy)BF whereas the presence of bulky tert-butyl groups disrupts efficient π-π interactions in the case of the BF and allows the red- shift of the emission compared to (dppy)BF. Time-resolved studies further support this similarity, with excited-state lifetimes of 3.57 ns for BOB and 3.89 ns for BF, while both systems display nearly identical photoluminescence quantum yields of 0.15 and 0.18 respectively (cf. Figure S10).

8

These results indicate that although the diboron framework modifies the absorption and emission profiles, the fundamental excited-state dynamics remain comparable between the two systems.

While the BOB and BF complexes display respectable photophysical characteristics, they remain modest in performance compared to benchmark systems such as BODIPY dyes, which are well-known for their very high molar and near-unity fluorescence quantum yields.[2,3,26a,28] Nonetheless, the observed mono-exponential lifetimes – 3.57 ns (BOB) and 3.89 ns (BF) – lie within the typical range for BODIPYs (1-10 ns), suggesting that the excited-state decay dynamics of our complexes are comparable.[26a,29] Our results also align with recently reported boron–spiro systems and luminescent blue emissive bis(alkynyl) borane compounds with a N,O-coordinated ligand which exhibit mono-exponential fluorescence lifetimes in the range of 2.7-3.9 ns, complemented by moderate efficiencies.[26a,30] Meanwhile, emerging dibora-anthracene (DBA) derivatives incorporating extended conjugated boron frameworks also achieve similar quantum yields (up to 0.15), but higher fluorescence lifetimes of up to 12.5 ns.[31] These systems demonstrate how greater structural rigidity and delocalization can substantially elevate emissive performance.

Conclusion

In summary, we have synthesized a new oxygen-bridged diboron complex (BOB) that generates a fluorinated monomeric analogue (BF) upon treatment with $NOPF_6$, and fully characterized both species using NMR, XRD, CV, absorption and emission spectroscopy as well as TCSPC. These studies provide insights into the structural and photophysical consequences of bridging versus monomeric coordination modes in boron-based chromophores. Single-crystal X-ray diffraction reveals that the monomer maintains a nearly ideal tetrahedral geometry at boron, whereas the diboron framework imposes greater angular distortion and elongated B-X bonds due to the bridging constraints. Electrochemical analysis establishes high stability across a broad potential window, with a quasi-reversible oxidation at +1.20 V vs. Fc/Fc^+ which is almost double the potential as compared to monomeric BF.

Photophysical studies further demonstrate that the diboron architecture enhances electronic conjugation, manifested in bathochromically shifted absorption and emission bands and increased extinction coefficients relative to the monomer. These effects are amplified by the presence of tert-butyl groups, which suppress the strong intermolecular π-π interactions typically observed in previously reported dppy-borane complexes. Despite these structural differences, both complexes exhibit similar excited-state dynamics, with nanosecond lifetimes (3.57 ns for BOB; 3.89 ns for BF) and moderate quantum yields in DCM (Φ = 0.15 and 0.18, respectively).

Compared to benchmark boron emitters such as BODIPYs and diboraanthracenes, the photophysical performance of these systems remains modest, but is comparable to that of dppy- and pyrimidine-based borane complexes. Overall, this work demonstrates the potential of oxygen-bridged architecture and the strategic incorporation of tert-butyl substituents as effective approaches for tuning electronic transitions, stabilizing excited states, and improving solubility in boron-containing chromophores. These design elements may be further optimized through ligand modification, extended conjugation, or structural rigidification to achieve enhanced luminescent efficiencies for optoelectronic and sensing applications.

Experimental Section

Materials and Methods

All experiments were carried out under an argon atmosphere using standard Schlenk or Glovebox techniques unless specified. Glassware was oven-dried at 130 °C prior to use. Dry solvents were obtained

from an MBraun SPS-800 solvent-drying system, degassed *via* sparging with argon and subsequently stored over a 4 Å molecular sieve. ^{1}H NMR spectra were recorded using Bruker Avance 500 and Bruker Ascent 700 spectrometers Chemical shifts are expressed in parts per million (ppm, δ) downfield from tetramethylsilane (TMS). The spectra were referenced to the residual proton signals of the respective deuterated solvent. All coupling constants (*J*) are absolute values and are expressed in Hertz (Hz). The spectra were analyzed according to first order. Electrospray ionization mass spectrometry spectra were recorded on a Waters Synapt G2 Quadrupole Time-of-Flight spectrometer, using acetonitrile as solvent. For cyclic voltammetry, dry acetonitrile was obtained by passing HPLC-grade acetonitrile (Fisher) over a column of MP Biomedicals MP Alumina N - Super I, which was activated in an oven at 150 °C for multiple days. The cyclic voltammetry measurements were performed at room temperature in a 0.1 M [nBu$_4$N][PF$_6$] acetonitrile solution with an analyte concentration of 0.001 M under a solvent-saturated argon atmosphere. A three-electrode arrangement with a 1 mm Pt working electrode, a Pt wire counter electrode (both Metrohm), and an Ag/AgCl reference electrode (custom built) was used with a Metrohm PGSTAT101 potentiostat. Ferrocene was added after the measurements as an internal standard. All potentials were referenced against the FcH$^{0/+}$ couple. The voltammograms were analysed using the NOVA software (version 2.1.3). The diagnostic criteria for reversibility were based on those proposed by Nicholson[32] and the Randles-Sevcik equation.[33] Dichloromethane of spectroscopic grade (SPECTRONORM VWR Acetonitrile) was used as the solvent for steady-state absorption spectroscopy (c = 0.1 mM), which were recorded using in quartz cuvettes (path length = 10 mm) using a Cary 50 or PerkinElmer Lambda 45 spectrometer. For steady-state emission spectroscopy at room temperature, dichloromethane of spectroscopic grade was used as the solvent. Steady-state emission spectra were recorded in 10 mm quartz cuvettes on an Edinburgh Instruments FLS1000 spectrometer with single monochromators and a red-extended PMT-980. The solutions for the measurements under argon were degassed using the freeze-pump-thaw technique. The samples were prepared analogous to the steady-state emission samples. Time correlated single photon counting was measured using a Horiba Ultima-01-DD (Horiba Jobin Yvon GmbH). The sample solution was excited at 374 nm using a Horiba DD375L laser diode with a maximum repetition rate of 100 MHz. The decays of the emissions were measured at the specified wavelengths. Repetitive start-stop signals were recorded by a multi-channel analyzer until one of the channels reached 10000 counts. The decays were analyzed together with the instrument response function (IRF) in the EzTime software from Horiba. The IRF was measured at 374 nm using a scatter solution of dispersed LUDOX in water. Fitting of the decays followed the procedure of increasing the number of fitted exponentials until the $\chi 2$ parameter was smaller than 1.2. The goodness of the fit was reviewed by looking at the residuals, to see, whether they are statistically aligned around 0. The presented X-ray single crystal data were measured on a *Bruker* Venture D8 three-cycle diffractometer equipped with a Mo K_α μ-source (λ=0.71073 Å), an *Incoatec* multilayer monochromator and a Photon III detector at 120 K. The data were integrated with SAINT and afterwards a multi-scan absorption correction was applied using SADABS. [34] Structure solution was achieved by direct methods in SHELXT and structure refinement was conducted using full-matrix least squares refinement based on F². [35]

Synthesis of 2,6-bis(3,5-di-tert-butyl-2-methoxyphenyl)pyridine (A): 1-Bromo-2-methoxy-3,5-di-tert-butylbenzene was synthesized according to the literature.[22] 2,6-bis(3,5-di-tert-butyl-2-methoxyphenyl)pyridine was synthesized according to modified synthesis.[23b] A mixture of 1-Bromo-2-methoxy-3,5-di-tert-butylbenzene (1.5 g, 5 mmol) and THF (10 mL) in a Schlenk tube fitted with a screw-in Teflon stopper was frozen in a cold well, along with a solution of nBuLi (0.67 g, 10.5 mmol, 2.1 eq) in hexanes (0.98 mL), in an inert atmosphere glove box. Both solutions were taken out of the box, and the nBuLi solution was added to the solution while allowing the latter to thaw. The mixture was stirred for 1 h while allowing to warm up to room temperature. $ZnCl_2$ (0.68 g, 5 mmol, 1.0 eq) was added with the aid of THF (20 mL). After stirring the reaction mixture for 30 minutes, 1,3-dibromobenzene (0.59 g, 2.5 mmol, 0.5 eq) and $Pd(PPh_3)_4$ (57.8 mg, 0.05 mmol, 0.01 eq) were added with the aid of some THF. The reaction

10

vessel was placed in an oil bath preheated to 75°C and stirred for 16 h, then allowed to cool to room temperature and quenched with water. Volatile materials were removed under vacuum and water was added. The mixture was extracted with Et_2O (3 x 50 mL). The combined organics were dried over $MgSO_4$, filtered, and concentrated by rotary evaporation. The product **A** was obtained as a colourless powder. (1.21 g, 2.35 mmol, 47 % yield). **^{1}H-NMR** (500 MHz, $CDCl_3$) δ (ppm) 7.80 – 7.72 (m, 3H), 7.69 (d, *J* = 2.6 Hz, 2H), 7.40 (d, *J* = 2.6 Hz, 2H), 3.42 (s, 6H), 1.46 (s, 18H), 1.36 (s, 18H). **^{13}C-NMR** (126 MHz, $CDCl_3$) δ (ppm) 157.89, 155.83, 145.60, 142.12, 136.39, 133.32, 126.99, 124.77, 122.67, 61.31, 35.50, 34.74, 31.63, 31.13.

Synthesis of BOB: **A** (0.85 g, 1.65 mmol) was dissolved in dry dichloromethane (50 mL) and boron tribromide (10.0 mL, 10.0 mmol, 10. eq) was added dropwise under argon and stirred overnight. The resulting solution was evaporated and resulting solid was stirred in methanol for 4 hours which was afterwards evaporated. The resulting yellow solid was then redissolved in toluene and crystallized. BOB was obtained as bright yellow crystals. (440 mg, 0.65 mmol, 40 % yield). **^{1}H-NMR** (500 MHz, $CDCl_3$) δ(ppm) 8.00 (t, *J* = 8.1 Hz, 1H), 7.82 (d, *J* = 8.1 Hz, 2H), 7.61 (d, *J* = 2.4 Hz, 2H), 7.52 (d, *J* = 2.3 Hz, 2H), 1.55 (s, 18H), 1.37 (s, 18H). **^{13}C-NMR** (176 MHz, $CDCl_3$) δ (ppm) 153.68, 149.37, 141.69, 140.58, 140.12, 128.74, 120.19, 117.80, 117.48, 35.52, 34.69, 31.74, 29.94.**^{11}B-NMR** (160 MHz, $CDCl_3$) δ (ppm) 2.38. **EA**: anal. calc. for $C_{68}H_{94}B_2N_2O_7$ incl. 2 MeOH: C 76.11 H 8.83 N 2.61 found: C 76.25 H 8.64 N 2.38

Synthesis of BF: BOB (35 mg, 0.05 mmol, 1 eq.) was dissolved in dichloromethane (3mL) and nitrosonium hexafluorophosphate (18.2 mg, 0.1 mmol, 2 eq.) was added to it and stirred for 2 hours. The resulting solution was then evaporated and redissolved in toluene, followed by crystallization. The product BF was obtained as yellow crystals (30 mg, 0.048 mmol, 92.4 % yield). **^{1}H-NMR** (700 MHz, $CDCl_3$) δ(ppm) 8.04 (t, *J* = 8.1 Hz, 1H), 7.86 (d, *J* = 8.1 Hz, 2H), 7.62 (d, *J* = 2.3 Hz, 2H), 7.54 (d, *J* = 2.3 Hz, 2H), 1.56 (s, 18H), 1.37 (s, 18H). **^{13}C-NMR** (176 MHz, $CDCl_3$) δ (ppm) 153.08, 149.52, 142.20, 141.05, 140.26, 129.03, 119.93, 117.70, 116.99, 35.54, 34.73, 31.73, 29.85. **^{11}B-NMR** (160 MHz, $CDCl_3$) δ (ppm) 1.41. **^{19}F-NMR** (282 MHz, $CDCl_3$) δ (ppm) -145.24. **EA** anal. calc. for $C_{33}H_{43}BNO_2$: C 76.38 H 8.06 N 2.87, found: C 76.36 H 8.14 N 2.78

Supporting Information

Additional NMR spectra, TD-DFT calculations and XRD tables can be found in the supporting information.The authors have cited additional references within the Supporting Information. [36][37][38][39][40][41][42]

Acknowledgements

No further acknowledgements

Keywords: Photochemistry • Fluorescence spectroscopy • Boron

References

[1] a) B. Valeur, M. N. Berberan-Santos, *Molecular Fluorescence;* Wiley, **2012**; b) S. Reineke, F. Lindner, G. Schwartz, N. Seidler, K. Walzer, B. Lüssem, K. Leo, *Nature* **2009**, *459*, 234–238; c) A. J. Clancy, M. K. Bayazit, S. A. Hodge, N. T. Skipper, C. A. Howard, M. S. P. Shaffer, *Chemical reviews* **2018**, *118*, 7363–7408;

[2] A. Loudet, K. Burgess, *Chemical reviews* **2007**, *107*, 4891–4932.
[3] N. Boens, V. Leen, W. Dehaen, *Chemical Society reviews* **2012**, *41*, 1130–1172.
[4] a) G. Ulrich, R. Ziessel, A. Harriman, *Angewandte Chemie (International ed. in English)* **2008**, *47*, 1184–1201; b) S. Mohnani, D. Bonifazi, *Coordination Chemistry Reviews* **2010**, *254*, 2342–2362; c) Z. M. Hudson, S. Wang, *Accounts of chemical research* **2009**, *42*, 1584–1596;
[5] a) H. Lu, J. Mack, Y. Yang, Z. Shen, *Chemical Society reviews* **2014**, *43*, 4778–4823; b) T. Kowada, H. Maeda, K. Kikuchi, *Chemical Society reviews* **2015**, *44*, 4953–4972;
[6] M. Lin, J. Liang, *HSET* **2024**, *116*, 321–327.
[7] J. Eyyathiyil, S. Ghosh, A. Cheran, S. Geremia, J. Kumar, N. Hickey, P. Thilagar, *Communications chemistry* **2025**, *8*, 126.
[8] M. Mamada, M. Hayakawa, J. Ochi, T. Hatakeyama, *Chemical Society reviews* **2024**, *53*, 1624–1692.
[9] A. Gorman, J. Killoran, C. O'Shea, T. Kenna, W. M. Gallagher, D. F. O'Shea, *Journal of the American Chemical Society* **2004**, *126*, 10619–10631.
[10] Y. Kubota, T. Tsuzuki, K. Funabiki, M. Ebihara, M. Matsui, *Organic letters* **2010**, *12*, 4010–4013.
[11] K. Paramasivam, C. B. Fialho, T. F. C. Cruz, A. I. Rodrigues, B. Ferreira, C. S. B. Gomes, D. Vila-Viçosa, A. Charas, J. M. S. S. Esperança, L. F. Vieira Ferreira, M. J. Calhorda, A. L. Maçanita, J. Morgado, P. T. Gomes, *Inorg. Chem. Front.* **2021**, *8*, 3960–3983.
[12] a) G. Ulrich, C. Goze, M. Guardigli, A. Roda, R. Ziessel, *Angewandte Chemie (International ed. in English)* **2005**, *44*, 3694–3698; b) C. Goze, G. Ulrich, R. Ziessel, *The Journal of organic chemistry* **2007**, *72*, 313–322; c) A. Kaloudi-Chantzea, N. Karakostas, F. Pitterl, C. P. Raptopoulou, N. Glezos, G. Pistolis, *Chemical communications (Cambridge, England)* **2012**, *48*, 12213–12215; d) X.-D. Jiang, Y. Fu, T. Zhang, W. Zhao, *Tetrahedron Letters* **2012**, *53*, 5703–5706; e) R. Ziessel, G. Ulrich, A. Haefele, A. Harriman, *Journal of the American Chemical Society* **2013**, *135*, 11330–11344; f) G. Duran-Sampedro, I. Esnal, A. R. Agarrabeitia, J. Bañuelos Prieto, L. Cerdán, I. García-Moreno, A. Costela, I. Lopez-Arbeloa, M. J. Ortiz, *Chemistry (Weinheim an der Bergstrasse, Germany)* **2014**, *20*, 2646–2653; g) C. Maeda, K. Nagahata, T. Ema, *Organic & biomolecular chemistry* **2017**, *15*, 7783–7788; h) A. Atilgan, M. M. Cetin, J. Yu, Y. Beldjoudi, J. Liu, C. L. Stern, F. M. Cetin, T. Islamoglu, O. K. Farha, P. Deria, J. F. Stoddart, J. T. Hupp, *Journal of the American Chemical Society* **2020**, *142*, 18554–18564; i) A. van Belois, R. R. Maar, M. S. Workentin, J. B. Gilroy, *Inorganic chemistry* **2019**, *58*, 834–843;
[13] a) Y. H. Lee, S. Park, J. Oh, J. W. Shin, J. Jung, S. Yoo, M. H. Lee, *ACS applied materials & interfaces* **2017**, *9*, 24035–24042; b) H. Mubarok, W. Lee, T. Lee, J. Jung, S. Yoo, M. H. Lee, *Frontiers in chemistry* **2020**, *8*, 538; c) Y. H. Lee, S. Park, J. Oh, S.-J. Woo, A. Kumar, J.-J. Kim, J. Jung, S. Yoo, M. H. Lee, *Advanced Optical Materials*

12

2018, *6*; d) A. Kumar, W. Lee, T. Lee, J. Jung, S. Yoo, M. H. Lee, *J. Mater. Chem. C* **2020**, *8*, 4253–4263; e) J. Kim, T. Lee, J. Y. Ryu, Y. H. Lee, J. Lee, J. Jung, M. H. Lee, *Organometallics* **2020**, *39*, 2235–2244;

[14] a) S. K. Mellerup, S. Wang, *Chemical Society reviews* **2019**, *48*, 3537–3549; b) S. K. Mellerup, S. Wang, *Trends in Chemistry* **2019**, *1*, 77–89;

[15] a) Y. Li, Y. Liu, W. Bu, J. Guo, Y. Wang, *Chem. Commun.* **2000**, 1551–1552; b) C. Diguet, A. Navarro, M. P. Fernández-Liencres, S. B. Jiménez-Pulido, N. A. Illán-Cabeza, J. Massue, S. Gauthier, F. Robin-le Guen, S. Achelle, J. Rodríguez-López, *Dyes and Pigments* **2025**, *236*, 112660;

[16] a) ZHU YUNHUI, WANG YANJIE, ZHANG QISHENG. Pyridine diphenoxy boron fluoride compound, application thereof and organic electroluminescent device containing compound(CN113105491A); b) S. S. Kothavale, J. Y. Lee, *Advanced Optical Materials* **2020**, *8*;

[17] a) H. Zhang, C. Huo, K. Ye, P. Zhang, W. Tian, Y. Wang, *Inorganic chemistry* **2006**, *45*, 2788–2794; b) H. Zhang, C. Huo, J. Zhang, P. Zhang, W. Tian, Y. Wang, *Chem. Commun.* **2006**, 281–283;

[18] S. Yamaguchi, A. Wakamiya, *Pure and Applied Chemistry* **2006**, *78*, 1413–1424.

[19] J. Zhou, Q. Liu, W. Feng, Y. Sun, F. Li, *Chemical reviews* **2015**, *115*, 395–465.

[20] a) P. Li, H. Chan, S.-L. Lai, M. Ng, M.-Y. Chan, V. W.-W. Yam, *Angewandte Chemie (International ed. in English)* **2019**, *58*, 9088–9094; b) P. Li, S.-L. Lai, Z. Chen, W. K. Tang, M.-Y. Leung, M. Ng, W.-K. Kwok, M.-Y. Chan, V. W.-W. Yam, *Chemical science* **2024**, *15*, 12606–12615; c) R. K. Konidena, K. R. Naveen, *Advanced Photonics Research* **2022**, *3*, e202103532;

[21] H. Uoyama, K. Goushi, K. Shizu, H. Nomura, C. Adachi, *Nature* **2012**, *492*, 234–238.

[22] K. Nakano, K. Kobayashi, K. Nozaki, *Journal of the American Chemical Society* **2011**, *133*, 10720–10723.

[23] a) C. Limberakis in , pp. 70–103; b) R. Fu, J. E. Bercaw, J. A. Labinger, *Organometallics* **2011**, *30*, 6751–6765;

[24] N. G. Connelly, W. E. Geiger, *Chemical reviews* **1996**, *96*, 877–910.

[25] Z. Shen, H. Röhr, K. Rurack, H. Uno, M. Spieles, B. Schulz, G. Reck, N. Ono, *Chemistry (Weinheim an der Bergstrasse, Germany)* **2004**, *10*, 4853–4871.

[26] a) G. Colombo, A. Cinco, S. Brenna, J. Furrer, B. Therrien, G. A. Ardizzoia, *Dyes and Pigments* **2023**, *220*, 111722; b) B. Y.-W. Wong, H.-L. Wong, Y.-C. Wong, M.-Y. Chan, V. W.-W. Yam, *Chemistry (Weinheim an der Bergstrasse, Germany)* **2016**, *22*, 15095–15106;

[27] N. J. Turro, V. Ramamurthy, J. C. Scaiano, *Photochem & Photobiology* **2012**, *88*, 1033.

[28] J. Bartelmess, M. Baldrighi, V. Nardone, E. Parisini, D. Buck, L. Echegoyen, S. Giordani, *Chemistry (Weinheim an der Bergstrasse, Germany)* **2015**, *21*, 9727–9732.

13

[29] M. Poddar, R. Misra, *Coordination Chemistry Reviews* **2020**, *421*, 213462.
[30] A. Cinco, G. A. Ardizzoia, S. Brenna, B. Therrien, G. Colombo, *Molecules (Basel, Switzerland)* **2025**, *30*.
[31] J. Jovaišaitė, S. Kirschner, S. Raišys, G. Kreiza, P. Baronas, S. Juršėnas, M. Wagner, *Angewandte Chemie (International ed. in English)* **2023**, *62*, e202215071.
[32] a) R. S. Nicholson, I. Shain, *Anal. Chem.* **1964**, *36*, 706–723; b) J. Heinze, *Angew. Chem. Int. Ed. Engl.* **1984**, *23*, 831–847;
[33] a) J. E. B. Randles, *Trans. Faraday Soc.* **1948**, *44*, 327–338; b) F. Scholz, A. M. Bond, R. G. Compton, D. A. Fiedler, G. Inzelt, H. Kahlert, Š. Komorsky-Lovrić, H. Lohse, M. Lovrić, F. Marken, A. Neudeck, U. Retter, F. Scholz, Z. Stojek, *Electroanalytical Methods;* Springer Berlin Heidelberg, Berlin, Heidelberg, **2010**;
[34] L. Krause, R. Herbst-Irmer, G. M. Sheldrick, D. Stalke, *Journal of applied crystallography* **2015**, *48*, 3–10.
[35] G. M. Sheldrick, *Acta crystallographica. Section A, Foundations and advances* **2015**, *71*, 3–8.
[36] F. Neese, *WIREs Comput Mol Sci* **2022**, *12*.
[37] V. N. Staroverov, G. E. Scuseria, J. Tao, J. P. Perdew, *The Journal of Chemical Physics* **2003**, *119*, 12129–12137.
[38] F. Weigend, R. Ahlrichs, *Physical chemistry chemical physics : PCCP* **2005**, *7*, 3297–3305.
[39] E. Caldeweyher, S. Ehlert, A. Hansen, H. Neugebauer, S. Spicher, C. Bannwarth, S. Grimme, *The Journal of Chemical Physics* **2019**, *150*, 154122.
[40] V. Barone, M. Cossi, *J. Phys. Chem. A* **1998**, *102*, 1995–2001.
[41] F. Plasser, *The Journal of Chemical Physics* **2020**, *152*, 84108.
[42] G. Knizia, J. E. M. N. Klein, *Angewandte Chemie (International ed. in English)* **2015**, *54*, 5518–5522.

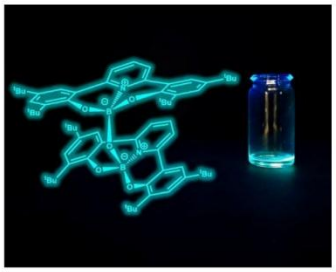

An oxygen-bridged diboron complex (BOB) and its fluorinated monomer (BF) were synthesized and compared to reveal how oxygen bridging modulates geometry, conjugation, and emission. Structural

distortion in BOB leads to red-shifted absorption and photophysical response, highlighting a tunable boron platform for luminescent materials design.

15

Chapter 3: Low Temperature Emissive Cyclometalated Cobalt(III) Complexes

In this chapter, the synthesis and characterization of the cobalt(III) CCC-complexes $[Co(^{R}ImP)_2][PF_6]$ with $H^{Me}ImP$ = 1,1'-(1,3-phenylene)bis(3-methyl-1-imidazol-2-ylidene)) and R= Me, Et, *i*Pr and *n*Bu is presented. The ImP ligand classified as a strong donor ligand had already proven useful in generating photoactive complexes for Fe^{II} and Fe^{III}.[93,143,144] Synthesis was based on methods developed by Hollis *et al. via* ligand activation with a zirconium reagent followed by transmetalation.[145,146] Ground state characterization was done using standard spectroscopic techniques including NMR, CV, UV-Vis and SEC-UV-Vis. They confirmed that the complex is in a low-spin d^6 state, analogous to previously reported photoactive iron(II) complex.[144] These complexes differ from them in that it does not exhibit room temperature emission, but shows phosphorescence at 77 K originating from the ^{3}MC state. The low temperature emission is also accompanied by excited state lifetimes of 1-5 ns depending on the alkyl substituent used. Long excited state lifetimes is a unique property so far for those Co(III) complexes whose excited state dynamics lies in the Marcus inverted region unlike those for its iron counterparts.[119] The strong donor properties of the cyclometalating functions as well as the inherently stronger ligand field splitting imposed the higher charge of the Co^{III} metal center compared to the isoelectronic Fe^{II} explain why the excited state dynamics lies in the Marcus inverted region. These claims are also backed by TD-DFT calculations. TD-DFT calculations explain the low temperature emission, which shows that the minimum energy crossing point to the ground-state is located only slightly above the MC energy. Therefore, the non radiative decay to the ground state is enabled. This pathway becomes inaccessible at 77 K due to the absence thermal relaxation pathways leading to the low temperature ^{3}MC emission. Thus, the complex shows promising results for establishing a class of photoactive Co^{III} complexes.

Participations in this project:

Athul Krishna: Design and synthesis of the title molecule, its standard characterization (NMR, MS, IR), cyclic voltammetry, UV-Vis spectroscopy, interpretation of the data, manuscript writing- Institute for Inorganic Chemistry and Center for Sustainable Systems Design (CSSD), Paderborn University, Paderborn 33098, Germany

Dr. Lorena Fritsch: TD-DFT calculations and review of the manuscript − Institute for Inorganic Chemistry and Center for Sustainable Systems Design (CSSD), Paderborn University, Paderborn 33098, Germany

Dr. Jakob Steube: Interpretation of the data, insightful discussions and review of the manuscript - Institute for Inorganic Chemistry and Center for Sustainable Systems Design (CSSD), Paderborn University, Paderborn 33098, Germany

Dr. Miguel A. Argüello Cordero: Measurement of Transient absorption spectra − Department of Life, Light and Matter and Institute of Physics, University of Rostock, Rostock 18051, Germany

Dr. Roland Schoch: X-ray diffraction measurements - Institute for Inorganic Chemistry and Center for Sustainable Systems Design (CSSD), Paderborn University, Paderborn 33098, Germany

Dr. Adam Neuba: Spectroelectrochemical UV-Vis measurements - Institute for Inorganic Chemistry and Center for Sustainable Systems Design (CSSD), Paderborn University, Paderborn 33098, Germany

Dr. Stefan Lochbrunner: Interpretation of the Transient absorption measurement data - Department of Life, Light and Matter and Institute of Physics, University of Rostock, Rostock 18051, Germany

Dr. Matthias Bauer: Project Supervisor - Institute for Inorganic Chemistry and Center for Sustainable Systems Design (CSSD), Paderborn University, Paderborn 33098, Germany

Publication is reprinted from https://doi.org/10.1021/acs.inorgchem.4c04479 under the license obtained from Journal of American Chemical Society and Copyright Clearance centre with license number 6181941403868

Inorganic Chemistry

pubs.acs.org/IC Article

Low Temperature Emissive Cyclometalated Cobalt(III) Complexes

Athul Krishna, Lorena Fritsch, Jakob Steube, Miguel A. Argüello Cordero, Roland Schoch, Adam Neuba, Stefan Lochbrunner, and Matthias Bauer*

Cite This: *Inorg. Chem.* 2025, 64, 1401−1409 Read Online

ACCESS | Metrics & More | Article Recommendations | Supporting Information

ABSTRACT: A series of Co^{III} complexes $[Co(^{R}ImP)_2][PF_6]$, with $H^{Me}ImP$ = 1,1′-(1,3-phenylene)bis(3-methyl-1-imidazole-2-ylidene)) and R = Me, Et, *i*Pr, *n*Bu, is presented in this work. The influence of the strong donor ligand on the ground and excited-state photophysical properties was investigated in the context of different alkyl substituents at the imidazole nitrogen. X-ray diffraction revealed no significant alterations of the structures and all differences in the series emerge from the electronic structures. These were probed via cyclic voltammetry and UV−vis spectroscopy, detailing the influence of the different alkyl substituents on the ground-state properties. All complexes are emissive at 77 K from a ^{3}MC state, which exhibits lifetimes in the range of 1−5 ns at room temperature, depending on the alkyl substituent. Therefore, it is clearly shown that even small differences in the electronic structure have a large impact on the details of the excited state landscape. The observed behavior was rationalized by a detailed DFT analysis, which shows that the minimum-energy crossing point to the ground-state is located only slightly above the MC energy: Consequently, nonradiative decay to the ground state at room temperature is enabled, while at 77 K this path is prohibited, leading to low-temperature ^{3}MC emission.

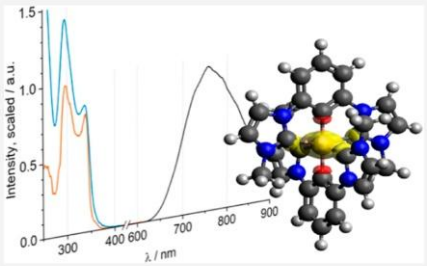

INTRODUCTION

Photochemistry of transition metal complexes has become an active and challenging field in the recent years, largely driven by the impending need for a transition from fossil-fuel based energy to more sustainable alternatives like solar energy. This transition can be facilitated by dye sensitized solar cells,[1] or through the conversion of solar energy to chemical energy via photocatalysis.[2−5] While precious-metal-based coordination complexes and organometallic compounds continue to play a significant role in photochemical applications, their high extraction costs and the limited abundance pose a serious dilemma in terms of their sustainability.[4,6−9]

Consequently, research efforts focus currently on replacing second- and third-row transition metals with abundant first-row transition metals, despite their challenging photophysical properties. The intrinsically low ligand-field splitting of 3d metals leads to energetically low-lying metal-centered (MC) states, which enable fast deactivation of catalytically active excited states. For instance, while ruthenium complexes with bipyridine ligands exhibit emissive long-lived metal-to-ligand charge-transfer (MLCT) states, similar iron complexes do not. This is attributed to the weaker ligand field splitting and increased nonradiative decay pathways in iron complexes.[10−14] Apart from the metal, the overall ligand field splitting is also influenced by the ligand. This is particularly evident when comparing nitrogen-coordinated ruthenium bipyridine complexes with their terpyridine counterparts, where the latter exhibit lower-energy dark ^{3}MC states. These become accessible from the emissive ^{3}MLCT state due to thermal relaxation, leading to observable emission only at 77 K.[14−16] However, it is possible to destabilize the MC states by introducing strong σ-donor ligands and stabilizing the MLCT state through the incorporation of π-acceptor ligands.[17−21] These approaches have successfully resulted in enhancing the MLCT lifetimes in Fe(II) complexes.[22−26]

In contrast to the research on Ru^{II} and Fe^{II} complexes, isoelectronic Co^{III} complexes are much less explored, with only a few publications so far: notable examples include the work of Zysman-Colman and co-workers, reporting blue emission from ligand-to-metal charge-transfer (LMCT) states in Co^{III} complexes,[27] and the work of Persson and co-workers demonstrating a strongly red-shifted emission originating from a ^{3}MC state.[28] These results are remarkable, since most first-row transition metal complexes exhibit only short excited-state lifetimes, whereas these cobalt complexes have been found to show lifetimes in the nano- and microsecond range. Although emissive metal-to-ligand charge-transfer (MLCT) states, analogous to Ru^{II} and Ir^{III}, have not yet been observed for Co^{III} complexes, their long-lived excited states have already

Received: October 21, 2024
Revised: December 21, 2024
Accepted: December 30, 2024
Published: January 14, 2025

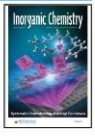

https://doi.org/10.1021/acs.inorgchem.4c04479
Inorg. Chem. 2025, 64, 1401−1409

been utilized for photoinduced electron transfer reactions, as shown by Wenger et al.[29]

Furthermore, polypyridyl cobalt complexes have shown promising reactivity in photocatalysis. While in hexadentate polypyridyl iron complexes destabilization of the MC state shortens its lifetime,[30,31] polypyridyl cobalt complexes exhibit the opposite behavior, allowing both the redox potential and the excited state lifetime to be increased simultaneously.[32] This difference can be explained by Marcus theory: In iron complexes, which display Marcus-normal behavior, the minimum of the MC potential energy surface (PES) (ΔG^0, driving force for ground-state recovery) is lower in energy than the reorganization energy (λ, energy of the ground state {GS} at the same nuclear coordinate). In contrast, polypyridyl cobalt complexes show Marcus-inverted behavior, where ΔG^0 is larger than λ. Visually, this can be understood as the minimum of the MC-PES being outside the GS-PES for normal behavior and inside for inverted behavior. Thereby, this result has been harnessed to apply these complexes in photocatalytic transformations.[32]

Thus, Co^{III} complexes offer undiscovered potential, especially when introducing strong donor ligands, which has already been proven to be a valid strategy for obtaining photoactive Fe^{III} complexes.[33,34] Recently, the Fe^{III} and Fe^{II} complexes $[Fe(^{Me}ImP)_2]^+$ (^{Me}ImP = (1,1′-(1,3-phenylene)bis-(3-methyl-1-imidazole-2-ylidene)), combining two strong carbon donor functions in form of *N*-heterocyclic carbenes and cyclometalating aryl moieties, has been published, where an emissive LMCT state was observed.[35,36] While the complexes $[Co(^{Me}ImP)_2]^+$ and $[Co(^{Bu}ImP)_2]^+$ were also reported,[37] thorough ground state characterization and especially the photophyiscs of this complex class remains unexplored.

Considering the promising applications of Co-complexes in photochemical reactions, this study aims to address the existing limitation in understanding by investigating the impact of the strong donor properties of the ImP ligand on the photophysical properties of a series of $[Co(^{R}ImP)_2](PF_6)$ complexes with R = Me (**Co1**), Et (**Co2**), *i*Pr (**Co3**), and *n*Bu (**Co4**). This systematic approach offers the opportunity to additionally study the influence of the alkyl substituents at the imidazole-nitrogen on both ground and excited states. Their ground- and excited-state characteristics are addressed by applying a combination of single-crystal X-ray diffraction, cyclic voltammetry, UV−vis and low-temperature emission spectroscopy, spectroelectrochemistry and transient absorption spectroscopy, overall complemented by (TD)-DFT calculations.

■ RESULTS AND DISCUSSIONS

Complexes **Co1**−**Co4** were obtained as shown in Scheme 1, starting from 1,3-di(imidazolyl)benzene, which was prepared according to the synthesis protocol reported by Braunstein et al.[38] Subsequent alkylation with 6 equiv. of the corresponding alkyl halide (MeI, EtI, *i*PrBr, BuI) in acetonitrile at 85 °C for 16 h yielded the proligands (cf. Scheme 1A), which were crystallized from acetone by layering with diethyl ether. The complexes were prepared by activation of the proligand with $[Zr(NMe_2)_4]$ and subsequent transmetalation with $CoCl_2$ followed by anion-exchange with potassium hexafluorophosphate in methanol (see Scheme 1B).[35,37] The resulting light-yellow solids were dissolved in acetone and crystallized by evaporation, giving complexes **Co1** to **Co4** as yellow crystals in moderate yields (**Co1**: 53%, **Co2**: 48%, **Co3**: 52%, **Co4**: 48%).

Scheme 1. Ligand and Complex Synthesis. (A) Synthetic Procedure for the Proligand. RX: Alkyl Halides MeI, EtI, *i*PrBr, *n*BuI. (B) Complex Synthesis: Activation of the Proligand with a Zirconium Reagent, Followed by Transmetalation and Anion Exchange. RT: Room Temperature

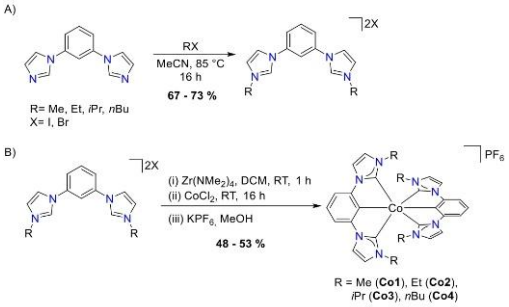

Single-crystals suitable for X-ray diffraction (scXRD) were obtained by the same procedure in the cases of **Co1**−**3**, for **Co2** and **Co3** single-crystals could be obtained from before anion exchange. For **Co4**, no suitable crystals could be grown.

The structure of **Co1**, exemplary for all complexes, is depicted in Figure 1. The structural parameters of the

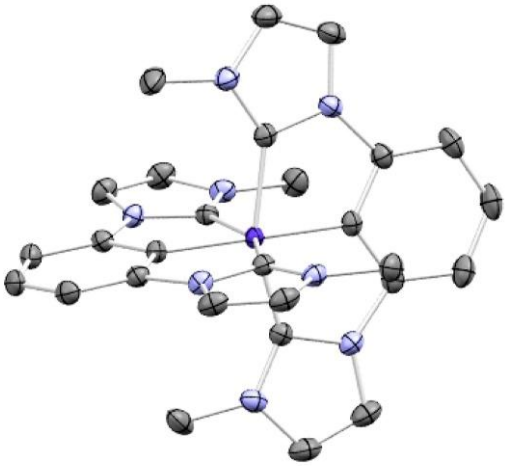

Figure 1. Single crystal structure of $[Co(^{Me}ImP)_2](PF_6)$ (**Co1**). Atoms are shown with anisotropic displacement parameters as ellipsoids at 50% probability level. Hydrogen atoms, the counterion and one solvent molecule are omitted for clarity. (Dark blue: Co, light blue: N, gray, C).

complexes **Co1**−**Co3** are shown in Table 1 and compared to the isoelectronic Fe^{II} complex.[36,39] All Co^{III} complexes exhibit a distorted octahedral symmetry. The bond lengths of approximately 1.91 Å for the Co−C_{CM} bond and 1.95 Å for the Co−C_{Im} bond, as well as the bite angle of around 158° for C_{Im}−Co-C_{Im} show no significant variation, regardless of the alkyl substituent. The structural parameters are in agreement with the isoelectronic Fe^{II} complex.[36,39]

https://doi.org/10.1021/acs.inorgchem.4c04479
Inorg. Chem. 2025, 64, 1401−1409

Table 1. Relevant Bond Lengths [Å] and Bite Angles [°] of Co1-3 (M = Co) and the Isoelectronic Fe^{II} Reference Complex (M = Fe).[36,39]

compound	Co1	Co2	Co3	Fe^{II} (ImP)[36,39]
M-C_{CM} mean distance (Å)	1.906(2)	1.909(1)	1.910(2)	1.918(2)
M-C_{Im} mean distance (Å)	1.944(2)	1.953(1)	1.952(2)	1.939(6)
C_{Im}-M-C_{Im} bite angle (deg)	157.9(1)	157.7(1)	157.9(1)	155.8(5)

Ground State Characterization. The redox properties of complexes **Co1** to **Co4** were investigated using cyclic voltammetry (Figure 2, for full data see Figure S5 in the Supporting Information), revealing a consistent general behavior across the series, irrespective of the substituents. While none of the complexes displayed ligand or cobalt-based reduction, two oxidation processes were observed. The first oxidation, a reversible process, occurs at 0.63, 0.67, 0.68, and 0.68 V vs $FcH^{0/+}$ for **Co1**, **Co2**, **Co3**, and **Co4**, respectively, and is attributed to the $Co^{III/IV}$ redox couple. The second oxidation is an irreversible peak at 1.87 V, corresponding to ligand oxidation. Despite the similarities in the redox potentials throughout the series, a general trend can be observed, i.e., with longer alkyl chains, the $Co^{III/IV}$ potentials are anodically shifted with respect to the methyl substituent. A similar trend can be observed in Fe^{II} complexes, based on the pyridine analogue of the ImP ligand, with methyl, isopropyl and hexyl *N*-alkyl substituents.[40−42] These trends can be attributed to the larger inductive effect of longer alkyl chains, thus increasing the σ-donating strength. Comparison with the isoelectronic Fe^{II} complex shows more cathodic potentials of 0.08 V for the $Fe^{II/III}$ couple, 1.16 V for the $Fe^{III/IV}$ couple, and 1.31 V for the ligand oxidation.[35] A similar pattern is observed in cobalt and iron complexes with $(PhB(MeIm)_3)$ ligands, where the cobalt complexes display higher oxidation potentials compared to their isoelectronic iron counterparts.[28] Additionally, the blue-emissive Co^{III} complexes reported by Zysman-Colman and colleagues exhibit quasireversible reduction waves at −0.58 and −0.39 V, corresponding to the $Co^{II/III}$ couple.[27] Conversely, in the $Co((L^{CNC})_2)^+$ complex from Wenger et al., no $Co^{II/III}$ reduction was observed, although ligand reduction occurred at −2.21 V.[29] In comparison, the cobalt complexes presented herein show neither a $Co^{II/III}$ transition nor ligand reduction, distinguishing them from the other reported systems. A likely explanation is that the strongly donating ligand exhibits high-lying π^*-orbitals, as indicated by the high-energy MLCT and ILCT transitions. An additional effect might be the inhibition of metal reduction.

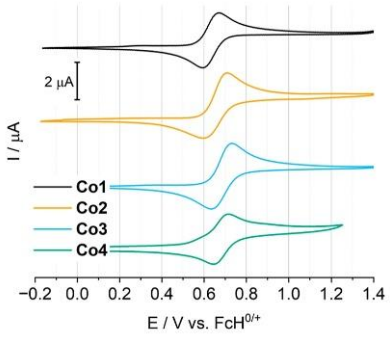

Figure 2. Cyclic voltammograms of Co1−4 in MeCN/$[n\mathrm{Bu_4N}][PF_6]$ at 0.001 M (0.1 V/s).

The experimental absorption spectra of complexes **Co1−4** (10 μM in MeCN) all display the same basic shape, with two prominent absorption bands in the UV region at 295 and 337 nm, along with a low-intensity shoulder at around 370 nm (Figure 3). It is noteworthy that the molar absorption coefficient (ε) across the **Co1−Co4** series remains similar, indicating only small differences in the overall electronic structure. At 337 nm, they exhibit an ε_{337nm} of around $0.8 \times 10^4\ M^{-1}\ cm^{-1}$, while for the 295 nm absorption band an ε_{295nm} of around $1.3 \times 10^4\ M^{-1}\ cm^{-1}$ is observed. Small deviations may be attributed to subtle variations in the electron-donating effects of the alkyl chains, which influence the electronic excited states involved. Additionally, the low-intensity shoulder at 370 nm shows an absorption coefficient slightly below $\varepsilon_{370nm} = 0.07 \times 10^4\ M^{-1}\ cm^{-1}$ and likely corresponds to a forbidden $d-d$ transition.

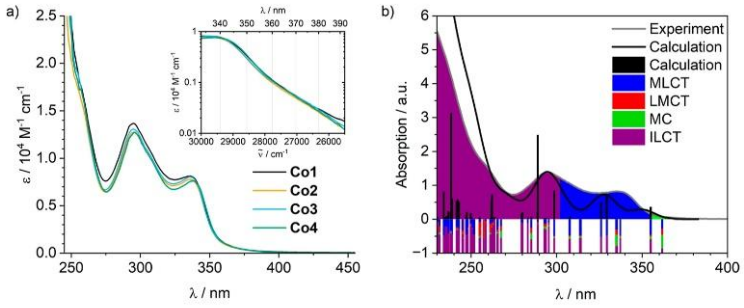

Figure 3. (a) Experimental absorption spectra of **Co1**, **Co2**, **Co3** and **Co4** (0.1 mM in MeCN). Inset: enlargement of the shoulder in the absorption spectrum, with ε plotted against wavenumbers and logarithmic *y*-axis to enhance the visibility. (b) TD-DFT calculated vertical transitions of **Co1** shown as sticks reflecting the oscillator strength and shown as spectrum with a broadening (fwhm) of 17 nm as a black solid line in comparison to the experimental spectrum in gray. The proportional character of the transitions is indicated below the spectrum by different colors, and the bands are colored according to the character of the main transitions.

https://doi.org/10.1021/acs.inorgchem.4c04479
Inorg. Chem. 2025, 64, 1401−1409

To further investigate the character of the absorption bands, TD-DFT calculations of the first 150 vertical transitions using the TPSSh functional along with the def2-TZVP basis-set were exemplarily performed for the optimized structure of **Co1**. The character and spatial distribution of the main donor and acceptor orbitals of selected transitions can be found as color coded bars in Figure 3 and in the Supporting Information, Table S2. Transitions of the band at 294 nm and at wavelengths below can be assigned to a mainly intraligand charge transfer (ILCT) character, however, the band also has partial MLCT character. The absorption in the region from 300−350 nm, including the band at 335 nm, can be attributed to MLCT transitions. From the transition densities (see Table S2), it is noticeable that the phenyl part of the ligand is in general more involved than the imidazole moieties. These observations are similar to the findings for the $Co((L^{CNC})_2)^+$ complex of Wenger et al. where a corresponding ILCT absorption at 408 nm and an MLCT absorption at 430 nm were identified.[29]

The energetically lowest calculated transition at 356 nm of **Co1** shows mainly MC character. Despite the low calculated oscillator strength of this transition, the low-intensity shoulder at 370 nm in the experimental spectrum can be attributed to this transition. Similarly, the $Co(PhB(MeIm)_3)_2$ complex of Persson et al.[19] exhibits weak absorption at 310 nm with a molar absorption coefficient $\varepsilon_{310nm} = 0.04 \times 10^4\ M^{-1}\ cm^{-1}$ which is also attributed to MC transitions.[28] Further similarities are found in $[Co(CN)_6]^{3-}$, which features strongly σ-donating CN^- groups and which has been inferred to display metal-centered (MC) transitions for its weak absorptions.[43]

Excited State Characterization and Dynamics. The complexes **Co1**−**Co4** do not exhibit any emission at room temperature. However, at 77 K when excited in butyronitrile (BuCN) at 340 nm, all complexes display a broad emission at 758 nm (see Figure 4 exemplarily for **Co1**; Supporting Information Figure S10 for **Co2**−**Co4**). The excitation spectra recorded at 758 nm align with the absorption spectra, substantiating that this emission originates from the complex.

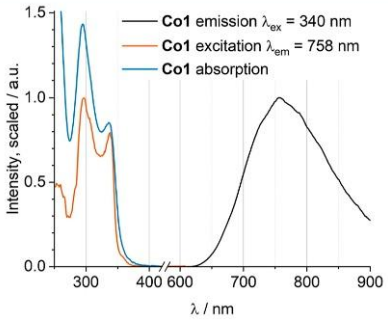

Figure 4. Normalized and scaled low temperature emission spectrum of **Co1** at 77 K after excitation at 340 nm in BuCN, together with the excitation and absorption spectrum.

The large Stokes shift of 2.01 eV observed in these complexes is similar to $[Co(PhB(MeIm)_3)_2]^+$ (2.22 eV) and $[Co(CN)_6]^{3-}$ (1.25 eV).[28,43,44] In both cases, the low-energy emission is assigned to a triplet metal-centered (^{3}MC) state. Therefore, it is likely that the lowest energy state in **Co1**−**Co4**, in accordance with Kasha's rule, is also a ^{3}MC state. To further explore the behavior of these complexes at room temperature, transient absorption spectroscopy was performed on MeCN solutions of the compounds. The optical excitation was carried out by sub-50 fs pulses with a center wavelength of 325 nm and for probing a white light continuum was used.[45] The polarizations of the pump and probe pulses were set at magic angle to avoid signal contributions from orientational relaxation processes. The obtained transient spectra are shown in Figure 5.

In all complexes, the transient absorption is dominated by a broad excited state absorption, which covers the visible and near-ultraviolet (UV) spectral range and decays within several nanoseconds. On the picosecond time scale, a partial reduction of the ESA occurs in the near UV. A global lifetime-analysis showed that three exponential decay components are necessary to reproduce the data. The fitting procedure yielded similar decay associated amplitude spectra (DAAS) for all four compounds, but different time constants. Hence, it can be concluded that the excited-state landscapes of all complexes are alike. Only the lifetimes of the involved states are affected by the variation of the alkyl substituents, which in turn indicates small changes of the relative energies of the involved electronic states. This finding is in agreement with the observations in the CVs. The time constant of the fastest decay component τ_1 amounts to a few picoseconds and is similar in all compounds. It describes mainly an excited state absorption (ESA) decrease between 350 and 400 nm, but also some increase at around 520 nm. The second time constant τ_2 varies between 7 and 11 ps, except for **Co2**. In this case, it is much longer with 162 ps. However, the corresponding DAAS is very weak, indicating that the component is not significant in **Co2**. The third time constant τ_3 is in the range of a few nanoseconds and amounts to 1.0 and 1.2 ns in **Co1** and **Co3**, respectively. The time constants of the long-lived components of **Co2** and **Co4** are considerably larger and in the order of 2 ± 0.2 and 5 ± 1 ns, respectively (see Table 2). Due to the maximal time delay of 1.9 ns accessible by the setup, the uncertainty is in these cases quite high. The spectrum of the long-lived component exhibits no signatures indicative for a charge-transfer state, as a comparison with the spectra of the oxidized species obtained by spectroelectrochemistry (SEC) shows (see Supporting Information Figure S12). Accordingly, the component is assigned to the ^{3}MC state. This result is in accordance with the findings concerning the low-temperature emission, which are also in line with the assumption that the ^{3}MC state is the energetically lowest electronically excited state and the source of the emission. The components with the decay times τ_1 and τ_2 are more difficult to assign, as especially the latter is only significant in the UV and negligible in the visible spectral region. Nevertheless, in the UV, the DAAS associated with τ_2 shows some inverse behavior compared to the DAAS of the long-lived component, therefore it could to a certain extent reflect population or a structural relaxation process of the ^{3}MC state. The τ_1-component shows an ESA between 350 and 400 nm, which seems to reflect absorption changes observed for the oxidation process in the SEC experiments (see Figure S12). However, in the red, the DAAS differs from the absorption band of the oxidized species. Thus, the decay times τ_1 and τ_2 showing up in the TA data cannot be unambiguously assigned but are probably related to a transient population of the ^{3}MLCT state and a structural relaxation of the ^{3}MC state. Based on the well-known excited state landscape of Fe^{II} complexes, we thus propose the established relaxation cascade

https://doi.org/10.1021/acs.inorgchem.4c04479
Inorg. Chem. 2025, 64, 1401−1409

Inorganic Chemistry pubs.acs.org/IC Article

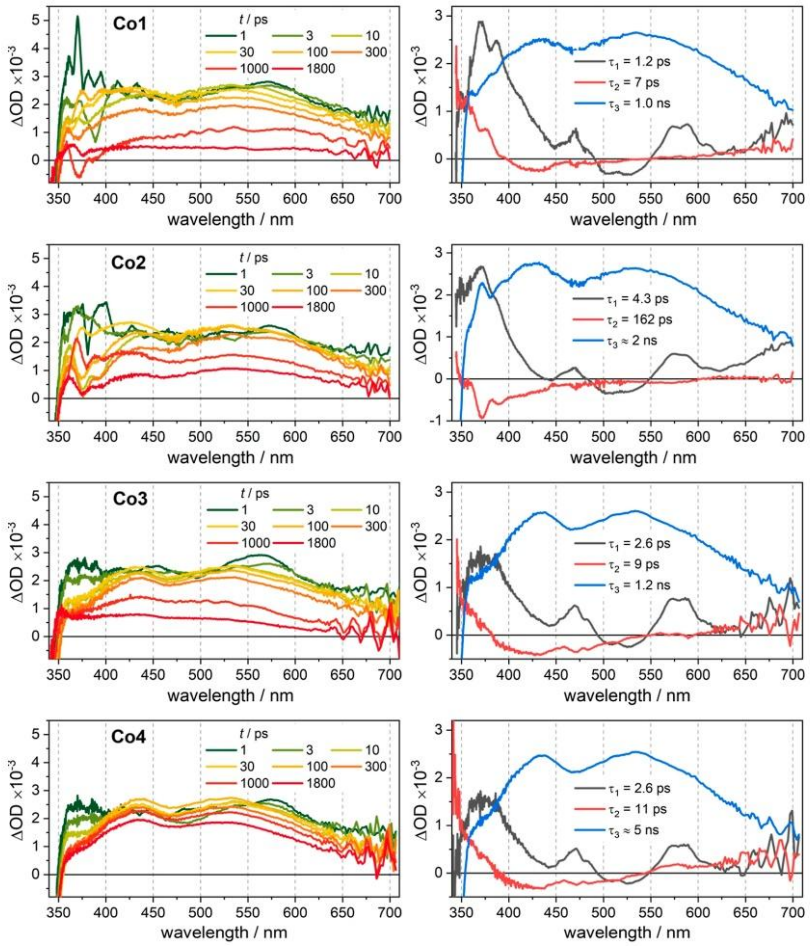

Figure 5. fsTA spectra and corresponding DAAS (decay associated amplitude spectra) of the investigated Co complexes in MeCN after optical excitation at 325 nm.

Table 2. Time Constants Obtained by a Global Lifetime Analysis of the TA Data of the Investigated Co Complexes

complex	τ_1 (ps)	τ_2 (ps)	τ_3 (ns)
Co1	1.2	7	1
Co2	4.3	162	2[a]
Co3	2.6	9	1.2
Co4	2.6	11	5[a]

[a]: Due to the decay exceeding the maximal time delay of the setup, these lifetimes have a relatively high uncertainty.

^{1}MLCT → ^{3}MLCT → ^{3}MC to be also present in the complexes studied here (Figure 6).

Concluding the excited-state characterization, all complexes possess a ^{3}MC state as energetically lowest electronically excited state, which is emissive at low temperatures and has a ns-lifetime. The highest lifetime is obtained for **Co4** with around 5 ns, the lowest for **Co1** with 1 ns, demonstrating that small changes in the electronic structure caused by the incorporation of different alkyl groups lead to large effects in the excited state dynamics.

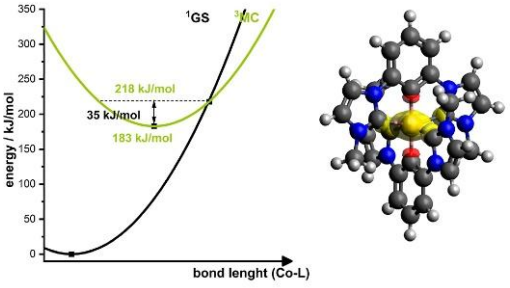

Figure 6. TD-DFT calculated MECP energy of the ^{3}MC and ^{1}GS potential surfaces. Inserted: spin density plot of the B3LYP-optimized triplet state of **Co1**.

https://doi.org/10.1021/acs.inorgchem.4c04479
Inorg. Chem. 2025, 64, 1401−1409

To gain a deeper understanding of the excited state dynamics, DFT calculations including a geometry optimization for the minimum energy triplet state of **Co1** were performed. The spin density of this structure is located at the metal center (Figure 6), confirming a ^{3}MC state. This lowest-lying triplet state is likely to serve as the emissive state, supporting the experimental findings obtained by low-temperature emission and transient absorption spectroscopy.[46] However, no explanation for the experimentally seen loss of the emission at room temperature was found. The most probable deactivation path for the nonradiative decay is a thermally activated surface crossing into the ground state at a low-lying minimum energy crossing point (MECP). DFT optimization of this geometry indicates an energy of 35 kJ/mol above the ^{3}MC minimum (Figure 6). For comparison, the barrier of thermally activated depopulation in $[Ru(bpy)_3]^{2+}$ was determined to be about 45 kJ/mol.[47,48] Based on this value, it can be assumed that the barrier of 35 kJ/mol can be overcome at room temperature, enabling nonradiative decay to the ground state. Furthermore, it was found that this class of complexes exhibits Marcus inverted behavior, as the calculated MECP is located at larger values of the nuclear coordinate than the ^{3}MC minimum, as recently also observed by McCusker, MacMillan and co-workers.[32] Consequently, an increase in MC energy through further ligand modifications could result in a lower redox potential, an extended lifetime, and, if the barrier is sufficiently high, the achievement of room-temperature luminescence.

■ CONCLUSIONS

In this work, $[Co(^{R}ImP)_2][PF_6]$ complexes, bearing different alkyl groups (R = Me, Et, *i*Pr, *n*Bu) at the imidazole nitrogen, have been investigated in their ground and excited states. While all complexes display an isostructural coordination environment, small deviations in the redox potentials are observed. Additionally, all complexes are emissive from a ^{3}MC state at 77 K and show lifetimes between 1 and 5 ns at room-temperature, dependent on the alkyl group. Therefore, it is obvious that small changes to the electronic structure can lead to subtle differences in terms of ground- and excited-state properties. Consequently, adaptation of this strategy to other complexes may yield better photoactive materials, as shown in this case by an increase of the MC lifetime by a factor 5. Moreover, DFT calculations suggest that the MECP to the ground state is located at a larger nuclear coordinate than the emissive state and, therefore, these complexes fall into the Marcus inverted region. Accordingly, further optimization of the ligand design, enabled by the easily modifiable ImP ligand-scaffold, can yield enhanced lifetimes and presumably even room-temperature emission, while tuning the redox potentials of the complexes. Exploring the excited-state reactivity of the MC state in these complexes can unlock potential applications in photochemical processes, such as photoredox or energy-transfer catalysis.

■ EXPERIMENTAL SECTION

All experiments were carried out under an argon atmosphere using standard Schlenk or Glovebox techniques unless specified. Glassware was oven-dried at 130 °C prior to use. Dry solvents were obtained from an MBraun SPS-800 solvent-drying system, degassed via sparging with argon and subsequently stored over a 4 Å molecular sieve. ^{1}H NMR spectra were recorded using a Bruker Avance 500 and a Bruker Ascent 700 spectrometer. Chemical shifts are expressed in parts per million (ppm, δ) downfield from tetramethylsilane (TMS). The spectra were referenced to the residual protonsignals of the respective deuterated solvent. All coupling constants (J) are absolute values and are expressed in Hertz (Hz). The spectra were analyzed according to first order. Electrospray ionization mass spectrometry spectra were recorded on a waters Synapt G2 Quadrupole Time-of-Flight spectrometer, using acetonitrile as solvent.

For cyclic voltammetry, dry acetonitrile was obtained by passing HPLC-grade acetonitrile (Fisher) over a column of MP Biomedicals MP alumina N-Super I, which was activated in an oven at 150 °C for multiple days. The cyclic voltammetry measurements were performed at room temperature in a 0.1 M $[n\mathrm{Bu_4N}][PF_6]$ acetonitrile solution with an analyte concentration of 0.001 M under a solvent-saturated argon atmosphere. A three-electrode arrangement with a 1 mm Pt working electrode, a Pt wire counter electrode (both Metrohm), and an Ag/AgCl reference electrode (custom built) was used with a Metrohm PGSTAT101 potentiostat. Ferrocene was added after the measurements as an internal standard. All potentials were referenced against the $FcH^{0/+}$ couple. The voltammograms were analyzed using the NOVA software (version 2.1.3). The diagnostic criteria for reversibility were based on those proposed by Nicholson[49,50] and the Randles–Sevcik equation.[51,52]

Acetonitrile of spectroscopic grade (SPECTRONORM VWR Acetonitrile) was used as the solvent for steady-state absorption spectroscopy (c = 0.1 mM), which were recorded using in quartz cuvettes (path length = 10 mm) using a Cary 50 or PerkinElmer Lambda 45 spectrometer.

Spectroelectrochemical measurements were performed at room temperature in an optically transparent cell (d = 1 mm) using a deoxygenated MeCN/0.1 M $[n\mathrm{Bu_4N}][PF_6]$ solution and a Pt wire mesh working electrode (counter electrode: Pt wire). Spectral changes during oxidations/reductions were recorded on a Varian Cary 50 spectrophotometer.

For steady-state emission spectroscopy at room temperature, acetonitrile of spectroscopic grade was used as the solvent. Steady-state emission spectra were recorded in 10 mm quartz cuvettes on an Edinburgh Instruments FLS1000 spectrometer with single monochromators and a red-extended PMT-980. The solutions for the measurements under argon were degassed using the freeze–pump–thaw technique. Low-temperature emission spectroscopy was performed in butyronitrile at 77 K.

The presented X-ray single crystal data were measured on a Bruker Venture D8 three-cycle diffractometer equipped with a Mo K_α μ-source (λ = 0.71073 Å), an Incoatec multilayer monochromator and a photon III detector at 120 K. The data were integrated with SAINT and afterward a multiscan absorption correction was applied using SADABS.[53] Structure solution was achieved by direct methods in SHELXT and structure refinement was conducted using full-matrix least-squares refinement based on F^2.[54]

Transient absorption spectra were recorded with a time resolution of about 100 fs employing a pump–probe setup based on a Ti:sapphire laser system (CPA-2001, Clark MXR), which operates at a center wavelength of 775 nm and a repetition rate of 1 kHz. The excitation pulses with a center wavelength of 325 nm were obtained by frequency doubling the output of a noncollinear optical parametric amplifier (NOPA) pumped by the Ti:sapphire system and tuned to 650 nm in a 100 μm thick BBO crystal.[45] The dispersion of the NOPA pulses was prior frequency doubling minimized by a compressor based on fused silica prisms. For the probe pulses, a white light continuum was generated in a CaF_2 crystal. To avoid effects caused by orientational relaxation, the polarizations of the pump and probe pulses were set at magic angle with respect to each other. Behind the sample, the probe was dispersed by a prism and the spectrally resolved absorption changes were recorded by a photodiode array detector. The compounds were dissolved in MeCN under argon and the sample solutions were filled into a fused silica cuvette with a thickness of 1 mm.

1,3-di(imidazolyl)benzene and 1,1′-(1,3-phenylene)bis(3-methyl-1-imidazolium) diiodide were prepared according to the literature.[38,55]

https://doi.org/10.1021/acs.inorgchem.4c04479
Inorg. Chem. 2025, 64, 1401−1409

The synthesis of **1,1′-(1,3-phenylene)bis(3-ethyl-1-imidazolium) diiodide** is based on the synthesis of 1,1′-(1,3-phenylene)bis(3-methyl-1-imidazolium) diiodide,[55] however was modified regarding the temperature. 1,3-di(imidazolyl)benzene (1051 mg, 5 mmol) was dissolved in acetonitrile before ethyl iodide (30 mmol, 2.4 mL) was added. The solution was refluxed for 16 h at 85 °C. After letting the suspension cool to room temperature, the volatiles were evaporated under reduced pressure. The resulting mixture was subsequently washed with acetone (3 × 30 mL) and diethyl ether (3 × 30 mL) alternatively, before drying under vacuum.

The product was obtained as a colorless solid (3.6 mmol, 2611 mg, 71.8%).

^{1}H NMR (700 MHz, DMSO-d_6): δ (ppm) = 9.95 (s, 2H), 8.42 (t, J = 1.9 Hz, 2H), 8.36 (t, J = 2.2 Hz, 1H), 8.15 (t, J = 1.8 Hz, 2H), 8.03 (m, 2H), 7.98 (t, J = 8.0 Hz, 1H), 4.34 (q, J = 7.3 Hz, 4H), 1.55 (t, J = 7.3 Hz, 6H). **^{13}C NMR** (176 MHz, DMSO-d_6): δ (ppm) = 135.71, 135.49, 131.95, 123.30, 122.62, 121.07, 115.69, 45.02, 14.76. **Elemental Analysis** (calculated, experimental for $C_{16}H_{20}N_4I_2$): C(36.80, 36.87), H (3.86, 3.96), N (10.73, 10.88).

1,1′-(1,3-phenylene)bis(3-isopropyl-1-imidazolium) dibromide was synthesized as described for 1,1′-(1,3-phenylene)bis(3-ethyl-1-imidazolium) diiodide, however employing isopropyl bromide as alkyl halide. The product was obtained as a colorless solid (4.8 mmol batch size: 3.3 mmol, 1506 mg, 69.3%).

^{1}H NMR (700 MHz, DMSO-d_6): δ (ppm) = 10.25 (t, J = 1.7 Hz, 2H), 8.60 (d, 2H), 8.27 (t, J = 1.9 Hz, 1H), 8.09 (dd, J = 8.2, 2.2 Hz, 2H), 7.96 (t, J = 8.2 Hz, 1H), 5.13−4.40 (m, 1H), 1.61 (d, J = 6.8 Hz, 7H). **^{13}C NMR** (176 MHz, DMSO-d_6): δ (ppm) = 135.80, 135.72, 134.66, 134.56, 131.80, 131.67, 122.34, 121.88, 121.17, 115.52, 53.26, 22.26. **Elemental Analysis** (calculated, experimental for $C_{18}H_{24}N_4Br_2$ with $0.5H_20$): C(46.47, 46.38), H (5.42, 5.44), N (12.04, 12.28).

1,1′-(1,3-phenylene)bis(3-butyl-1-imidazolium) diiodide was synthesized as described for 1,1′-(1,3-phenylene)bis(3-ethyl-1-imidazolium) diiodide, however employing butyl iodide as alkyl halide. The product was obtained as a colorless solid (3 mmol batch size: 2.2 mmol, 1272 mg, 73.3%).

^{1}H NMR (700 MHz, DMSO-d_6): δ (ppm) = 9.99 (t, J = 1.7 Hz, 2H), 8.44 (s, 2H), 8.36 (t, J = 2.2 Hz, 1H), 8.14 (t, J = 1.8 Hz, 2H), 8.07−8.01 (m, 2H), 7.98 (t, J = 7.82 Hz, 1H), 4.30 (d, J = 7.3 Hz, 4H), 2.11−1.78 (m, 4H), 1.58−1.15 (m, 4H), 0.95 (t, J = 7.4 Hz, 6H). **^{13}C NMR** (176 MHz, DMSO-d_6): δ (ppm) = 135.68, 131.91, 123.59, 122.67, 121.12, 115.76, 49.34, 31.03, 18.83, 13.32. **Elemental Analysis** (calculated, experimental for $C_{20}H_{28}N_4I_2$): C(41.54, 41.70), H (4.88, 4.92), N (9.69, 9.87).

The synthesis of complex **Co1** was reported previously,[35] complexes **Co2−Co4** were synthesized accordingly in 0.405 mmol batch sizes:

The according ligand (0.405 mmol) and tetrakis(dimethylamino)-zirconium (271 mg, 1 mmol) were suspended in dry DCM (10 mL) in a glovebox. The yellow suspension was allowed to stir for 1 h before cobalt(II) chloride (53 mg, 0.405 mmol) was added. The mixture was allowed to stir for another 16 h. The dark green mixture was worked up under ambient atmosphere. Initially, water (1 mL) was added to quench the reaction. The suspension was filtered through a cotton pad and through a porous glass frit. The respective filter cakes were washed with DCM (10 mL) thrice. The red solution was evaporated under reduced pressure. The solid was dissolved in minimal methanol, before KPF_6 (140 mg, 0.75 mmol) was added. The compound was precipitated by the addition of water and filtered off. The process was repeated four times to ensure full exchange of the counterion. The suspension was filtered, and the light-yellow solid was dried under reduced pressure. It was then dissolved in a minimal amount of acetone and allowed to crystallize under ambient atmosphere.

Co2: the product was obtained as a yellow solid (0.203 mmol, 150 mg, 50.1%).

^{1}H NMR (700 MHz, CD_3CN): δ (ppm) = δ 7.76 (d, J = 2.0 Hz, 4H), 7.52−7.33 (m, 6H), 6.86 (d, J = 2.0 Hz, 4H), 2.87 (d, J = 7.2 Hz, 8H), 0.43 (t, 7.2 Hz 12H). **^{13}C NMR** (176 MHz, CD_3CN): δ (ppm) = 184.79, 176.94, 149.29, 125.38, 123.81, 116.63, 108.28, 44.21, 16.82. **Elemental Analysis** (calculated, experimental for $C_{32}H_{34}N_8CoPF_6$): C(52.32, 52.45), H (4.67, 4.89), N (15.25, 15.54). **ESI-MS** ($[M]^+$ for $C_{32}H_{34}N_8Co^+$): m/z 589.2238, Found: 589.2233.

Co3: The product was obtained as a yellow solid (0.195 mmol, 155 mg, 48.1%).

^{1}H NMR (700 MHz, CD_3CN): δ(ppm) = δ 7.78 (d, J = 2.1 Hz, 4H), 7.55−7.29 (m, 6H), 6.96 (d, J = 2.1 Hz, 4H), 3.15 (p, J = 6.8 Hz, 4H), 0.62 (d, J = 6.9 Hz, 24H). **^{13}C NMR** (176 MHz, CD_3CN): δ(ppm) = 184.05, 176.28, 149.18, 125.49, 119.59, 116.73, 108.10, 50.35, 22.93. **Elemental Analysis** (calculated, experimental for $C_{36}H_{42}N_8CoPF_6$): C:(54.69, 54.71), H (5.35, 5.30), N (14.17, 14.19). **ESI-MS** ($[M]^+$ for $C_{36}H_{42}N_8Co^+$): m/z 645.2864; found, 645.2871.

Co4: the product was obtained as a yellow solid (0.206 mmol, 175 mg, 50.8%).

^{1}H NMR (700 MHz, CD_3CN): δ(ppm) = δ 7.77 (d, J = 2.0 Hz, 4H), 7.44 (m, 6H), 6.84 (d, J = 2.0 Hz, 4H), 2.80 (t, J = 7.1 Hz, 8H), 0.76−0.61 (m, 28H). **^{13}C NMR** (176 MHz, CD_3CN): δ(ppm) = 184.84, 177.05, 149.31, 125.28, 124.17, 116.38, 108.31, 49.40, 34.50, 20.26, 14.10. **Elemental Analysis** (calculated, experimental for $C_{40}H_{50}N_8CoPF_6$): C (56.74, 56.90), H (5.95, 6.15), N (13.23, 13.32). **ESI-MS** ($[M]^+$ for $C_{40}H_{50}N_8Co^+$): m/z 701.3490; found, 701.3501.

■ ASSOCIATED CONTENT

Supporting Information

The Supporting Information is available free of charge at https://pubs.acs.org/doi/10.1021/acs.inorgchem.4c04479.

Details on single crystal X-ray analysis, cyclic voltammetry, UV−vis spectroscopy, spectroelectrochemistry, transient absorption spectroscopy, computational details, as well as spectra (PDF)

Accession Codes

Deposition Numbers 2386766−2386768 contain the supplementary crystallographic data for this paper. These data can be obtained free of charge via the joint Cambridge Crystallographic Data Centre (CCDC) and Fachinformationszentrum Karlsruhe AccessStructuresservice.

■ AUTHOR INFORMATION

Corresponding Author

Matthias Bauer − *Institute for Inorganic Chemistry and Center for Sustainable Systems Design (CSSD), Paderborn University, Paderborn 33098, Germany*; orcid.org/0000-0002-9294-6076; Email: matthias.bauer@upb.de

Authors

Athul Krishna − *Institute for Inorganic Chemistry and Center for Sustainable Systems Design (CSSD), Paderborn University, Paderborn 33098, Germany*

Lorena Fritsch − *Institute for Inorganic Chemistry and Center for Sustainable Systems Design (CSSD), Paderborn University, Paderborn 33098, Germany*

Jakob Steube − *Institute for Inorganic Chemistry and Center for Sustainable Systems Design (CSSD), Paderborn University, Paderborn 33098, Germany*; orcid.org/0000-0003-3178-4429

Miguel A. Argüello Cordero − *Department of Life, Light and Matter and Institute of Physics, University of Rostock, Rostock 18051, Germany*

Roland Schoch − *Institute for Inorganic Chemistry and Center for Sustainable Systems Design (CSSD), Paderborn University, Paderborn 33098, Germany*

https://doi.org/10.1021/acs.inorgchem.4c04479
Inorg. Chem. 2025, 64, 1401−1409

Adam Neuba – *Institute for Inorganic Chemistry and Center for Sustainable Systems Design (CSSD), Paderborn University, Paderborn 33098, Germany*

Stefan Lochbrunner – *Department of Life, Light and Matter and Institute of Physics, University of Rostock, Rostock 18051, Germany;* orcid.org/0000-0001-9729-8277

Complete contact information is available at: https://pubs.acs.org/10.1021/acs.inorgchem.4c04479

Author Contributions

The manuscript was written through contributions of all authors. All authors have given approval to the final version of the manuscript.

Notes

The authors declare no competing financial interest.

■ ACKNOWLEDGMENTS

The grant of computer time at the Paderborn Center for Parallel Computing PC2 is acknowledged. This work was performed in the framework of the SPP 2102 funded by the Deutsche Forschungsgemeinschaft (BA 4467/7-1 and BA 4467/7-2, LO 714/11-1 and LO 714/11-2, project nr. 404479188). M.B. also acknowledges funding by the DFG in frame of project BA 4467/10-1 and S.L. financial support through the SFB 1477 'Light–Matter Interactions at Interfaces', project no. 441234705.

■ REFERENCES

(1) Zhang, S.; Yang, X.; Numata, Y.; Han, L. Highly efficient dye-sensitized solar cells: progress and future challenges. *Energy Environ. Sci.* **2013**, *6* (5), 1443.

(2) Arias-Rotondo, D. M.; McCusker, J. K. The photophysics of photoredox catalysis: a roadmap for catalyst design. *Chem. Soc. Rev.* **2016**, *45* (21), 5803–5820.

(3) Cheng, X.; Hu, X.; Lu, Z. Visible-Light-Promoted Aerobic Homogenous Oxygenation Reactions. *Chin. J. Org. Chem.* **2017**, *37* (2), 251.

(4) Büldt, L. A.; Larsen, C. B.; Wenger, O. S. Luminescent Ni^0 Diisocyanide Chelates as Analogues of Cu^I Diimine Complexes. *Chem. Eur. J.* **2017**, *23* (36), 8577–8580.

(5) Hockin, B. M.; Li, C.; Robertson, N.; Zysman-Colman, E. Photoredox catalysts based on earth-abundant metal complexes. *Catal. Sci. Technol.* **2019**, *9* (4), 889–915.

(6) Wenger, O. S. Photoactive Complexes with Earth-Abundant Metals. *J. Am. Chem. Soc.* **2018**, *140* (42), 13522–13533.

(7) Fukuzumi, S.; Lee, Y.-M.; Nam, W. Thermal and photocatalytic production of hydrogen with earth-abundant metal complexes. *Coord. Chem. Rev.* **2018**, *355*, 54–73.

(8) Larsen, C. B.; Wenger, O. S. Photoredox Catalysis with Metal Complexes Made from Earth-Abundant Elements. *Chem. Eur. J.* **2018**, *24* (9), 2039–2058.

(9) Dierks, P.; Vukadinovic, Y.; Bauer, M. Photoactive iron complexes: more sustainable, but still a challenge. *Inorg. Chem. Front.* **2022**, *9* (2), 206–220.

(10) Ishida, H.; Tobita, S.; Hasegawa, Y.; Katoh, R.; Nozaki, K. Recent advances in instrumentation for absolute emission quantum yield measurements. *Coord. Chem. Rev.* **2010**, *254* (21–22), 2449–2458.

(11) Sun, Q.; Mosquera-Vazquez, S.; Suffren, Y.; Hankache, J.; Amstutz, N.; Lawson Daku, L. M.; Vauthey, E.; Hauser, A. On the role of ligand-field states for the photophysical properties of ruthenium(II) polypyridyl complexes. *Coord. Chem. Rev.* **2015**, *282–283*, 87–99.

(12) Soupart, A.; Dixon, I. M.; Alary, F.; Heully, J.-L. DFT rationalization of the room-temperature luminescence properties of $Ru(bpy)_3^{2+}$ and $Ru(tpy)_2^{2+}$: ^{3}MLCT-^{3}MC minimum energy path from NEB calculations and emission spectra from VRES calculations. *Theor. Chem. Acc.* **2018**, *137* (3), 159.

(13) Förster, C.; Heinze, K. Photophysics and photochemistry with Earth-abundant metals - fundamentals and concepts. *Chem. Soc. Rev.* **2020**, *49* (4), 1057–1070.

(14) McCusker, J. K. Electronic structure in the transition metal block and its implications for light harvesting. *Science* **2019**, *363* (6426), 484–488.

(15) Amini, A.; Harriman, A.; Mayeux, A. The triplet excited state of ruthenium(II) bis(2,2′:6′,2″-terpyridine): Comparison between experiment and theory. *Phys. Chem. Chem. Phys.* **2004**, *6* (6), 1157–1164.

(16) Wenger, O. S. Is Iron the New Ruthenium? *Chem. Eur. J.* **2019**, *25* (24), 6043–6052.

(17) Schulze, B.; Escudero, D.; Friebe, C.; Siebert, R.; Görls, H.; Sinn, S.; Thomas, M.; Mai, S.; Popp, J.; Dietzek, B.; González, L.; Schubert, U. S. Ruthenium(II) photosensitizers of tridentate click-derived cyclometalating ligands: a joint experimental and computational study. *Chem. Eur. J.* **2012**, *18* (13), 4010–4025.

(18) Brown, D. G.; Sanguantrakun, N.; Schulze, B.; Schubert, U. S.; Berlinguette, C. P. Bis(tridentate) ruthenium-terpyridine complexes featuring microsecond excited-state lifetimes. *J. Am. Chem. Soc.* **2012**, *134* (30), 12354–12357.

(19) Abrahamsson, M.; Jäger, M.; Osterman, T.; Eriksson, L.; Persson, P.; Becker, H.-C.; Johansson, O.; Hammarström, L. A 3.0 micros room temperature excited state lifetime of a bistridentate RuII-polypyridine complex for rod-like molecular arrays. *J. Am. Chem. Soc.* **2006**, *128* (39), 12616–12617.

(20) Otto, S.; Dorn, M.; Förster, C.; Bauer, M.; Seitz, M.; Heinze, K. Understanding and exploiting long-lived near-infrared emission of a molecular ruby. *Coord. Chem. Rev.* **2018**, *359*, 102–111.

(21) Otto, S.; Nauth, A. M.; Ermilov, E.; Scholz, N.; Friedrich, A.; Resch-Genger, U.; Lochbrunner, S.; Opatz, T.; Heinze, K. Photo-Chromium: Sensitizer for Visible-Light-Induced Oxidative C–H Bond Functionalization—Electron or Energy Transfer? *ChemPhotoChem.* **2017**, *1* (8), 344–349.

(22) Chábera, P.; Kjaer, K. S.; Prakash, O.; Honarfar, A.; Liu, Y.; Fredin, L. A.; Harlang, T. C. B.; Lidin, S.; Uhlig, J.; Sundström, V.; Lomoth, R.; Persson, P.; Wärnmark, K. FeII Hexa N-Heterocyclic Carbene Complex with a 528 ps Metal-to-Ligand Charge-Transfer Excited-State Lifetime. *J. Phys. Chem. Lett.* **2018**, *9* (3), 459–463.

(23) Mukherjee, S.; Torres, D. E.; Jakubikova, E. HOMO inversion as a strategy for improving the light-absorption properties of Fe(II) chromophores. *Chem. Sci.* **2017**, *8* (12), 8115–8126.

(24) Jiang, T.; Bai, Y.; Zhang, P.; Han, Q.; Mitzi, D. B.; Therien, M. J. Electronic structure and photophysics of a supermolecular iron complex having a long MLCT-state lifetime and panchromatic absorption. *Proc. Natl. Acad. Sci. U.S.A.* **2020**, *117* (34), 20430–20437.

(25) Leis, W.; Argüello Cordero, M. A.; Lochbrunner, S.; Schubert, H.; Berkefeld, A. A Photoreactive Iron(II) Complex Luminophore. *J. Am. Chem. Soc.* **2022**, *144* (3), 1169–1173.

(26) Steube, J.; Burkhardt, L.; Päpcke, A.; Moll, J.; Zimmer, P.; Schoch, R.; Wölper, C.; Heinze, K.; Lochbrunner, S.; Bauer, M. Excited-State Kinetics of an Air-Stable Cyclometalated Iron(II) Complex. *Chem. Eur. J.* **2019**, *25* (51), 11826–11830.

(27) Pal, A. K.; Li, C.; Hanan, G. S.; Zysman-Colman, E. Blue-Emissive Cobalt(III) Complexes and Their Use in the Photocatalytic Trifluoromethylation of Polycyclic Aromatic Hydrocarbons. *Angew. Chem., Int. Ed. Engl.* **2018**, *57* (27), 8027–8031.

(28) Kaufhold, S.; Rosemann, N. W.; Chábera, P.; Lindh, L.; Bolaño Losada, I.; Uhlig, J.; Pascher, T.; Strand, D.; Wärnmark, K.; Yartsev, A.; Persson, P. Microsecond Photoluminescence and Photoreactivity of a Metal-Centered Excited State in a Hexacarbene-Co(III) Complex. *J. Am. Chem. Soc.* **2021**, *143* (3), 1307–1312.

(29) Sinha, N.; Pfund, B.; Wegeberg, C.; Prescimone, A.; Wenger, O. S. Cobalt(III) Carbene Complex with an Electronic Excited-State

Structure Similar to Cyclometalated Iridium(III) Compounds. *J. Am. Chem. Soc.* **2022**, *144* (22), 9859−9873.
(30) Jamula, L. L.; Brown, A. M.; Guo, D.; McCusker, J. K. Synthesis and characterization of a high-symmetry ferrous polypyridyl complex: approaching the $^5T_2/^3T_1$ crossing point for Fe(II). *Inorg. Chem.* **2014**, *53* (1), 15−17.
(31) Moll, J.; Förster, C.; König, A.; Carrella, L. M.; Wagner, M.; Panthöfer, M.; Möller, A.; Rentschler, E.; Heinze, K. Panchromatic Absorption and Oxidation of an Iron(II) Spin Crossover Complex. *Inorg. Chem.* **2022**, *61* (3), 1659−1671.
(32) Chan, A. Y.; Ghosh, A.; Yarranton, J. T.; Twilton, J.; Jin, J.; Arias-Rotondo, D. M.; Sakai, H. A.; McCusker, J. K.; MacMillan, D. W. C. Exploiting the Marcus inverted region for first-row transition metal-based photoredox catalysis. *Science* **2023**, *382* (6667), 191−197.
(33) Chábera, P.; Liu, Y.; Prakash, O.; Thyrhaug, E.; Nahhas, A. E.; Honarfar, A.; Essén, S.; Fredin, L. A.; Harlang, T. C. B.; Kjær, K. S.; Handrup, K.; Ericson, F.; Tatsuno, H.; Morgan, K.; Schnadt, J.; Häggström, L.; Ericsson, T.; Sobkowiak, A.; Lidin, S.; Huang, P.; Styring, S.; Uhlig, J.; Bendix, J.; Lomoth, R.; Sundström, V.; Persson, P.; Wärnmark, K. A low-spin Fe(III) complex with 100-ps ligand-to-metal charge transfer photoluminescence. *Nature* **2017**, *543* (7647), 695−699.
(34) Kjær, K. S.; Kaul, N.; Prakash, O.; Chábera, P.; Rosemann, N. W.; Honarfar, A.; Gordivska, O.; Fredin, L. A.; Bergquist, K.-E.; Häggström, L.; Ericsson, T.; Lindh, L.; Yartsev, A.; Styring, S.; Huang, P.; Uhlig, J.; Bendix, J.; Strand, D.; Sundström, V.; Persson, P.; Lomoth, R.; Wärnmark, K. Luminescence and reactivity of a charge-transfer excited iron complex with nanosecond lifetime. *Science* **2019**, *363* (6424), 249−253.
(35) Steube, J.; Kruse, A.; Bokareva, O. S.; Reuter, T.; Demeshko, S.; Schoch, R.; Argüello Cordero, M. A.; Krishna, A.; Hohloch, S.; Meyer, F.; Heinze, K.; Kühn, O.; Lochbrunner, S.; Bauer, M. Janus-type emission from a cyclometalated iron(III) complex. *Nat. Chem.* **2023**, *15* (4), 468−474.
(36) Johnson, C. E.; Schwarz, J.; Deegbey, M.; Prakash, O.; Sharma, K.; Huang, P.; Ericsson, T.; Häggström, L.; Bendix, J.; Gupta, A. K.; Jakubikova, E.; Wärnmark, K.; Lomoth, R. Ferrous and ferric complexes with cyclometalating N-heterocyclic carbene ligands: a case of dual emission revisited. *Chem. Sci.* **2023**, *14* (37), 10129−10139.
(37) Reilly, S. W.; Webster, C. E.; Hollis, T. K.; Valle, H. U. Transmetallation from CCC-NHC pincer Zr complexes in the synthesis of air-stable CCC-NHC pincer Co(III) complexes and initial hydroboration trials. *Dalton Trans.* **2016**, *45* (7), 2823−2828.
(38) Raynal, M.; Pattacini, R.; Cazin, C. S. J.; Vallée, C.; Olivier-Bourbigou, H.; Braunstein, P. Reaction Intermediates in the Synthesis of New Hydrido, N-Heterocyclic Dicarbene Iridium(III) Pincer Complexes. *Organometallics* **2009**, *28* (14), 4028−4047.
(39) Steube, J.; Fritsch, L.; Kruse, A.; Bokareva, O. S.; Demeshko, S.; Elgabarty, H.; Schoch, R.; Alaraby, M.; Egold, H.; Bracht, B.; Schmitz, L.; Hohloch, S.; Kühne, T. D.; Meyer, F.; Kühn, O.; Lochbrunner, S.; Bauer, M. Isostructural Series of a Cyclometalated Iron Complex in Three Oxidation States. *Inorg. Chem.* **2024**, *63*, 16964.
(40) Zimmer, P.; Müller, P.; Burkhardt, L.; Schepper, R.; Neuba, A.; Steube, J.; Dietrich, F.; Flörke, U.; Mangold, S.; Gerhards, M.; Bauer, M. N-Heterocyclic Carbene Complexes of Iron as Photosensitizers for Light-Induced Water Reduction. *Eur. J. Inorg. Chem.* **2017**, *2017* (11), 1504−1509.
(41) Liu, Y.; Harlang, T.; Canton, S. E.; Chábera, P.; Suárez-Alcántara, K.; Fleckhaus, A.; Vithanage, D. A.; Göransson, E.; Corani, A.; Lomoth, R.; Sundström, V.; Wärnmark, K. Towards longer-lived metal-to-ligand charge transfer states of iron(II) complexes: an N-heterocyclic carbene approach. *Chem. Commun.* **2013**, *49* (57), 6412−6414.
(42) Duchanois, T.; Etienne, T.; Beley, M.; Assfeld, X.; Perpète, E. A.; Monari, A.; Gros, P. C. Heteroleptic Pyridyl-Carbene Iron Complexes with Tuneable Electronic Properties. *Eur. J. Inorg. Chem.* **2014**, *2014* (23), 3747−3753.
(43) Viaene, L.; D'Olieslager, J.; Ceulemans, A.; Vanquickenborne, L. G. Excited-state spectroscopy of hexacyanocobaltate(III). *J. Am. Chem. Soc.* **1979**, *101* (6), 1405−1409.
(44) Viaene, L.; D'Olieslager, J. Luminescence from and absorption by the 3T1g level of the hexacyanocobaltate(III) ion. *Inorg. Chem.* **1987**, *26* (6), 960−962.
(45) Päpcke, A.; Friedrich, A.; Lochbrunner, S. Revealing the initial steps in homogeneous photocatalysis by time-resolved spectroscopy. *J. Phys.: Condens. Matter* **2020**, *32* (15), 153001.
(46) Kasha, M. Characterization of electronic transitions in complex molecules. *Discuss. Faraday Soc.* **1950**, *9*, 14.
(47) Caspar, J. V.; Meyer, T. J. Photochemistry of tris(2,2'-bipyridine)ruthenium(2+) ion ($Ru(bpy)_3^{2+}$). Solvent effects. *J. Am. Chem. Soc.* **1983**, *105* (17), 5583−5590.
(48) Barigelletti, F.; Juris, A.; Balzani, V.; Belser, P.; Von Zelewsky, A. Excited-state properties of complexes of the tris(diimine)-ruthenium(2+) ion family. *Inorg. Chem.* **1983**, *22* (22), 3335−3339.
(49) Nicholson, R. S.; Shain, I. Theory of Stationary Electrode Polarography. Single Scan and Cyclic Methods Applied to Reversible, Irreversible, and Kinetic Systems. *Anal. Chem.* **1964**, *36* (4), 706−723.
(50) Heinze, J. Cyclic Voltammetry—"Electrochemical Spectroscopy". New Analytical Methods(25). *Angew. Chem., Int. Ed.* **1984**, *23* (11), 831−847.
(51) Randles, J. E. B. A cathode ray polarograph. Part II.—The current-voltage curves. *Trans. Faraday Soc.* **1948**, *44* (0), 327−338.
(52) Scholz, F.; Bond, A. M.; Compton, R. G.; Fiedler, D. A.; Inzelt, G.; Kahlert, H.; Komorsky-Lovrić, S.ˇ.; Lohse, H.; Lovrić, M.; Marken, F.; Neudeck, A.; Retter, U.; Scholz, F.; Stojek, Z. *Electroanalytical Methods*; Springer Berlin Heidelberg, 2010; ..
(53) Krause, L.; Herbst-Irmer, R.; Sheldrick, G. M.; Stalke, D. Comparison of silver and molybdenum microfocus X-ray sources for single-crystal structure determination. *J. Appl. Crystallogr.* **2015**, *48* (1), 3−10.
(54) Sheldrick, G. M. SHELXT − Integrated space-group and crystal-structure determination. *Acta. Crystallogr. A* **2015**, *71* (1), 3−8.
(55) Collado, A.; Bohnenberger, J.; Oliva-Madrid, M.; Nun, P.; Cordes, D. B.; Slawin, A. M. Z.; Nolan, S. P. Synthesis of Au^{I}- and Au^{III}-Bis(NHC) Complexes: Ligand Influence on Oxidative Addition to Au^{I} Species. *Eur. J. Inorg. Chem.* **2016**, *2016* (25), 4111−4122.

https://doi.org/10.1021/acs.inorgchem.4c04479
Inorg. Chem. 2025, 64, 1401−1409

Chapter 4: Photogeneration of Cobalt Stabilized Aminium Radical

The focus of this chapter is build on the results from chapter 3 and overcome the drawbacks of the parent $[Co(ImP)_2]^+$ system by functionalizing the backbone of the ImP ligand system with dimethylamino groups. Hence, this chapter details the synthesis, characterization and observed photoreactivity of the novel $[Co(ImP^{NMe_2})_2][BF_4]$ complex. $[Co(ImP^{NMe_2})_2][BF_4]$ undergoes a clean and fully reversible photooxidation upon mild UV irradiation or chemical oxidation. This process generates the dicationic species $[Co(ImPNMe_2)]^{2+}$, featuring a ligand-centered aminium radical.

A defining characteristic of this system is the extensive delocalization of the unpaired electron associated with the aminium radical. Spin density is distributed along the phenyl-Co-phenyl axis rather than being localized at a single nitrogen atom, providing substantial stabilization of the open-shell state. The electronic structure of the radical species is further supported by complementary UV-Vis absorption spectroscopy, spectroelectrochemical UV-Vis measurements, X-ray absorption spectroscopy, and EPR spectroscopy. The number of unpaired electrons was estimated by employing evans NMR method. Formation of the aminium radical is accompanied by the appearance of two intense and well-defined absorption bands, which serve as convenient spectroscopic markers for monitoring the photo-redox process. The reversibility of these spectral changes makes the system particularly well suited for mechanistic investigations of light-induced electron-transfer chemistry.

Overall, this work establishes a rare example of a light-induced, ligand-centered radical in a cobalt complex and demonstrates how targeted ligand design can decouple redox activity from the metal center. These findings provide valuable insight into the stabilization and characterization of reactive open-shell intermediates and highlight the potential of such systems for photo-induced reactivity and future photocatalytic applications.

Publication is reprinted from https://doi.org/10.26434/chemrxiv-2026-7f3nd .

Participations in this project:

Athul Krishna: Design and synthesis of the title molecule, its standard characterization (NMR, MS), cyclic voltammetry, UV-Vis spectroscopy, interpretation of the data, manuscript writing- Institute for Inorganic Chemistry and Center for Sustainable Systems Design (CSSD), Paderborn University, Paderborn 33098, Germany

Timur Biktagirov: EPR simulations - Institute for Inorganic Chemistry and Center for Sustainable Systems Design (CSSD), Paderborn University, Paderborn 33098, Germany

Daniel Leitner: Illuminated EPR measurements- Department of General, Inorganic and Theoretical Chemistry, University of Innsbruck, Innrain 80-82, A-6020 Innsbruck, Austria

Ayla Kruse: Transient absorption measurement data - Department of Life, Light and Matter and Institute of Physics, University of Rostock, Rostock 18051, Germany

Hamada Rezk: TD-DFT calculations - Leibniz Institute for Catalysis (LIKAT), 18059 Rostock, Germany

Fridolin Hennhoefer: EPR measurements - Institute of Chemistry and Biochemistry, Inorganic Chemistry, Freie Universität Berlin, Kaiserswerther Str. 16-18, 14195 Berlin, Germany

Jannik Löseke: TD-DFT calculations and review of the manuscript – Institute for Inorganic Chemistry and Center for Sustainable Systems Design (CSSD), Paderborn University, Paderborn 33098, Germany

Michal Nowakowski: Measurement and interpretation of XAS - Institute for Inorganic Chemistry and Center for Sustainable Systems Design (CSSD), Paderborn University, Paderborn 33098, Germany

Dr. Lorena Fritsch: TD-DFT calculations and review of the manuscript - Institute for Inorganic Chemistry and Center for Sustainable Systems Design (CSSD), Paderborn University, Paderborn 33098, Germany

Dr. Jakob Steube: Interpretation of the data, insightful discussions and review of the manuscript - Institute for Inorganic Chemistry and Center for Sustainable Systems Design (CSSD), Paderborn University, Paderborn 33098, Germany

Anke Schoch: Gas MS measurements- Institute for Inorganic Chemistry and Center for Sustainable Systems Design (CSSD), Paderborn University, Paderborn 33098, Germany

Dr. Hossam Elgabarty: Theoretical calculations- Institute for Inorganic Chemistry and Center for Sustainable Systems Design (CSSD), Paderborn University, Paderborn 33098, Germany

Dr. Olga Bokareva: Interpretation of TD-DFT calculations - Leibniz Institute for Catalysis (LIKAT), 18059 Rostock, Germany

Dr. Adam Neuba: Spectroelectrochemical UV-Vis measurements - Institute for Inorganic Chemistry and Center for Sustainable Systems Design (CSSD), Paderborn University, Paderborn 33098, Germany

Dr. Hans Egold: NMR measurements- Institute for Inorganic Chemistry and Center for Sustainable Systems Design (CSSD), Paderborn University, Paderborn 33098, Germany

Dr. Roland Schoch: X-ray diffraction measurements - Institute for Inorganic Chemistry and Center for Sustainable Systems Design (CSSD), Paderborn University, Paderborn 33098, Germany

Katharina Lorena Franzke: Theoretical calculations for EPR simulations- Institute for Inorganic Chemistry and Center for Sustainable Systems Design (CSSD), Paderborn University, Paderborn 33098, Germany

Prof. Dr. Uwe Gerstmann: Theoretical calculations for EPR simulations- Institute for Inorganic Chemistry and Center for Sustainable Systems Design (CSSD), Paderborn University, Paderborn 33098, Germany

Prof. Dr. Stephan Hohloch: Illuminated EPR measurements- Department of General, Inorganic and Theoretical Chemistry, University of Innsbruck, Innrain 80-82, A-6020 Innsbruck, Austria

Prof. Dr. Oliver Kühn: TD-DFT Calculations- TD-DFT calculations- Institute of Physics, University of Rostock, 18051 Rostock, Germany

Prof. Dr. Biprajith Sarkar: Interpretation of EPR measurements - Institute of Chemistry and Biochemistry, Inorganic Chemistry, Freie Universität Berlin, Kaiserswerther Str. 16-18, 14195 Berlin, Germany

Prof. Dr. Stefan Lochbrunner: Interpretation of the Transient absorption measurement data -Department of Life, Light and Matter and Institute of Physics, University of Rostock, Rostock 18051, Germany

Jun. Prof. Dr. Felix Fischer: Review of the manuscript- Institute for Inorganic Chemistry and Center for Sustainable Systems Design (CSSD), Paderborn University, Paderborn 33098, Germany

Prof. Dr. Wolf Gero Schmidt: Interpretation of EPR data - Institute for Inorganic Chemistry and Center for Sustainable Systems Design (CSSD), Paderborn University, Paderborn 33098, Germany

Prof. Dr. Matthias Bauer: Project Supervisor - Institute for Inorganic Chemistry and Center for Sustainable Systems Design (CSSD), Paderborn University, Paderborn 33098, Germany

Photogeneration of Cobalt-Stabilized Aminium Radical

A. Krishna[a], T. Biktagirov[a], D. Leitner[b], A. Kruse[c], H. Rezk[d], F. Hennhoefer[e], J. Löseke[a], M. Nowakowski[a], L. Fritsch[a], J. Steube[a], A. Schoch[a], H. Elgabarty[a], O. S. Bokareva[d], A. Neuba[a], H. Egold[a], R. Schoch[a], K.L. Franzke[a], U. Gerstmann[a], S. Hohloch[b], O. Kühn[c], B. Sarkar[e], S. Lochbrunner[c], F. R. Fischer[a], W. G. Schmidt[a], M. Bauer[a]*

[a] Institute of Inorganic Chemistry and Center for Sustainable Systems Design (CSSD), Paderborn University, Warburger Str. 100, 33098 Paderborn, Germany. E-mail: matthias.bauer@upb.de

[b] Department of General, Inorganic and Theoretical Chemistry, University of Innsbruck, Innrain 80-82, A-6020 Innsbruck, Austria

[c] Institute of Physics, University of Rostock, 18051 Rostock, Germany

[d] Leibniz Institute for Catalysis (LIKAT), 18059 Rostock, Germany

[e] Institute of Chemistry and Biochemistry, Inorganic Chemistry, Freie Universität Berlin, Kaiserswerther Str. 16-18, 14195 Berlin, Germany

Abstract: Transition metal-stabilized radical systems have been of interest in the field of redox chemistry. However, ligand-centered radicals still remain difficult to access and control photochemically in first-row transition-metal complexes. Here we report a cobalt complex based on a dimethylamino-functionalized ImP (bis(imidazolylidene)phenyl) ligand scaffold that undergoes a clean and reversible photooxidation to generate a $[Co(ImP^{NMe2})]^{2+}$ featuring a ligand centered aminium radical upon exposure to mild UV irradiation or chemical oxidation. The unpaired electron of the aminium nitrogen is delocalized along the phenyl-Co-phenyl axis, enabling direct characterization by NMR spectroscopy in addition to UV-Vis, SEC-UV-Vis, XAS and EPR spectroscopy. Formation of the radical is accompanied by the emergence of two intense absorption bands, allowing convenient spectroscopic monitoring of the photo-redox process. Together, these results establish a rare example of a light-induced ligand-centered radical in a cobalt complex and highlight its potential for photo-induced reactivity.

Introduction

Radicals play an important role in maintaining and regulating a variety of key biological and chemical reactions.[1–3] In general, radicals are highly reactive species possessing considerably small lifetimes. However, their chemical reactivity and stability are influenced by various means: Both altering the steric properties and extending the delocalization of the unpaired electron into extended π-systems have been successful.[4–6]

One prominent example is N,N,N',N'-tetramethyl phenylenediamine (TMPD), which leads to a stable radical cation upon oxidation, known as Wurster's Blue.[7–9] Notably, aromatic (di)amines such as TMPD or benzidine can be oxidized photochemically in the presence of electron acceptors, such as a suitable solvent like dichloromethane.[10] The nitrogen centers in these mixed-valence compounds are coupled, where the coupling strength can lead to either a localized or delocalized charge.[11,12] The coupling and localization are heavily dependent on multiple factors, such as the bridge between the redox centers.[13] Here, even transition metal complexes can be employed, such as platinum alkynyl or porphyrin complexes.[14,15] Identifying the location of unpaired electrons in transition metal complexes with potentially radical-bearing ligands has often been aided by combining spectroscopic and improved computational techniques, with electron paramagnetic resonance (EPR) spectroscopy being one of the most important experimental methods.[16–22] In Ru^{II} terpyridine complexes bearing dianisylamino functional groups in the backbone, strong coupling with localized charges was observed, with minor contributions of the ruthenium center.[23–25] This concept has been extended to asymmetric Ru/N mixed valence compounds, where ruthenium is employed as one redox center.[26–28] Hence, introduction of metal centers to mixed valence compounds is an interesting approach, which may find application in molecular electronics.[29–32] However, the applicability of these complexes can suffer from the requirement of an additional oxidizing agent or harsh conditions to form the radical.[22,33–35] Consequently, light-induced radical generation is a major advantage, which can be exploited for potential photoswitching.[12,36]

Recently, Bauer *et al*. have shown that $[Co(ImP^{H})_2]^+$ ($HImP^{H}$ = 1,1′-(1,3-phenylene)bis(3-methyl-1-imidazol-2-ylidene)) complexes exhibit long-lived excited MC states,[37] which are known to be redox-active for other Co^{III} complexes.[38,39] Based on this work, a dimethylamine-decorated $[Co(ImP^{NMe2})_2]^+$($HImP^{NMe2}$ = N,N-dimethyl-3,5-bis(3-methyl-1-imidazol-2-ylidene)aniline) complex is presented here, which can be photochemically oxidized to form an aminium radical

cation. Both species and the formation process have been investigated extensively by various methods, including NMR, UV-Vis, EPR and X-ray absorption spectroscopy (XAS). In addition, transient absorption (TA) spectroscopy and trajectory surface hopping (TSH) simulations give deeper insight into the excited-state kinetics of the complex.

Results and discussion

Synthesis

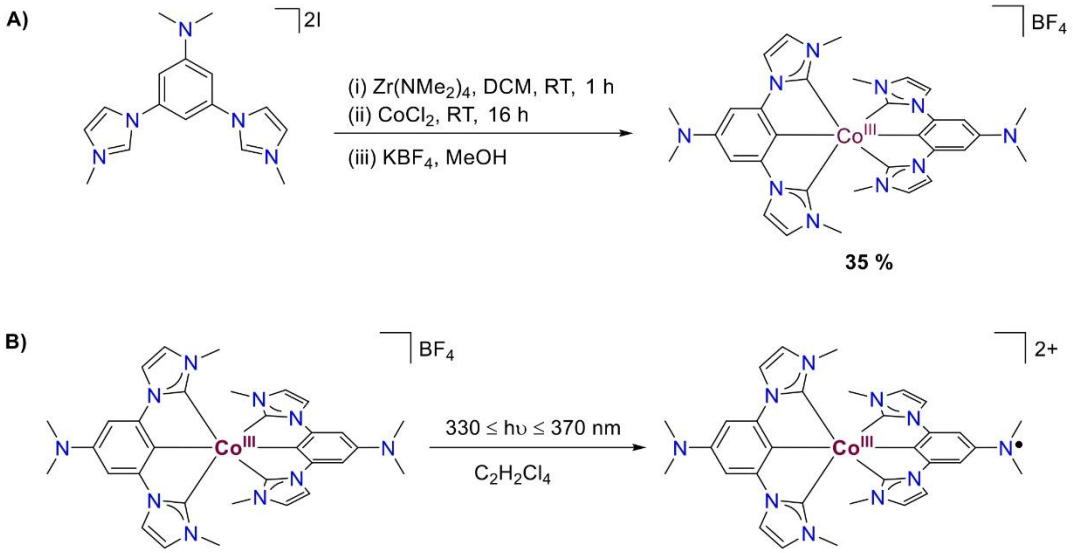

Scheme 1: A) Complex synthesis: Activation of the proligand with a zirconium reagent, followed by transmetalation and anion exchange. RT: room temperature. **B)** Radical generation using light in the spectral range between 330 and 370 nm in TeCA.

The synthesis of $[Co(ImP^{NMe2})_2]^+$ followed known protocols: The proligand was obtained as reported in the literature by methylation of dibromoaniline and subsequent coupling with imidazole.[40,41] Both the following methylation and complex synthesis were adapted from previously published synthesis protocols.[37,42] Potassium tetrafluoroborate in methanol was used for anion exchange. Yellow crystals of $[Co(ImP^{NMe2})_2](BF_4)$ suitable for single-crystal X-ray diffraction were obtained in 35 % yield upon diffusion of n-pentane into a solution of the complex in dichloromethane in the dark. Since solutions of this yellow complex took on a greenish tint over time in dichloromethane, the controlled oxidation of this compound was

investigated. The one-electron oxidized complex $[Co(ImP^{NMe2})_2]^{2+}$ was obtained by reaction with oxidizing agents, such as $K_2S_2O_8$, or by irradiating the base complex in the presence of chlorinated solvents such as dichloromethane (DCM) and tetrachloroethane (TeCA) with light between 330 and 370 nm (cf. Supporting Information: Fig. S10-15). The full list of investigated substrates as electron acceptors can be found in the Supporting Information (cf. Supporting Information: Table S1). This behavior is in good agreement with literature on the photoinduced electron transfer from TMPD and derivatives to dichloromethane and other electron acceptors.[10] Due to the long-term instability of $[Co(ImP^{NMe2})_2]^{2+}$, no crystals could be obtained. Further oxidation leads to precipitation, indicating either insolubility or instability of the formed $[Co(ImP^{NMe2})_2]^{3+}$.

Cyclic voltammetry

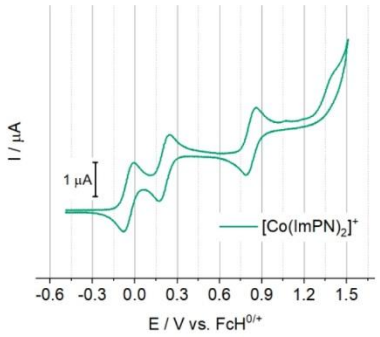

Figure 1: Cyclic voltammogram of 1 mM $[Co(ImP^{NMe2})_2][BF_4]$ in 0.1 M $[N(nBu_4)][PF_6]$ acetonitrile (MeCN) solution.

To classify the observed redox behavior, cyclic voltammetry (CV) was employed. In the voltammograms, three reversible oxidation processes were observed (Fig. 1). The first two events at -0.01 and 0.24 V vs. $FcH^{0/+}$ can be attributed to the oxidation of the two amines at the ligand backbone. Coulometry confirms that two electrons are transferred within these two redox events (cf. Supporting Information: Fig. S28). While oxidation of dimethylamine moieties was not observed in amine functionalized bis-NHC-pyridine-Ru^{II} or Fe^{II} complexes,[43,44] both polypyridyl and cyclometalated Ru^{II} compounds decorated with diphenylamine moieties show such oxidation events.[23,27] The third oxidation event at 0.85 V is attributed to the $Co^{III/IV}$ redox couple, anodically shifted compared to $[Co(ImP^{H})_2]^{+}$ (0.63 V). [37] This observation can be explained by

the appended aminium radical cations, drawing electron density from the cobalt center, in accordance with the literature.[23]

Identification of the radical character

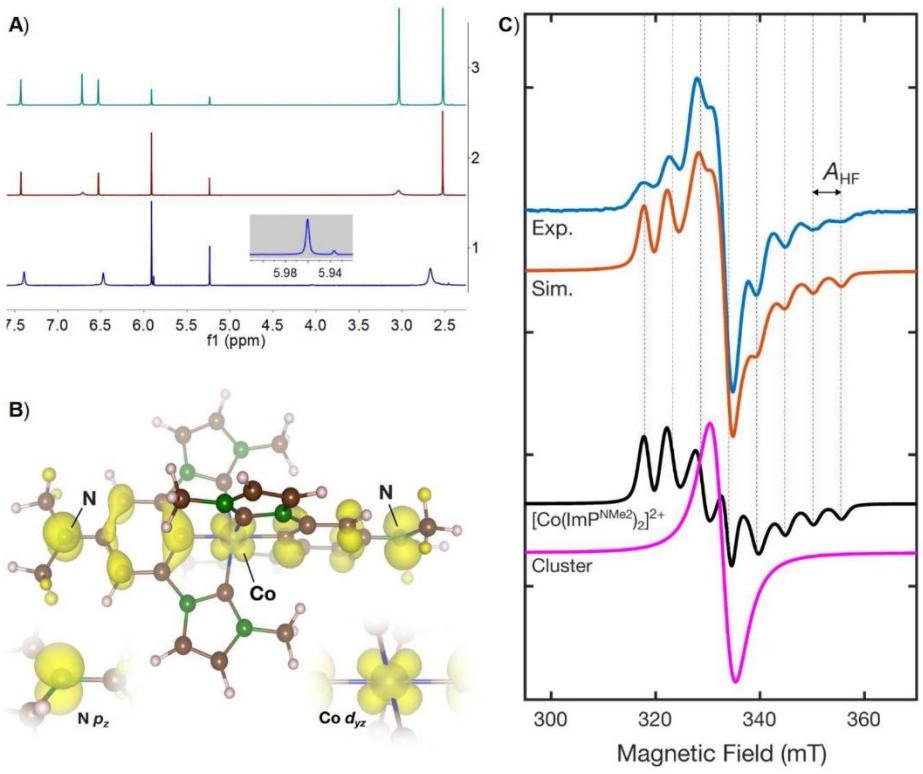

Figure 2: A) ^{1}H NMR spectra with a capillary containing a $C_2D_2Cl_4$ solution of (i) $[Co(ImP^{NMe2})_2][BF_4]$(top), (ii) $[Co(ImP^{NMe2})_2][BF_4]$ after 5 mins of irradiation (middle) and (iii) $[Co(ImP^{NMe2})_2]^{2+}$(bottom). (iv) The inset shows the shifted signal of the capillary inside. **B)** DFT-calculated spin density distribution of $[Co(ImP^{NMe2})_2]^{2+}$. Yellow lobes represent the isosurface at 0.002 e/Å^3. Insets: Enlarged views of the spin density localized on the N pz orbital and Co d_{yz} orbital. **C)** X-band CW EPR spectrum of $[Co(ImP^{NMe2})_2]^{2+}$ recorded at 113 K, with a simulation based on DFT-derived spin Hamiltonian parameters of $[Co(ImP^{NMe2})_2]^{2+}$ (cf. Supporting Information: Table S3). The simulation comprises two components: $[Co(ImP^{NMe2})_2]^{2+}$and a tentatively assigned exchange-coupled cluster of $[Co(ImP^{NMe2})_2]^{2+}$.

To further elucidate and confirm the nature of the species generated by oxidation, NMR measurements in TeCA-d_2 were performed. An experimental μ_{eff} of 1.1 BM was determined for the oxidized complex with the Evans method. This value is in the expected range for the paramagnetic susceptibility exerted by one unpaired electron (Fig. 2A).[45] The ^{1}H- and ^{13}C-NMR spectroscopic shifts of $[Co(ImP^{NMe2})_2]^{+/2+}$ are listed in the Supporting Information (cf. Supporting Information: Table S2). All peaks in the ^{1}H-NMR spectra become noticeably broader upon irradiation of the initial compound, indicating the formation of a paramagnetic species. The shifts observed under irradiation are in accordance with those obtained by chemical oxidation. A detailed comparison of the parent and oxidized species reveals the disappearance of signals corresponding to the aryl (a) and dimethylamine protons (d) (Fig. 3). The imidazole (b, c) and N-methyl imidazole protons (e) are slightly shifted for the radical complex. The latter experiences a downfield shift from 2.52 to 2.72 ppm, indicating a reduction in electron density in the phenyl-Co-phenyl axis after oxidation. However, it should be noted that these shifts are minor compared to the chemical shifts observed for the $[Fe^{II/III}(ImP^{H})_2]^{+/2+}$ complexes reported by Bauer *et al.*, where metal-centered oxidations are observed.[46,47] In the ^{15}N-HMBC spectra for the parent complex, signals for the amine and imidazole moieties are visible, while the amine signal vanishes for the paramagnetic oxidized complex. The imidazole signals remain unaffected by the oxidation. These results suggest that oxidation takes place at the nitrogen and indicate that the radical cation is delocalized along the N-phenyl-Co-phenyl-N-axis. These results are supported by DFT analysis: the calculated spin density distribution (Fig. 2B) reveals that the unpaired electron is in fact delocalized over the d_{yz} orbital of the Co center, the π-systems of both phenylene units and the p_z orbitals of the aminium N atom. The Mulliken spin population analysis yields 0.20 on the Co center and 0.16 on each aminyl N atom (Fig. 2B).

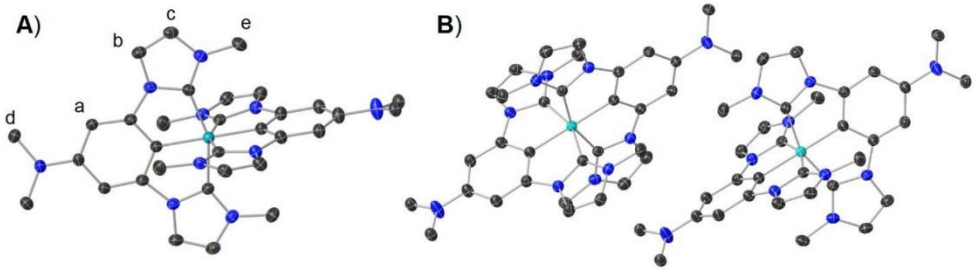

Figure 3: **A)** Molecular structure of $[Co(ImP^{NMe2})_2]^+$ obtained from single crystal analysis including the used nomenclature for NMR assignment. **B)** Packing of two complexes. Anisotropic displacement ellipsoids drawn on a 50% probability level. Counter ions (BF_4), solvent molecules (dichloromethane) and hydrogen atoms are omitted for clarity.

Further evidence comes from EPR spectroscopy. X-band EPR of $[Co(ImP^{NMe2})_2]^+$ in TeCA was measured after irradiation of the frozen solution and subsequent thawing and refreezing. The spectrum is centered at a g-factor of 2.03 but now exhibits an equidistant pattern of eight lines, characteristic of an S = 1/2 spin state split due to the coupling with the I = 7/2 nuclear spin of ^{59}Co. The electron-nuclear hyperfine (HF) coupling strength, determined from the splitting, is AHF = 150 MHz (5.4 mT), consistent with DFT calculations for a doubly charged oxidized species in an S = 1/2 spin state (cf. Supporting Information: Table S3). The EPR spectrum was then simulated using the principal values of the g and HF tensors obtained from the DFT model of $[Co(ImP^{NMe2})_2]^{2+}$, which were subsequently fine-tuned to achieve optimal agreement (for details, see SI). As shown in Fig. 2C, the experimental spectrum can be described as a superposition of $[Co(ImP^{NMe2})_2]^{2+}$ and a second species, which appears as a broad signal in the central region (magenta trace in Fig. 2C). We cannot rule out the influence of paramagnetic solvent radical anions. The g-factor of the second species (g = 2.033) matches however the average g-factor of $[Co(ImP^{NMe2})_2]^{2+}$, and thus can be tentatively assigned to pairs or small clusters of $[Co(ImP^{NMe2})_2]^{2+}$ in which anisotropies of the g- tensors and ^{59}Co HF tensors are averaged due to magnetic exchange interaction among neighboring spin centers with slightly differently oriented molecular axes.[48,49] Here the structural information from X-ray diffraction of the solid state yields the central motif of structural entangled molecular complexes (Fig. 3b), which should also be present in solution. Having in mind the quite small Co-Co distance of

neighboring Co-complexes in the solid state (8.92 Å, Fig. 3b) and given the fact that the minimum distance of decisive parts of the spin distribution are localized even much closer (5.66 Å for the central Co and an aminyl N atom of a neighboring complex), the observation of an intense exchange line appears to be straightforward even in solution, where averaging of tensor anisotropies is facilitated.

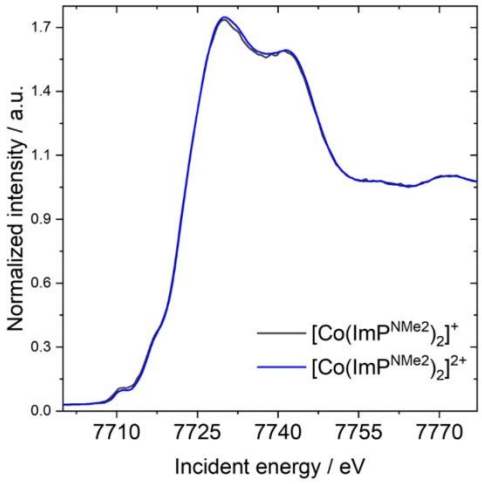

Figure 4: XANES spectra of the $[Co(ImP^{NMe2})_2]^{+/2+}$

In addition, XAS spectra of $[Co(ImP^{NMe2})_2]^{+/2+}$ were recorded and are shown in Fig. 4. It can be noted that no distinct differences between the spectra are observable. The pre-edge region (up to ~7712 eV) consists of visible transitions at 7707-7711 eV smoothly transitioning to the shoulder 7715 eV, typically associated with the admixtures of unoccupied ligand p-orbitals to the absorber's empty 4p orbitals. The pre-edge signals emerge due to mixing of metal 3d unoccupied states with the unoccupied ligand 2p and metal 4p orbitals. However, in O_h symmetry the 3d-4p overlap is weak and increases when the system gets distorted. The pre-edge region (7700 – 7715 eV) was more closely investigated with TDDFT calculations (cf. Supporting Information: Fig. S30-33, Table S7-9). The broadened transitions of both compounds reproduce the tiny intensity difference in the pre-edge region at 7712 eV. However, transitions in the oxidized species are much more numerous and weaker due to the open-shell nature of the radical system. Upon rebinning with a 0.2 eV window, their number is significantly reduced. Consequently, the outcome distribution significantly overlaps with the parent species and explains the lack of

visible differences in the experiment. However, it must be noted that the experimental spectrum of $[Co(ImP^{NMe2})_2]^{2+}$ still contains some parent compound, which additionally obscures expected spectral differences. Since Co K-edge XAS probes the p-projected electronic structure locally from the Co point of view, the lack of spectral changes indicates that the unpaired electron of $[Co(ImP^{NMe2})_2]^{2+}$ is indeed located on the amine. Therefore, changes in the electronic structure around the Co-center only have secondary character or are too weak to be experimentally resolved.

UV/Vis spectroscopy and spectroelectrochemistry

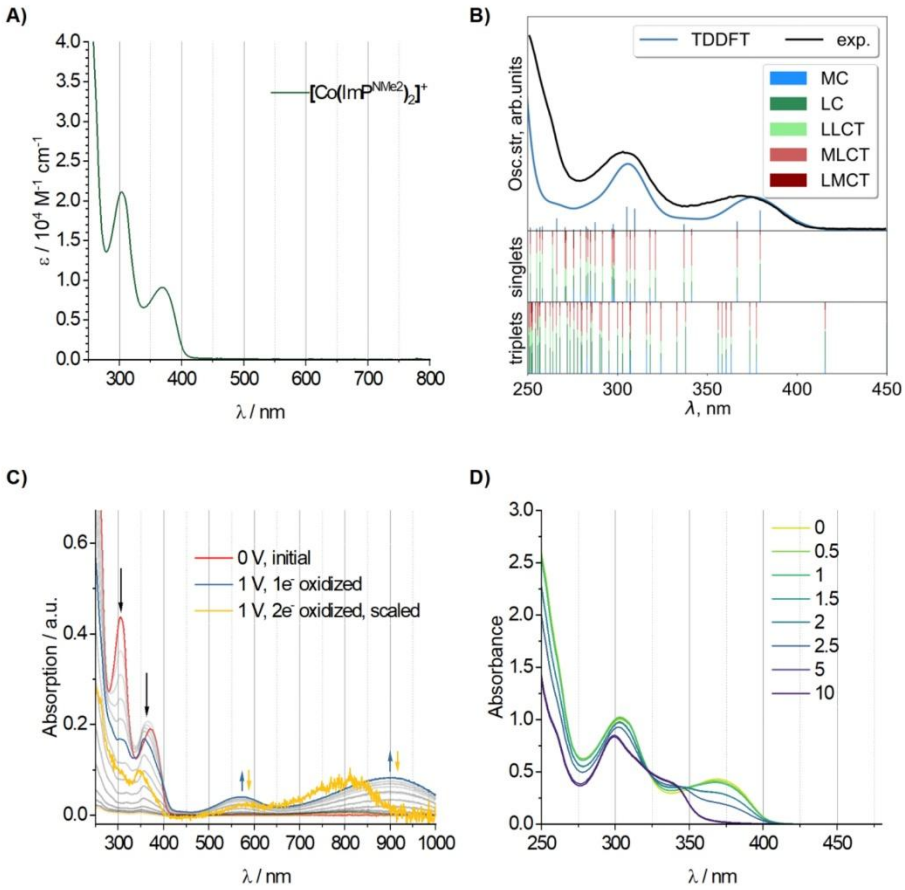

Figure 5: A) Experimental absorption spectra of $[Co(ImP^{NMe2})_2][BF_4]$ (10 µM in MeCN). **B)** Overlay of the simulated optical absorption spectrum for $[Co(ImP^{NMe2})_2][BF_4]$in dichloromethane (blue line) and the experimental spectrum (grey line). The lower two panels show the density-matrix analysis of the corresponding excited states. **C)** Spectroelectrochemical oxidation of $[Co(ImP^{NMe2})_2][BF_4]$ in dichloromethane. **D)** Protonation of $[Co(ImP^{NMe2})_2][BF_4]$ in MeCN using 0-10 eq. of HCl.

Consequently, the aminium radical character of $[Co(ImP^{NMe2})_2]^{2+}$ could be confirmed by different methods. To address the photooxidation properties of the parent compound, electronic absorption spectra of $[Co(ImP^{NMe2})_2]^{+}$ were recorded both in acetonitrile (MeCN) (10 µM, Fig. 5A) and TeCA (10 µM, cf. Supporting Information: Fig. S27). In the spectra, similar features to those of

$[Co(ImP^{H})_2]^+$ are observable.[37] Two prominent absorption bands are visible at 302 nm (ε_{302} = 2.1 × 10^4 M^{-1} cm^{-1}) and 368 nm (ε_{368} = 0.9 × 10^4 M^{-1} cm^{-1}) respectively. These two absorption bands share the same absorption profile as $[Co(ImP^{H})_2]^+$ (294 and 335 nm), even though they are shifted to lower energies. TD-DFT calculations show that both discernable bands are dominated by mixed MLCT/LC transitions, with the energetically lowest being mostly LC character (Fig. 5B). This is in accordance with the experimentally determined ligand-based HOMO. The region below 275 nm is dominated by LC transitions. Hence, introduction of the dimethylamine moiety not only increases the π-energy of the ligand but also decreases its π*-energy, as neither MC- nor ligand-to-metal charge-transfer bands are observed.

Upon oxidation of $[Co(ImP^{NMe2})_2]^+$ by electrochemical means at 1 V, two absorption bands at 570 nm and 900 nm simultaneously rise first, attributed to $[Co(ImP^{NMe2})_2]^{2+}$ (Fig. 5C). Unfortunately, it was not possible to only oxidize the compound once, therefore, all bands lose intensity over time due to precipitation of the newly formed $[Co(ImP^{NMe2})_2]^{3+}$. However, scaling the spectrum reveals that the band around 570 nm remains at the same position, while a blueshift to around 800 nm is observed for the low-energy band. Applying a voltage of 0 V leads to a complete reversion of these changes (Fig. 5C).

Since the dimethylamine functionality can serve as a base, the protonation of $[Co(ImP^{NMe2})_2]^+$ was investigated via UV-Vis (Fig. 5D). After the addition of 10 eq. HCl, the spectra resemble those of $[Co(ImP^{H})_2]^+$, including the positioning of the peaks. This observation is in accordance with a doubly protonated species, due to the absence of the intense dimethylamine-involving LC bands. With 2.5 eq. of acid, the LC-dominated band at 370 nm is reduced in intensity and an additional feature at around 340 nm, also found in the 10 eq. HCl spectra, emerged, resembling a mixed form of $[Co(ImP^{H})_2]^+$ and $[Co(ImP^{NMe2})_2]^+$. However, the intermediate spectra cannot be reproduced perfectly by a linear combination of the 0 and 10 eq. spectra, hence, the presence of another species is suspected. Consequently, the protonation of $[Co(ImP^{NMe2})_2]^+$ leads to a doubly protonated species and is observed via an intermediary singly protonated species. However, the similarity of all species does not allow for a reliable extraction of the corresponding spectrum.

Excited state dynamics

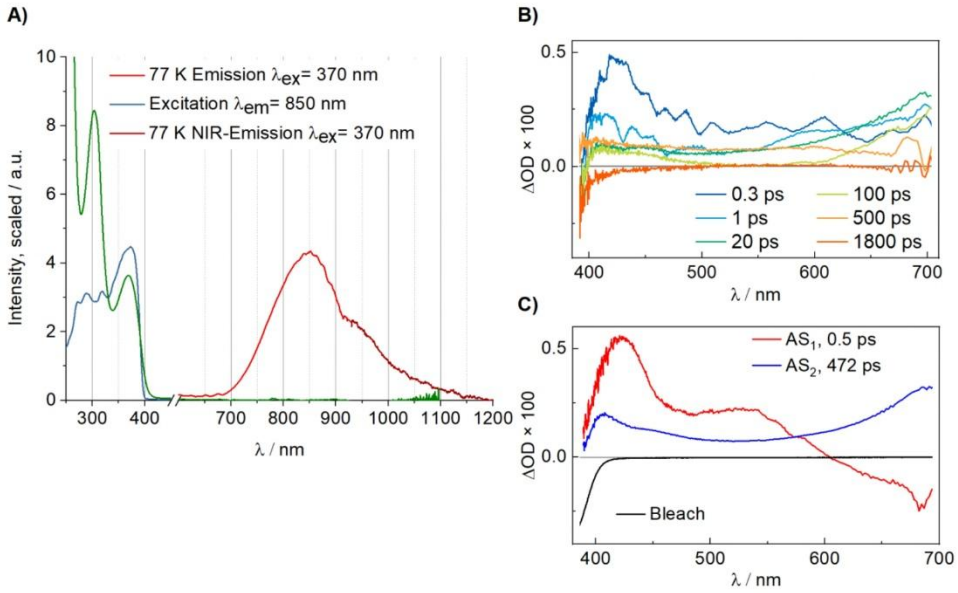

Figure 6: A) Normalized and scaled low temperature emission spectrum of $[Co(ImP^{NMe2})_2]^{2+}$ at 77 K after excitation at 340 nm in BuCN (red and brown), together with the excitation (blue) and absorption spectrum (green). **B)** fsTA spectra at specified delay times and **C)** corresponding DAAS of the investigated Co complex in MeCN after optical excitation at 335 nm.

Like $[Co(ImP^{H})_2]^{+}$, $[Co(ImP^{NMe2})_2]^{+}$ only shows an emission at 77 K (Fig. 6A). Here, the emission maximum is observed at 850 nm which tails beyond 1200 nm, compared to the 760 nm emission of the parent compound.[37] The stark redshift of the emission maximum is surprising, since stronger donors should increase the energy of the excited state. Therefore, it can be assumed that the energetically lowest state is not an MC state in this case. However, the excitation spectrum reveals some discrepancies with the absorption spectrum: While the absorption band at 370 nm is reproduced well, the 300 nm band is not observed in the excitation spectrum. Since multiple explanations are valid for this behavior, the excited state dynamics were further investigated.

Ultrafast transient absorption measurements using excitation pulses at 335 nm were performed on $[Co(ImP^{NMe2})_2][BF_4]$ dissolved in MeCN (Fig. 6B) and DCM (cf. Supporting Information: Fig. S34). While in MeCN no significant photooxidation takes place, in DCM, $[Co(ImP^{NMe2})_2]^{+}$ behaves similar as in TeCA. For both solvents, the temporal evolution of the TA was globally

fitted with two exponential decay components. In addition, a weak third component with a ns-lifetime was necessary to obtain also at large delay times good agreement. However, this component was also observed in the pure solvent and is thus attributed to a shift of the baseline. The decay-associated amplitude spectrum (DAAS) of the decay component with the time constant τ_1 (0.5 ps in MeCN, 0.6 ps in DCM) is characterized by an excited state absorption (ESA) with a maximum at 430 nm (Fig 6B, Supporting Information: Fig. S35). In addition, a negative band above 600 nm spanning into the NIR is observable. This feature mirrors the excited state absorption found in the DAAS of the decay component with the time constant τ_2 (472 ps in MeCN, 651 ps in DCM), indicating that the fast component reflects population of the state responsible for the ESA in the red spectral region. Here, a broad ESA band with a maximum outside the measurement range is observed, reminiscent of the spectrum of $[Co(ImP^{NMe2})_2]^{2+}$, shown in Fig. 5c. However, the characteristic band at 560 nm is missing. Consequently, the long-lived ESA is not attributed to a charge-transfer state but preliminary to a ligand-centered triplet(^{3}LC) state, based on lifetime and appearance. The behavior is different to that of the previously studied $[Co(ImP^{H})_2]^{+}$complex in which the population of a long-lived MC state was observed.[37] The broad ESA band extending from 370 to 700 nm, which is characteristic for the MC state, is missing in the case of $[Co(ImP^{NMe2})_2]^{+}$, indicating that MC states are not contributing to the observed dynamics. While photooxidation of $[Co(ImP^{NMe2})_2]^{+}$occurs in DCM, no component attributable to the radical is found in the TA data. Therefore, electron transfer presumably only takes place in a small fraction of the optically excited molecules and is thus not observable in TA.

Further insight is gained from theoretical investigations (additional details are shown in the Supporting Information: Nonadiabatic dynamics simulations). According to TDDFT, the energetically lowest triplet state has mainly LC character. Trajectory surface hopping (TSH) simulations propose the following relaxation cascade, starting from an initially populated ^{1}MLCT state: First, intersystem crossing (ISC) into a ^{3}MLCT state or relaxation into the energetically lower ^{1}LC is observed, which can undergo ISC into the ^{3}MLCT state. Most of the population is then transferred to a slowly decaying ^{3}LC, while a minor fraction persists in the ^{3}MLCT state within the simulation time. This behavior can be explained by either a relatively stable triplet configuration or a slower deactivation channel. The lifetimes of the ^{3}MLCT and ^{3}LC states, obtained by TSH, are 2.6 and 15 ps, respectively. While these lifetimes are not comparable to those observed in TA, they show that both states are good candidates to be observed in TA.

Therefore, the simulations support the assignment of τ_2 as the ^{3}LC state, while τ_1 may be attributed to the ^{3}MLCT state. However, the general shape of the corresponding DAAS is in accordance with a ^{3}MLCT state, where red-shifted ESA are usually observed due to LMCT absorptions of the oxidized metal center.[50] In general, the calculations reveal that the excited state decay of $[Co(ImP^{NMe2})_2]^+$ is based on an intricate interplay and coupling of both MLCT and LC states in singlet and triplet multiplicities. Therefore, excitation at different energies may result in different branching ratios at the intersections of these states. Consequently, excitation at higher energies may lead to a lesser population of the ^{3}LC state; a reduction in emission intensity is thus observed for the higher-energy band. While this explanation is fitting for the observed behavior, it is only tentative, and more work is needed for verification. From the analysis of nuclear motions during the dynamics, a two-step relaxation mechanism is suggested: an initial, fast axial distortion (Co–C_{Cm}) facilitates electronic transition and ISC, while a slower, more extensive equatorial rearrangement (Co–C_{Im}) governs the structural stabilization of the long-lived excited state. This finding highlights the anisotropic nature of the excited-state dynamics in $Co(ImP^{NMe2})_2^+$ and illustrates how different ligand environments contribute distinctively to the relaxation process.

Photogeneration and reactivity

Nevertheless, the investigation of the excited state kinetics revealed that photooxidation is possible from the ^{3}LC state of the compound. The formation of $[Co(ImP^{NMe2})_2]^{2+}$ was therefore investigated further. First, more insight was obtained from EPR, where a frozen solution of $[Co(ImP^{NMe2})_2]^+$ in TeCA was measured directly after irradiation, prior to thawing (cf. Supporting Information: Fig. S25). Here, a spectrum centered around a g-factor of 2.03 is obtained, where the form indicates a largely nitrogen-based radical and only minor contributions from the cobalt. This indicates that the cobalt center only gets involved in the spin-delocalization after thawing. The DFT geometry of the oxidized complex shows bond lengths in the aminium-radical cation ligand (cf. Supporting Information: Fig. S38) similar to those observed in the TMPD radical cation.[10] Since the solution is frozen, the structural rearrangement may be hindered and a charge-transfer complex involving a localized aminium radical cation and a solvent radical anion is formed initially. Only after thawing, charge recombination or cage escape is observed.

In addition to TeCA, a similar behavior was observed in MeCN (cf. Supporting Information: Fig. S26) under different conditions. However, after thawing and refreezing, no significant signal corresponding to $[Co(ImP^{NMe2})_2]^{2+}$ was observed in these cases. Therefore, while oxidation of $[Co(ImP^{NMe2})_2]^{+}$ is possible in multiple solvents, charge recombination is faster than cage escape with these solvents, or with these solvents as electron acceptors. This observation is in accordance with the cage escape yield from solvent cages being a governing factor in photoredox catalysis.[51–56] Since efficient radical formation is observed in mixtures of MeCN and TeCA, the cage-escape seems to be more related to TeCA as an electron acceptor. Therefore, the general reaction of $[Co(ImP^{NMe2})_2]^{+}$ with TeCA under irradiation was investigated. Due to the characteristic absorption band of $[Co(ImP^{NMe2})_2]^{2+}$, the general reaction can be followed easily via UV-Vis. In pure TeCA, the absorption at 900 nm reaches its maximum after around three minutes and slowly decays within the next 30 minutes (Supporting Information: Fig. S36-37). At this point, the absorption spectrum resembles the doubly protonated species observed in the titration experiments.

Three different reaction pathways can be imagined for its formation: The first involves hydrogen atom transfer (HAT) from TeCA or its radical to the aminium radical to form the protonated species, which then can create an aminium radical again, and finally undergoes HAT again to form the doubly protonated species. Secondly, the aminium radical gets protonated and subsequently undergoes HAT or thirdly, the singly protonated species gets protonated again. Since the reaction proceeds quickly, the exact mechanism is not discernible. Therefore, a mixture of TeCA and MeCN (1:5) was investigated (Fig. 7). Here, the formation of $[Co(ImP^{NMe2})_2]^{2+}$ is much slower and the maximum is observed after about 2.5 h. Again, the signal decays slowly, after a total of 16 h, the signal corresponding to the radical has vanished. As seen for pure TeCA, the final spectrum corresponds to the doubly protonated species.

To test the possibility of the first reaction pathway a fit utilizing a kinetic model in accordance with that pathway was performed. To simplify the fit, a singular value decomposition (SVD) of the entire dataset was performed, resulting in four orthogonal components not identified as noise. In the fitting process, the kinetic constants were the optimization parameters. For each set of kinetic constants, the time evolution of the complex species was calculated, and the time evolution of the ligand species was derived from that. Utilizing the pseudo-inverse of the ligand time evolution and the spectra SVD components, the best-guess ligand spectra were calculated

and used to fit the original data. Additionally, a penalty term to avoid physically unreasonable negative absorption features was utilized. Further, similar fits including additional pathways representing path two and three described above were conducted but did not lead to a significant improvement in the fit quality. The residuals of the fit are provided in the SI (cf. Supporting Information: Figure S39).

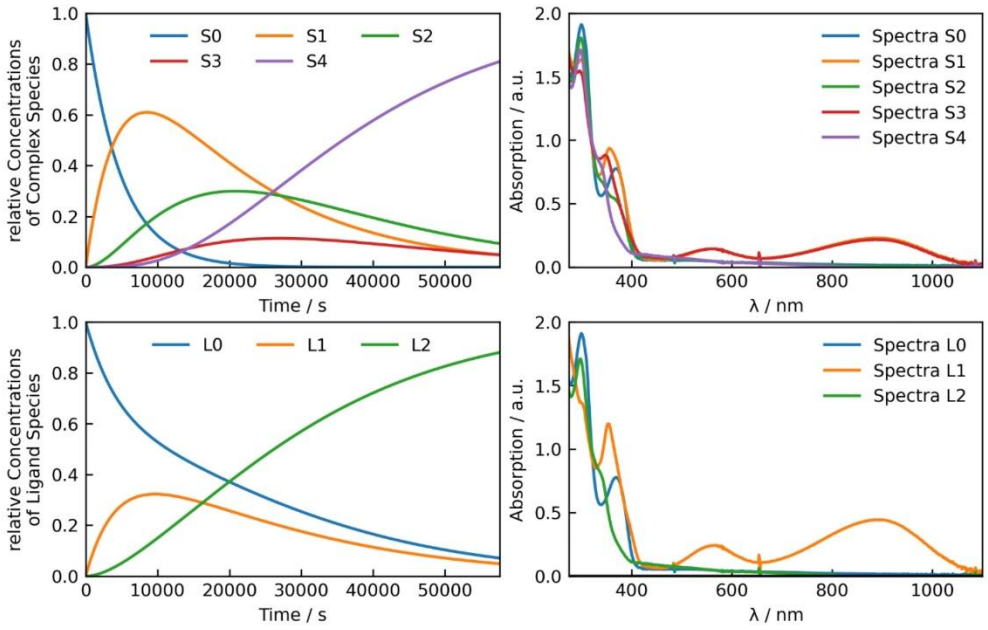

Figure 7: Time evolution of the different species (upper left) and associated spectra (upper right) for a fit of the first reaction pathway described above. To simplify the fit, the species spectra were assumed to be combinations of the base ligand (blue), aminium radical ligand (orange) and protonated ligand (green) spectra and only the spectra associated with the different ligand states (lower right) were used for the fit process.

Since the doubly-protonated species is observed both in TeCA/MeCN mixtures and in pure TeCA, the protons originate most likely from TeCA. While the exact reaction pathway of the TeCA-radical side is still unclear, a quaternary ^{13}C NMR peak at 120 ppm after chemical oxidation hints towards tetrachloroethylene as the product. An investigation of this side of the reaction is subject to further investigation.

Based on these results, the reactivity of this electrophilic radical is clearly observed. Therefore, different reactions were performed to investigate the reactivity further. First, $[Co(ImP^{NMe2})_2]^+$ was irradiated in TeCA-d_2 in the presence of TEMPO. Here, no formation of $[Co(ImP^{NMe2})_2]^{2+}$ is observed, even after 2 h of irradiation (cf. Supporting Information: Fig. S40). Upon irradiation in the presence of ascorbic acid, no radical is observed either (cf. Supporting Information: Fig. S41). However, formation of dehydroascorbic acid is observable, hinting towards ascorbic acid regenerating $[Co(ImP^{NMe2})_2]^+$. In addition, the reactivity of $[Co(ImP^{NMe2})_2]^{2+}$ towards tributyltin hydride was tested, to support further that it can undergo hydrogen transfer reactions (cf. Supporting Information: Fig. S42). Here, the addition of $[Co(ImP^{NMe2})_2]^{2+}$ to a solution of tributyltin hydride in isopropanol leads to immediate bubbling. Gas-MS confirms that hydrogen is generated (see Supporting Information: Chapter, Gas- MS for details). In addition, ^{119}Sn NMR and EXAFS analysis show that bis(tributyltin) is formed (cf. Supporting Information: Fig. S42-46). Hydrogen generation was also confirmed with polymethylhydrosiloxane as hydride source, which is a greener alternative to tributyltin hydride. Consequently, the versatility in reactivity of $[Co(ImP^{NMe2})_2]^{2+}$ was shown under different conditions.

Conclusion and Outlook

To the best of our knowledge, this work establishes the first example of a photogenerated ligand centered radical in a cobalt complex. The $[Co(ImP^{NMe2})_2]^+$ system, incorporating electron donating dimethylamino substituents on ImP ligand scaffold, undergoes a clean and reversible ligand-based oxidation to yield $[Co(ImP^{NMe2})_2]^{2+}$ which features the aminium radical that is delocalized along the phenyl-Co-phenyl axis. Unlike many other transition-metal based radical systems, this open shell system is very well documented by an array of spectroscopic methods including UV-Vis, SEC-UV-Vis, EPR, X-Ray absorption and NMR spectroscopy reflecting its unusually well-behaved electronic structure.

To further increase its credibility, the radical state can be generated both photochemically under mild UV irradiation and chemically using weak oxidants, demonstrating the intrinsic redox flexibility of the ligand framework. The observed reactivity towards electron donors and its involvement in hydrogen evolution experiments highlights the functional relevance of ligand centered reactivity in cobalt complexes as an alternate photoreaction pathway. Accordingly,

$[Co(ImP^{NMe2})_2]^+$ provides a versatile platform to probe metal-ligand cooperativity in radical generation as well as reactivity in earth-abundant transition metal complexes.

However, there is still a lot of room for improvement as the susceptibility of the aminium radical towards protonation by the solvent molecules could be identified as a limitation of the current system and provides a rational direction for future optimization. Increasing steric protection around the amine through the introduction of bulkier substituents is a method that has already been used for the stabilization of aminium radical species directly coordinated to transition metals.[22,33,57] The flexibility of the ImP ligand system could be exploited for this purpose as well. Overall, the reversible and light-induced generation of ligand centered radicals in this cobalt framework opens attractive avenues for sustainable photo redox-catalysis.

References

(1) Fridovich, I. Superoxide radical: an endogenous toxicant. *Annual review of pharmacology and toxicology* **1983**, *23*, 239–257. DOI: 10.1146/annurev.pa.23.040183.001323.

(2) Beckman, J. S.; Beckman, T. W.; Chen, J.; Marshall, P. A.; Freeman, B. A. Apparent hydroxyl radical production by peroxynitrite: implications for endothelial injury from nitric oxide and superoxide. *Proceedings of the National Academy of Sciences of the United States of America* **1990**, *87* (4), 1620–1624. DOI: 10.1073/pnas.87.4.1620.

(3) Halliwell, B. Reactive oxygen species and the central nervous system. *Journal of neurochemistry* **1992**, *59* (5), 1609–1623. DOI: 10.1111/j.1471-4159.1992.tb10990.x.

(4) Adamo, C.; Subra, R.; Di Matteo, A.; Barone, V. Structure and magnetic properties of benzyl, anilino, and phenoxyl radicals by density functional computations. *The Journal of Chemical Physics* **1998**, *109* (23), 10244–10254. DOI: 10.1063/1.477720.

(5) Williams, D. E. Structure of 2,2-Diphenyl-1-picrylhydrazyl Free Radical 1. *J. Am. Chem. Soc.* **1966**, *88* (23), 5665–5666. DOI: 10.1021/ja00975a064.

(6) Miura, Y.; Tomimura, T. First isolation of N-alkoxyaminyl radicals. *Chem. Commun.* **2001** (7), 627–628. DOI: 10.1039/b100698n.

(7) Michaelis, L.; Schubert, M. P.; Granick, S. The Free Radicals of the Type of Wurster's Salts. *J. Am. Chem. Soc.* **1939**, *61* (8), 1981–1992. DOI: 10.1021/ja01877a013.

(8) Wurster, C.; Schobig, E. Ueber die Einwirkung oxydirender Agentien auf Tetramethylparaphenylendiamin. *Ber. Dtsch. Chem. Ges.* **1879**, *12* (2), 1807–1813. DOI: 10.1002/cber.187901202156.

(9) Weitz, E. Zur Theorie der Chinhydrone. *Zeitschrift für Elektrochemie und angewandte physikalische Chemie* **1928**, *34* (9), 538–546. DOI: 10.1002/bbpc.19280340921.

(10) Boilet, L.; Buntinx, G.; Lefumeux, C.; Poizat, O. Ultrafast photoinduced electron transfer from N,N,N′,N′-tetramethyl-p-phenylenediamine and N,N,N′,N′-tetramethylbenzidine to dichloromethane. *Journal of Photochemistry and Photobiology A: Chemistry* **2004**, *163* (3), 529–536. DOI: 10.1016/j.jphotochem.2004.02.011.

(11) Hankache, J.; Wenger, O. S. Organic mixed valence. *Chemical reviews* **2011**, *111* (8), 5138–5178. DOI: 10.1021/cr100441k. Published Online: May. 16, 2011.

(12) Wenger, O. S. Photoswitchable mixed valence. *Chemical Society reviews* **2012**, *41* (10), 3772–3779. DOI: 10.1039/c2cs15339d. Published Online: Mar. 8, 2012.

(13) Barlow, S.; Risko, C.; Coropceanu, V.; Tucker, N. M.; Jones, S. C.; Levi, Z.; Khrustalev, V. N.; Antipin, M. Y.; Kinnibrugh, T. L.; Timofeeva, T.; Marder, S. R.; Brédas, J.-L. A mixed-valence bis(diarylamino)stilbene: crystal structure and comparison of electronic coupling with biphenyl and tolane analogues. *Chem. Commun.* **2005** (6), 764–766. DOI: 10.1039/b415018j. Published Online: Feb. 1, 2005.

(14) Jones, S. C.; Coropceanu, V.; Barlow, S.; Kinnibrugh, T.; Timofeeva, T.; Brédas, J.-L.; Marder, S. R. Delocalization in platinum-alkynyl systems: a metal-bridged organic mixed-valence compound. *Journal of the American Chemical Society* **2004**, *126* (38), 11782–11783. DOI: 10.1021/ja045869m.

(15) Sakamoto, R.; Sasaki, T.; Honda, N.; Yamamura, T. 5,15-Bis(di-p-anisylamino)-10,20-diphenylporphyrin: distant and intense electronic communication between two amine sites. *Chemical communications (Cambridge, England)* **2009** (34), 5156–5158. DOI: 10.1039/b907413a. Published Online: Jul. 16, 2009.

(16) Adhikari, D.; Mossin, S.; Basuli, F.; Huffman, J. C.; Szilagyi, R. K.; Meyer, K.; Mindiola, D. J. Structural, spectroscopic, and theoretical elucidation of a redox-active pincer-type ancillary applied in catalysis. *J. Am. Chem. Soc.* **2008**, *130* (11), 3676–3682. DOI: 10.1021/ja7108486. Published Online: Feb. 27, 2008.

(17) Radosevich, A. T.; Melnick, J. G.; Stoian, S. A.; Bacciu, D.; Chen, C.-H.; Foxman, B. M.; Ozerov, O. V.; Nocera, D. G. Ligand reactivity in diarylamido/bis(phosphine) PNP complexes of Mn(CO)3 and Re(CO)3. *Inorganic chemistry* **2009**, *48* (19), 9214–9221. DOI: 10.1021/ic9010218.

(18) van der Vlugt, J. I. Radical-Type Reactivity and Catalysis by Single-Electron Transfer to or from Redox-Active Ligands. *Chemistry (Weinheim an der Bergstrasse, Germany)* **2019**, *25* (11), 2651–2662. DOI: 10.1002/chem.201802606. Published Online: Nov. 26, 2018.

(19) Mankad, N. P.; Antholine, W. E.; Szilagyi, R. K.; Peters, J. C. Three-coordinate copper(I) amido and aminyl radical complexes. *J. Am. Chem. Soc.* **2009**, *131* (11), 3878–3880. DOI: 10.1021/ja809834k.

(20) Melzer, M. M.; Mossin, S.; Dai, X.; Bartell, A. M.; Kapoor, P.; Meyer, K.; Warren, T. H. A three-coordinate copper(II) amide from reductive cleavage of a nitrosamine. *Angewandte Chemie (International ed. in English)* **2010**, *49* (5), 904–907. DOI: 10.1002/anie.200905171.

(21) Penkert, F. N.; Weyhermüller, T.; Bill, E.; Hildebrandt, P.; Lecomte, S.; Wieghardt, K. Anilino Radical Complexes of Cobalt(III) and Manganese(IV) and Comparison with Their Phenoxyl Analogues. *J. Am. Chem. Soc.* **2000**, *122* (40), 9663–9673. DOI: 10.1021/ja001637l.

(22) Büttner, T.; Geier, J.; Frison, G.; Harmer, J.; Calle, C.; Schweiger, A.; Schönberg, H.; Grützmacher, H. A stable aminyl radical metal complex. *Science (New York, N.Y.)* **2005**, *307* (5707), 235–238. DOI: 10.1126/science.1106070.

(23) Yao, C.-J.; Yao, J.; Zhong, Y.-W. Electronic communication between two amine redox centers bridged by a bis(terpyridine)ruthenium(II) complex. *Inorganic chemistry* **2011**, *50* (15), 6847–6849. DOI: 10.1021/ic200701j. Published Online: Jul. 7, 2011.

(24) Yao, C.-J.; Zheng, R.-H.; Nie, H.-J.; Cui, B.-B.; Shi, Q.; Yao, J.; Zhong, Y.-W. A combined experimental and computational study of linear ruthenium(II) coordination oligomers with end-capping organic redox sites: insight into the light absorption and charge delocalization. *Chemistry (Weinheim an der Bergstrasse, Germany)* **2013**, *19* (37), 12376–12387. DOI: 10.1002/chem.201301319. Published Online: Aug. 6, 2013.

(25) Nie, H.-J.; Yao, C.-J.; Sun, M.-J.; Zhong, Y.-W.; Yao, J. Ruthenium- bis -terpyridine Complex with Two Redox-Asymmetric Amine Substituents: Potential-Controlled Reversal of the Direction of Charge-Transfer. *Organometallics* **2014**, *33* (21), 6223–6231. DOI: 10.1021/om500904k.

(26) Yao, C.-J.; Zheng, R.-H.; Shi, Q.; Zhong, Y.-W.; Yao, J. 1,4-Benzene-bridged covalent hybrid of triarylamine and cyclometalated ruthenium: a new type of organic-inorganic mixed-valent system. *Chemical communications (Cambridge, England)* **2012**, *48* (45), 5680–5682. DOI: 10.1039/c2cc32471g. Published Online: May. 1, 2012.

(27) Yao, C.-J.; Nie, H.-J.; Yang, W.-W.; Shao, J.-Y.; Yao, J.; Zhong, Y.-W. Strongly coupled cyclometalated ruthenium-triarylamine hybrids: tuning electrochemical properties, intervalence charge transfer, and spin distribution by substituent effects. *Chemistry (Weinheim an der Bergstrasse, Germany)* **2014**, *20* (52), 17466–17477. DOI: 10.1002/chem.201404549. Published Online: Nov. 4, 2014.

(28) Rosenthal, M.; Lindner, J. K. N.; Gerstmann, U.; Meier, A.; Schmidt, W. G.; Wilhelm, R. A photoredox catalysed Heck reaction via hole transfer from a Ru(ii)-bis(terpyridine) complex to graphene oxide. *RSC advances* **2020**, *10* (70), 42930–42937. DOI: 10.1039/D0RA08749A. Published Online: Nov. 25, 2020.

(29) Cui, B.-B.; Yao, C.-J.; Yao, J.; Zhong, Y.-W. Electropolymerized films as a molecular platform for volatile memory devices with two near-infrared outputs and long retention time. *Chem. Sci.* **2014**, *5* (3), 932–941. DOI: 10.1039/C3SC52815D.

(30) Cui, B.-B.; Zhong, Y.-W.; Yao, J. Three-state near-infrared electrochromism at the molecular scale. *Journal of the American Chemical Society* **2015**, *137* (12), 4058–4061. DOI: 10.1021/jacs.5b00586. Published Online: Mar. 17, 2015.

(31) Gong, Z.-L.; Zhong, Y.-W.; Yao, J. Conformation-determined through-bond versus through-space electronic communication in mixed-valence systems with a cross-conjugated urea bridge. *Chemistry (Weinheim an der Bergstrasse, Germany)* **2015**, *21* (4), 1554–1566. DOI: 10.1002/chem.201405332. Published Online: Nov. 24, 2014.

(32) Li, Z.-J.; Shen, J.-J.; Shao, J.-Y.; Zhong, Y.-W. Substituent Effects on the Electrochemistry and Electronic Coupling of Terphenyl-Bridged Cyclometalated Ruthenium-Amine Conjugated Complexes. *ACS omega* **2018**, *3* (12), 16744–16752. DOI: 10.1021/acsomega.8b03058. Published Online: Dec. 5, 2018.

(33) Rodríguez-Lugo, R. E.; Bruin, B. de; Trincado, M.; Grützmacher, H. A Stable Aminyl Radical Coordinated to Cobalt. *Chemistry (Weinheim an der Bergstrasse, Germany)* **2017**, *23* (28), 6795–6802. DOI: 10.1002/chem.201605624. Published Online: Mar. 6, 2017.

(34) Donati, N.; Stein, D.; Büttner, T.; Schönberg, H.; Harmer, J.; Anadaram, S.; Grützmacher, H. Rhodium and Iridium Amino, Amido, and Aminyl Radical Complexes. *Eur J Inorg Chem* **2008**, *2008* (30), 4691–4703. DOI: 10.1002/ejic.200800702.

(35) Maire, P.; Königsmann, M.; Sreekanth, A.; Harmer, J.; Schweiger, A.; Grützmacher, H. A tetracoordinated rhodium aminyl radical complex. *J. Am. Chem. Soc.* **2006**, *128* (20), 6578–6580. DOI: 10.1021/ja0612798.

(36) He, B.; Wenger, O. S. Photoswitchable organic mixed valence in dithienylcyclopentene systems with tertiary amine redox centers. *Journal of the American Chemical Society* **2011**, *133* (42), 17027–17036. DOI: 10.1021/ja207025x. Published Online: Oct. 3, 2011.

(37) Krishna, A.; Fritsch, L.; Steube, J.; Argüello Cordero, M. A.; Schoch, R.; Neuba, A.; Lochbrunner, S.; Bauer, M. Low Temperature Emissive Cyclometalated Cobalt(III) Complexes. *Inorganic chemistry* **2025**, *64* (3), 1401–1409. DOI: 10.1021/acs.inorgchem.4c04479. Published Online: Jan. 14, 2025.

(38) Chan, A. Y.; Ghosh, A.; Yarranton, J. T.; Twilton, J.; Jin, J.; Arias-Rotondo, D. M.; Sakai, H. A.; McCusker, J. K.; MacMillan, D. W. C. Exploiting the Marcus inverted region for first-row transition metal-based photoredox catalysis. *Science (New York, N.Y.)* **2023**, *382* (6667), 191–197. DOI: 10.1126/science.adj0612. Published Online: Oct. 12, 2023.

(39) Kaufhold, S.; Rosemann, N. W.; Chábera, P.; Lindh, L.; Bolaño Losada, I.; Uhlig, J.; Pascher, T.; Strand, D.; Wärnmark, K.; Yartsev, A.; Persson, P. Microsecond Photoluminescence and Photoreactivity of a Metal-Centered Excited State in a Hexacarbene-Co(III) Complex. *J. Am. Chem. Soc.* **2021**, *143* (3), 1307–1312. DOI: 10.1021/jacs.0c12151. Published Online: Jan. 15, 2021.

(40) Park, K.-S.; Seo, Y.; Kim, M. K.; Kim, K.; Kim, Y. K.; Choo, H.; Chong, Y. A curcumin-based molecular probe for near-infrared fluorescence imaging of tau fibrils in Alzheimer's disease. *Organic & biomolecular chemistry* **2015**, *13* (46), 11194–11199. DOI: 10.1039/C5OB01847A.

(41) Raynal, M.; Pattacini, R.; Cazin, C. S. J.; Vallée, C.; Olivier-Bourbigou, H.; Braunstein, P. Reaction Intermediates in the Synthesis of New Hydrido, N-Heterocyclic Dicarbene Iridium(III) Pincer Complexes. *Organometallics* **2009**, *28* (14), 4028–4047. DOI: 10.1021/om900226c.

(42) Reilly, S. W.; Webster, C. E.; Hollis, T. K.; Valle, H. U. Transmetallation from CCC-NHC pincer Zr complexes in the synthesis of air-stable CCC-NHC pincer Co(iii) complexes and initial hydroboration trials. *Dalton transactions (Cambridge, England : 2003)* **2016**, *45* (7), 2823–2828. DOI: 10.1039/C5DT04752H. Published Online: Jan. 27, 2016.

(43) Fritsch, L.; Vukadinovic, Y.; Lang, M.; Naumann, R.; Bertrams, M.-S.; Kruse, A.; Schoch, R.; Müller, P.; Neuba, A.; Dierks, P.; Lochbrunner, S.; Kerzig, C.; Heinze, K.; Bauer, M. Chemical and photophysical properties of amine functionalized bis-NHC-pyridine-Ru II complexes. *ChemPhotoChem* **2024**, *8* (4), 280. DOI: 10.1002/cptc.202300281.

(44) Vukadinovic, Y.; Burkhardt, L.; Päpcke, A.; Miletic, A.; Fritsch, L.; Altenburger, B.; Schoch, R.; Neuba, A.; Lochbrunner, S.; Bauer, M. When Donors Turn into Acceptors: Ground and Excited State Properties of Fe II Complexes with Amine-Substituted Tridentate Bis-imidazole-2-ylidene Pyridine Ligands. *Inorg. Chem.* **2020**, *59* (13), 8762–8774. DOI: 10.1021/acs.inorgchem.0c00393.

(45) Evans, D. F. 400. The determination of the paramagnetic susceptibility of substances in solution by nuclear magnetic resonance. *J. Chem. Soc.* **1959**, 2003. DOI: 10.1039/JR9590002003.

(46) Steube, J.; Fritsch, L.; Kruse, A.; Bokareva, O. S.; Demeshko, S.; Elgabarty, H.; Schoch, R.; Alaraby, M.; Egold, H.; Bracht, B.; Schmitz, L.; Hohloch, S.; Kühne, T. D.; Meyer, F.; Kühn, O.; Lochbrunner, S.; Bauer, M. Isostructural Series of a Cyclometalated Iron Complex in Three Oxidation States. *Inorganic chemistry* **2024**, *63* (37), 16964–16980. DOI: 10.1021/acs.inorgchem.4c02576. Published Online: Sep. 2, 2024.

(47) Steube, J.; Kruse, A.; Bokareva, O. S.; Reuter, T.; Demeshko, S.; Schoch, R.; Argüello Cordero, M. A.; Krishna, A.; Hohloch, S.; Meyer, F.; Heinze, K.; Kühn, O.; Lochbrunner, S.; Bauer, M. Janus-type emission from a cyclometalated iron(III) complex. *Nature chemistry* **2023**, *15* (4), 468–474. DOI: 10.1038/s41557-023-01137-w. Published Online: Feb. 27, 2023.

(48) Golcuk, K.; Altun, A.; Guner, S.; Kumru, M.; Aktas, B. Thermal, vibrational and EPR studies of Cu(II) bromide bis(p-methylaniline) and bis(m-methylaniline) complexes. *Spectrochimica acta. Part A, Molecular and biomolecular spectroscopy* **2004**, *60* (1-2), 303–309. DOI: 10.1016/S1386-1425(03)00242-7].

(49) Kultaeva, A.; Bon, V.; Weiss, M. S.; Pöppl, A.; Kaskel, S. Elucidating the Formation and Transformation Mechanisms of the Switchable Metal-Organic Framework ELM-11 by Powder and

Single-Crystal EPR Study. *Inorganic chemistry* **2018**, *57* (19), 11920–11929. DOI: 10.1021/acs.inorgchem.8b01241. Published Online: Sep. 12, 2018.

(50) Brown, A. M.; McCusker, C. E.; McCusker, J. K. Spectroelectrochemical identification of charge-transfer excited states in transition metal-based polypyridyl complexes. *Dalton Trans.* **2014**, *43* (47), 17635–17646. DOI: 10.1039/c4dt02849j.

(51) Goodwin, M. J.; Dickenson, J. C.; Ripak, A.; Deetz, A. M.; McCarthy, J. S.; Meyer, G. J.; Troian-Gautier, L. Factors that Impact Photochemical Cage Escape Yields. *Chemical reviews* **2024**, *124* (11), 7379–7464. DOI: 10.1021/acs.chemrev.3c00930. Published Online: May. 14, 2024.

(52) Kreijger, S. de; Ripak, A.; Elias, B.; Troian-Gautier, L. Investigation of the Excited-State Electron Transfer and Cage Escape Yields Between Halides and a Fe(III) Photosensitizer. *J. Am. Chem. Soc.* **2024**, *146* (15), 10286–10292. DOI: 10.1021/jacs.4c02808. Published Online: Apr. 3, 2024.

(53) Kreijger, S. de; Glaser, F.; Troian-Gautier, L. From photons to reactions: key concepts in photoredox catalysis. *Chem Catalysis* **2024**, *4* (11), 101110. DOI: 10.1016/j.checat.2024.101110.

(54) Olmsted, J.; Meyer, T. J. Factors affecting cage escape yields following electron-transfer quenching. *J. Phys. Chem.* **1987**, *91* (6), 1649–1655. DOI: 10.1021/j100290a071.

(55) Ripak, A.; Vega Salgado, A. K.; Valverde, D.; Cristofaro, S.; Gary, A. de; Olivier, Y.; Elias, B.; Troian-Gautier, L. Factors Controlling Cage Escape Yields of Closed- and Open-Shell Metal Complexes in Bimolecular Photoinduced Electron Transfer. *J. Am. Chem. Soc.* **2024**, *146* (32), 22818–22828. DOI: 10.1021/jacs.4c08158. Published Online: Jul. 30, 2024.

(56) Wang, C.; Li, H.; Bürgin, T. H.; Wenger, O. S. Cage escape governs photoredox reaction rates and quantum yields. *Nat. Chem.* **2024**, *16* (7), 1151–1159. DOI: 10.1038/s41557-024-01482-4. Published Online: Mar. 18, 2024.

(57) Hicks, R. G. Metal complexes of aminyl radicals. *Angewandte Chemie (International ed. in English)* **2008**, *47* (39), 7393–7395. DOI: 10.1002/anie.200802713.

Associated Content

Supporting Information

The supporting information is available free of charge at http://pubs.acs.org.

Details on single crystal X-ray analysis, cyclic voltammetry, UV-Vis spectroscopy, NMR spectroscopy, EPR spectroscopy, low-temperature emission spectroscopy, X-Ray absorption spectroscopy, spectroelectrochemistry, transient absorption spectroscopy, computational details, as well as spectra (PDF).

Author Information

Corresponding Author

*Matthias Bauer; Email: matthias.bauer@upb.de

Author Contributions

The manuscript was written through contributions of all authors. All authors have given approval to the final version of the manuscript.

Notes

The authors declare no competing financial interest.

Acknowledgements

Dr. Frederic Mentink-Vigier for helpful discussions.

The grant of computer time at the Paderborn Center for Parallel Computing PC2 is acknowledged. This work was performed in the framework of the SPP 2102 funded by the Deutsche Forschungsgemeinschaft (BA 4467/7-1 and BA 4467/7-2, LO 714/11-1 and LO 714/11-2, KU 952/12-1 and KU 952/12-2, project nr. 404479188).

For table of contents only:

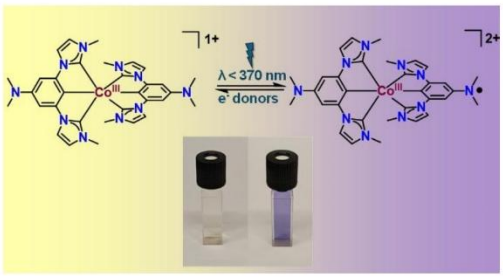

Conclusion

The overall objective of this thesis is to find new alternatives for rare earth transition metal photosensitisizers. To accomplish this goal, organo-boron based photosensitizers were synthesized as this class of complexes have been known to display excellent photophysical properties. One of the main drawbacks of the already existing systems was their reduced photostability and solubility. To increase the photostability, a more rigid coordination environment had to be created around the boron center. This was accomplished by introducing an oxygen bridge between two boron centers. Introduction of tert-butyl groups to these scaffolds, not only increases their solubility, but also enforces a more stable coordination geometry as they interlocked the two units preventing isomer formation due to the rotation along oxygen bridge. The increased ground state stability was experimentally observed through cyclic voltammetry which provided insights into the redox stability of the complex. Excited state characterisation revealed the complexes photochemical performances were comparable to already existing systems. Hence, we successfully designed a more stable boron system with a new coordination framework. The complexes currently emit from a singlet state, but the lifetimes are still long enough to be potentially used in photochemical applications. The lifetimes could be further extended by introducing heavy atoms into the scaffold, but this could also lead to the reduction in the photostability.

To tackle the problem of photostability, it was deemed better to investigate organometallic photosensitizers. Hence a new cobalt based photosenistizer was synthesized and fully characterised. It was shown that these cobalt based photosenisitizers provided very long-lived excited states, emerging from a ^{3}MC state. Further substitutions on the imidazole nitrogen of these complexes were carried out to see how this would affect the photophysical properties. Changing the imidazole alkyl group from a methyl substituent to butyl substituent increased the excited state lifetimes of the respective cobalt complexes that were synthesized. All the complexes synthesized were only emissive at 77 K. This meant that the practical applicability of these complexes would be limited. Hence it was evident that further improvements needed to be made on this system. The ImP ligand scaffold offers great potential in this regard as it has high customisability. Cyclometalated backbone of the ligand could still be functionalized to further tune the ground state as well as excited state properties.

Functionalizing the backbone of the ImP ligand with dimethylamine groups provided fascinating results. Drastic changes were already observable in ground state characterisation. It was found that the complex forms a radical species upon irradiation with UV-light in the presence of chlorinated species. Formation of the aminium radical was confirmed using a variety of spectroscopic techniques. The unique coordination environment of the ImP ligand scaffold in combination with the cobalt center provided

the radical to be delocalized along the phenyl-Co-phenyl axis. This hypothesis was supported by NMR and EPR spectroscopy. Spin density calculations further provided insight on the location of the unpaired electron density. This coincided with the atomic positions that were missing in the NMR spectra. Evans NMR measurements were used to quantify the number of unpaired electrons. Photooxidation, spectroelectrochemical oxidation as well as chemical oxidation yielded the same product. Transient absorption measurements gave further insights into the excited state dynamics. It was observed that this complex exhibits a different excited state pathway compared to the parent [Co(ImP)][PF_6] complex. The presence of dimethylamino groups facilitates the relaxation into ^{3}LC excited state after excitation, from which it was assumed that the radical formation is initiated. Kinetic studies of the radical formation revealed that the radical later undergoes protonation by abstracting a hydride from the solvent. This was also tested by acid titration of the base complex and checked if identical spectra were observable with UV-Vis spectroscopy. These findings pointed towards a highly reactive radical once formed and was tested for reactivity against electron donating substrates. Positive test reactions were found against hydride donors and mild oxidizing agents. These findings show the immense potential of this newly designed system, while at the same time, there is a lot of room for improvement. The protonation of the radical species prevents the active species from showcasing consistent reactivity. Further modifications of this system could be realized by introducing bulkier groups on the aminyl nitrogen which could prevent easy protonation of the radical species once its formed. It could also be used in tandem with bases that abstract the proton once its protonated. Therefore, future works should focus on exploring these strategies to unlock the full potential of these complexes.

Experimental Details

General work techniques

All reactions carried out under inert atmosphere were performed either in an argon-filled glovebox or using standard Schlenk techniques under a continuous argon flow. Vacuum (down to approximately 10^{-3} mbar) was generated using a rotary vane pump. Prior to use, glassware was dried under vacuum with a heat gun, then filled with argon and allowed to cool; this evacuation and argon refill cycle was repeated three times. Solid reagents were transferred under counter-flow conditions, whereas liquids were added via syringe through a septum. Dry solvents were dispensed from an MBraun SPS-800 solvent purification system and subsequently stored over 3 Å molecular sieves. Dry acetonitrile for spectroscopic measurements was prepared by passing the solvent through a column packed with MP Biomedicals MP Alumina N-Super I that had been activated at 150 °C for several days. Degassing of solvents and solutions was achieved either by bubbling argon through the liquid or by applying the freeze-pump-thaw procedure. In the latter method, the sample in a Schlenk flask was frozen in liquid nitrogen, evacuated to low pressure, and then thawed under static vacuum in a lukewarm water bath. This sequence was repeated until no pressure increase was observed upon refreezing. Unless otherwise stated, chemicals were used as received without additional purification. Solvents were of technical grade, except acetonitrile (HPLC grade) and those specifically used for spectroscopic measurements. Reactions were heated using oil baths or aluminum heating blocks, and the reported temperatures correspond to the set values.

Analytical and spectroscopic methods

Column chromatography

Manual column chromatography was carried out using silica gel (60 Å pore size) or neutral alumina, depending on the separation requirements. Automated chromatographic separations were performed on a Teledyne Isco CombiFlash RF+ MPLC system with prepacked silica cartridges. Thin-layer chromatography on silica plates containing a fluorescent indicator was used to monitor fractions and to optimize suitable eluent systems.

NMR spectroscopy

NMR measurements were carried out on Bruker Avance 300 and 500 instruments, as well as on a Bruker Ascent 700 spectrometer. Chemical shifts are reported in ppm and coupling constants in Hz. The spectra were referenced to the residual proton signals of the respective deuterated solvents.[147]

IR Spectroscopy

Infrared spectra were recorded on a Bruker Vertex 70 FT-IR spectrometer using the ATR accessory, allowing the samples to be measured directly without the need for an additional matrix or medium.

Mass spectrometry

Electrospray ionization (ESI) mass spectra were recorded on a Waters SYNAPT G2 quadrupole time-of-flight (Q-TOF) mass spectrometer. Samples were analyzed from acetonitrile or water solutions with concentrations of approximately 10^{-5} M.

Elemental analysis

Elemental analyses were performed on an Elementar vario MicroCube analyzer to determine the carbon, hydrogen, nitrogen, and sulfur contents of the samples.

Single-crystal X-ray diffraction

Single-crystal X-ray diffraction data were collected on a Bruker SMART CCD area-detector diffractometer equipped with a graphite monochromator. Measurements were performed using Mo Kα radiation (λ = 0.71073 Å) at 120(2) K.

Cyclic voltammetry

Cyclic and square-wave voltammetry were carried out at room temperature in dry acetonitrile containing 0.1 M $[(nBu)_4N][PF_6]$ as the supporting electrolyte and an analyte concentration of 1 mM. Measurements were performed under an argon atmosphere saturated with solvent vapor. A three-electrode setup was employed, consisting of a 1 mm platinum disk working electrode, a platinum wire counter electrode (Metrohm), and a custom Ag/AgCl reference electrode, all connected to a Metrohm PGSTAT101 potentiostat. Ferrocene was added after each experiment as an internal standard, and all reported potentials are referenced to the $Fc^{0/+}$ redox couple. Data analysis was carried out using NOVA software (version 2.1.3). Electrochemical reversibility was evaluated according to the criteria described by Nicholson and using the Randles–Sevcik relationship.[148–151]

UV-Vis absorption spectroscopy

UV-Vis absorption spectra were collected using a Varian Cary 50 and a PerkinElmer Lambda 465 single-beam spectrophotometer. Measurements were performed in acetonitrile at concentrations of approximately 10^{-5} M using 10 mm quartz cuvettes. The exact concentrations were determined gravimetrically by weighing both solute and solvent, with the solvent volume calculated from its density. Extinction coefficients were obtained from Beer-Lambert analysis and plotted as a function of wavelength.

Steady-state emission spectroscopy

Samples for fluorescence measurements were degassed using the procedures described earlier. Emission spectra were recorded on an Edinburgh Instruments FLS1000

spectrometer equipped with single monochromators and a red-extended PMT-980 detector. Low temperature emission spectra were recorded at 77 K.

Time-correlated single-photon counting (TCSPC)

Samples for lifetime measurements were prepared in the same way as for the steady-state emission experiment. Time-correlated single-photon counting measurements were performed on a Horiba Ultima-01-DD system (Horiba Jobin Yvon GmbH). Excitation was carried out at 374 nm using a Horiba DD375L laser diode operated at repetition rates of up to 100 MHz. Emission decays were collected at the corresponding detection wavelengths. Photon arrival times were recorded in repetitive start-stop mode with a multi-channel analyzer until the most intense channel accumulated approximately 10000 counts. The resulting decay curves were stored as histograms over 16383 channels spanning a total time window of 100 ns (6.4 ps per channel). Data analysis was carried out in EzTime (Horiba), using the instrument response function (IRF) measured at 374 nm with a LUDOX scattering solution in water. Decay curves were fitted using a mono- and progressively multi-exponential model, increasing the number of components until χ^2 dropped below 1.2. The quality of the fits was further assessed visually by inspection of the residuals to ensure random distribution around zero.

Appendix

A1. List of Figures and Tables

A2. Supplementary information for the publication “Emissive oxygen bridged pyridine phenolate complex”

Supplementary Information for Emissive Oxygen Bridged Pyridine Phenolate Boron Complex

Athul Krishna*[a], Jannik Lösecke[a], J. Steube[a], Lorena Fritsch[a], Michal Nowakowski[a], Roland Schoch[a], Stephan Hohloch[b], Matthias Bauer[a], Felix Fischer*[a]

Table of Contents

NMR

2,6-bis(3,5-di-tert-butyl-2-methoxyphenyl)pyridine

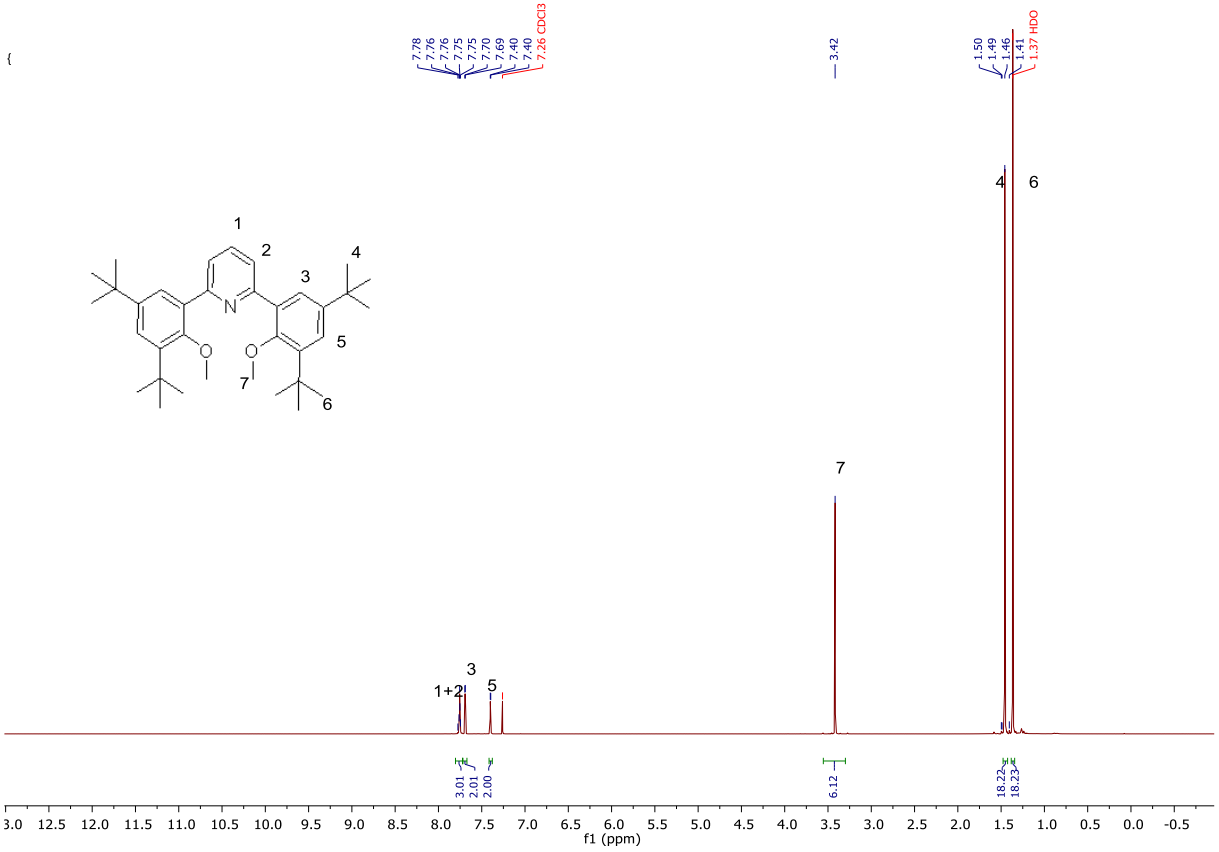

Figure S 1: ^{1}H NMR of 2,6-bis(3,5-di-tert-butyl-2-methoxyphenyl)pyridine in $CDCl_3$

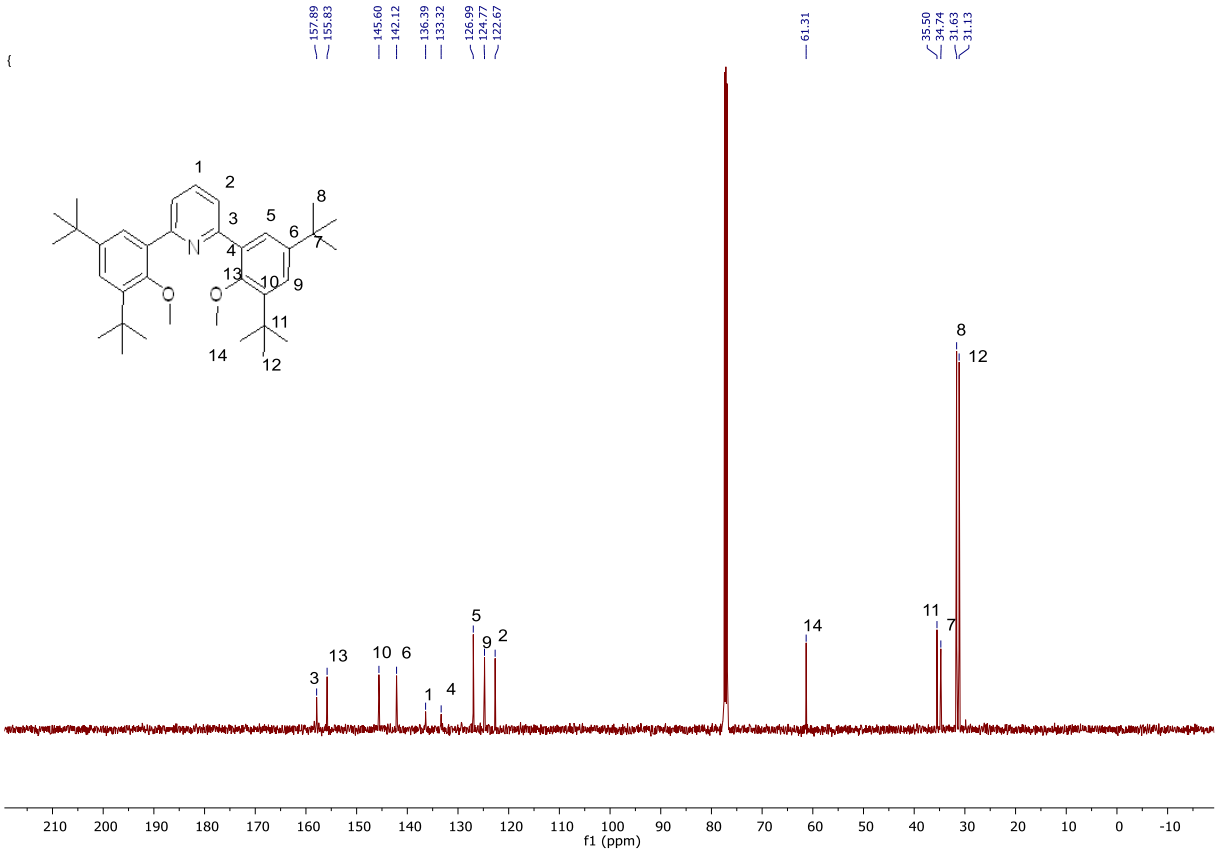

Figure S 2: ^{13}C NMR of 2,6-bis(3,5-di-tert-butyl-2-methoxyphenyl)pyridine in $CDCl_3$

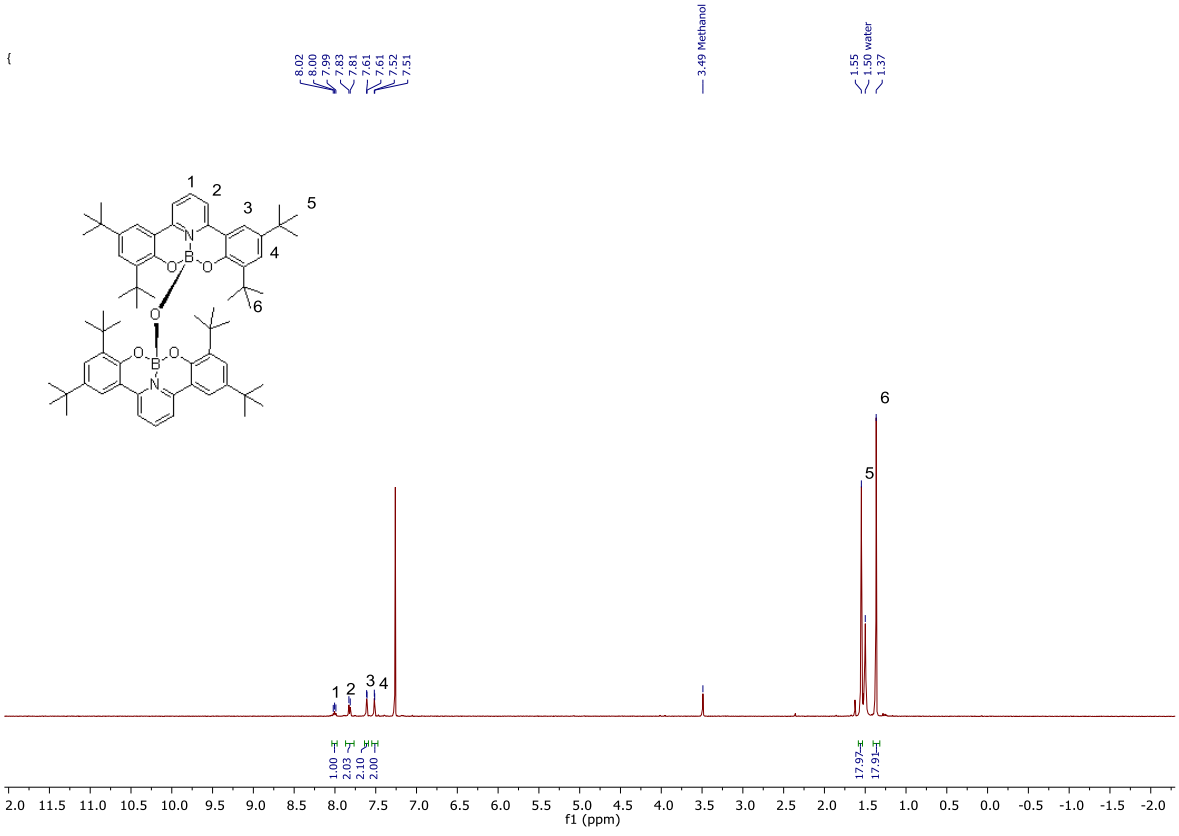

Figure S 3: ^{1}H NMR of BOB in $CDCl_3$

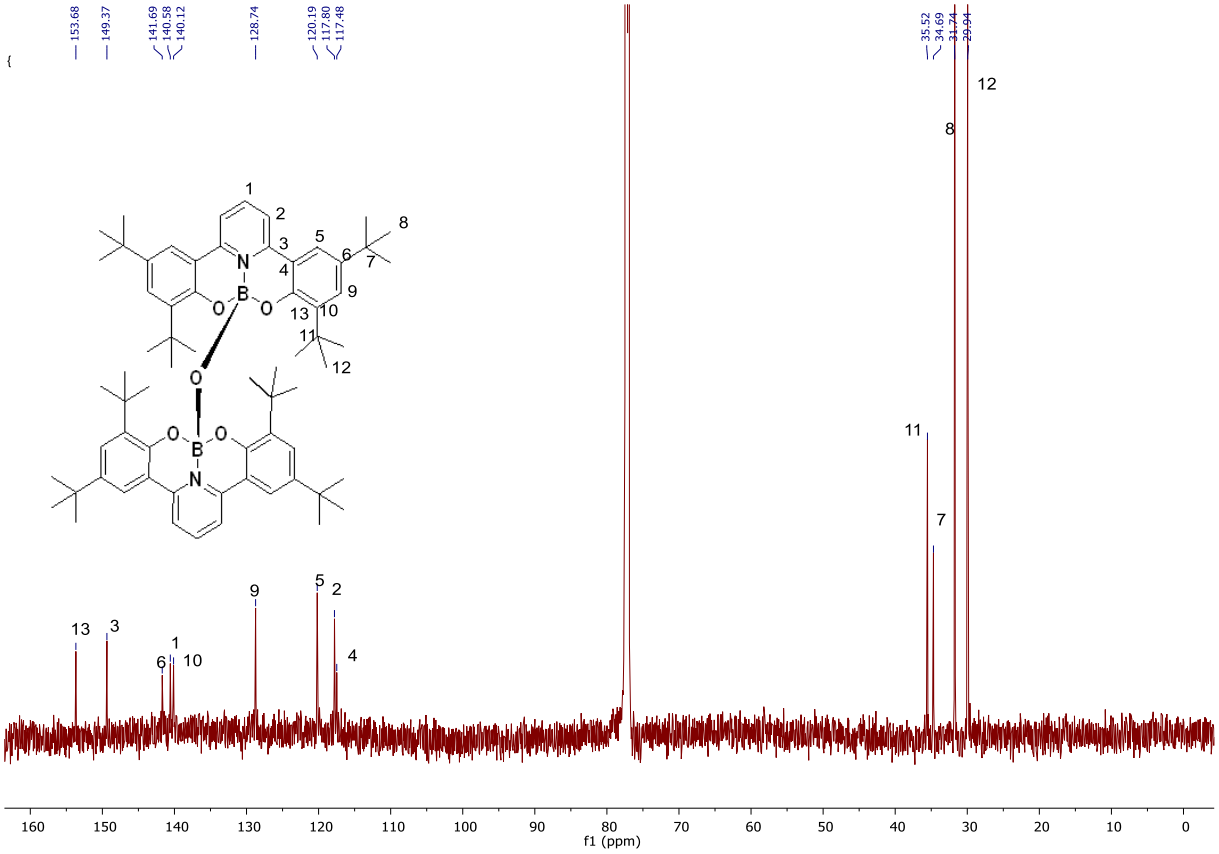

Figure S 4: ^{13}C NMR of BOB in $CDCl_3$

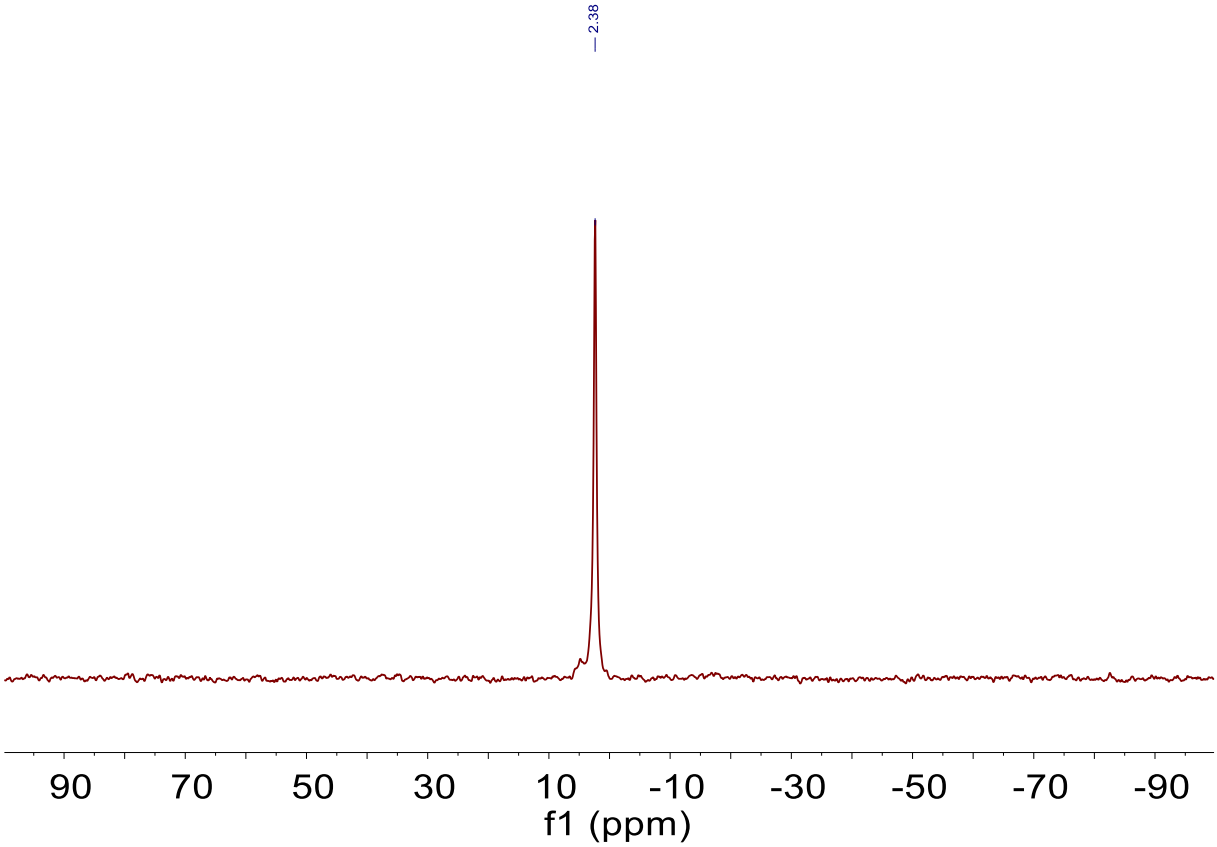

Figure S 5: ^{11}B NMR of BOB in $CDCl_3$

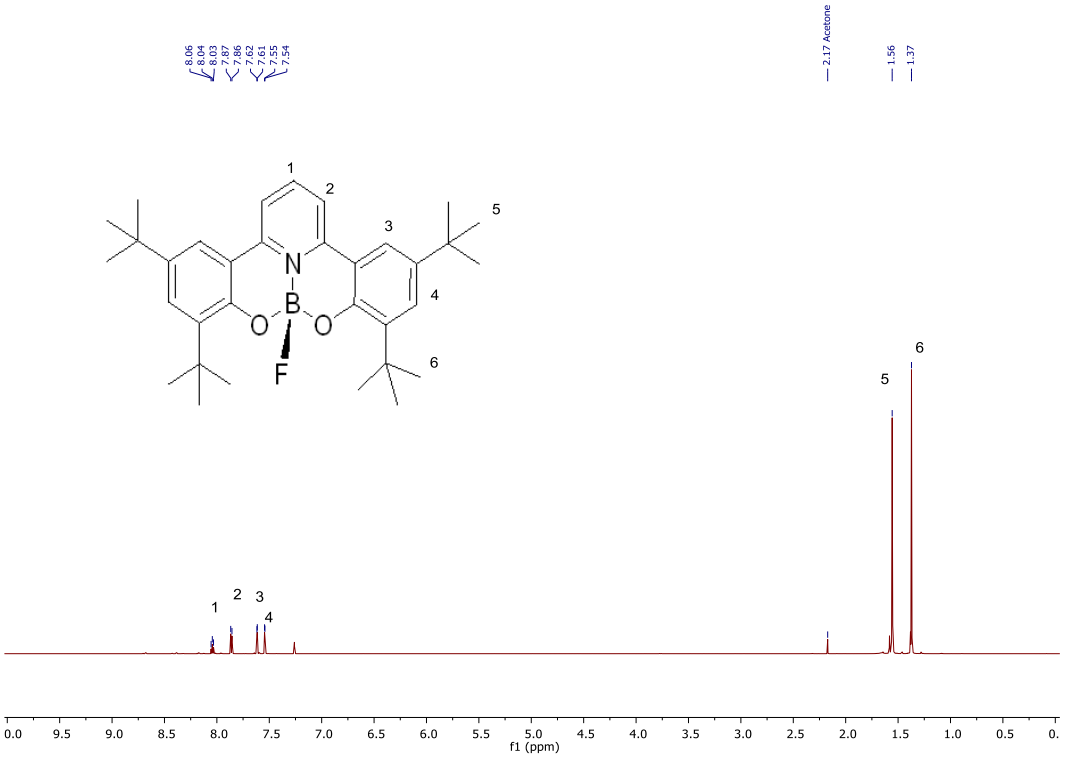

Figure S 6: ^{1}H NMR of BF in $CDCl_3$

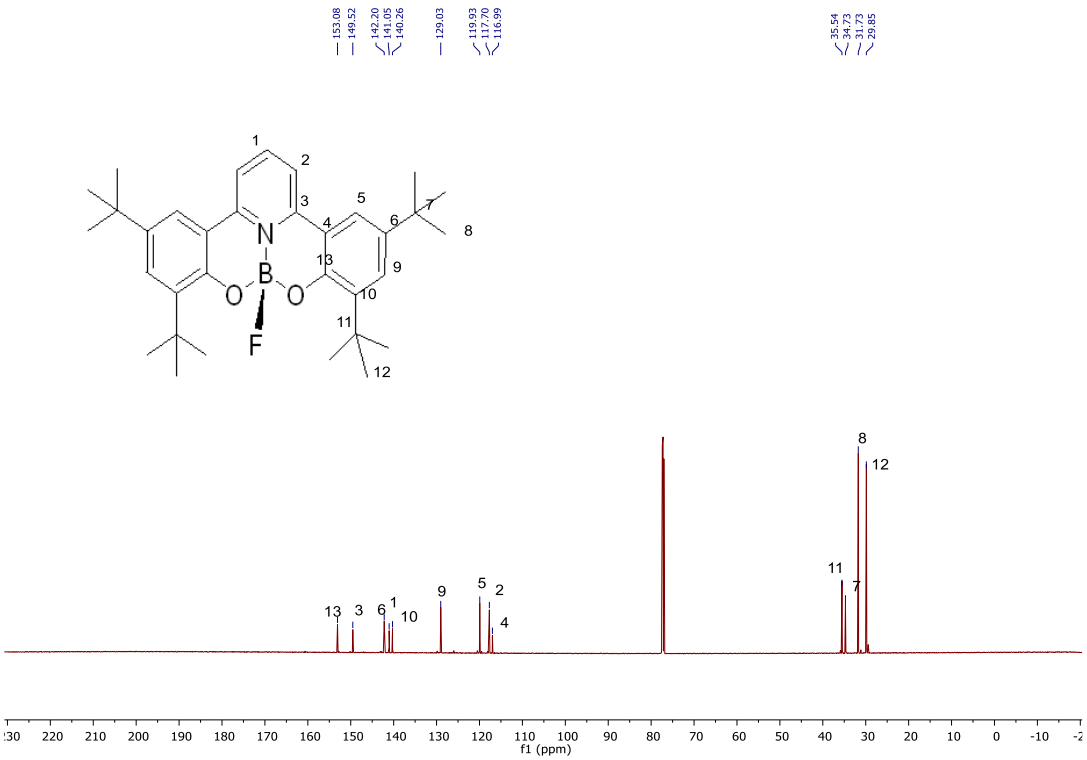

Figure S 7: ^{13}C NMR of BF on $CDCl_3$

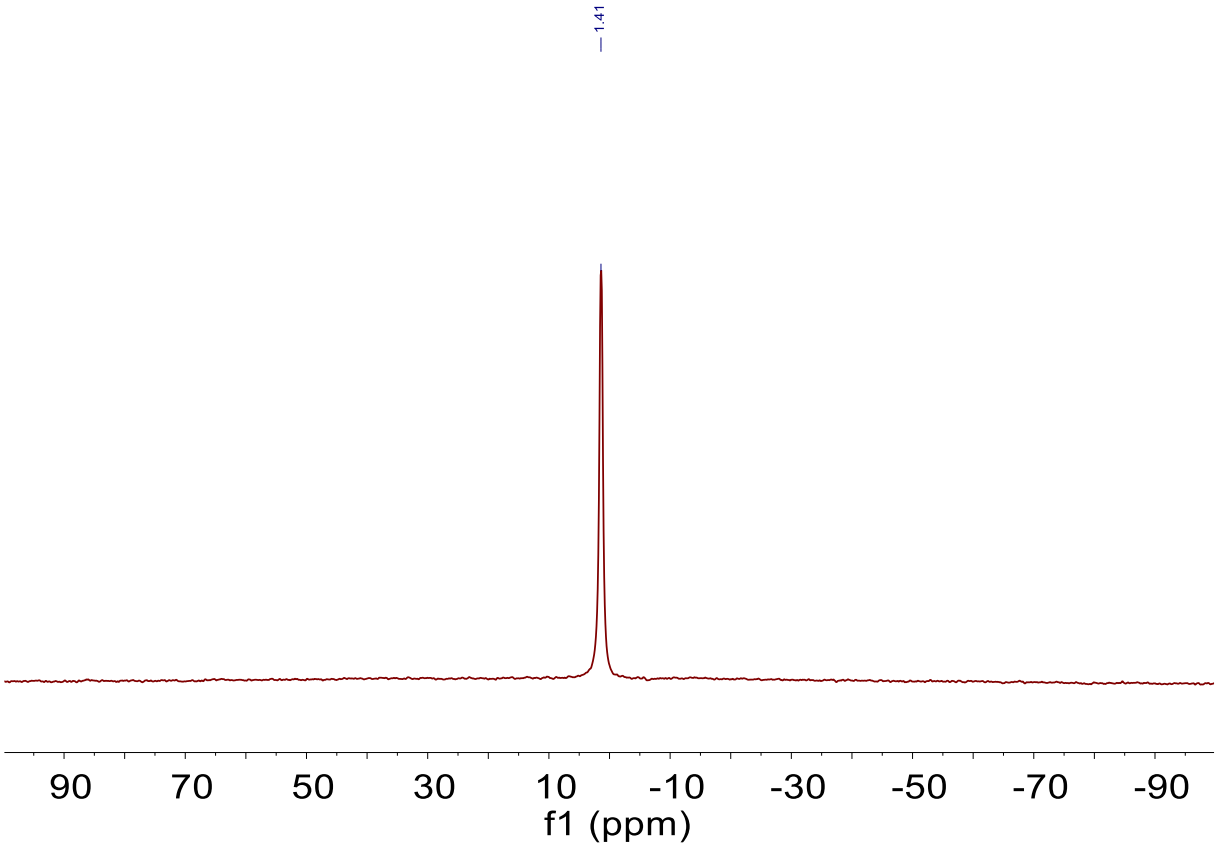

Figure S 8: ^{11}B NMR of BF on $CDCl_3$

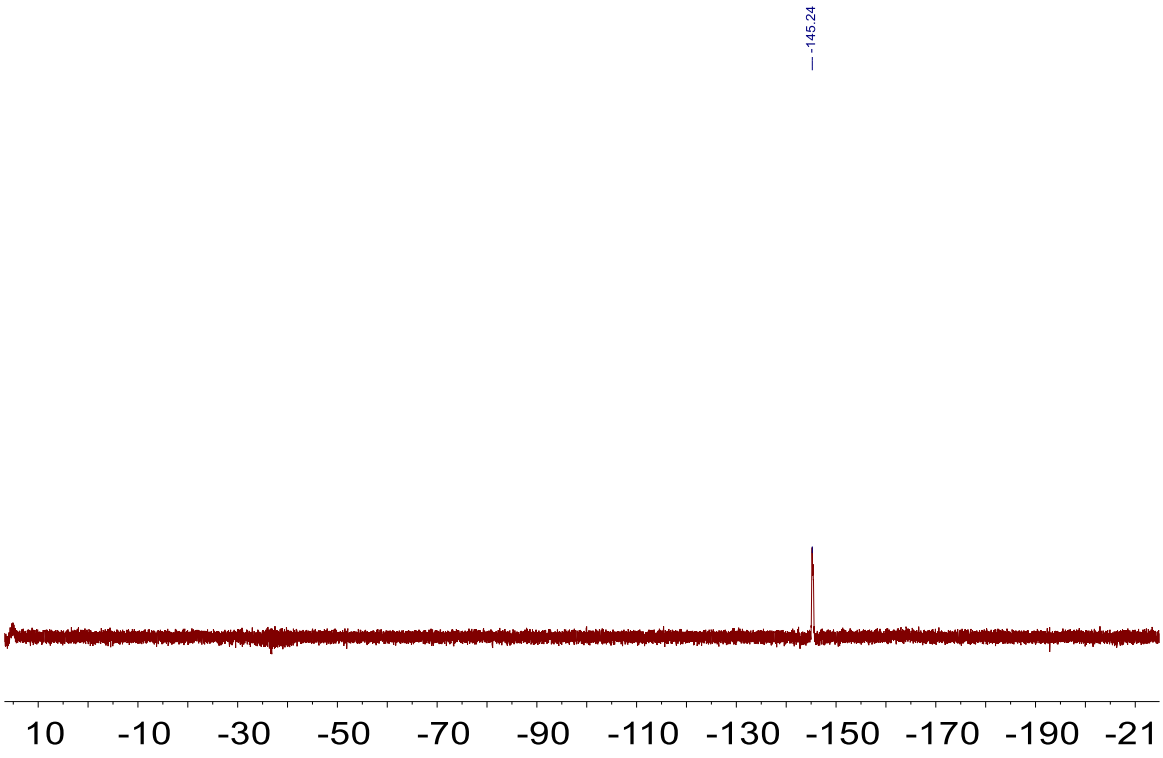

Figure S 9: ^{19}F NMR of BF on $CDCl_3$

Quantum Yield

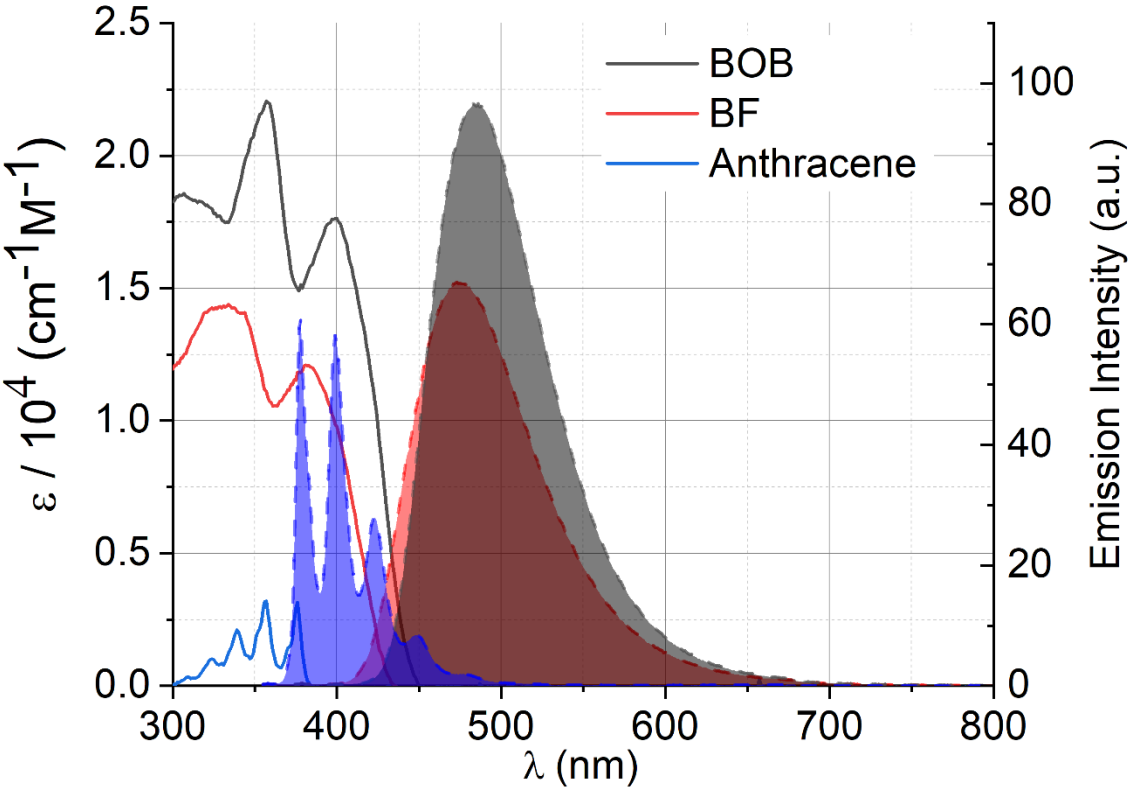

Figure S 10: Absorption and emisson spectra of BOB, BF and anthracene to determine the quantum yield in DCM at the excitation wavelength of 340 nm.

The emission quantum yields of the BOB and BF complexes were determined relative to anthracene in ethanol (Φ_{std} = 0.27). All measurements were performed at room temperature using optically diluted solutions in 1 cm quartz cuvettes. The excitation wavelength was set to 340 nm. Integrated emission intensities were obtained by numerical integration of the baseline-corrected spectra between 360 and 650 nm, giving $I_{anthracene}$=2.10 x 10^7, I_{BF} =6.48 x 10^7, and I_{BOB}= 8.69 x 10^7.

The absorbances at 340 nm were derived from Beer–Lambert's law using experimentally determined molar absorption coefficients: ε = 2059 M^{-1} cm^{-1} (anthracene, EtOH), 14074 M^{-1} cm^{-1} (BF, DCM), and 18691 M^{-1} cm^{-1} (BOB, DCM) at concentrations of 1.36 x 10^{-5} M, 1.00 x 10^{-5} M, and 1.20 x 10^{-5} M, respectively. The corresponding absorbances were A_{anth}=0.0280, A_{BF}= 0.1407, and A_{BOB}= 0.2243.

Using these parameters, the relative quantum yields were obtained as Φ(BF, DCM) = 0.18 and Φ(BOB, DCM) = 0.15.

TDDFT Investigation

Computational Methods

The Orca 5.0.3 program package was utilized for DFT and time dependent DFT (TD-DFT) calculations of the two molecules.[36] Initially, the XRD structures were optimized utilizing the PBEh-3c composite method with the verytighopt convergence criterion. Frequency analysis confirmed the convergence into local minimum for both molecules. Subsequently, the vertical transitions were calculated using time TD-DFT. For this purpose, the TPSSh functional,[37] def2-TZVP basis set [38] as well as D4 dispersion correction [39] and the conductor-like continuum model (CPCM)[40] for acetonitrile were used. To generate the theoretical spectra Gaussian broadening of the transitions with a standard deviation of 1200cm-1 and no arbitrary shift were applied. The transition density analysis was performed using the TheoDORE software package.[41] The Kohn-Sham orbital visualizations were produced with IboView. [42]

Orbital structure and symmetry discussion

Investigating the structures of the frontier orbitals most important for the strongest vertical transitions, a matching of one Kohn-Sham orbital of BF with two Kohn-Sham orbitals of BOB was identified. A listing of the identified orbitals exhibiting similar structures is curated in **Table S1**. Furthermore, visualizations of these orbitals can be found in

Table S1: Listing of BF orbitals and the BOB orbitals exhibiting similar orbital structures.

Occupied BF orbital	Occupied BOB orbital	Unoccupied BF orbital	Unoccupied BOB orbital
138	271, 272	139	273, 274
137	269, 270	140	275, 276
136	167. 268		

Table S2: Relevant TD-DFT transitions together with the occupied Kohn-Sham orbital isosurfaces of BF- (80% Isosurfaces) and BOB-complex (60% Isosurfaces). Each column compares the orbital of the BF-complex with

the corresponding two orbitals of the BOB-compound. To simplify the graphics The tert-butyl groups of the BOB-complexare hidden for simplicity.

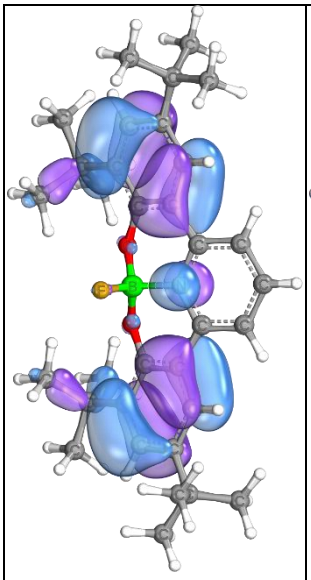 BF-135	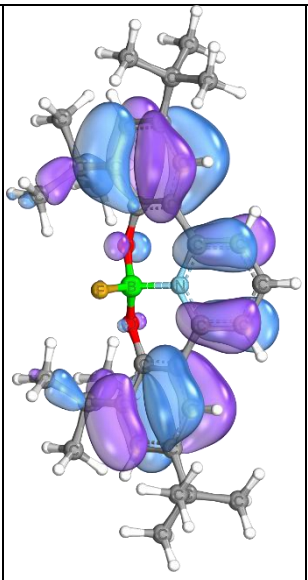 BF-136	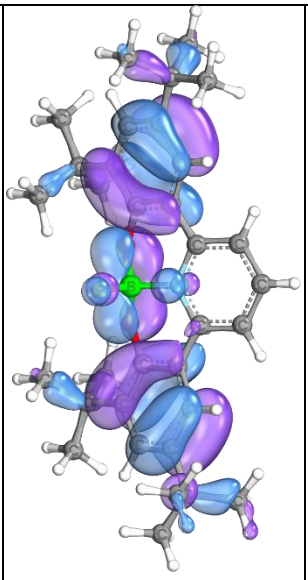 BF-137	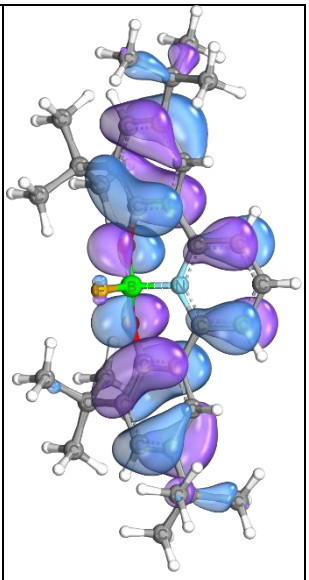 BF-138
	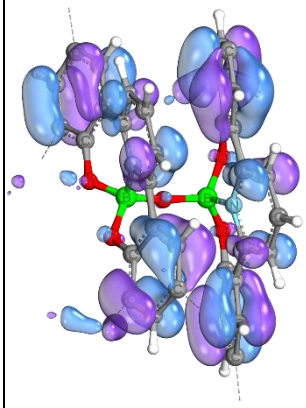 BOB-267	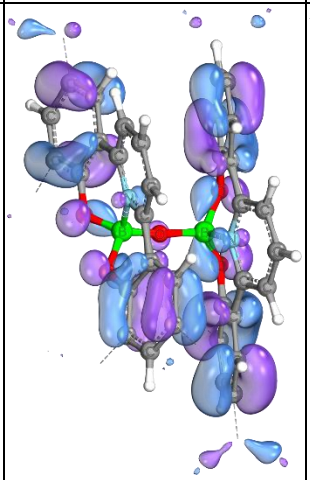 BOB-269	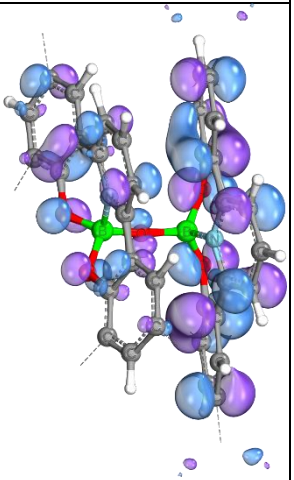 BOB-271
	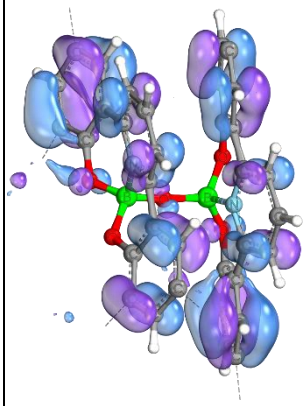 BOB-268	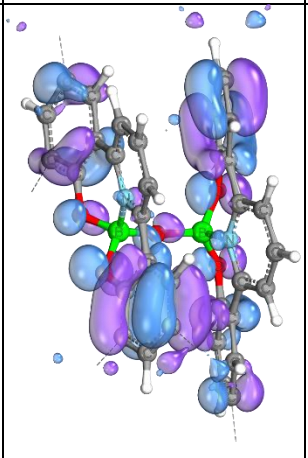 BOB-270	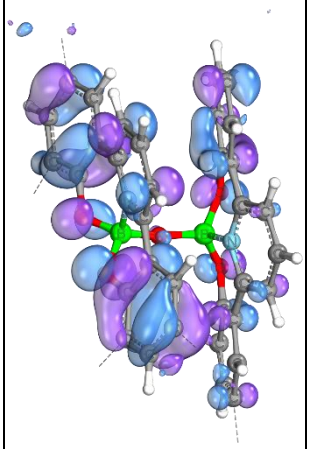 BOB-272

Table S3: Relevant TD-DFT transitions together with the occupied Kohn-Sham orbital isosurfaces of BF- (80% Isosurfaces) and BOB-complex (60% Isosurfaces). Each column compares the orbital of the BF-complex with the corresponding two orbitals of the BOB-compound. To simplify the graphics The tert-butyl groups of the BOB-complexare hidden for simplicity.

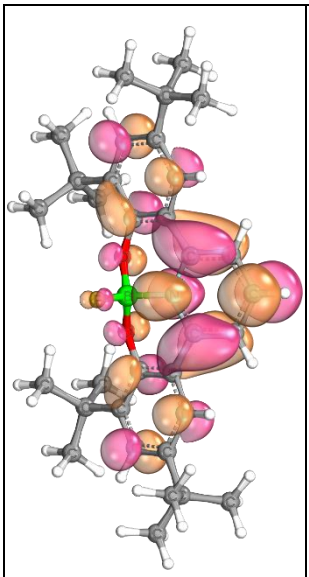 BF-139	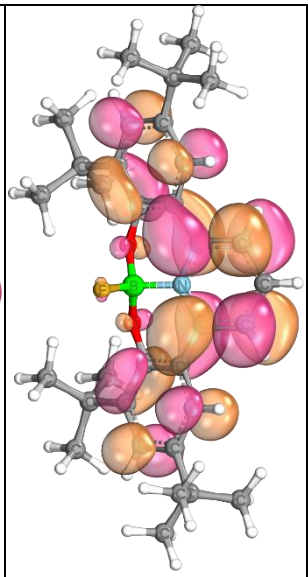 BF-140	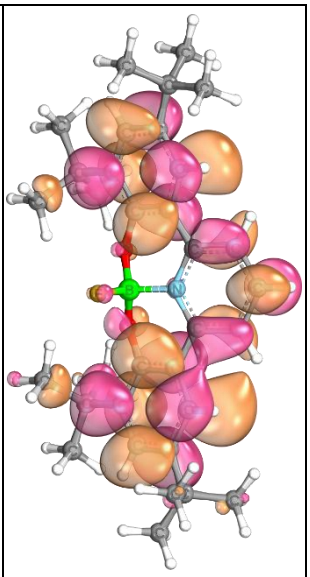 BF-141
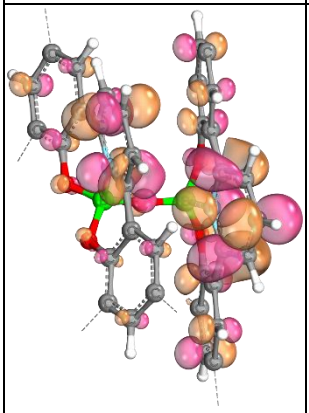 BOB-273	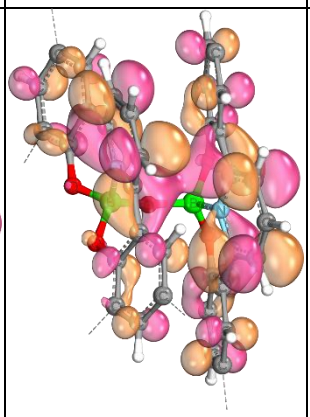 BOB-275	
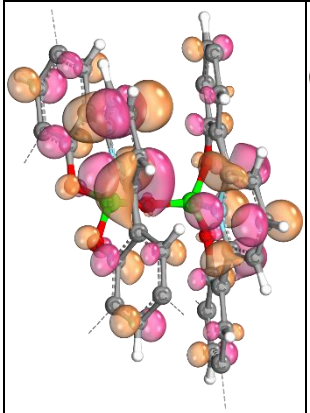 BOB-274	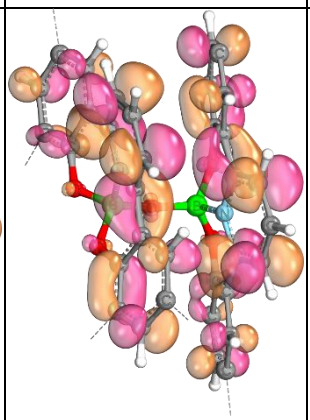 BOB-276	

Absorption spectra analysis

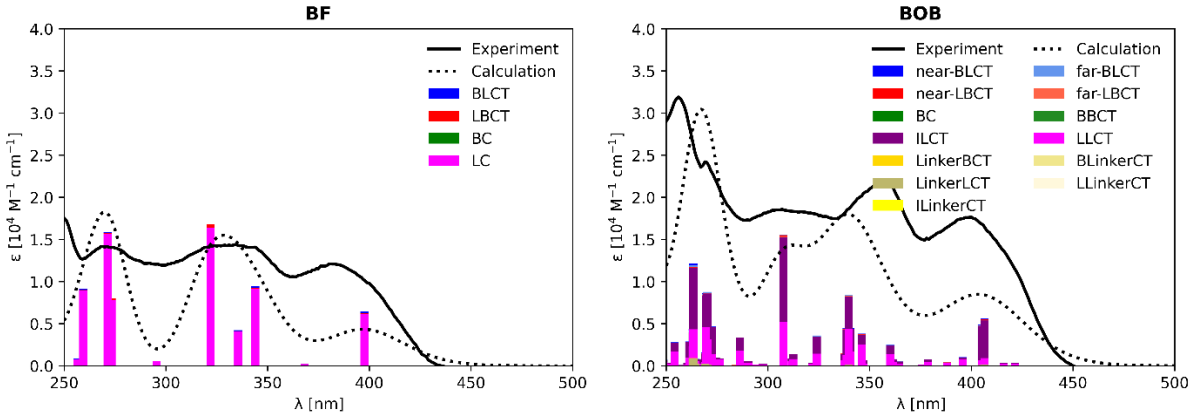

Figure S 11: Comparison between TD-DFT calculated and experimentally measured absorption spectra of BF- and BOB-complexes. TD-DFT calculated vertical transitions are shown as sticks reflecting the oscillator strength and shown as a spectrum with a broadening (fwhm) of 2825. 75 cm-1 as a dotted line in comparison to the experimental spectrum as a black solid line. The colors indicate different transition characters.

Table 4: Collection of identified absorption bands, the most relevant corresponding TD-DFT states and the associated orbital transitions. Structural corresponding orbitals of BF and BOB are marked by the same color

Band	States	Transitions	Band	States	Transitions
383	**1**	**138 -> 139 (96%)**	**400**	**3**	**272 -> 274 (36%)** **271 -> 274 (34%)**
				4	**271 -> 274 (47%)** **271 -> 273 (38%)**
330	**3**	**137 -> 140 (54%)** **137 -> 139 (32%)**	**357**	**13**	**270 -> 276 (28%)** **269 -> 275 (28%)** 271 -> 276 (18%)
	4	**137 -> 140 (93%)**		**14**	**270 -> 276 (21%)** **269 -> 273 (16%)** **268 -> 274 (14%)** 271 -> 276 (12%) **268 -> 273 (11%)**
	5	**136 -> 139 (94%)**		**15**	**268 -> 273 (41%)** **269 -> 275 (20%)** **268 -> 274 (14%)**
				16	**269 -> 275 (28%)** **268 -> 273 (25%)** **270 -> 276 (25%)** **268 -> 274 (13%)**
270	**7**	**135 -> 139 (64%)** **136 -> 140 (19%)**	**306**	**22**	**267 -> 274 (87%)**

	8 **9**	**135 -> 140 (82%)** **138 -> 141 (81%)**			

Error! Reference source not found.1 displays the experimentally measured and theoretically calculated absorption spectra for BF- and BOB-complex. Each vertical transition is visually attributed to the different transition characters possible. In comparison to Figure 5, which only explains the major electronic transitions of the absorption spectra, all differentiated transition characters are listed in **Error! Reference source not found.**.

A listing of the relevant TD-DFT states and the most significant Kohn-Sham orbitals of each vertical transition are provided in Table 4. Orbitals of BF and BOB identified to exhibit high similarity, as listed in **Table S1**, are highlighted in the same color. Using this highlighting of the orbital similarities, similarities of the 383 nm BF absorption band with the 400 nm BOB absorption band as well as the 330 nm BF absorption band with the 357 nm BOB absorption band can be easily verified.

Excitation Spectrum

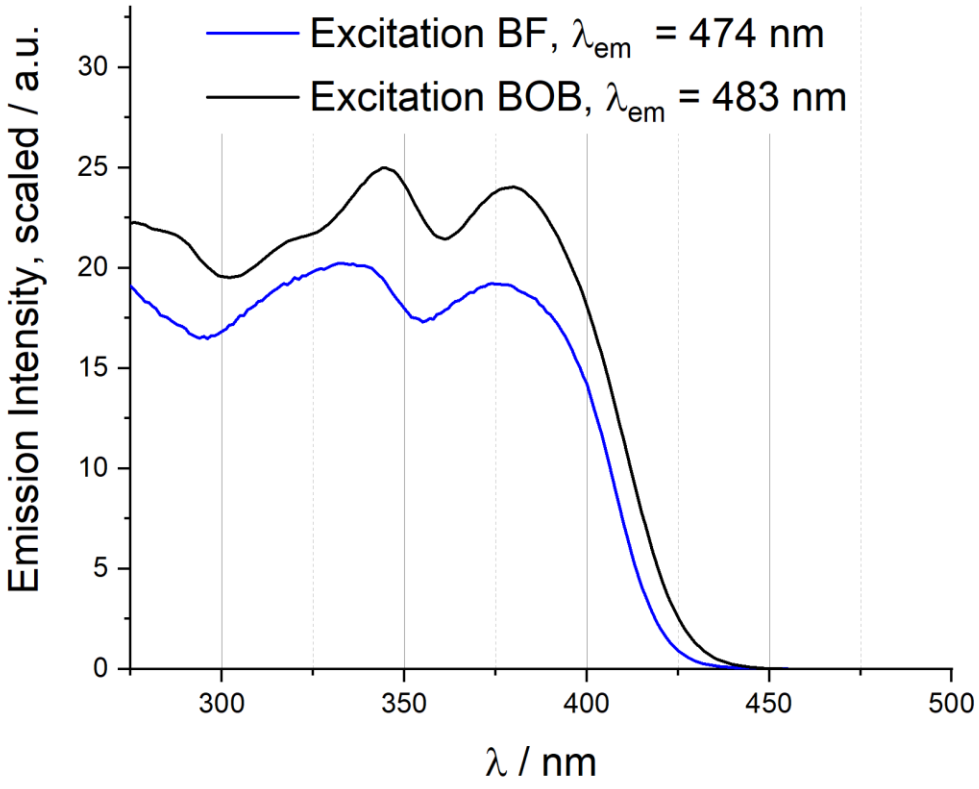

Figure S 12: Excitation Spectrum of 10µM solution of BOB and BF in DCM.

Cyclic Voltammetry

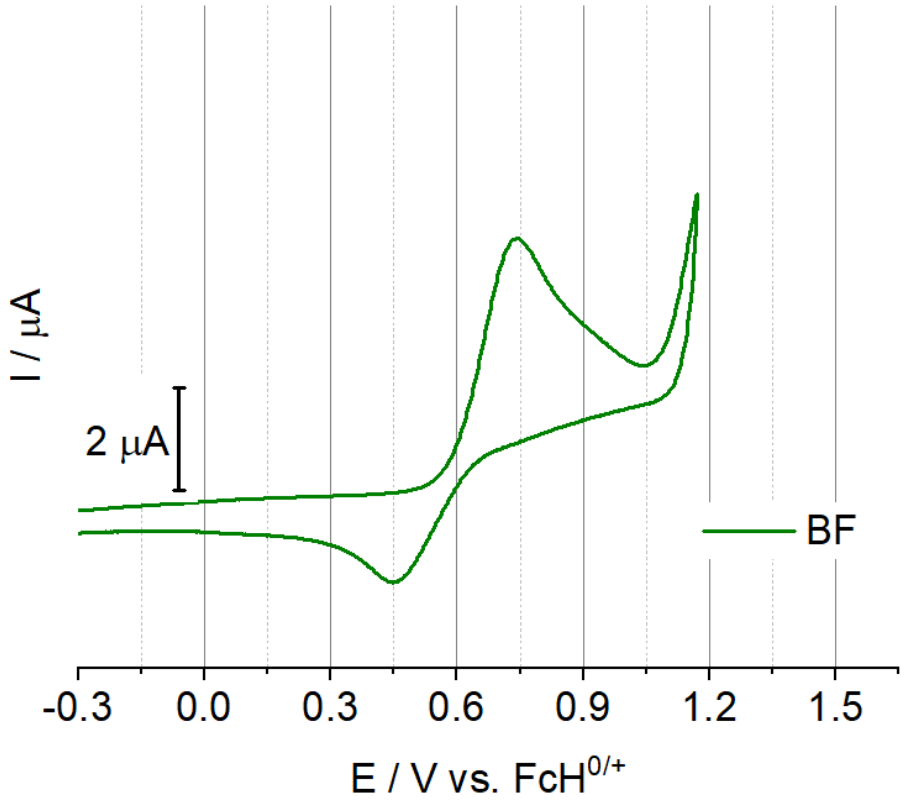

Figure S 13: Cyclic voltammetry spectrum of BF complex in (1 mM solution in MeCN) with (nBu_4N)(PF_6) as the electrolyte at 0.1 V/s.

XRD

BF

$C_{33}H_{43}BFNO_2$, M_r = 515.49 Da, colourless block, size 0.16 x 0.22 x 0.26 mm³, monoclinic space group $P2_1$ (4) with Z=2, a=11.6830(14), b=8.8066(10) Å, c=14.3903(17) Å, β=91.272(4)°, V=1480.2(3) Å³, D_c=1.157 g/cm³, μ=0.074 mm^{-1}, F(000)=556, θ_{max}=30.61°, reflections collected: 85999, independent reflections: 9073, R_{int}=0.0403, refinement converged at R1=0.0370 [I>2σ(I)], wR2=0.1066 [all data], min./max. ΔF: -0.18 eÅ³ (0.60 Å from C1) / 0.30 eÅ³ (0.79 Å from N1), **CCDC No.: 2517569.**

The crystal was obtained from evaporation of a toluene solution. One tert-butyl group is found disordered over two positions. All affected carbon atoms could be refined anisotropically. All non-hydrogen-atoms are refined anisotropically, while the aromatic hydrogen atom positions were refined at idealized positions riding on the carbon atoms with isotropic displacement parameters U_{iso}(H)=1.2 U_{eq}(C) and C-H bond lengths of 0.950 Å (HFIX 43). The methyl groups are idealized with tetrahedral angles in a combined rotating and rigid group refinement with the 1.5-fold isotropic displacement parameters of the equivalent Uij of the corresponding carbon atom at a distance of 0.98 Å (HFIX 137).

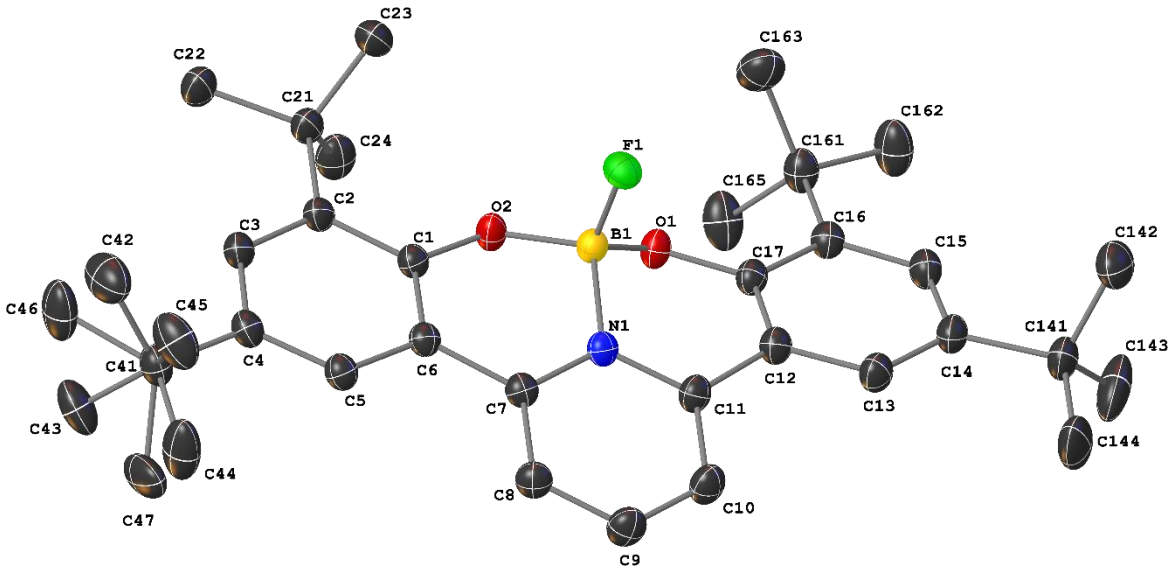

Figure S 14: Crystal structure of BF. Anisotropic displacement ellipsoids drawn on a 50% probability level. Hydrogen atoms were omitted for clarity.

BOB

$C_{66}H_{86}B_2N_2O_5$, C_7H_8, M_r = 1101.12 Da, yellow block, size 0.13 x 0.14 x 0.15 mm³, triclinic space group $P\bar{1}$ (2) with Z=2, a=14.2416(4), b=16.0918(5) Å, c=16.3273(5) Å, α=102.8480(10)°, β=115.6810(10)°, γ=95.179(2)°, V=3212.71(17) Å³, D_c=1.138 g/cm³,

μ=0.069 mm^{-1}, F(000)=1192, θ_{max}=27.505°, reflections collected: 228724, independent reflections: 14723, R_{int}=0.0838, refinement converged at R1=0.0595 [I>2σ(I)], wR2=0.1647 [all data], min./max. ΔF: -0.46 eÅ³ (1.35 Å from C2A) / 0.65 eÅ³ (0.90 Å from H29D), **CCDC No.: 2516895.**

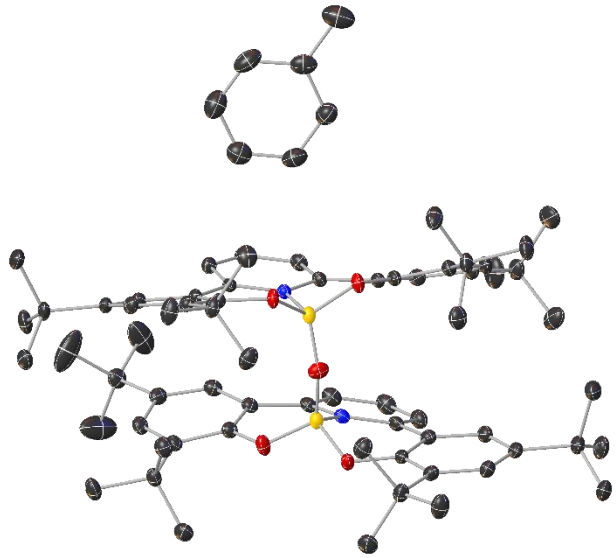

Figure S 15: Asymmetric unit of the BOB single crystal structure. Anisotropic displacement ellipsoids drawn on a 50% probability level. Hydrogen atoms were omitted for clarity.

The crystal was obtained from evaporation of a toluene solution. One toluene molecule was incorporate in the asymmetric unit of the crystal structure. All affected carbon atoms could be refined anisotropically. All non-hydrogen-atoms are refined anisotropically, while the aromatic hydrogen atom positions were refined at idealized positions riding on the carbon atoms with isotropic displacement parameters U_{iso}(H)=1.2 U_{eq}(C) and C-H bond lengths of 0.950 Å (HFIX 43). The methyl groups are idealized with tetrahedral angles in a combined rotating and rigid group refinement with the 1.5-fold isotropic displacement parameters of the equivalent Uij of the corresponding carbon atom at a distance of 0.98 Å (HFIX 137).

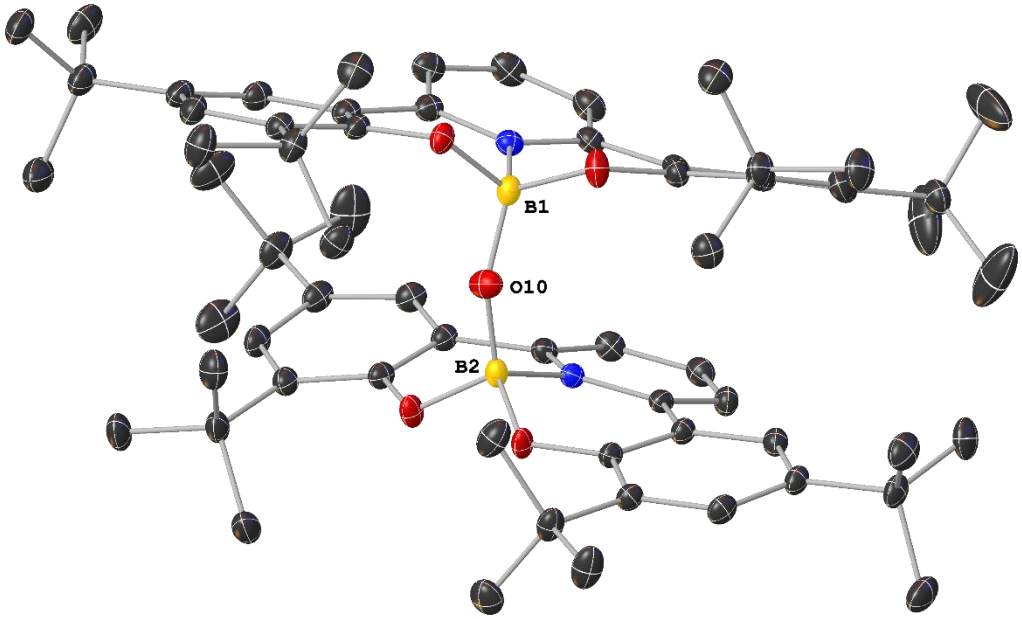

Figure S 16: Single crystal structure of BOB with anisotropic displacement ellipsoids drawn on a 50% probability level and hydrogen atoms omitted for clarity.

References

[36] F. Neese, *WIREs Comput Mol Sci* **2022**, *12*.

[37] V. N. Staroverov, G. E. Scuseria, J. Tao, J. P. Perdew, *The Journal of Chemical Physics* **2003**, *119*, 12129–12137.

[38] F. Weigend, R. Ahlrichs, *Physical chemistry chemical physics : PCCP* **2005**, *7*, 3297–3305.

[39] E. Caldeweyher, S. Ehlert, A. Hansen, H. Neugebauer, S. Spicher, C. Bannwarth, S. Grimme, *The Journal of Chemical Physics* **2019**, *150*, 154122.

[40] V. Barone, M. Cossi, *J. Phys. Chem. A* **1998**, *102*, 1995–2001.

[41] F. Plasser, *The Journal of Chemical Physics* **2020**, *152*, 84108.

[42] G. Knizia, J. E. M. N. Klein, *Angewandte Chemie (International ed. in English)* **2015**, *54*, 5518–5522

A3. Supplementary information for the publication “Low temperature emissive cyclometalated cobalt complexes”

AMERICAN CHEMICAL SOCIETY LICENSE
TERMS AND CONDITIONS

Jan 04, 2026

This Agreement between Athul Krishna ("You") and American Chemical Society ("American Chemical Society") consists of your license details and the terms and conditions provided by American Chemical Society and Copyright Clearance Center.

License Number	6181941403868
License date	Jan 04, 2026
Licensed Content Publisher	American Chemical Society
Licensed Content Publication	Inorganic Chemistry
Licensed Content Title	Low Temperature Emissive Cyclometalated Cobalt(III) Complexes
Licensed Content Author	Athul Krishna, Lorena Fritsch, Jakob Steube, et al
Licensed Content Date	Jan 1, 2025
Licensed Content Volume	64
Licensed Content Issue	3
Volume number	64
Issue number	3
Type of Use	Thesis/Dissertation
Requestor type	Author (original work)
Format	Electronic

Portion	Full article
Title of new work	Organic and Organometallic Photosensitizers for electron transfer reactions
Institution name	Paderborn University
Expected presentation date	Feb 2026
The Requesting Person / Organization to Appear on the License	Athul Krishna
Requestor Location	Warburger Str. 100 Paderborn, 33098 Germany
Payment Type	Invoice
Email Address	athul@mail.uni-paderborn.de
Billing Address	Paderborn University Warburger Str. 100 Paderborn, Germany 33098
Total	0.00 EUR

Terms and Conditions

American Chemical Society's Policy on Thesis and Dissertations

If your university requires you to obtain permission, you must use the RightsLink permission system.

See RightsLink instructions at
http://pubs.acs.org/page/copyright/permissions.html.

This is regarding request for permission to include **your** paper(s) or portions of text from **your** paper(s) in your thesis.
Permission is now automatically granted; please pay special attention to the **implications** paragraph below. The Copyright Subcommittee of the Joint Board/Council Committees on Publications approved the following:

Copyright permission for published and submitted material from thesis and dissertations
ACS extends blanket permission to students to include in their thesis and dissertations their own articles, or portions thereof, that have been published in ACS journals or submitted to ACS journals for publication, provided that the ACS copyright credit line is noted on the appropriate page(s).

Publishing implications of electronic publication of thesis and dissertation material
Students and their mentors should be aware that posting of thesis and dissertation material on the Web prior to submission of material from that thesis or dissertation to an ACS journal may affect publication in that journal. Whether Web posting is considered prior publication may be evaluated on a case-by-case basis by the journal's editor. If an ACS journal editor considers Web posting to be "prior publication", the paper will not be accepted for publication in that journal. If you intend to submit your unpublished paper to ACS for publication, check with the appropriate editor prior to posting your manuscript electronically.

Reuse/Republication of the Entire Work in Thesis or Collections: Authors may reuse all or part of the Submitted, Accepted or Published Work in a thesis or dissertation that the author writes and is required to submit to satisfy the criteria of degree-granting institutions. Such reuse is permitted subject to the ACS' "Ethical Guidelines to Publication of Chemical Research" (http://pubs.acs.org/page/policy/ethics/index.htmlb); the author should secure written confirmation (via letter or email) from the respective ACS journal editor(s) to avoid potential conflicts with journal prior publication*/embargo policies. Appropriate citation of the Published Work must be made. If the thesis or dissertation to be published is in electronic format, a direct link to the Published Work must also be included using the ACS Articles on Request author-directed link - see http://pubs.acs.org/page/policy/articlesonrequest/index.html

* Prior publication policies of ACS journals are posted on the ACS website at http://pubs.acs.org/page/policy/prior/index.html

If your paper has not yet been published by ACS, please print the following credit line on the first page of your article: "Reproduced (or 'Reproduced in part') with permission from [JOURNAL NAME], in press (or 'submitted for publication'). Unpublished work copyright [CURRENT YEAR] American Chemical Society." Include appropriate information.

If your paper has already been published by ACS and you want to include the text or portions of the text in your thesis/dissertation, please print the ACS copyright credit line on the first page of your article: "Reproduced (or 'Reproduced in part') with permission from [FULL REFERENCE CITATION.] Copyright [YEAR] American Chemical Society." Include appropriate information.

Submission to a Dissertation Distributor: If you plan to submit your thesis to UMI or to another dissertation distributor, you should not include the unpublished ACS paper in your thesis if the thesis will be disseminated electronically, until ACS has published your paper. After publication of the paper by ACS, you may release the entire thesis (**not the individual ACS article by itself**) for electronic dissemination through the distributor; ACS's copyright credit line should be printed on the first page of the ACS paper.

v1.4

Questions? customercare@copyright.com.

Supplementary information for:

Low Temperature emissive cyclometalated Cobalt (III) complexes

Athul Krishna[1], Lorena Fritsch[1], Jakob Steube[1], Miguel A. Argüello Cordero[2], Roland Schoch[1], Adam Neuba[1], Stefan Lochbrunner[2], Matthias Bauer[1*]

1: Institute for Inorganic Chemistry and Center for Sustainable Systems Design (CSSD), Paderborn University, 33098 Paderborn, Germany

2: Department of Life, Light and Matter and Institute of Physics, University of Rostock, 18051 Rostock, Germany

*E-mail: matthias.bauer@uni-paderborn.de

Table of contents

Single Crystal X-ray Analysis

The Cambridge Crystallographic Data Centre provides the presented structures free of charge via www.ccdc.cam.ac.uk assigned to the deposition numbers 2386766, 2386767, 2386768.

$Co(L\text{-}Me_2)_2$ (Co1)

$(C_{28}H_{26}N_8Co)^+$, $(PF_6)^-$, C_3H_6O, M_r = 736.59 Da, pale yellow block, size 0.30 x 0.28 x 0.24 mm³, monoclinic space group $P2_1/n$ with Z=4, a=17.9279(8), b=8.5704(4) Å, c=20.7528(10) Å, β=93.355(2)°, V=3183.2(3) Å³, D_c=1.537 g/cm³, μ=0.665 mm^{-1}, F(000)=1512, θ_{max}=27.483°, reflections collected: 167611, independent reflections: 7263, R_{int}=0.0279, refinement converged at R1=0.0357 [I>2σ(I)], wR2=0.0896 [all data], min./max. ΔF: -0.74 eÅ³ (0.54 Å from F132) / 0.90 eÅ³ (0.53 Å from F132), **CCDC No.: 2386766.**

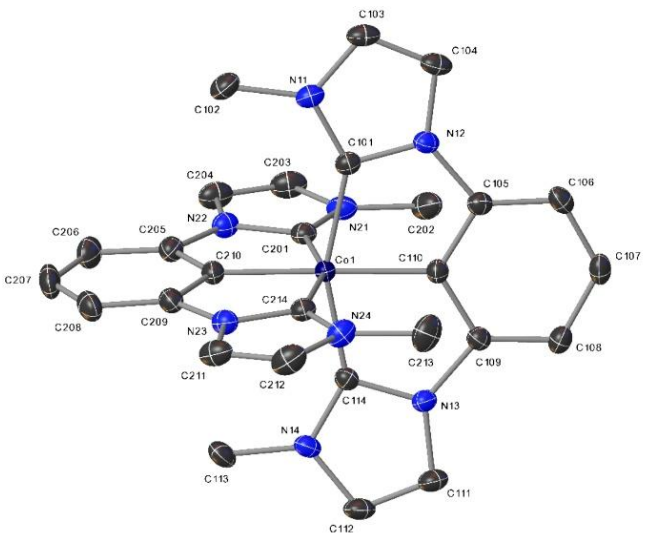

Figure S1: Cystal structure of $Co(L\text{-}Me_2)_2$ shown with anisotropic displacement ellipsoids drawn at 50% probability level). Hydrogen atoms, one $(PF_6)^-$ and one acetone molecule were omitted for reasons of clarity.

Four equatorial arranged F-atoms of the $(PF_6)^-$ anion present in the asymmetric unit are disordered over three positions (SOF=34.8:48.8:16.4) and could therefore not be refined anisotropically. In addition to the complex and one $(PF_6)^-$ anion, one acetone molecule was found in the asymmetric unit.

Except the mentioned F-atoms, all non-hydrogen-atoms were refined anisotropically, while the aromatic hydrogen atom positions were refined at idealized positions riding on the carbon atoms with isotropic displacement parameters U_{iso}(H)=1.2 U_{eq}(C) and C-H bond lengths of 0.950 Å (HFIX 43). Methyl groups are idealized with tetrahedral angles in a combined rotating and rigid group refinement with 1.5 fold isotropic displacement parameters of the equivalent U_{ij} of the corresponding carbon atom at a distance of d(C-H)=0.980 Å (HFIX 137).

Co(L-Et$_2$)$_2$ (Co2)

($C_{32}H_{38}N_8Co$)$^+$, I^-, 2(C_3H_6O), M_r = 832.66 Da, yellow block, size 0.26 x 0.16 x 0.10 mm^3, monoclinic space group *P2$_1$/c* with Z=4, a=10.0090(4), b=19.0969(7) Å, c=20.2404(8) Å, β=95.3590(10)°, V=3851.9(3) Å^3, D_c=1.436 g/cm^3, μ=1.291 mm^{-1}, F(000)=1704, θ_{max}=36.371°, reflections collected: 688412, independent reflections: 18717, R_{int}=0.0445, refinement converged at R1=0.0230 [I>2σ(I)], wR2=0.0626 [all data], min./max. ΔF: -0.57 eÅ^3 (0.54 Å from Co1) / 0.89 eÅ^3 (0.64 Å from I1), **CCDC No.: 2386767.**

In addition to the complex molecule and one iodide, two acetone molecules are present in the asymmetric unit.

All non-hydrogen-atoms were refined anisotropically, while the aromatic hydrogen atom positions were refined at idealized positions riding on the carbon atoms with isotropic displacement parameters U_{iso}(H)=1.2 U_{eq}(C) and C-H bond lengths of 0.950 Å (HFIX 43). Methyl groups are idealized with tetrahedral angles in a combined rotating and rigid group refinement with 1.5 fold isotropic displacement parameters of the equivalent U_{ij} of the corresponding carbon atom at a distance of d(C-H)=0.980 Å (HFIX 137).

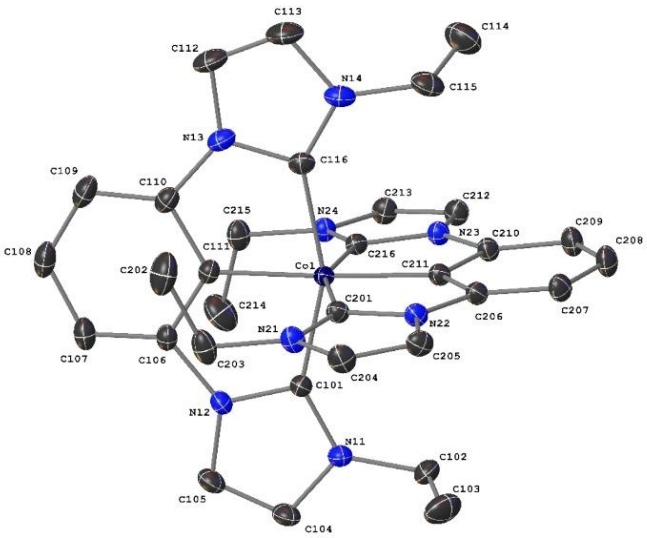

Figure S2: Cystal structure of Co(L-Et$_2$)$_2$ shown with anisotropic displacement ellipsoids drawn at 50% probability level). Hydrogen atoms, one iodide and two acetone molecules were omitted for reasons of clarity.

Co(L-iPr$_2$)$_2$ (Co3)

$(C_{36}H_{42}N_8Co)^+$, Br^-, 2.25 (C_3H_6O), M_r = 856.29 Da, yellow shere, size 0.20 x 0.20 x 0.20 mm³, tetragonal space group *P4* with Z=4, a=20.0218(7), b=20.0218(7) Å, c=11.1531(5) Å, V=4471.0(4) Å³, D_c=1.272 g/cm³, μ=1.321 mm^{-1}, F(000)=1792, θ_{max}=30.519°, reflections collected: 309546, independent reflections: 13661, R_{int}=0.0428, refinement converged at R1=0.0240 [I>2σ(I)], wR2=0.0654 [all data], min./max. ΔF: -0.60 eÅ³ (0.22 Å from Br01) / 0.66 eÅ³ (0.71 Å from Br03), **CCDC No.: 2386768.**

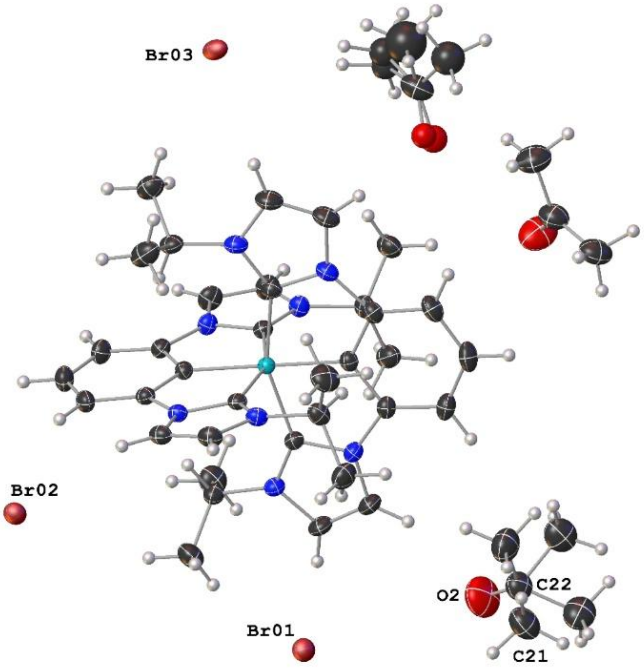

Figure S3: Asym. Unit of the cystal structure of Co(L-iPr$_2$)$_2$ shown with anisotropic displacement ellipsoids drawn at 50% probability level) including the disordered Br^- anion and acetone molecules.

The structure was refined as a 2-component inversion twin (Flack-parameter: 0.013(5)). The asymmetric unit contains one complex molecule, one bromide ion and 2.25 acetone molecules. The bromide is disordered over three special positions: SOF=0.25 Br^- at

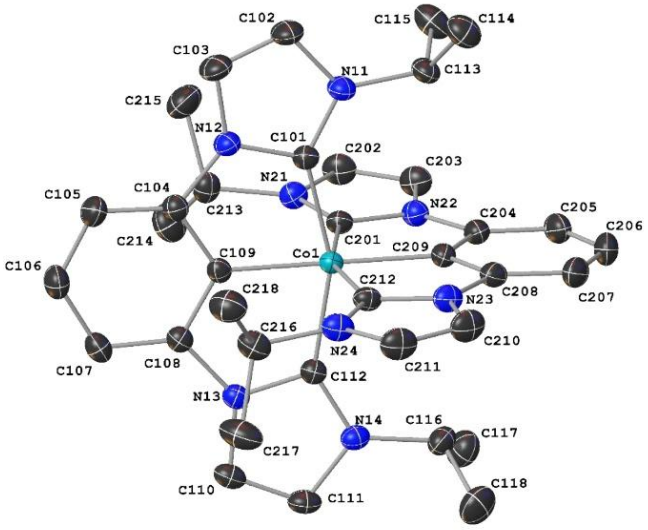

Figure S4: Cystal structure of Co(L-iPr$_2$)$_2$ shown with anisotropic displacement ellipsoids drawn at 50% probability level). H atoms, one Br^- and 2.25 acetone molecules were omitted for reasons of clarity.

Wyckoff letter 1a, SOF=0.25 Br^- at Wyckoff letter 1b (both four-fold rotation axes) and SOF=0.5 Br^- at Wyckoff letter 2c (a two-fold rotation axis). The methyl groups as well as the oxygen atom of one acetone molecule (No. 3) are disordered over two positions (SOF=0.38) and could only be refined isotropically. The carbonyl-carbon atom and the oxygen atom of acetone molecule 2 are located on a four-fold rotation axis (Wyckoff letter 1b) and therefore exhibit a SOF=0.25. The methyl-carbon atom is positioned on a general position with a SOF=0.5, resulting in one acetone molecule in the unit cell, whose methyl carbon atoms are disordered over two positions.

Except for the mentioned carbon and oxygen atoms, all non-hydrogen-atoms were refined anisotropically, while the aromatic hydrogen atom positions were refined at idealized positions riding on the carbon atoms with isotropic displacement parameters $U_{iso}(H)=1.2\ U_{eq}(C)$ and C-H bond lengths of 0.950 Å (HFIX 43). Methyl groups are idealized with tetrahedral angles in a combined rotating and rigid group refinement with 1.5 fold isotropic displacement parameters of the equivalent U_{ij} of the corresponding carbon atom at a distance of d(C-H)=0.980 Å (HFIX 137).

Cyclic voltammetry

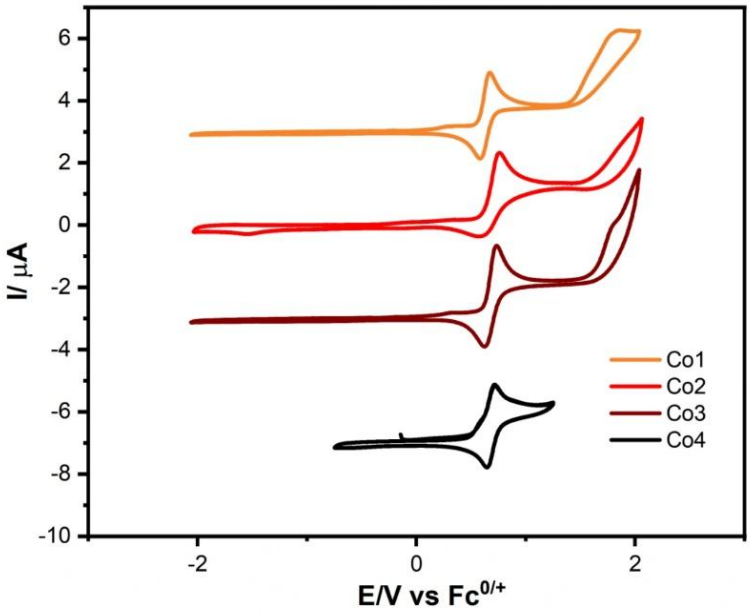

Figure S5: Cyclic voltammograms of **Co1**-**Co4** in $CH_3CN/[nBu_4N][PF_6]$ vs $FcH^{0/+}$.

For **Co4**, a new batch of solvent was used. This did not allow us to measure on the same range, hence no ligand oxidation was observed in this case.

Spectroelectrochemistry

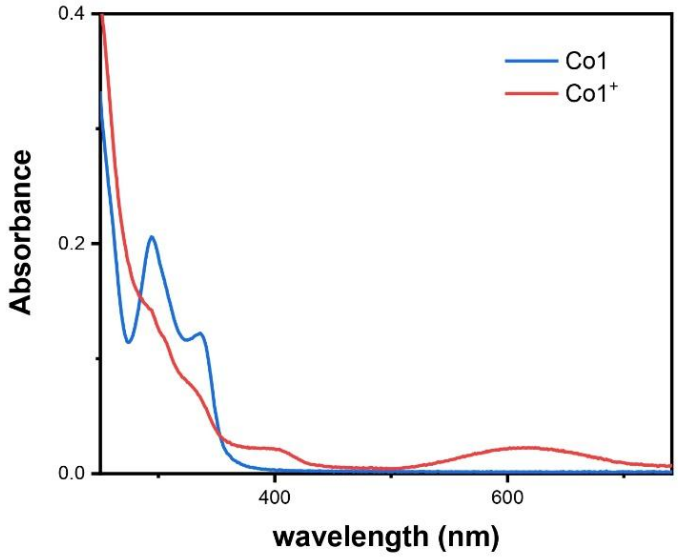

Figure S6: Spectroelectrochemical UV-Vis spectra of **Co1**. Spectroelectrochemical UV-Vis spectra measured in $CH_3CN/[nBu_4N][PF_6]$ before (blue) and after (red) electrochemical oxidation.

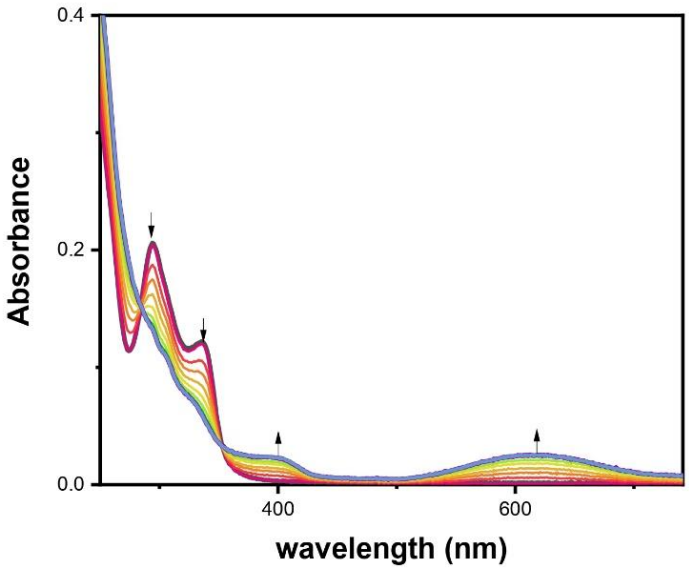

Figure S7: Spectroelectrochemical oxidation UV-Vis spectra of **Co1**. Time resolved spectroelectrochemical UV-Vis spectra measured in CH3CN/[nBu_4N][PF_6] showing the formation of new absorption bands at 400 and 620 nm and disappearance of the bands at 340 and 290 nm.

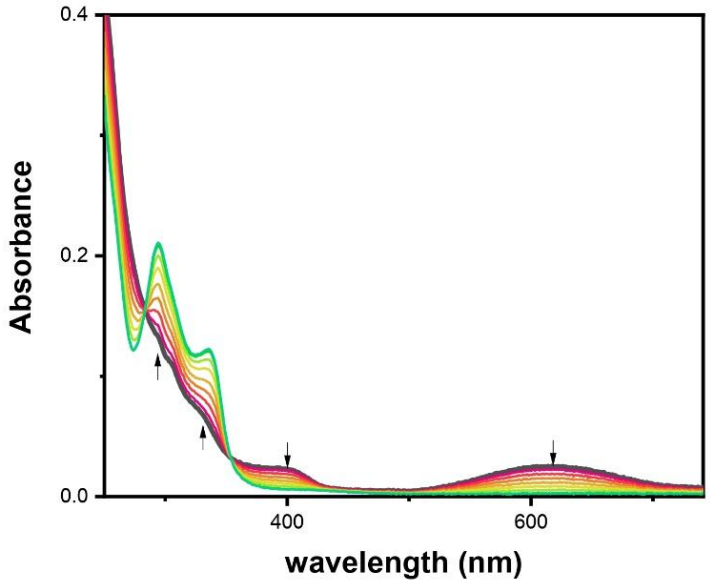

Figure S8: Spectroelectrochemical reduction UV-Vis spectra of **Co1.** Time resolved spectroelectrochemical UV-Vis spectra measured in $CH_3CN/[nBu_4N][PF_6]$ showing the disappearance of new absorption bands at 400 and 620 nm and reappearance of the bands at 340 and 290 nm.

Low-Temperature Emission Spectroscopy

Due to a signal originating from the butyronitrile (see Figure S10), the spectra were corrected for the signal by subtracting the solvent spectrum.

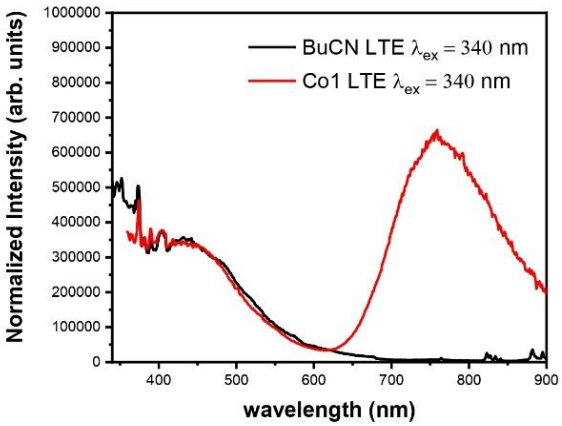

Figure S9: Normalized low temperature emission spectra of blank BuCN and **Co1** overlayed after excitation at 340 nm.

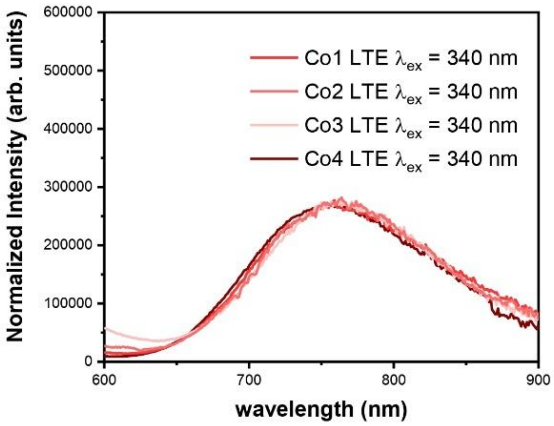

Figure S10: Normalized low temperature emission spectra of **Co1-4** in BuCN after excitation at 340 nm.

Room-Temperature Emission Spectroscopy

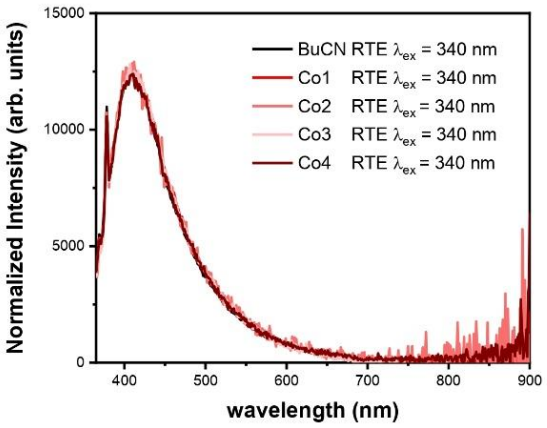

Figure S11: Normalized room temperature emission spectra of blank BuCN and **Co1, Co2, Co3 and Co4** overlayed after excitation at 340 nm. No emission was recorded other than the signal originating from blank butyronitrile

Transient Absorption

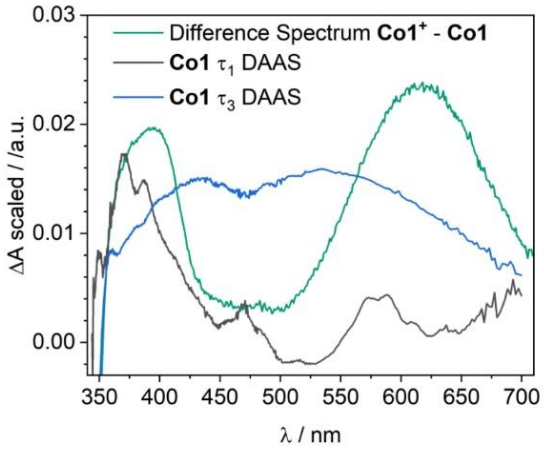

Figure S12: Difference spectrum of **Co1**$^+$ - **Co1** in comparison with the τ_1 and τ_3 DAAS from the **Co1** TA measurement.

Computational Methods

All quantum chemical calculations were performed using the Orca 5.0.3 program package.[1] The singlet ground state geometries (Table S1) were optimized using the PBEh-3c composite method.[2] Vibrational frequency analysis confirmed the local minima of the optimized geometry by obtaining no negative values for **Co1**, **Co2** and **Co4**. However, for **Co3** a small negative frequency of -13.57 cm^{-1} was found, which can be attributed to the rotation of the isopropyl groups and the isoenergetic character of the different rotational states.

To investigate the electronic transitions in the absorption spectrum, time-dependent (TD-) DFT calculations were conducted to compute the first 150 vertical transitions by single point calculations on the vacuum ground-state geometry in acetonitrile, employing the TPSSh functional,[3] the def2-TZVP basis set,[4] and the continuum polarizable continuum model (CPCM) for MeCN.[5] The tight convergence criterion was imposed on all calculations and the D4 dispersion correction was always employed when not using the PBEh-3c method.[6,7] The calculated transitions are shown in Figure 3b with an additional (arbitrary) shift of 3000 cm^{-1} to the red region of the spectrum to better match with the experimental UV-Vis spectrum, which is common practice and a similar values can be found in literature.[8–10] The

analysis of the character of the transitions by colour code is done using the TheoDORE package.[11] Spatial distributions of orbitals were visualized using Avogadro 1.2.0.[12]

To calculate the MECP energy, an optimization of the PES crossing point (keyword surfcrossopt) between the ^{3}MC and ^{1}GS PES was conducted, starting from the ^{3}MC optimized geometry. Here, the standard B3LYP[13] functional alongside with the def2-TVZP, the CPCM model for MeCN and the D4 correction was used for the ^{1}GS, ^{3}MC and MECP calculation.

Table S1: *Structural parameter of the PbEh-3c optimized complexes; averaged over all equivalent bond lengths. (phen = phenyl fragment; im = imidazole fragment) Crystal structure parameters for comparison in square brackets.*

Complex	$d_{ø}$ (Co-C_{phen}) / Å	$d_{ø}$ (Co-C_{im}) / Å	∢ chelate bite angle / °
Co1	1.893 [1.906]	1.956 [1.944]	159.0 [157.9]
Co2	1.894 [1.909]	1.957 [1.953]	158.9 [157.7]
Co3	1.896 [1.910]	1.975 [1.952]	158.9 [157.9]
Co4	1.896 [-]	1.978 [-]]	158.74 [-]]

Table S2: *Analysis of selected (highest oscillator strength) TD-DFT calculated states of Co1. (Ph = phenyl part; NHC = NHC part of the ligand framework). The assignments of the transitions were made by the character shown by colour code in Figure 4. The shown donor and acceptor orbitals reflect the largest contribution to the transition.*

State	l / nm	f_{osc}	Donor orbital	Acceptor orbital	Transition density	Assign-ment
1	356	0.000157994	135 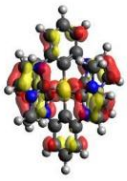	142 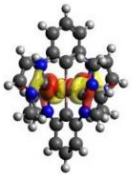	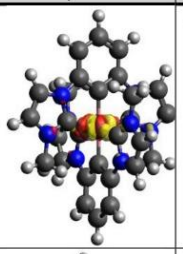	MC
2	350	0.032795290	137 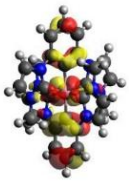	138 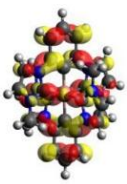	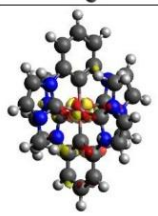	MLCT

3	350	0.033214414	136 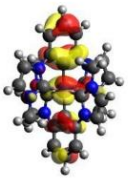	138 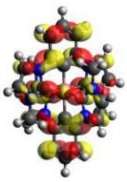	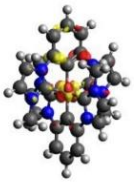	MLCT
7	329	0.063186845	137 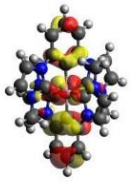	139 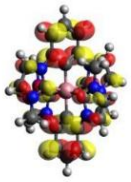	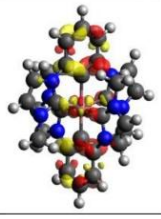	MLCT
8	328	0.062683347	136 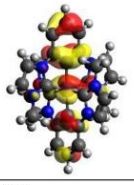	139 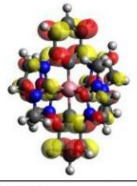	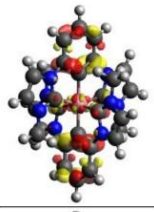	MLCT
9	326	0.045706826	135 	139 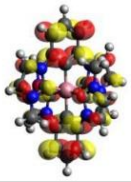	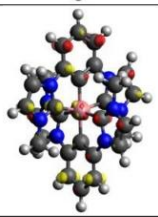	MLCT
14	302	0.078016977	136 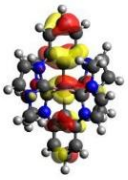	140 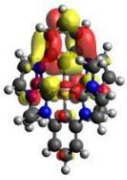	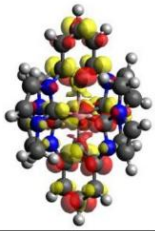	MLCT
18	294	0.228733732	134 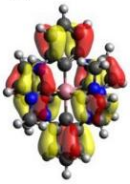	138 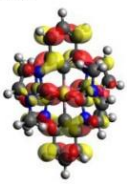	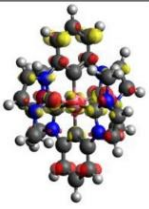	ILCT

S13

33	270	0.067190826	130 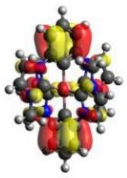	139 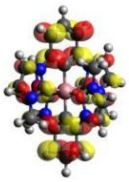	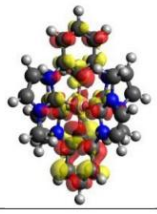	ILCT

Table S3: *Fragment contributions (%) for selected ground state molecular orbitals of Co1 using the Loewdin population analysis.*

orbital	Character / %			
	Co d	C_{ph} p	C_{im} p	N p
130	8	48	9	14
134	0	37	36	9
135	47 (d_{xy})	11	22	8
136	41 (d_{xy})	33	7	4
137	42 (d_{xy})	33	6	4
138	6	36	27	6
139	0	44	26	1
140	6	38	19	7
141	6	38	19	7
142	56 (d_{x2-y2})	0	17	2

Table S4: *B3LYP optimized geometries of Co1 for the ^{1}GS, ^{3}MC and MECP state. Energy difference towards the ^{1}GS and Co-Ligand distance for each state are given.*

^{1}GS	^{3}MC	MECP
d(Co-L):1.94; ΔE=0	d(Co-L):2.07; ΔE=183 kJ/mol	d(Co-L):2.17; ΔE=218 kJ/mol
		

Spectra

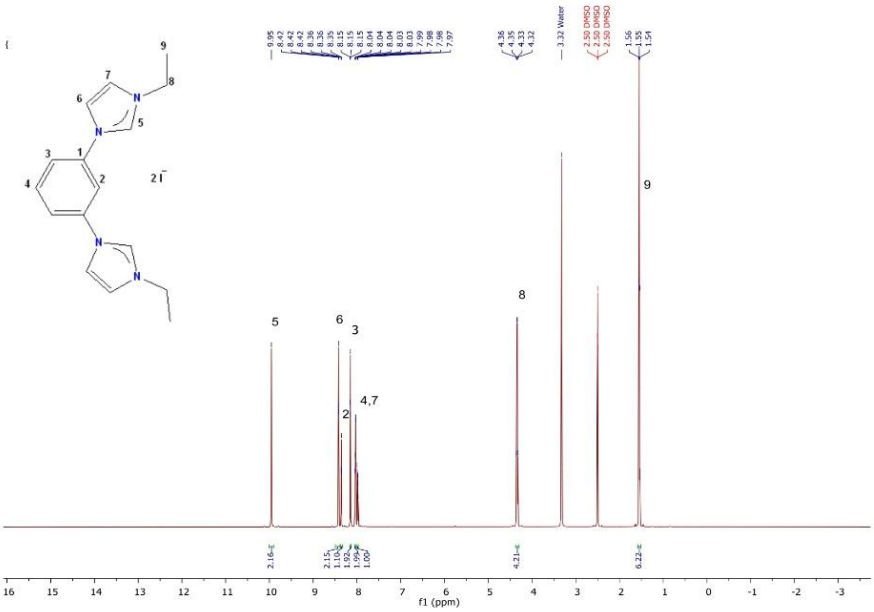

Figure S13: ^{1}H-NMR spectrum of 1,1'-(1,3-phenylene)bis(3-ethyl-1-imidazolium) diiodide.

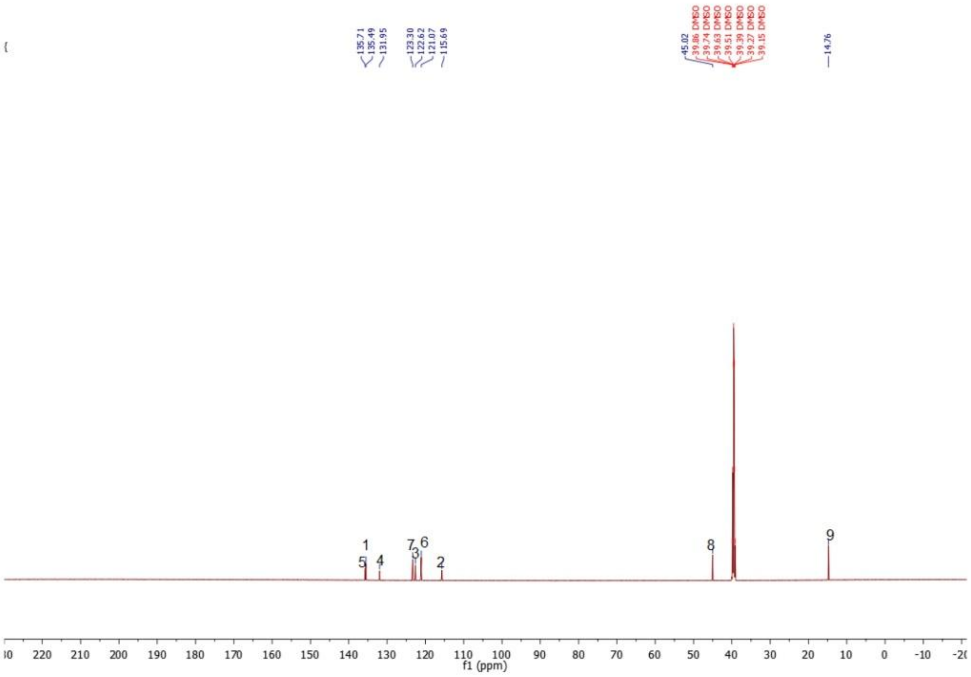

Figure S14: ^{13}C-NMR spectrum of 1,1'-(1,3-phenylene)bis(3-ethyl-1-imidazolium) diiodide.

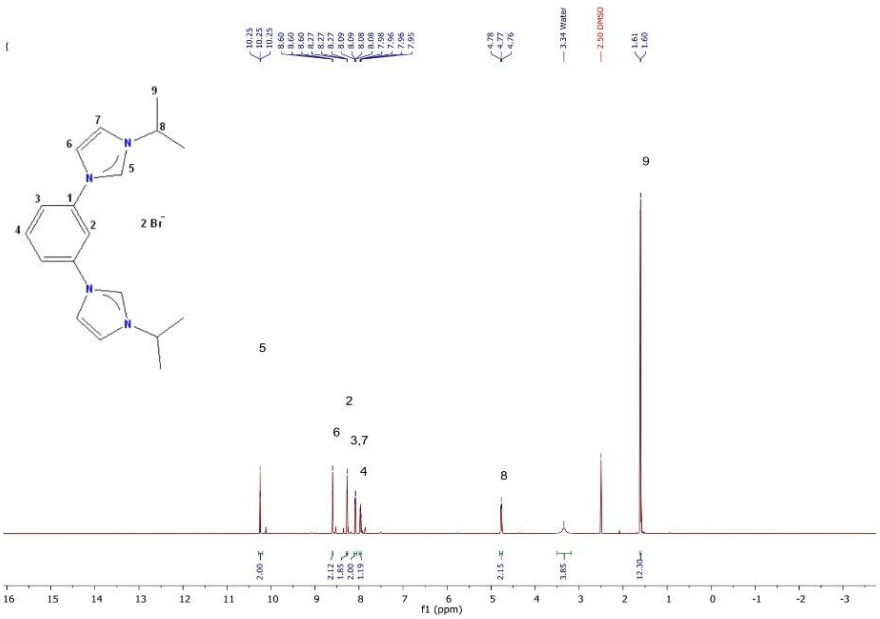

Figure S15: ^{1}H-NMR spectrum of 1,1'-(1,3-phenylene)bis(3-isopropyl-1-imidazolium) dibromide.

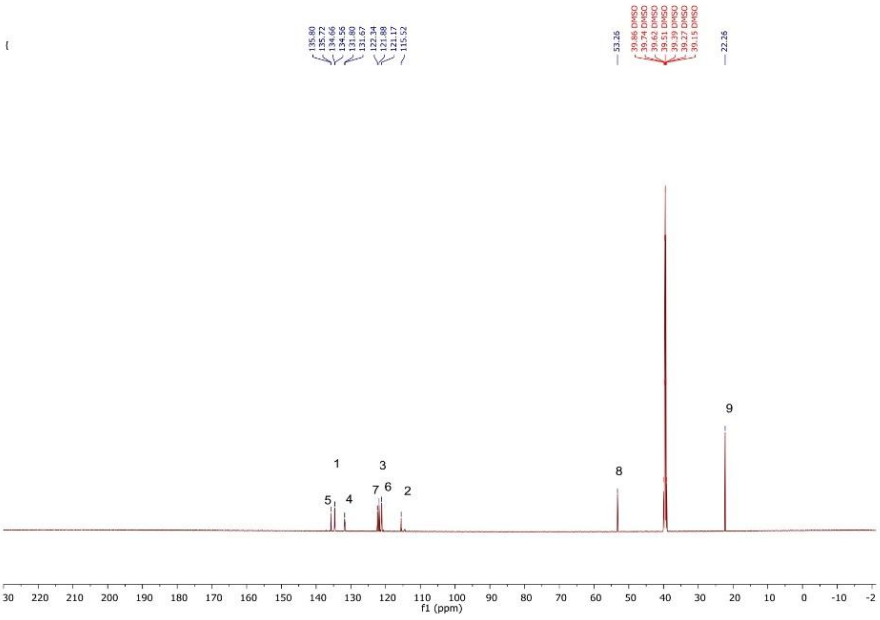

Figure S16: ^{13}C-NMR spectrum of 1,1'-(1,3-phenylene)bis(3-isopropyl-1-imidazolium) dibromide.

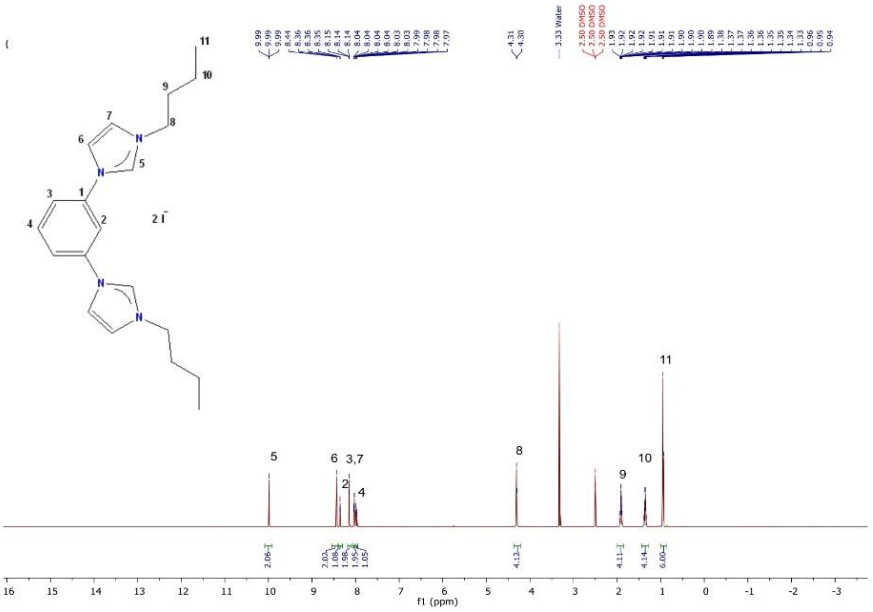

Figure S17: ^{1}H-NMR spectrum of 1,1'-(1,3-phenylene)bis(3-butyl-1-imidazolium) diiodide.

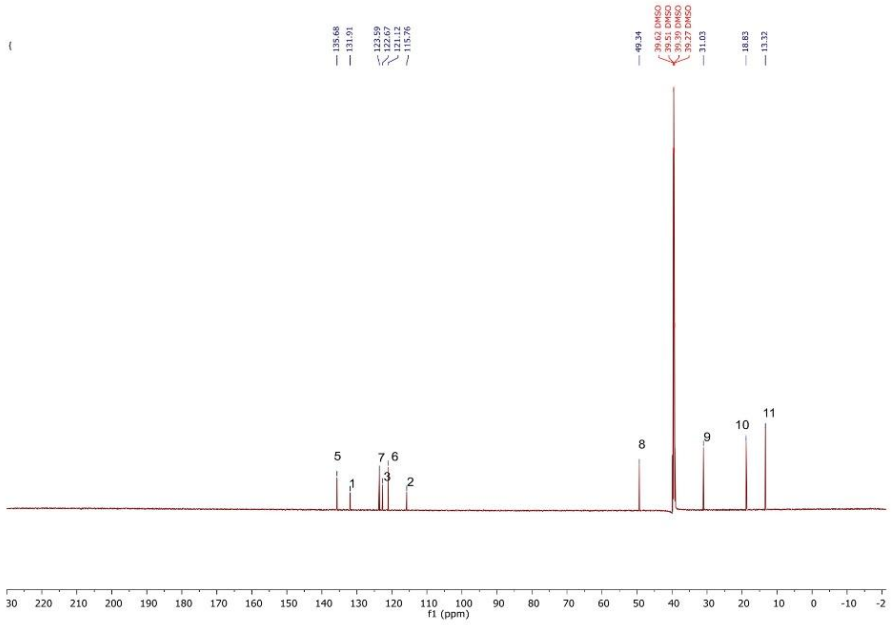

Figure S18: ^{13}C-NMR spectrum of 1,1'-(1,3-phenylene)bis(3-butyl-1-imidazolium) diiodide.

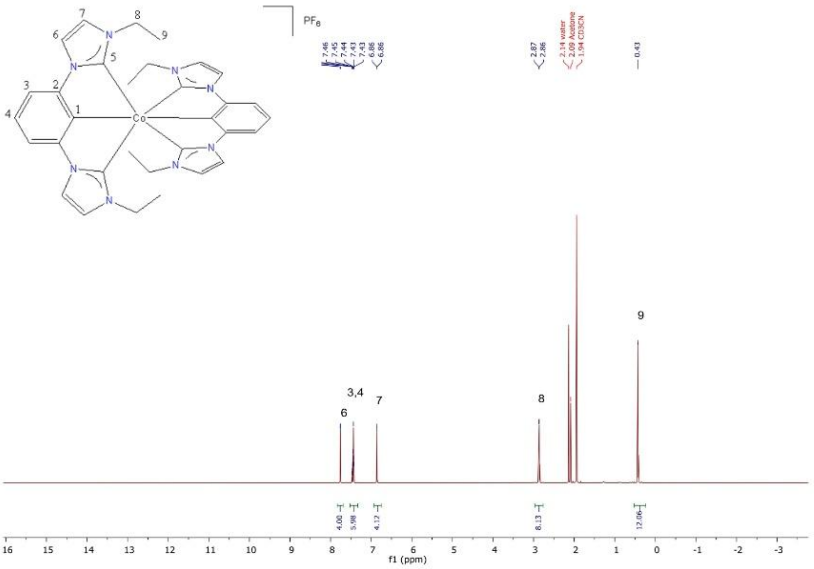

Figure S19: ^{1}H-NMR spectrum of **Co2**.

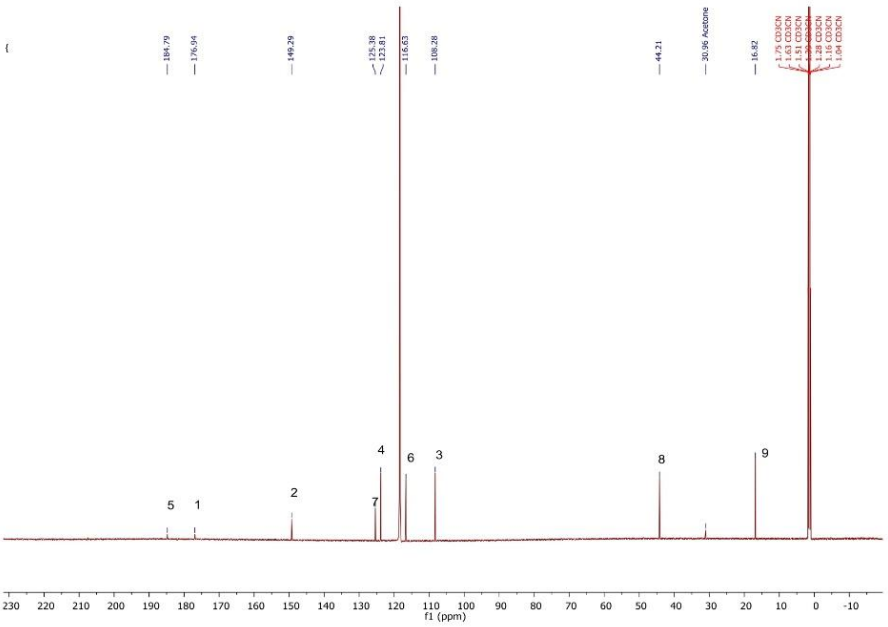

Figure S20: ^{13}C-NMR spectrum of **Co2**.

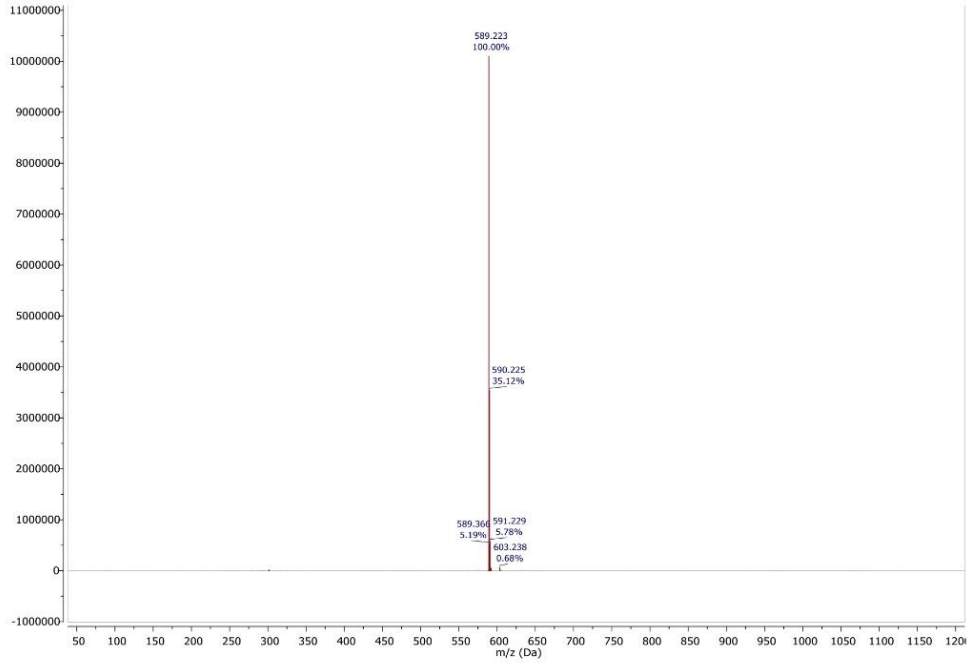

Figure S21: ESI-MS measurement of **Co2**.

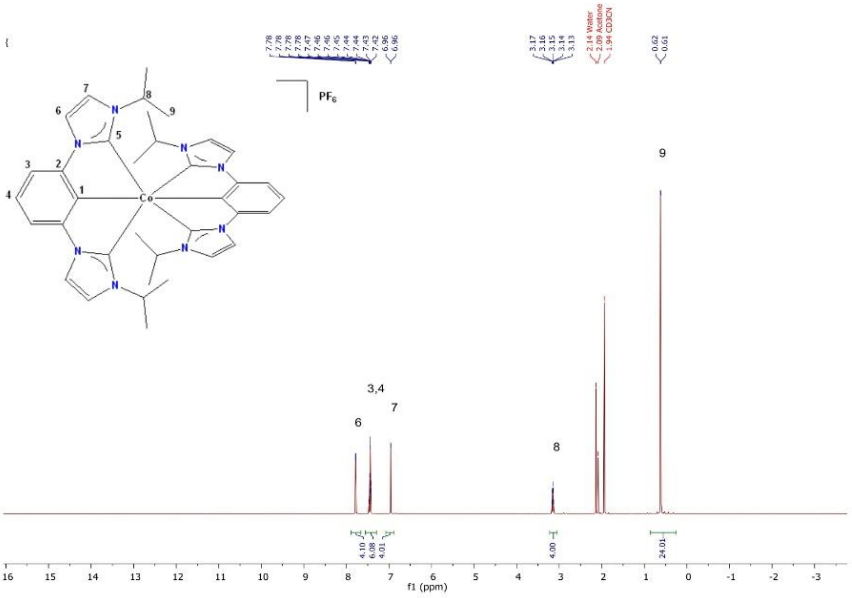

Figure S22: ^{1}H-NMR spectrum of **Co3**.

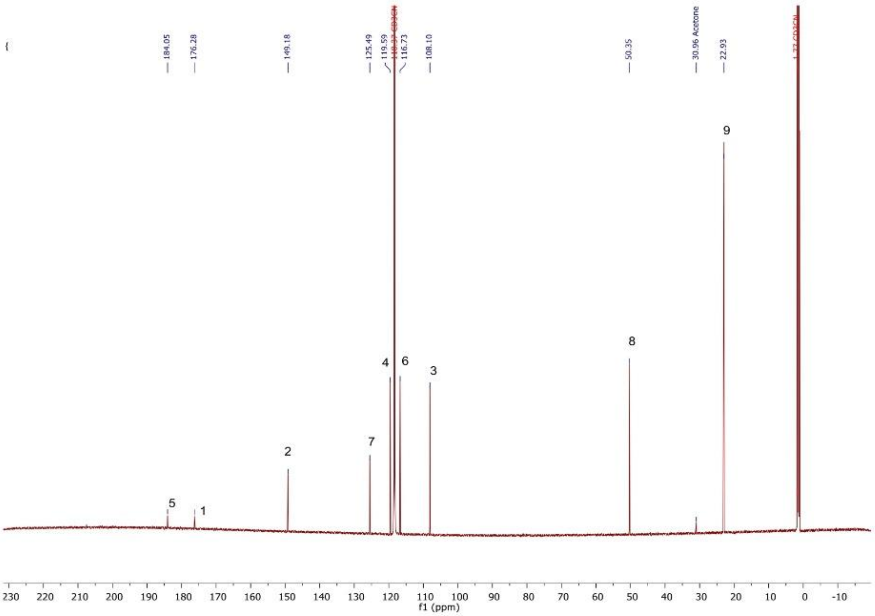

Figure S23: ^{13}C-NMR spectrum of **Co3**.

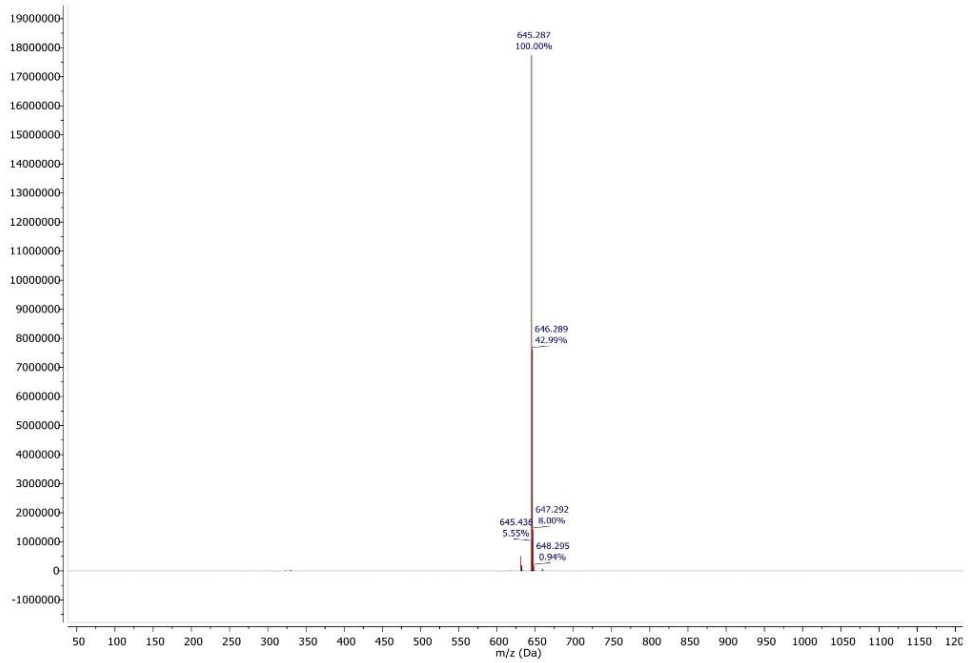

Figure S24: ESI-MS measurement of **Co3**.

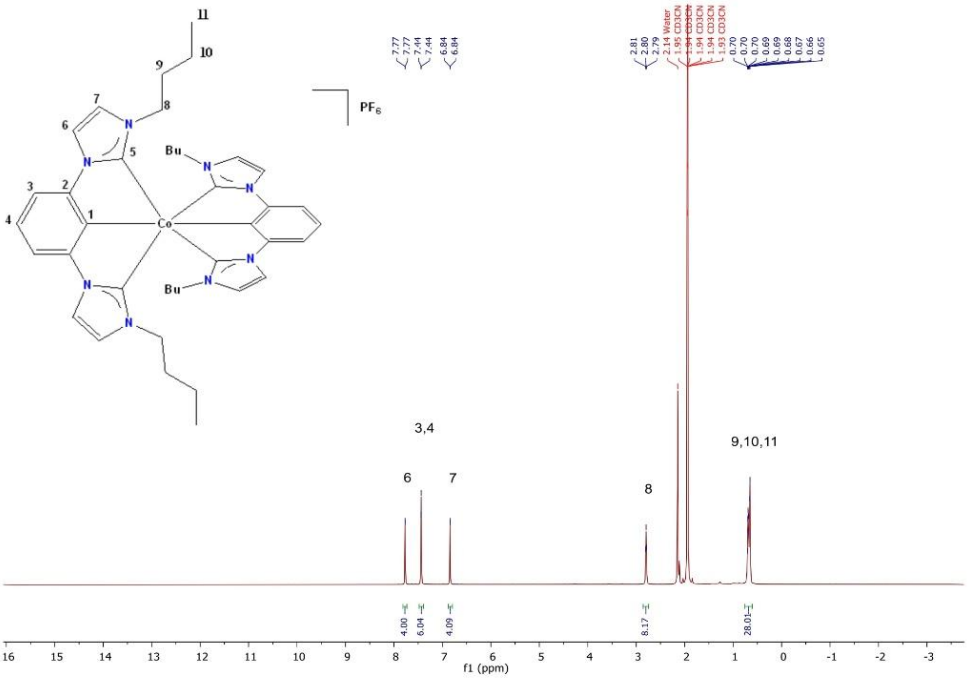

Figure S25: ^{1}H-NMR spectrum of **Co4.**

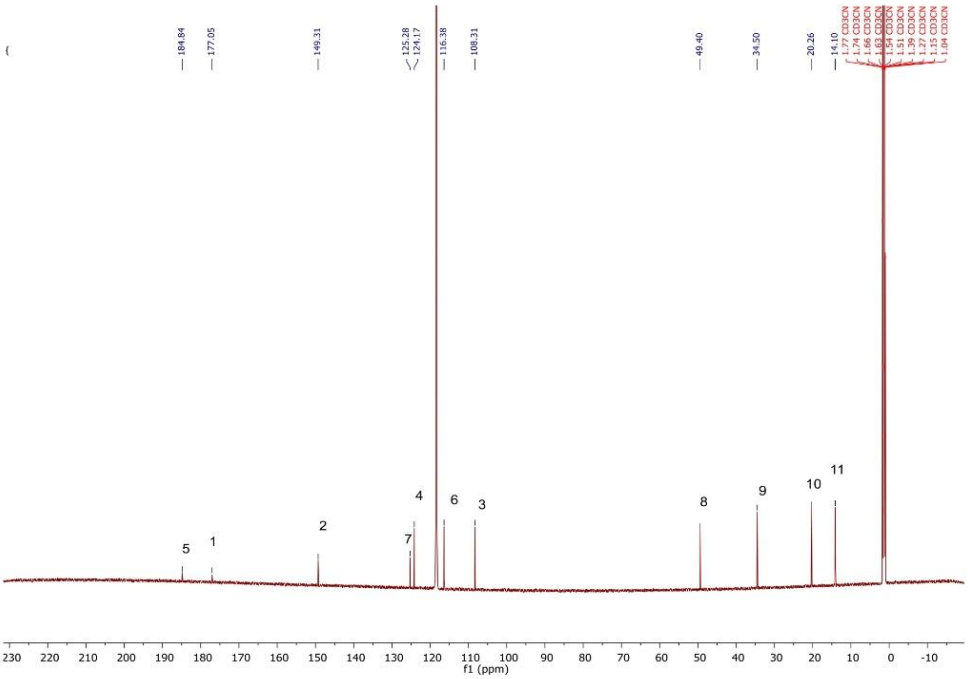

Figure S26: ^{13}C-NMR spectrum of **Co4**.

S22

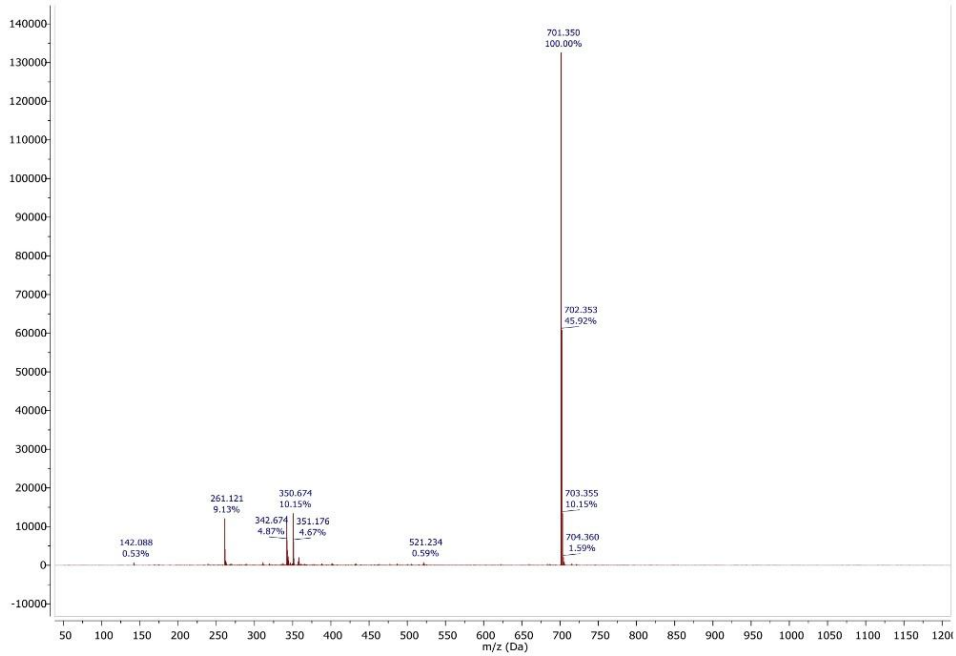

Figure S27: ESI-MS measurement of Co4.

References

(1) Frank Neese. The ORCA program system. *Wiley Interdisciplinary Reviews: Computational Molecular Science* **2012**, *2* (1), 73–78. DOI: 10.1002/wcms.81.

(2) Grimme, S.; Brandenburg, J. G.; Bannwarth, C.; Hansen, A. Consistent structures and interactions by density functional theory with small atomic orbital basis sets. *J. Chem. Phys.* **2015**, *143* (5). DOI: 10.1063/1.4927476.

(3) Staroverov, V. N.; Scuseria, G. E.; Tao, J.; Perdew, J. P. Comparative assessment of a new nonempirical density functional: Molecules and hydrogen-bonded complexes. *J. Chem. Phys.* **2003**, *119* (23), 12129–12137. DOI: 10.1063/1.1626543.

(4) Weigend, F.; Ahlrichs, R. Balanced basis sets of split valence, triple zeta valence and quadruple zeta valence quality for H to Rn: Design and assessment of accuracy. *Phys. Chem. Chem. Phys.* **2005**, *7* (18), 3297–3305. DOI: 10.1039/B508541A.

(5) Maurizio Cossi; Nadia Rega; Giovanni Scalmani; Vincenzo Barone. Energies, structures, and electronic properties of molecules in solution with the C-PCM solvation model. *Journal of Computational Chemistry* **2003**, *24* (6), 669–681. DOI: 10.1002/jcc.10189.

(6) Caldeweyher, E.; Ehlert, S.; Hansen, A.; Neugebauer, H.; Spicher, S.; Bannwarth, C.; Grimme, S. A generally applicable atomic-charge dependent London dispersion correction. *J. Chem. Phys.* **2019**, *150* (15), 154122. DOI: 10.1063/1.5090222.

(7) Neese, F.; Wennmohs, F.; Hansen, A.; Becker, U. Efficient, approximate and parallel Hartree–Fock and hybrid DFT calculations. A 'chain-of-spheres' algorithm for the Hartree–Fock exchange. *Chemical Physics* **2009**, *356* (1-3), 98–109. DOI: 10.1016/j.chemphys.2008.10.036.

(8) Sinha, N.; Pfund, B.; Wegeberg, C.; Prescimone, A.; Wenger, O. S. Cobalt(III) Carbene Complex with an Electronic Excited-State Structure Similar to Cyclometalated Iridium(III) Compounds. *J. Am. Chem. Soc.* **2022**, *144* (22), 9859–9873. DOI: 10.1021/jacs.2c02592.

(9) Conradie, M. M. UV-Vis Spectroscopy, Electrochemical and DFT Study of Tris(β-diketonato)iron(III) Complexes with Application in DSSC: Role of Aromatic Thienyl Groups. *Molecules* **2022**, *27* (12). DOI: 10.3390/molecules27123743.
(10) Dorn, M.; Kalmbach, J.; Boden, P.; Kruse, A.; Dab, C.; Reber, C.; Niedner-Schatteburg, G.; Lochbrunner, S.; Gerhards, M.; Seitz, M.; Heinze, K. Ultrafast and long-time excited state kinetics of an NIR-emissive vanadium(III) complex I: synthesis, spectroscopy and static quantum chemistry. *Chemical Science* **2021**, *12* (32), 10780–10790. DOI: 10.1039/D1SC02137K.
(11) Plasser, F. TheoDORE: A toolbox for a detailed and automated analysis of electronic excited state computations. *J. Chem. Phys.* **2020**, *152* (8), 84108. DOI: 10.1063/1.5143076.
(12) Hanwell, M. D.; Curtis, D. E.; Lonie, D. C.; Vandermeersch, T.; Zurek, E.; Hutchison, G. R. Avogadro: an advanced semantic chemical editor, visualization, and analysis platform. *Journal of cheminformatics* **2012**, *4* (1), 17. DOI: 10.1186/1758-2946-4-17.
(13) Becke, A. D. Density-functional thermochemistry. III. The role of exact exchange. *J. Chem. Phys.* **1993**, *98* (7), 5648–5652. DOI: 10.1063/1.464913.

A4. Supplementary information for the publication “Photogeneration of cobalt stabilized aminium radical”

Supplementary information for:

Photogeneration of Cobalt Stabilized Aminium Radical

A. Krishna[a], T. Biktagirov[a], D. Leitner[b], A. Kruse[c], H. Rezk[d], F. Hennhoefer[e], J. Löseke[a], M. Nowakowski[a], L. Fritsch[a], J. Steube[a], A. Schoch[a], H. Elgabarty[a], O. S. Bokareva[d], A. Neuba[a], H. Egold[a], R. Schoch[a], K.L. Franzke[a], U. Gerstmann[a], S. Hohloch[b], O. Kühn[c], B. Sarkar[e], S. Lochbrunner[c], W. G. Schmidt[a], M. Bauer[a]*

[a] Institute of Inorganic Chemistry and Center for Sustainable Systems Design (CSSD), Paderborn University, Warburger Str. 100, 33098 Paderborn, Germany.

[b] Department of General, Inorganic and Theoretical Chemistry, University of Innsbruck, Innrain 80-82, A-6020 Innsbruck, Austria

[c] Institute of Physics, University of Rostock, 18051 Rostock, Germany

[d] Leibniz Institute for Catalysis (LIKAT), 18059 Rostock, Germany

[e] Institute of Chemistry and Biochemistry, Inorganic Chemistry, Freie Universität Berlin, Kaiserswerther Str. 16-18, 14195 Berlin, Germany

*E-mail: **matthias.bauer@uni-paderborn.de**

Table of contents

Experimental Details

Materials and Methods

All experiments were carried out under an argon atmosphere using standard Schlenk or Glovebox techniques unless specified. Glassware was oven-dried at 130 °C prior to use. Dry solvents were obtained from an MBraun SPS-800 solvent-drying system, degassed *via* sparging with argon, and subsequently stored over a 4 Å molecular sieve. ^{1}H NMR spectra were recorded using Bruker Avance 500 and Bruker Ascent 700 spectrometers. Chemical shifts are expressed in parts per million (ppm, δ) downfield from tetramethylsilane (TMS). The spectra were referenced to the residual proton signals of the respective deuterated solvent. All coupling constants (J) are absolute values and are expressed in Hertz (Hz). The spectra were analyzed according to the first order. Electrospray ionization mass spectrometry spectra were recorded on a Waters Synapt G2 Quadrupole Time-of-Flight spectrometer, using acetonitrile as solvent.

For cyclic voltammetry, dry acetonitrile was obtained by passing HPLC-grade acetonitrile (Fisher) over a column of MP Biomedicals MP Alumina N - Super I, which was activated in an oven at 150 °C for multiple days. The cyclic voltammetry measurements were performed at room temperature in a 0.1 M [nBu$_4$N][PF$_6$] acetonitrile solution with an analyte concentration of 0.001 M under a solvent-saturated argon atmosphere. A three-electrode arrangement with a 1 mm Pt working electrode, a Pt wire counter electrode (both Metrohm), and an Ag/AgCl reference electrode (custom-built) was used with a Metrohm PGSTAT101 potentiostat. Ferrocene was added after the measurements as an internal standard. All potentials were referenced against the FcH$^{0/+}$ couple. The voltammograms were analysed using the NOVA software (version 2.1.3). The diagnostic criteria for reversibility were based on those proposed by Nicholson[1,2] and the Randles-Sevcik equation.[3,4]

Acetonitrile of spectroscopic grade (SPECTRONORM VWR Acetonitrile) was used as the solvent for steady-state absorption spectroscopy (c = 0.1 mM), which was recorded using quartz cuvettes (path length = 10 mm) with a Cary 50 or PerkinElmer Lambda 45 spectrometer.

EPR spectra were recorded from 5 mM solutions at 300 K using a Bruker Magnettech 5000 EPR spectrometer (microwave frequency, 9.46 GHz; microwave power, 5 mW; modulationamplitude, 0.5 mT).

Spectroelectrochemical measurements were performed at room temperature in an optically transparent cell (d = 1 mm) using a deoxygenated MeCN/0.1 M [nBu$_4$N][PF$_6$] solution and a Pt wire mesh working electrode (counter electrode: Pt wire). Spectral changes during oxidations/reductions were recorded on a Varian Cary 50 spectrophotometer.

Coulometric experiments were performed in a coulometric cell with an integrated Hellma cuvette (d = 1 mm) and following conditions: DCM/ 0.2 M NBu_4PF_6, platinum gauze working electrode (50 mesh), Ag/ 0.01 M $AgNO_3$, 0.2 M NBu_4PF_6 in MeCN as reference, and Pt wire counter electrode. The complex was first dissolved in 0.2 mL of MeCN and then added to the DCM solution. During oxidations/reductions, spectral changes were recorded on a Cary 50 spectrophotometer in the range of 190-1100 nm. All measurements were carried out at room temperature under an argon atmosphere, with absolute and vented solvents.

For steady-state emission spectroscopy at room temperature, acetonitrile of spectroscopic grade was used as the solvent. Steady-state emission spectra were recorded in 10 mm quartz cuvettes on an Edinburgh Instruments FLS1000 spectrometer with single monochromators and a red-extended PMT-980 and an InGaAs IR detector. The solutions for the measurements under argon were degassed using the freeze-pump-thaw technique. Low-temperature emission spectroscopy was performed in butyronitrile at 77 K.

Transient absorption spectra were recorded with a time resolution of about 100 fs employing a pump-probe setup based on a Ti:sapphire laser system (CPA-2001, Clark MXR), which operates at a centre wavelength of 775 nm and a repetition rate of 1 kHz. The excitation pulses with a center wavelength of 335 nm were obtained by frequency doubling the output of a noncollinear optical parametric amplifier (NOPA) pumped by the Ti:sapphire system and tuned to 650 nm in a 100 µm thick BBO crystal.[5] The dispersion of the NOPA pulses was minimized by a compressor based on fused silica prisms prior to frequency doubling. For the probe pulses, a white light continuum was generated in a CaF_2 crystal. To avoid effects caused by orientational relaxation, the polarizations of the pump and probe pulses were set at a magic angle with respect to each other. Behind the sample, the probe was dispersed by a prism, and the spectrally resolved absorption changes were recorded by a photodiode array detector. The compounds were dissolved in MeCN and DCM under argon, and the sample solutions were filled into a fused silica cuvette with a thickness of 1 mm.

The presented X-ray single crystal data were measured on a *Bruker* Venture D8 three-cycle diffractometer equipped with a Mo K_α µ-source (λ=0.71073 Å), an *Incoatec* multilayer monochromator, and a Photon III detector at 120 K. The data were integrated with SAINT, and afterwards a multi-scan absorption correction was applied using SADABS. [6] Structure solution was achieved by direct methods in SHELXT, and structure refinement was conducted using full-matrix least squares refinement based on F^2. [7]

3,5-Dibromo-N, N-dimethylaminophenylene was synthesized according to the literature.

The headspace analysis was performed by a mass spectrometer (MS)HPR-20 EGA Gas Analysis System (Hiden Analytical). The MS was flushed with Ar (5.0), and the background was measured

during the Ar flow. Respective blank measurements for the reagents were also done prior to the measurement.

Computational details

All (TD)DFT calculations were performed using the ORCA package (6.0.0[8] for EPR, 5.0.3 [9] for TPSSH UV-Vis and X-ray spectra, and ORCA 4.2.1 software package[9,10]). For radical systems, an open-shell UKS method was used. Solvent effects (for tetrachloroethane, MeCN, or dichloromethane) were modeled using the conductor-like polarizable continuum model (CPCM).

Initially, the **ground state geometries** (singlet for $[Co(ImP^{NMe2})_2]^+$ and doublet for $[Co(ImP^{NMe2})_2]^{2+}$ were optimized using the PBEh-3c composite method[11]. The local minima were confirmed via vibrational frequency analysis as the only occurring negative frequencies of -14 cm^{-1} and -12 cm^{-1} for $[Co(ImP^{NMe2})_2]^+$, as well as -34 cm^{-1} and -14 cm^{-1} found for $[Co(ImP^{NMe2})_2]^{2+}$ can be attributed to rotating methyl groups. The same set of small imaginary frequencies was found with the LC-BLYP functional (see below). This finding is attributed to the convergence and grid settings in ORCA. Reoptimizing the geometry with Gaussian 16 at the same level of theory led to imaginary-frequency-free minima with an RMSD of 0.0126 Å between two different optimizations and no visual differences.

The r2SCAN exchange-correlation functional [12] was employed in conjunction with the def2-TZVP basis set to compute ***g*- and HF tensors**. [13]

For calculations of X-Ray spectra, the geometry was first optimized using the composite PBEh-3c approach [14], including the atom-pairwise dispersion correction with the Becke-Johnson damping scheme (D3BJ) [14–16] and the geometrical counterpoise correction gCP [14] along with the def2-mSVP basis set and def2/J auxiliary basis set [17]. The TDDFT transitions were obtained via TPSSh functional [18] with D4 dispersion correction [19,20] def2-TZVPP basis set [21], modified with CP(PPP) extended orbital basis for Co to improve accuracy, and def2/J auxiliary basis set. The obtained transitions were broadened with 1.5 eV broadening to account for the experimental resolution and natural linewidth of observed transitions.

The UV-Vis spectra were calculated via TDDFT calculations using the same approach as for X-Ray spectra: TPSSH[14]/def2-TZVP[15] level of theory, imposing the tight convergence criterion, and D4 dispersion correction.[20,22,23] The first 150 vertical transitions in acetonitrile were computed. Further, an (arbitrary) shift of 250 cm^{-1} $[Co(ImP^{NMe2})_2]^+$ or 50 cm^{-1} $[Co(ImP^{NMe2})_2]^{2+}$ to the red region of the spectrum was applied to improve the match to the experimental UV-Vis spectrum.

For excited-states dynamics, the optimally-tuned, two-parameter long-range corrected functional LC-BLYP[24]**[ref]** (particularly suited for all charge-transfer properties) together with a mixed basis set (def2-TZVP[15] for cobalt and 6-311G(d,p) for all other atoms) was employed. The functional was tuned using the ΔSCF method[25–27], yielding parameters of α = 0 (short-range exact

exchange) and a long-range separation parameter of 0.15 $Bohr^{-1}$. TDDFT calculations were conducted in dichloromethane PCM solvent. **Tully Surface Hopping (TSH) simulations** were carried out using the SHARC 3.1[28] using the linear vibronic coupling Hamiltonian. To determine the linear vibronic coupling (LVC) parameters, electronic structure calculations were performed at the Franck–Condon (FC) geometry and at distorted geometries along selected vibrational modes. Two-sided displacements of $\Delta q_i = \pm 0.05$ were applied using numerical differentiation.

Synthesis and Characterization

Synthesis of Ligand Precursor

A mixture of 3,5-Dibromo-N, N-dimethylaminophenylene (2.82 g, 10.1 mmol), imidazole (1.72 g, 25.3 mmol), CuO (322 mg, 4.05 mmol), and K_2CO_3 (3.49 g, 25.3 mmol) in DMSO (50 mL) was reacted at 150 ºC for 72 hrs. The solvent was removed under vacuum at 100 ºC. The remaining solid was extracted in 500 mL of EtOAc and filtered through a short silica pad. The filtrate was concentrated in vacuum. The residue was passed through a silica gel column (CH_2Cl_2/MeOH = 10/1, v/v)

The product was obtained as a pale yellow solid. (1.82 g, 7.2 mmol, 72 % yield).

^{1}H NMR (700 MHz, DMSO) δ = 8.37 (t, J = 1.1 Hz, 2H), 7.86 (d, J = 1.4 Hz, 2H), 7.15 (t, J = 1.8 Hz, 1H), 7.11 (s, 2H), 6.83 (d, J = 1.9 Hz, 2H), 3.04 (s, 6H). **^{13}C NMR** (176 MHz, DMSO) δ 152.13, 138.73, 135.83, 129.61, 118.30, 101.73, 99.61, 40.42. **Elemental Analysis** (calculated, experimental for $C_{14}H_{15}N_5$): C (66.38, 66.47), H (5.97, 6.18), N (27.65, 27.55).

Synthesis of Ligand $LNMe_2$

Ligand precursor (1.0 g, 3.95 mmol) was dissolved in acetonitrile before methyl iodide (15.8 mmol, 0.98 mL) was added. The solution was refluxed for 16 h at 85 ˚C. After letting the suspension cool to room temperature, the volatiles were evaporated under reduced pressure. The resulting mixture was subsequently washed with acetone (3x30 mL) and diethyl ether (3x30 mL) alternatively, before drying under vacuum.

The product was obtained as a colorless solid. (1.46 g, 2.72 mmol, 68.8 % yield).

^{1}H NMR (700 MHz, DMSO) δ 9.90 (q, J = 0.9 Hz, 2H), 8.35 (s, 2H), 8.00 (t, J = 1.8 Hz, 2H), 7.41 (t, J = 1.9 Hz, 1H), 7.17 (d, J = 1.8 Hz, 2H), 3.98 (s, 6H), 3.11 (s, 6H). **^{13}C NMR** (176 MHz, DMSO) δ 152.13, 138.73, 135.83, 129.61, 118.30, 101.73, 99.61, 40.42. **Elemental Analysis** (calculated, experimental for $C_{16}H_{21}N_5I_2$): C (35.77, 35.77), H (3.94, 4.15), N (13.04, 13.10).

Synthesis of Complex $[Co(ImP^{NMe2})_2][BF_4]$

The ligand (0.372 mmol) and tetrakis(dimethylamino)zirconium (250 mg, 0.93 mmol) were suspended in dry DCM (10 mL) in a glovebox. The yellow suspension was allowed to stir for 1 h before cobalt(II) chloride (53 mg, 0.41 mmol) was added. The mixture was allowed to stir for another 16 h. The dark green mixture was worked up under ambient atmosphere. Initially, water (1 mL) was added to quench the reaction. The suspension was filtered through a cotton pad and through a porous glass frit. The respective filter cakes were washed with DCM (10 mL) thrice. The red solution was evaporated under reduced pressure, followed by washing of the resulting yellow solid in hexane (3x 30 mL). The solid was dissolved in minimal methanol before dropping it into a saturated KBF_4 solution. The compound was precipitated out of the solution and filtered off. The resulting precipitate was dissolved in minimal DCM and crystallized out by vapour diffusion using pentane as the counter-solvent. The crystallization process was carried out under dark conditions.

The product was obtained as yellow crystals. (81 mg, 0.13 mmol, 35.1 % yield).

^{1}H NMR (700 MHz, $C_2D_2Cl_4$) δ 7.43 (d, J = 2.0 Hz, 1H), 6.72 (s, 1H), 6.53 (d, J = 2.0 Hz, 1H), 3.03 (s, 3H), 2.52 (s, 3H). **^{13}C NMR** (176 MHz, $C_2D_2Cl_4$) δ 186.91, 148.12, 123.67, 114.39, 94.41, 42.41, 35.83. **Elemental Analysis** (calculated, experimental for $C_{35}H_{48}N_{10}BF_4Co$ with 1 DCM molecule): C (50.09, 49.67), H (4.84, 5.00), N (17.70, 17.70).

Synthesis of Complex $[Co(ImP^{NMe2})_2]^{2+}$

0.5 mM solution of $[Co(ImP^{NMe2})_2][BF_4]$ was dissolved in 3 mL of $C_2D_2CL_4$ and irradiated for 10 minutes using a sun-simulator with a long pass filter of 330 nm. The initial yellow color solution gradually changes into a dark purple solution. UV-Vis spectra of the solution were also measured at 2-minute intervals to check the completion of the product formation.

^{1}H NMR (700 MHz, $C_2D_2Cl_4$) δ 7.38 (s, 1H), 6.47 (s, 1H), 2.66 (s, 3H). **^{13}C NMR** (176 MHz, $C_2D_2Cl_4$) δ 124.32, 120.58, 114.33, 36.16.

List of Investigated Substrates

Table S1: List of electron acceptors tested. Acceptors with * were monitored using UV-Vis absorption spectroscopy and checked for the formation of the absorption bands at 570 nm and 900 nm. Acceptors without * were monitored using NMR spectroscopy.

Substrate	Conditions (r.t.)	Observations
Dichloromethane	Irradiation for 3h	Broadening of aryl and aminyl hydrogen in 1H NMR (Fig. S10)
Chloroform in MeCN	Irradiation for 3h	Complete disappearance of aryl and aminyl peaks in 1H NMR (Fig. S11)
1,1,2,2 Tetrachloroethane	Irradiation for 1h	Complete disappearance of aryl and aminyl peaks along with notable chemical shift of all peaks (Fig. S13-S15)

Carbon Tetrachloride in MeCN	Irradiation for 5 mins	Complete disappearance of aryl and aminyl peaks along with chemical shifts of peaks (Fig. S12)
$K_2S_2O_8$ in MeCN	30 minutes	Complete disappearance of aryl and aminyl peaks along with notable chemical shift of all peaks (Fig. S18-S21)
Acetone*	Irradiation for 3h	No Changes observed
Methyl Viologen in MeCN*	Irradiation for 3h	No Changes observed
Chloranil in MeCN*	≤1 minute	Changes observed in UV-Vis without irradiation. (Fig. S1)
DDQ in MeCN*	≤1 minute	Changes observed in UV-Vis without irradiation. (Fig. S2)
Nitrobenzene in MeCN*	Irradiation for 3h	No Changes observed
Tetracyanoethylene in MeCN*	≤1 minute	Instant degradation
Benzoquinone in MeCN*	Irradiation for 3h	No Changes observed
Maleic acid in MeCN*	Irradiation for 3h	No Changes observed

UV-Vis Spectra for electron acceptor investigation

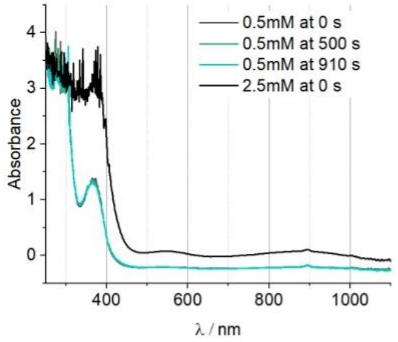

Figure S1: Absorption spectra of the electron acceptor test for chloranil. 50 µM solution of $[Co(ImP^{NMe2})_2]^+$ containing 0.5 mM of chloranil was illuminated for 910 seconds. The spectra remained unchanged from 0 to 910 seconds, but formation of very low-intense absorption bands at 570 nm and 900 nm was observed. These were confirmed by using a 2.5 mM solution.

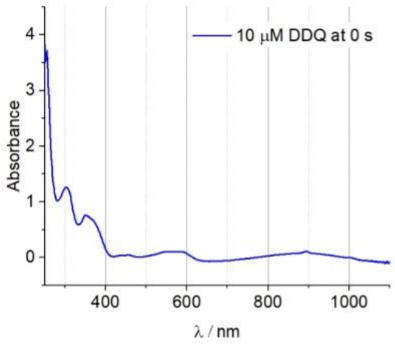

Figure S2: Absorption spectra of the electron acceptor test for DDQ. 10 µM solution of $[Co(ImP^{NMe2})_2]^+$ containing 10 µM of DDQ was measured. Formation of bands at 570 nm and 900 nm was already observed before irradiation.

NMR Spectra

NMR Spectra of Ligand and Ligand Precursor

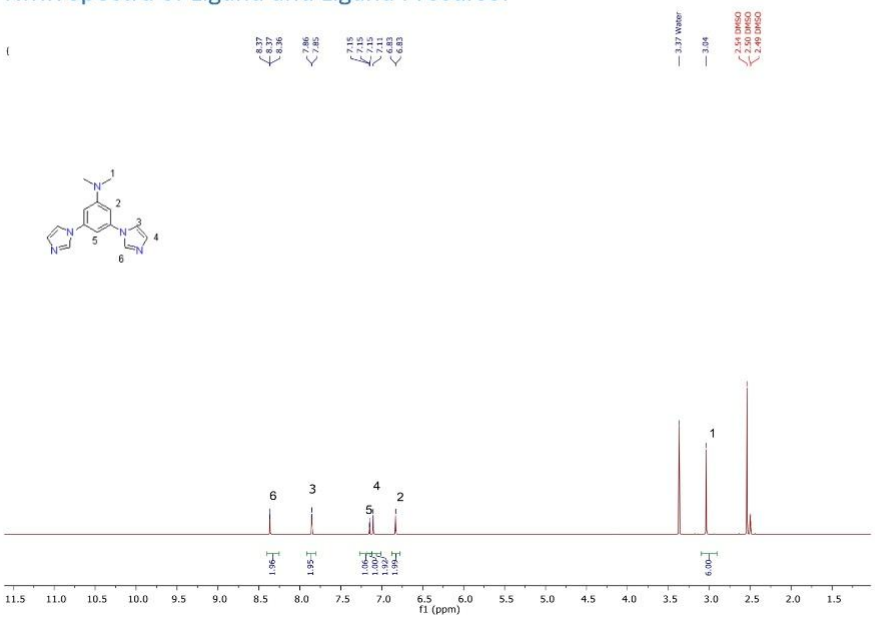

Figure S3: ^{1}H-NMR spectrum of 3,5-di(1H-imidazol-1-yl)-N,N-dimethylaminophenylene in DMSO.

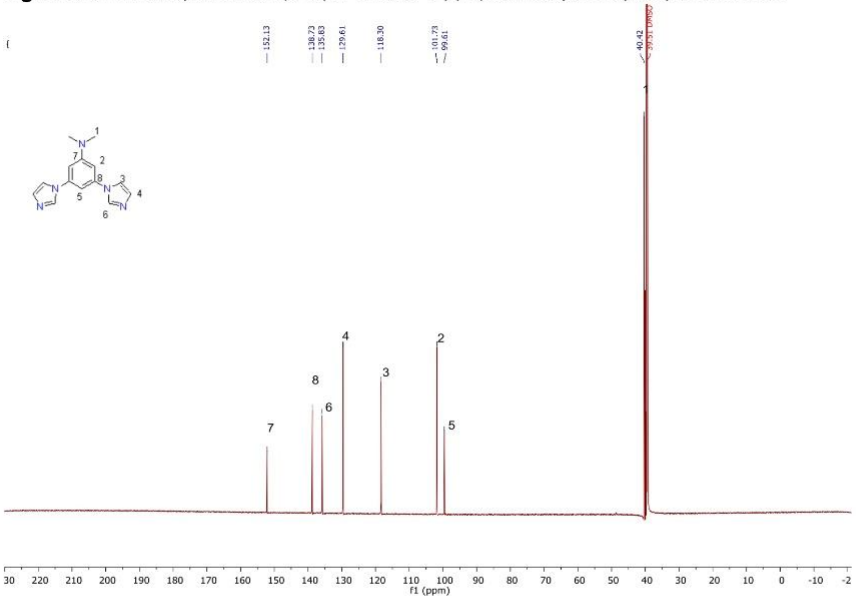

Figure S4: ^{13}C-NMR spectrum of 3,5-di(1H-imidazol-1-yl)-N,N-dimethylphenylene in DMSO.

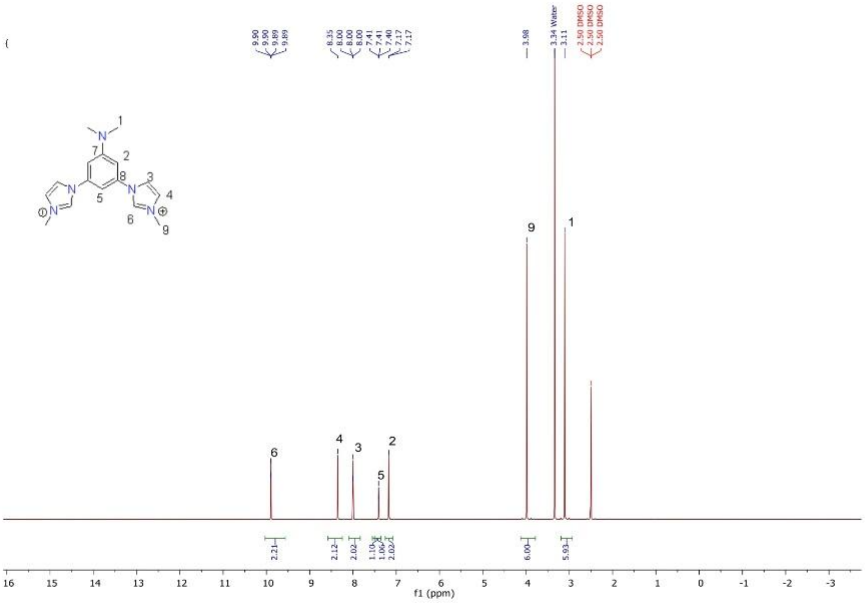

Figure S5: ^{1}H-NMR spectrum of $LNMe_2$ in DMSO.

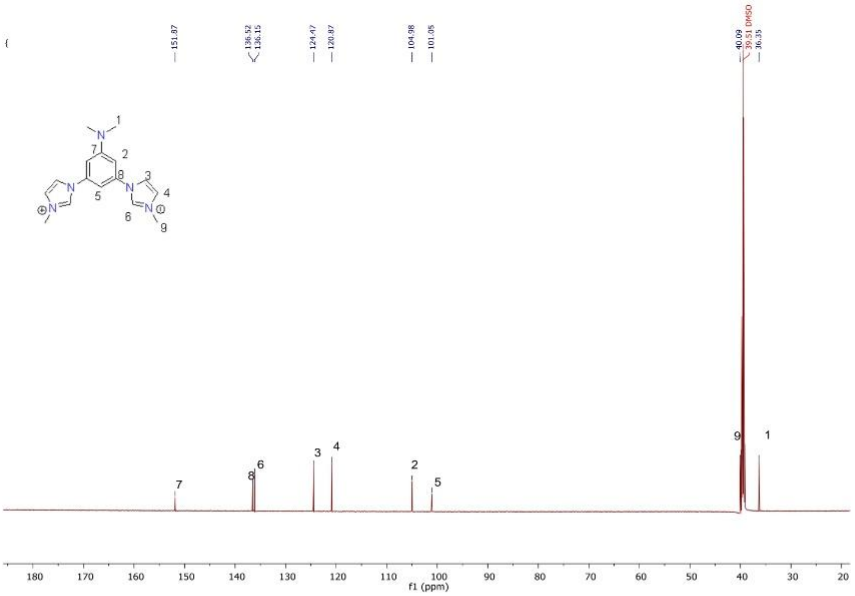

Figure S6: ^{13}C-NMR spectrum of $LNMe_2$ in DMSO.

NMR Spectra of Complexes

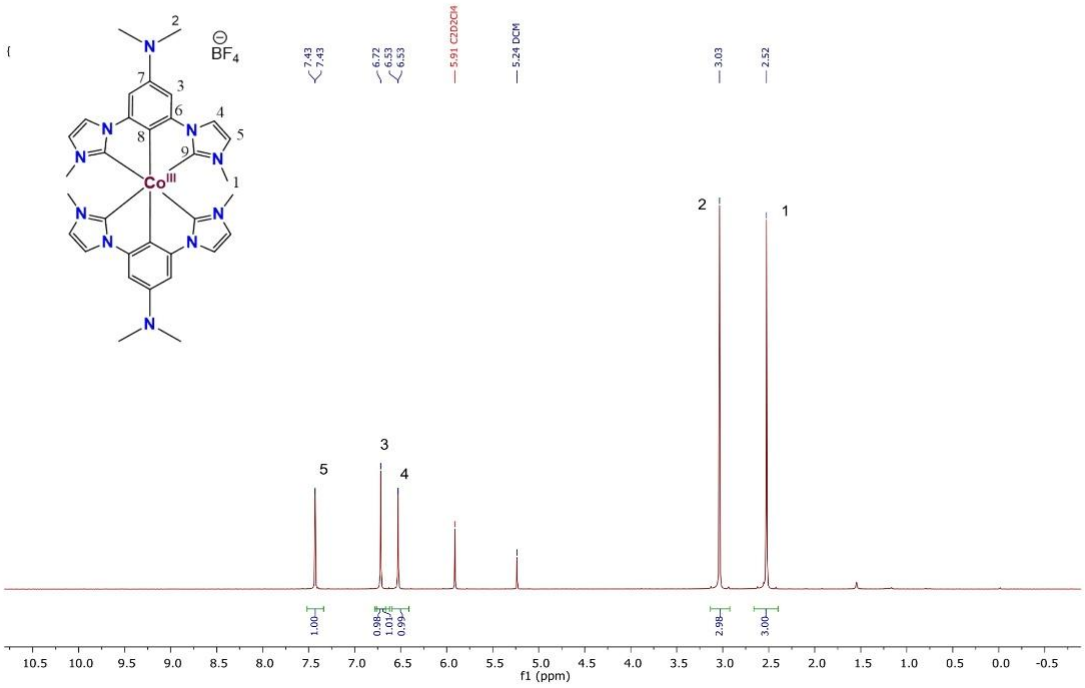

Figure S7: 1H-NMR spectrum of $[Co(ImP^{NMe2})_2][BF_4]$ in $C_2D_2Cl_4$.

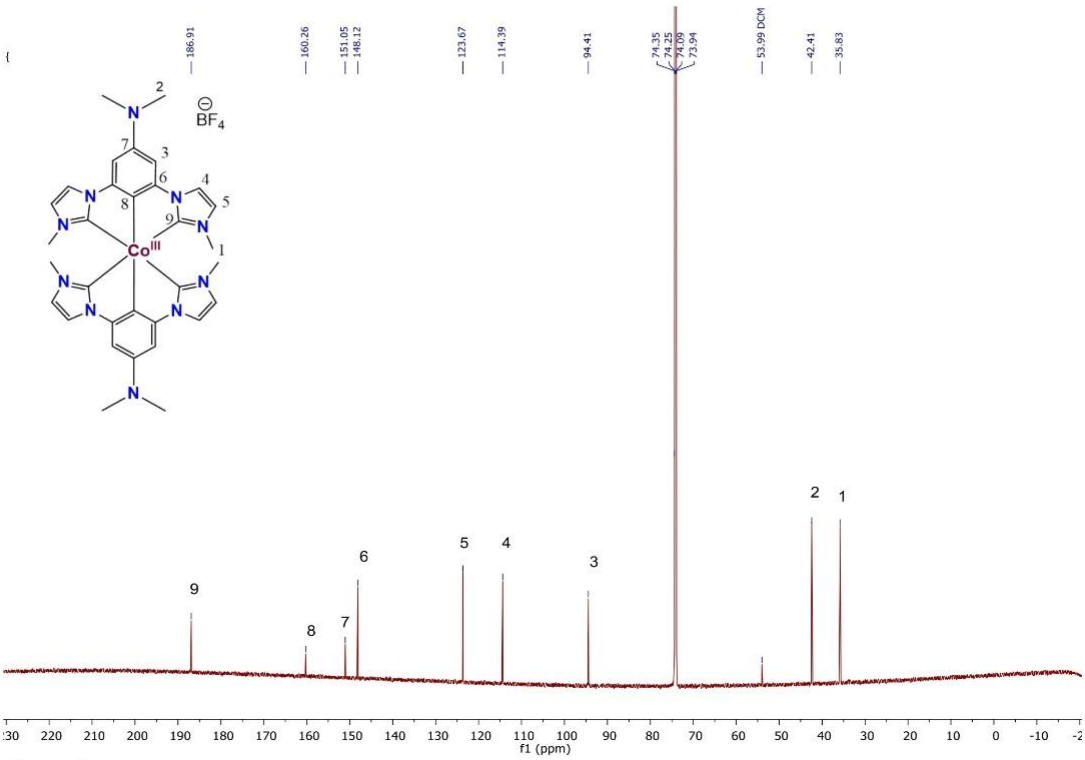

Figure S8: ^{13}C-NMR spectrum of [Co(ImP^{NMe2})$_2$][BF_4] in $C_2D_2Cl_4$.

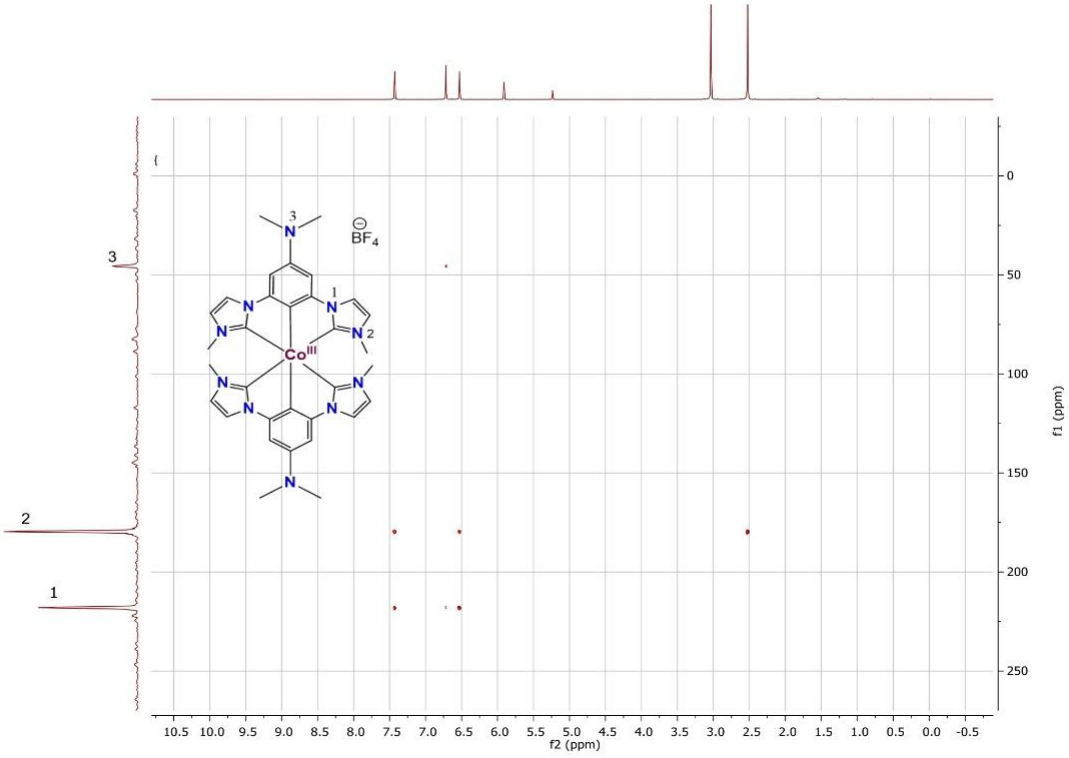

Figure S9: ^{15}N HMBC of $[Co(ImP^{NMe2})_2][BF_4]$ in $C_2D_2Cl_4$.

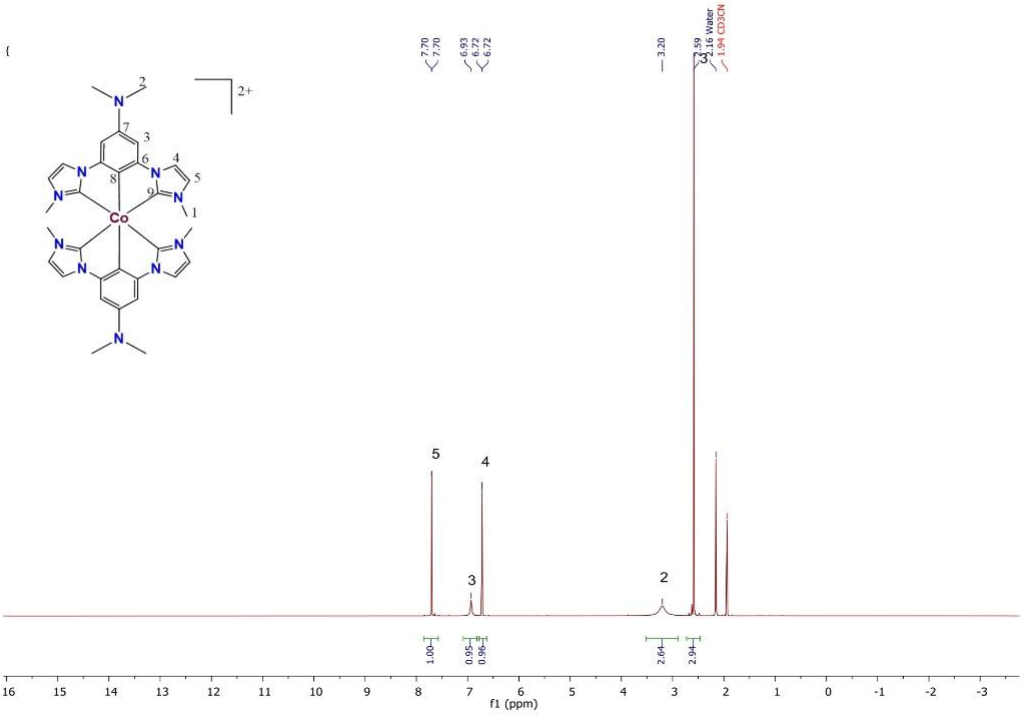

Figure S10: ^{1}H-NMR spectrum of $[Co(ImP^{NMe2})_2]^{2+}$ in CD_3CN after irradiation in CH_2Cl_2.

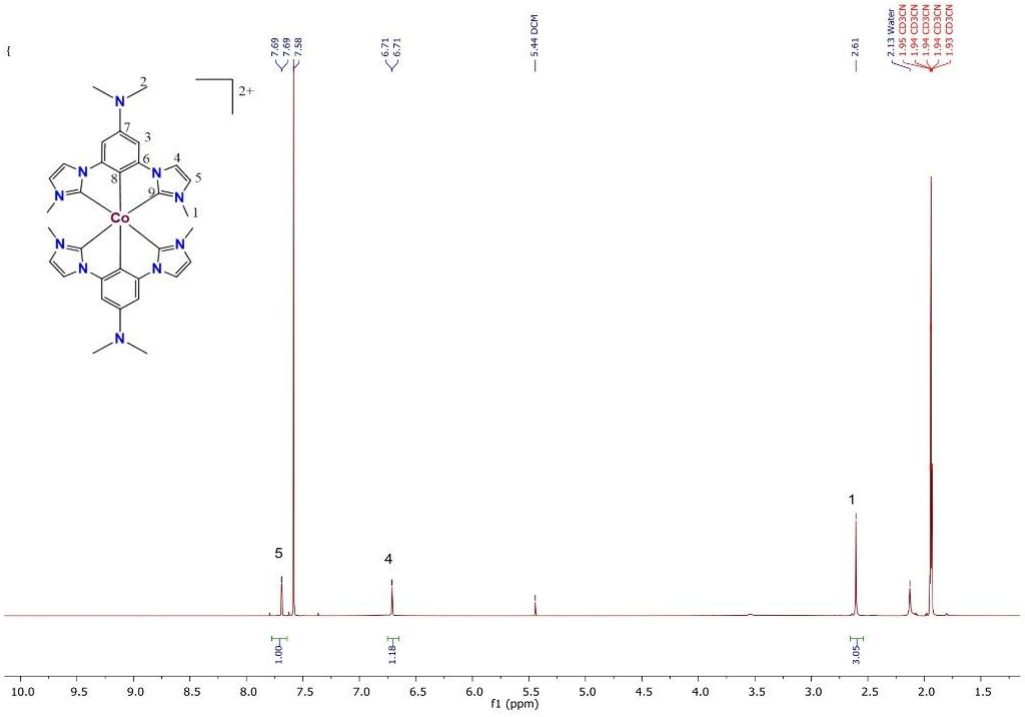

Figure S11: ^{1}H-NMR spectrum of $[Co(ImP^{NMe2})_2]^{2+}$ in CD_3CN with 1 µL of $CHCl_3$.

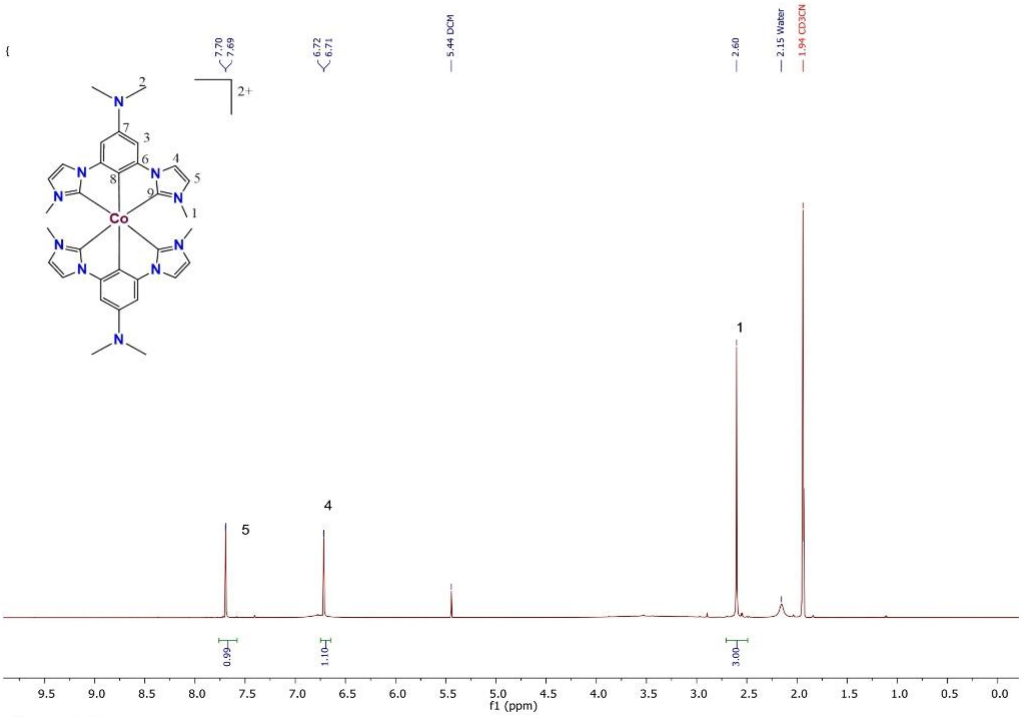

Figure S12: ^{1}H-NMR spectrum of $[Co(ImP^{NMe2})_2]^{2+}$ in CD_3CN with 1 µL of CCl_4.

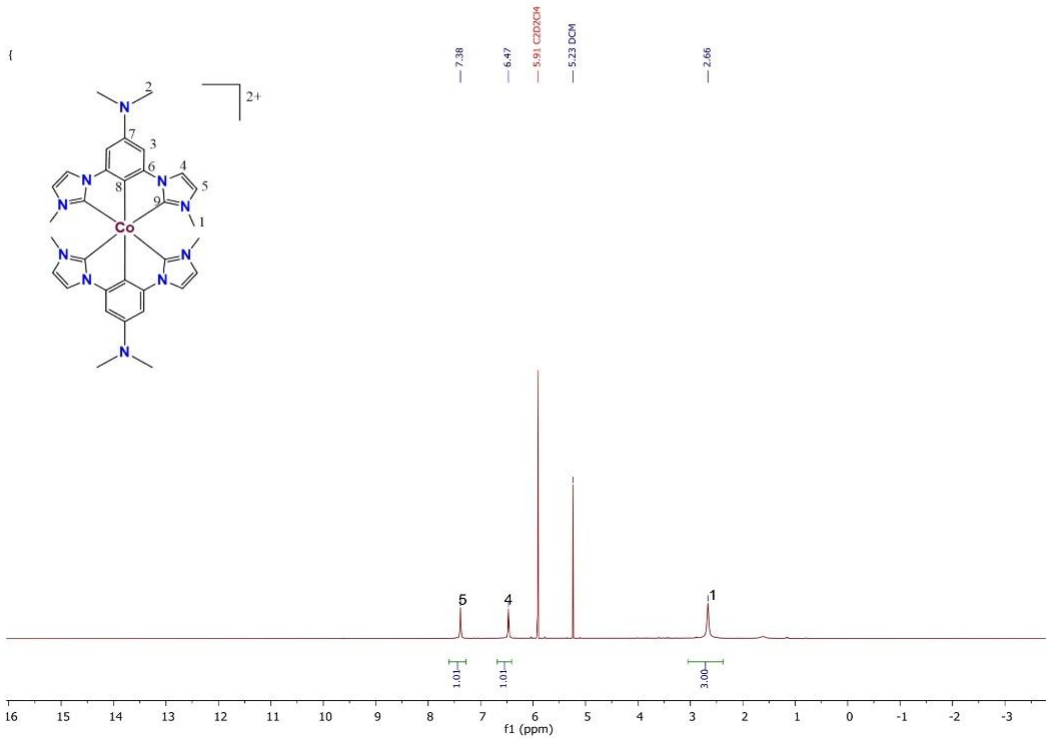

Figure S13: ^{1}H-NMR spectrum of $[Co(ImP^{NMe2})_2]^{2+}$ $C_2D_2Cl_4$.

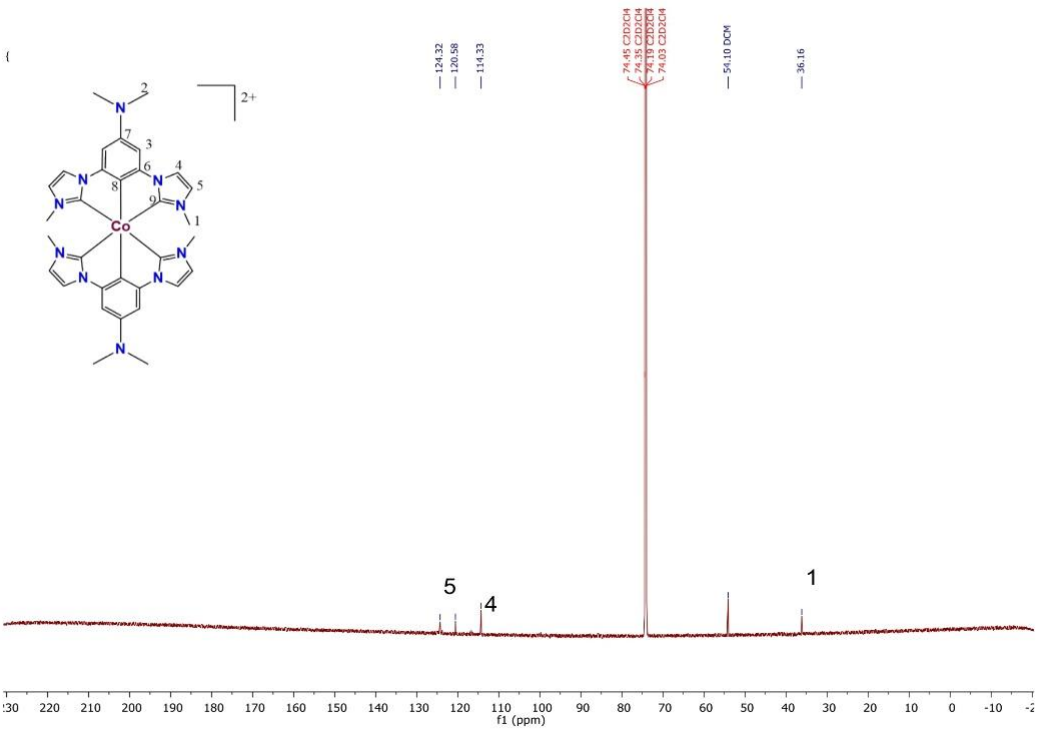

Figure S14: ^{13}C-NMR spectrum of $[Co(ImP^{NMe2})_2]^{22+}$ in $C_2D_2Cl_4$.

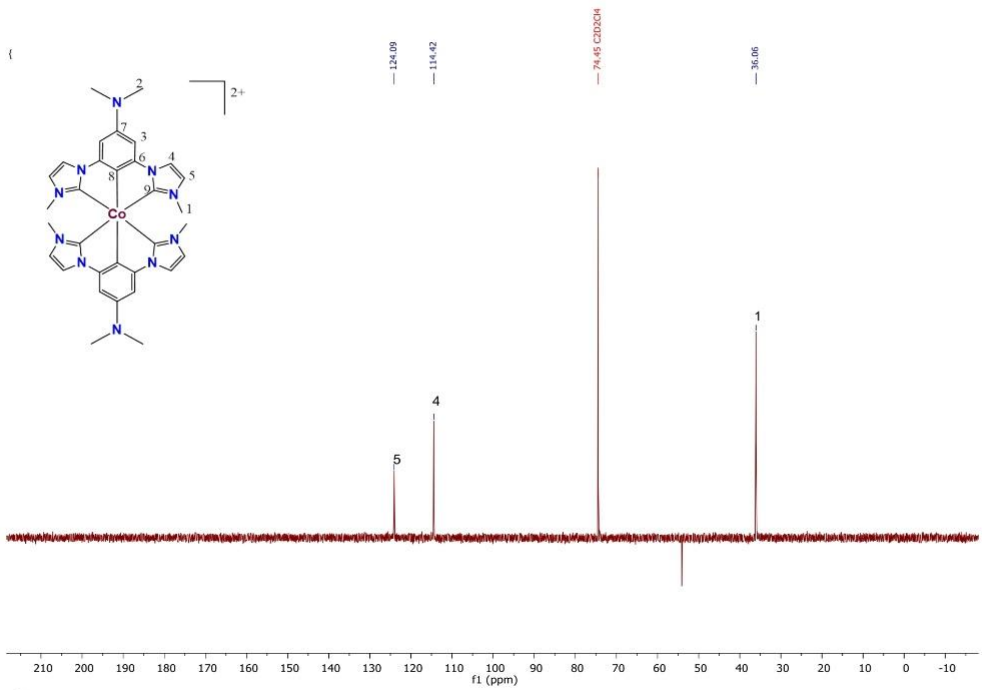

Figure S15: ^{13}C-DEPT NMR of $[Co(ImP^{NMe2})_2]^{2+}$ in $C_2D_2Cl_4$.

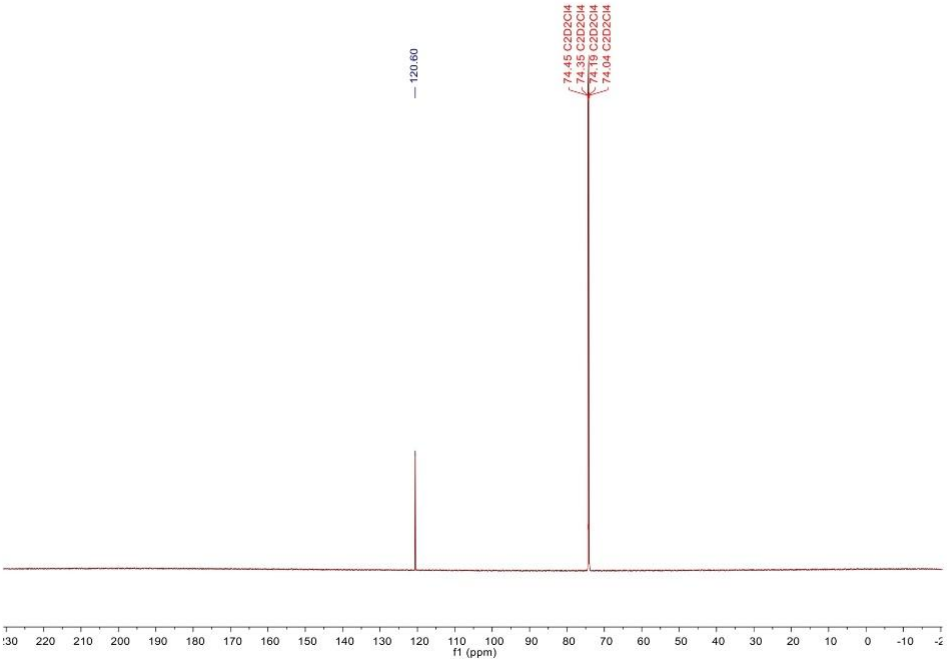

Figure S16: ^{13}C NMR of C_2Cl_4 in $C_2D_2Cl_4$.

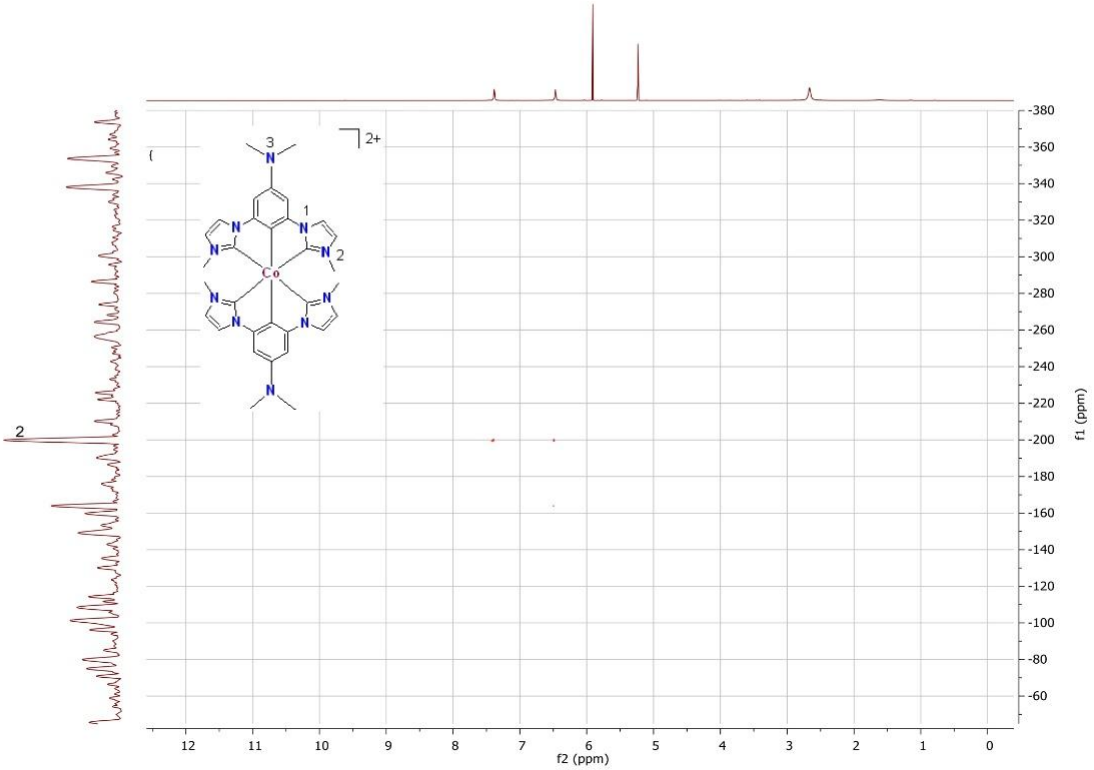

Figure S17: ^{15}N-HMBC NMR spectrum of $[Co(ImP^{NMe2})_2]^{2+}$ in $C_2D_2Cl_4$.

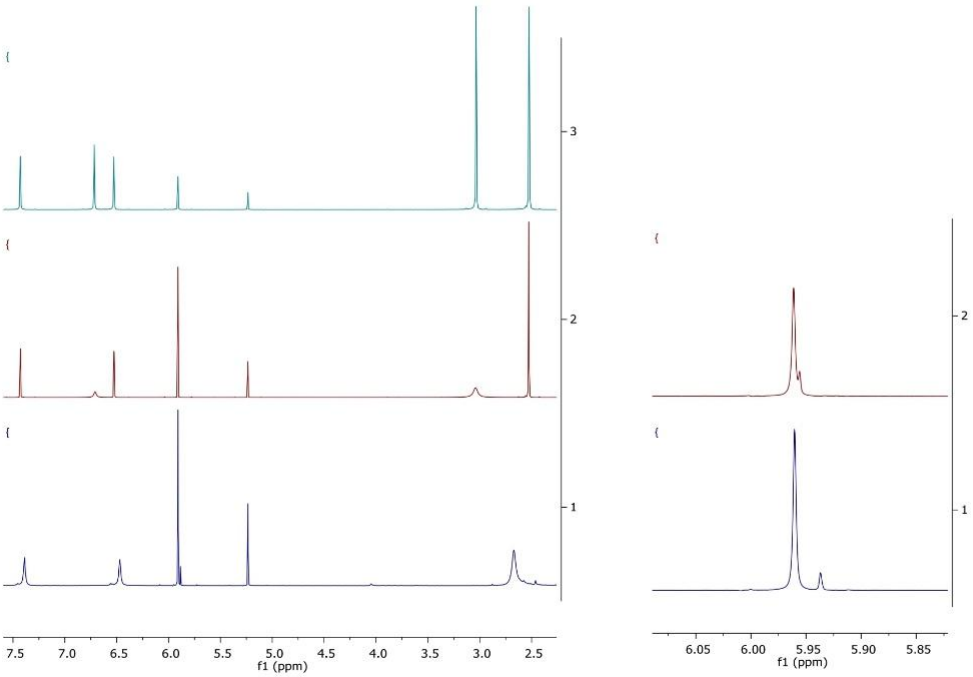

Figure S18: ^{1}H NMR spectrum of $[Co(ImP^{NMe2})_2]^+$ to $[Co(ImP^{NMe2})_2]^{2+}$ in $C_2D_2Cl_4$ in 5 min intervals of irradiation (top to bottom) recorded with a capillary of $C_2D_2Cl_4$ inside the NMR tube to measure the effective magnetic moment of the solution.

Table S2: Relevant NMR shifts.

	$[Co(ImP^{NMe2})_2]^+$		$[Co(ImP^{NMe2})_2]^{2+}$	
Data in ppm	**^{1}H NMR**	**^{13}C NMR**	**^{1}H NMR**	**^{13}C NMR**
a	6.72	94.41	-	-
b	6.53	114.39	6.47	114.3
c	7.43	123.67	7.38	124.3
d	3.03	42.41	-	-
e	2.52	35.83	2.66	36.16

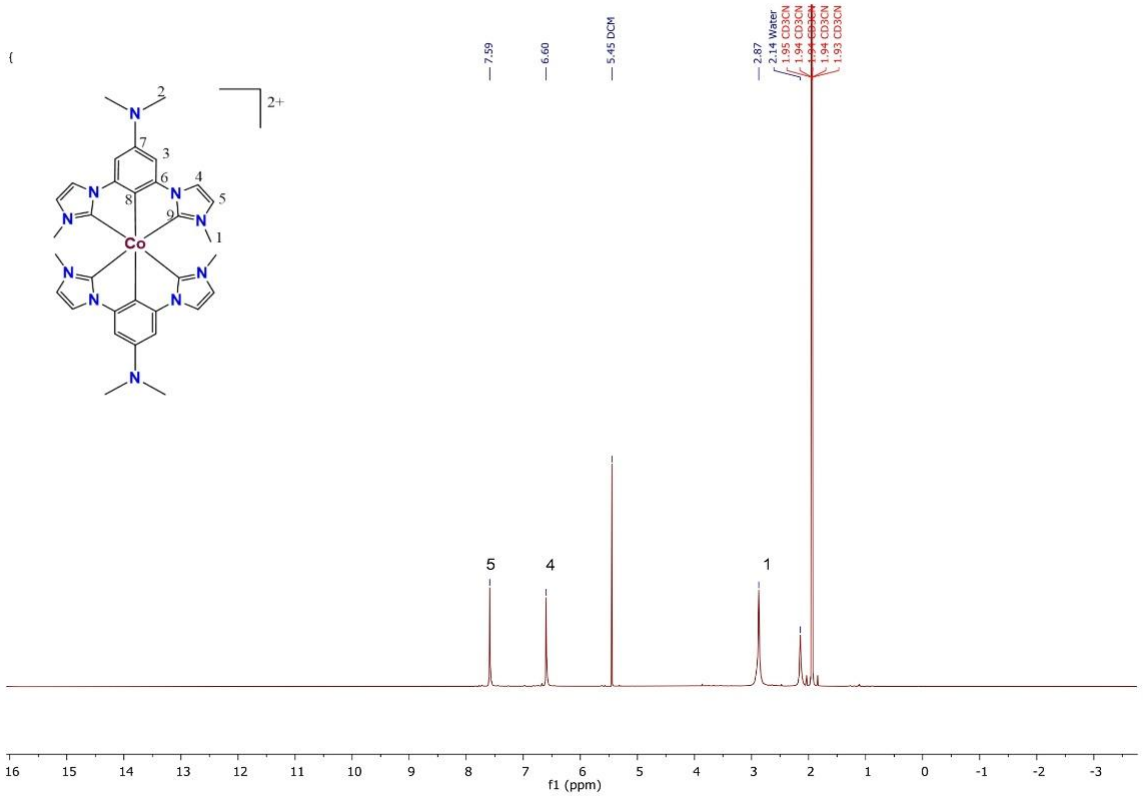

Figure S19: ^{1}H-NMR spectrum of $[Co(ImP^{NMe2})_2]^{2+}$ in CD_3CN after oxidation with $K_2S_2O_8$.

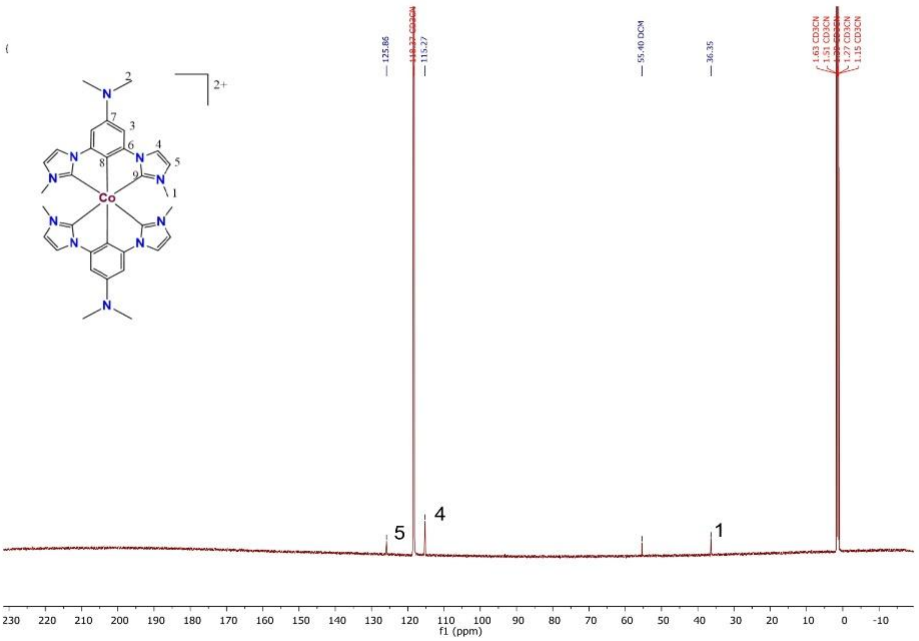

Figure S20: ^{13}C-NMR spectrum of $[Co(ImP^{NMe2})_2]^{2+}$ in CD_3CN after oxidation with $K_2S_2O_8$.

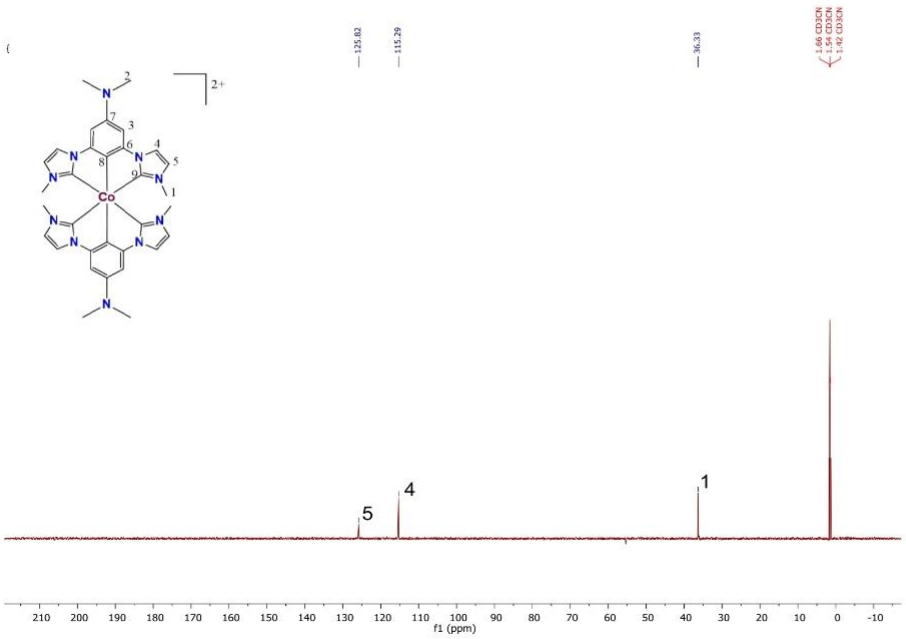

Figure S21: ^{13}C DEPT-NMR spectrum of $[Co(ImP^{NMe2})_2]^{2+}$ CD_3CN after oxidation with $K_2S_2O_8$.

Mass Spectra

Mass Spectra of Ligand and Ligand Precursor

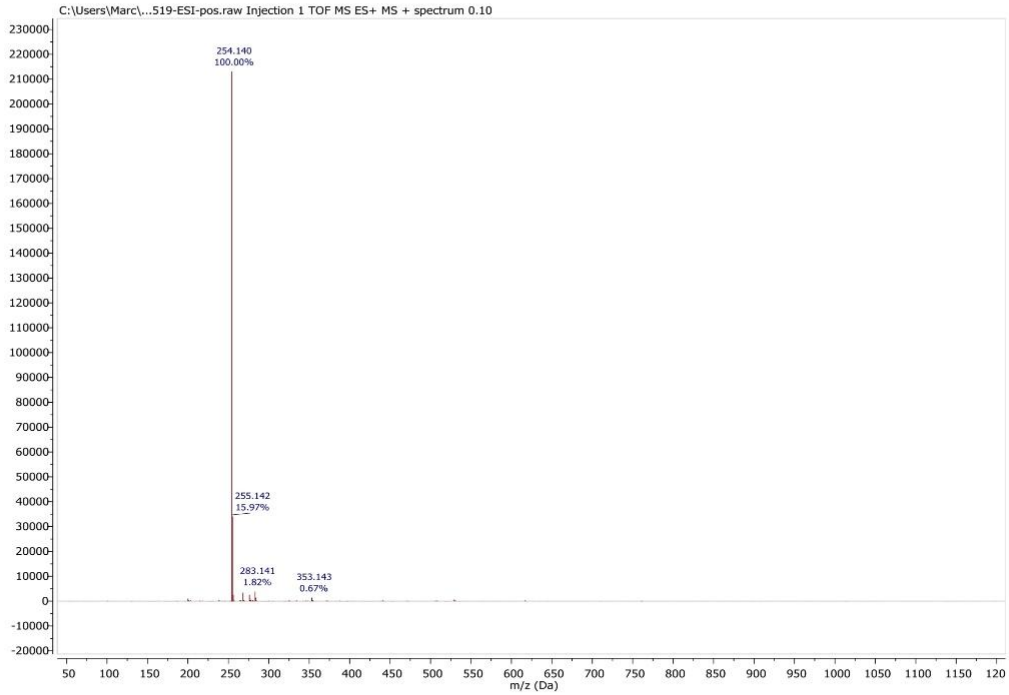

Figure S22: Mass Spectra of Ligand precursor.

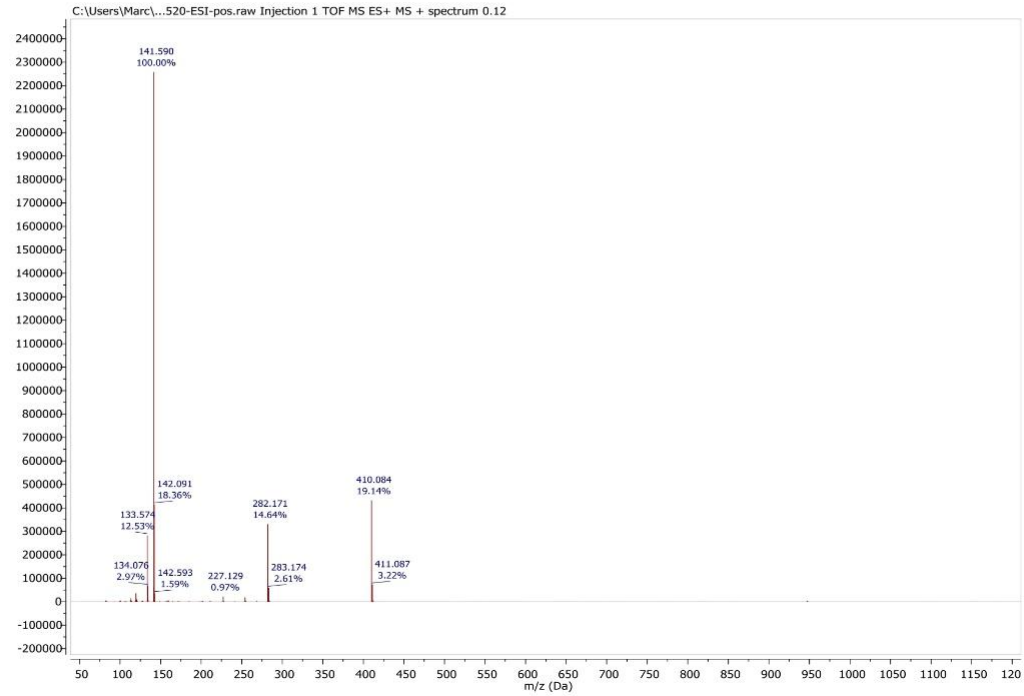

Figure S23: Mass Spectra of Ligand. 282.171 is the ligand with one positive charge, and 410.084 is the aggregation with the Iodide anion.

Mass Spectra of $[Co(ImP^{NMe2})_2][BF_4]$

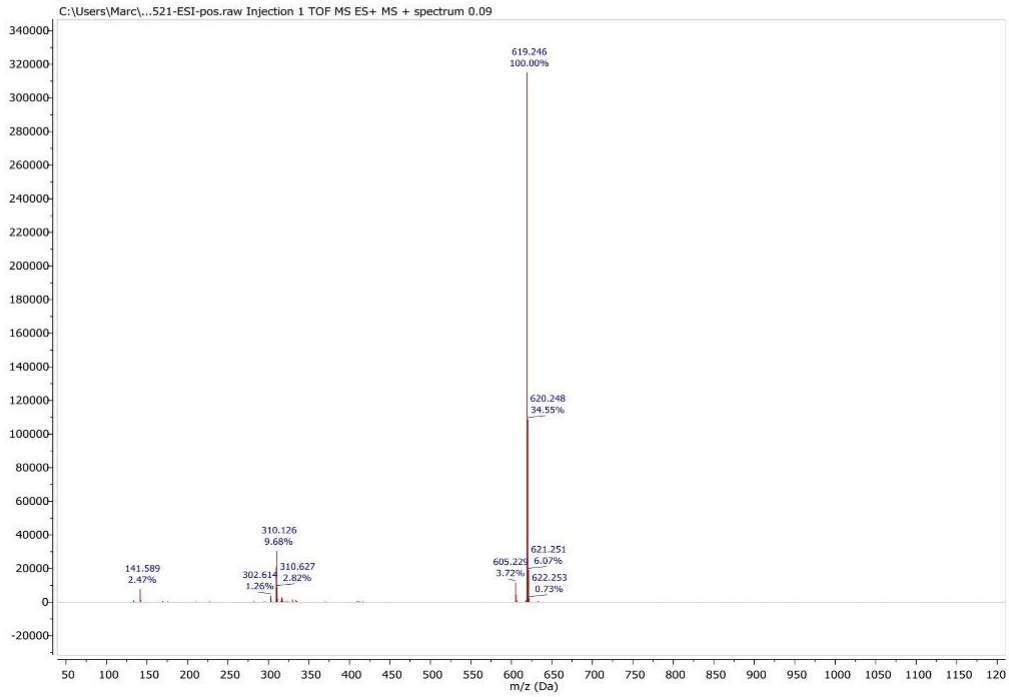

Figure S24: Mass Spectra of Complex. 310.126 is the complex with two positive charges.

EPR Spectra

Experimental results

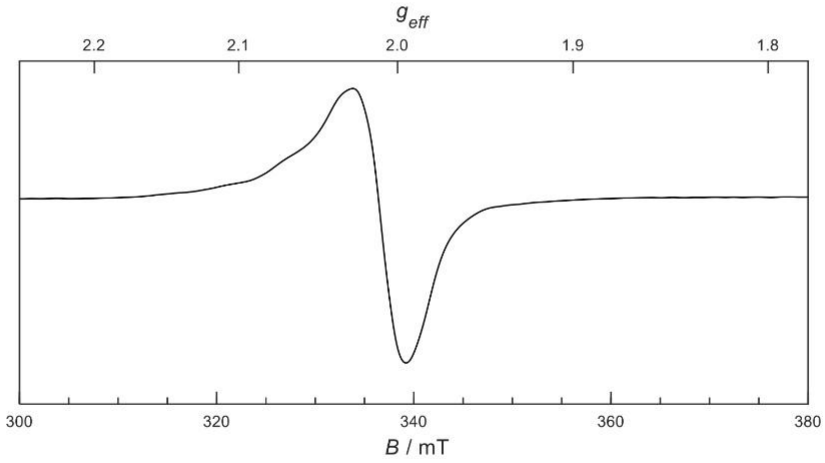

Figure S25: EPR spectrum of the complex measured in TeCA, frozen (98 K) and irradiated for 60 s.

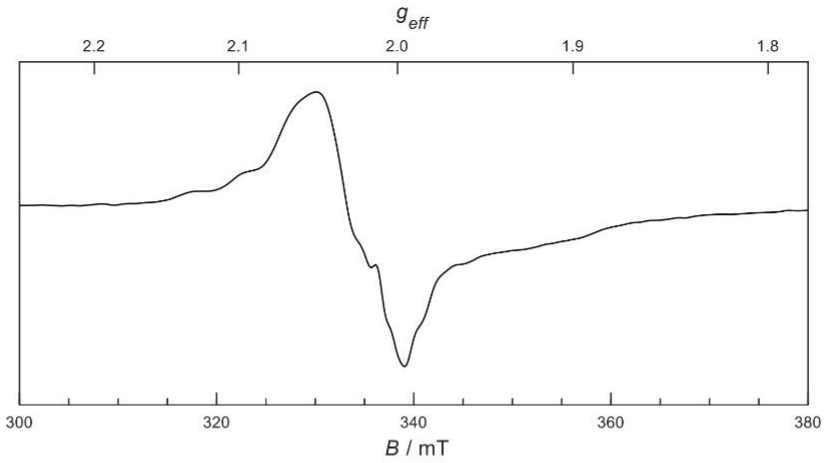

Figure S26: EPR spectrum of the complex measured in MeCN, frozen (98 K) and irradiated for 60 s.

Theoretical modelling

CW EPR powder simulations were carried out using the EasySpin toolbox [29] in MATLAB. The EPR spectrum was modeled as a superposition of two spin centers. The first component, $[Co(ImPN)_2]^{2+}$, was simulated using the following spin Hamiltonian:

$$\hat{H} = \mu_B B \cdot g \cdot \hat{S} + \hat{S} \cdot A_{HF} \cdot \hat{I}$$

that includes anisotropic Zeeman interaction (first term) and anisotropic HF interactions between the electron spin and the ^{59}Co nuclear spin (second term). Here, $\hat{S}$ and $\hat{I}$ are the electron spin and ^{59}Co nuclear spin operators (with the eigenvalues of S = 1/2 and I = 7/2), **g** is g-tensor, A_{HF} is the ^{59}Co HF coupling tensor, μ_B is the Bohr magneton, and B is the applied magnetic field. DFT-derived principal values of **g** and A_{HF} (Table S2) were used as a starting point and refined during spectral fitting.

The second component, tentatively attributed to exchange-coupled $[Co(ImPN)_2]^{2+}$clusters, was simulated assuming isotropic Zeeman interaction only, using a single average g-value. Final spin Hamiltonian parameters for both species are listed in Table S2.

Table S3. DFT-calculated and fitted spin Hamiltonian parameters: principal components of the g-tensor (g_{xx}, g_{yy}, g_{zz}), isotropic g-value (g_{iso}; defined as an average of g_{xx}, g_{yy}, and g_{zz}), and ^{59}Co HF tensor (A_{xx}, A_{yy}, A_{zz}).

	g-tensor		^{59}Co HF coupling, MHz
	g_{xx}, g_{yy}, g_{zz}	g_{iso}	A_{xx}, A_{yy}, A_{zz}
DFT			
$[Co(ImP^{NMe2})_2]^{2+}$	2.0026, 2.0407, 2.0827	2.0421	–22.72, 88.06, 142.23
Simulation			
$[Co(ImP^{NMe2})_2]^{2+}$	2.0080, 2.0200, 2.0710	2.0330	–20.0, 50.0, 150.0
Cluster	–	2.0330	–

UV-Vis absorption spectra

Experimental spectrum

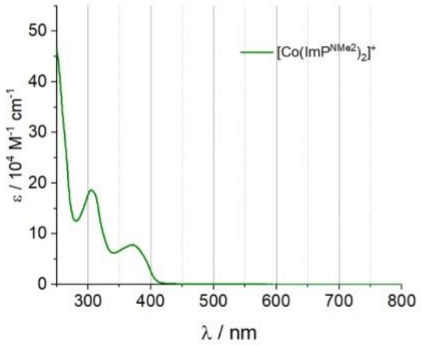

Figure S27: Experimental absorption spectrum of the complex taken in 50 µM in TeCA.

Theoretical spectra

The main contributing bands for $[Co(ImP^{NMe2})_2]$ as predicted by TPSSH/def2-TZVP are summarized in Table S4, while the contributions of the different fragments to the Kohn-Sham orbitals are collected in Table S5.

Table S4: Visualization of the main contributing donor and acceptor orbitals of the absorption band found at 370 and 305 nm, as well as the first component of the broad ligand-centered adsorption energies larger than 275 nm for $[Co(ImP^{NMe2})_2]^+$.

Band (nm)	Donor Orbitals	Acceptor Orbitals
Pre 280	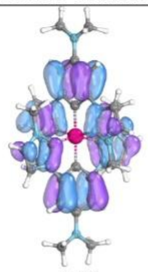 156	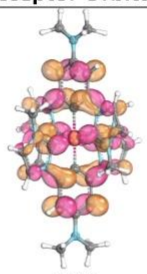 162

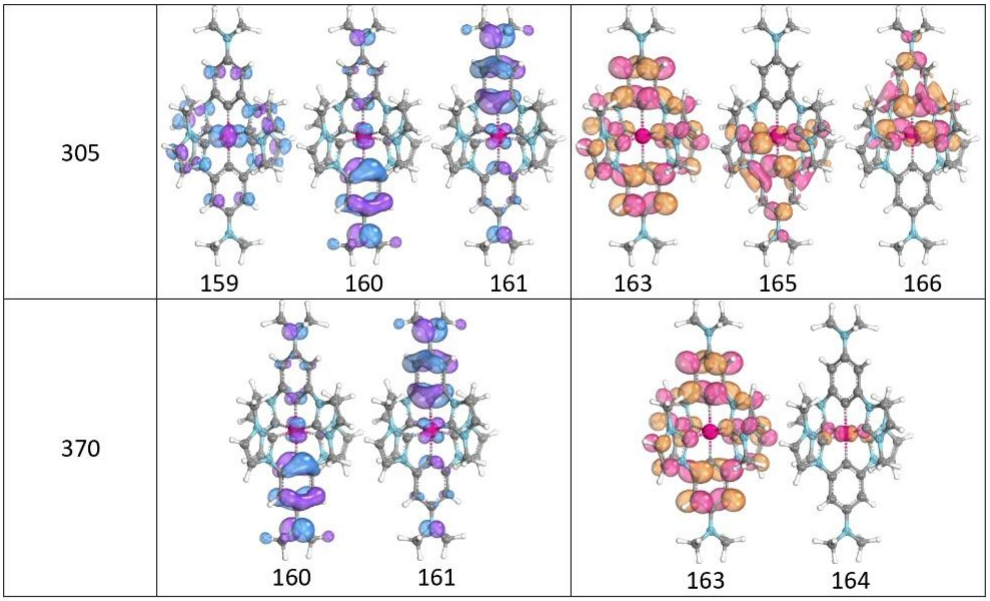

Table S5: Contributions of the different fragments to the Kohn-Sham orbitals relevant for the investigated absorption bands of $[Co(ImP^{NMe2})_2]^+$ according to Loewdin reduced orbital population analysis. The displayed fragments are Co center atom, the bottom and top ligands of the above pictures, the sum of all Ph-NMe_2 fragments, and the sum of all imidazol fragments. The most influencial fragments/ligands are highlighted for each orbital.

Orb. No	Co	Bottom Ligand	Top Ligand	Ph-NMe_2	Imidazoles
156	0.2	48.1	48.3	52.2	44.2
159	48.4	24.8	24.6	15.4	34.0
160	14.9	63.7	17.0	75.1	5.6
161	14.5	17.2	64.1	75.0	6.3
162	6.0	45.9	45.0	49.4	41.5
163	0.0	48.1	49.1	58.0	39.2
164	57.6	18.3	18.3	0.4	36.2
165	5.1	84.7	6.3	34.4	56.6
166	5.1	6.1	84.7	34.2	56.6

For $[Co(ImP^{NMe2})_2]^{2+}$, theory predicts an absorption band around 450 nm, which can not be observed experimentally. For this transition, the spatial distributions of the relevant orbitals are similar to those of the 570 nm and 900 nm bands. The differences in amplitude and band position of these three bands can be attributed to the solvent interaction at the aminyl functional group. Tables S6 and S7 provide the main donor and acceptor orbitals for the identified band, as well as contributions of the different fragments to the Kohn-Sham orbitals.

S33

Table S6: Visualization of the main contributing donor and acceptor orbitals of the absorption band found at 900, 570, 450, 358, and 303 nm for $[Co(ImP^{NMe2})_2]^{2+}$.

Band (nm)	Donor Orbitals	Acceptor Orbitals
303	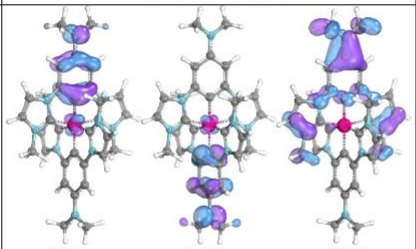 160a 161a 142b	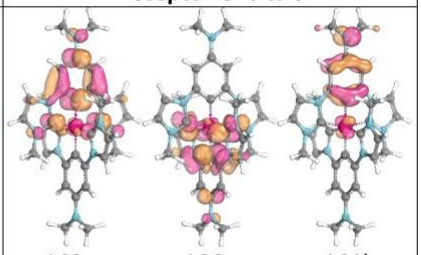 163a 166a 161b
358	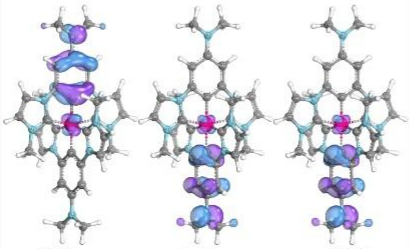 160a 161a 160b	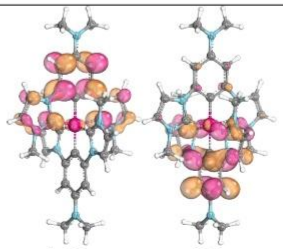 162a 164a 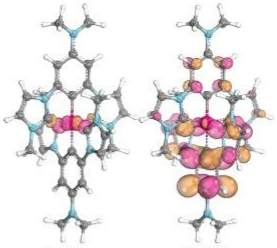 165a 163b
"450"	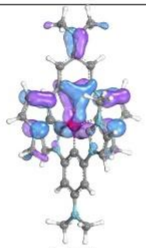 149b	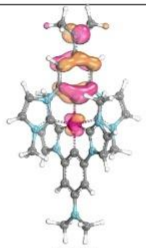 161b

570	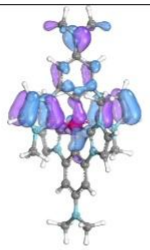 153b	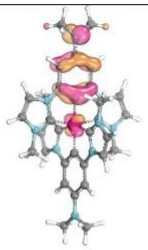 161b
900	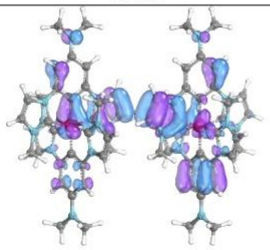 157b 158b	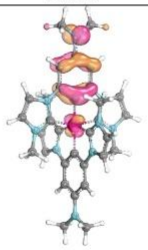 161b

Table S7: Contributions of the different fragments to the Kohn-Sham orbitals relevant for the investigated absorption bands of $[Co(ImP^{NMe2})_2]^{2+}$ according to Loewdin reduced orbital population analysis. The displayed fragments are the Cobalt center atom, the bottom and top ligands of the above pictures, the sum of all Ph-NMe_2 fragments, and the sum of all imidazole fragments. The most influential fragments/ligands are highlighted for each orbital.

Orb. No	Co	Bottom Ligand	Top Ligand	Ph-NMe_2	Imidazoles
160a	16.2	2.4	78.1	70.3	10.2
161a	7.5	88.7	1.0	84.6	5.1
163a	5.6	4.8	85.5	56.9	33.4
164a	3.0	86.3	7.6	53.3	40.6
165a	54.5	22.6	17.9	2.0	38.5
166a	4.0	85.3	6.2	29.9	61.6
142b	1.4	2.3	92.6	54.9	40.0
149b	15.4	9.0	71.0	29.8	50.2
153b	8.9	6.1	81.3	32.2	55.2
157b	32.6	18.2	45.8	27.7	36.3
158b	19.8	30.4	46.4	33.5	43.3
160b	8.5	88.1	1.1	84.1	5.1
161b	17.7	1.9	77.5	71.4	8.0
163b	1.7	82.2	13.9	55.8	40.3

Spectroelectrochemistry

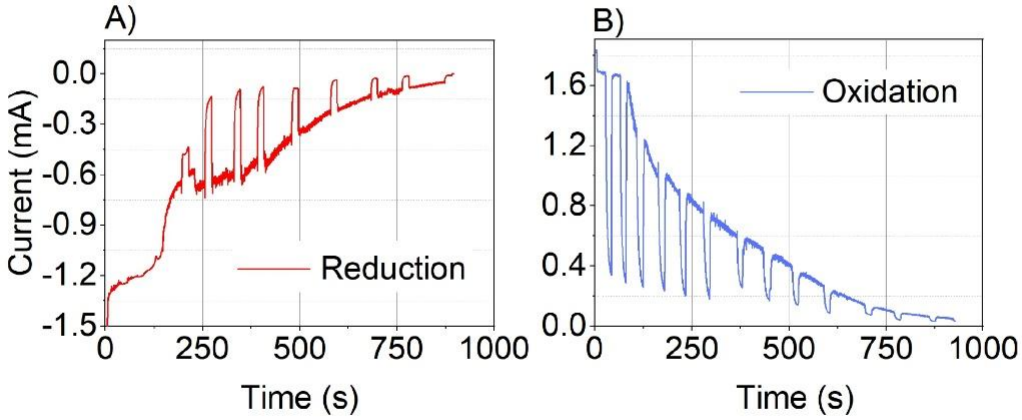

Figure S28. Chronoamperometric current–time plots obtained during controlled-potential coulometry of [Co(ImP^{NMe2})] [BF_4] (MW = 706.45 g mol^{-1}, 1.79 mg in DCM/MeCN). (A) reduction at 0V (red) and (B) Coulometric oxidation at 1V (blue). Integrated charge values of 0.44 C and 0.40 C correspond to 1.64 and 1.81 electrons per molecule, consistent with a reversible two-electron redox process.

Low-Temperature Emission Spectroscopy

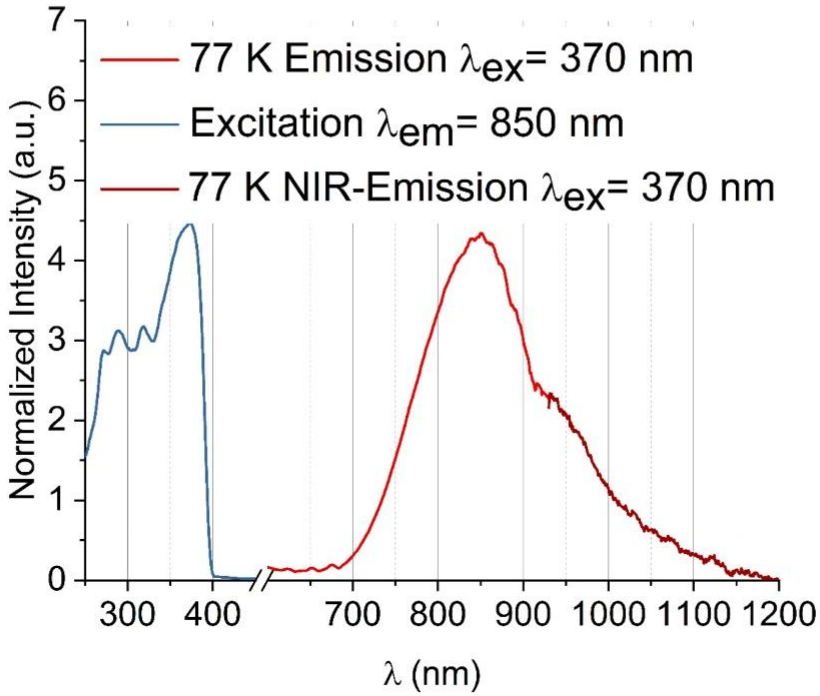

Figure S29: Low temperature emission spectra of 10 µM $[Co(ImP^{NMe2})_2][BF_4]$ in BuCN.

X-Ray Absorption Spectra

$[Co(ImP^{NMe2})_2]^+$ and $[Co(ImP^{NMe2})_2]^{2+}$ (5 mmol in 1:6 1,1,2,2- tetrachloroethane/acetonitrile) were studied using Co K-edge (E_0 = 7709 eV) X-ray absorption spectroscopy in the fluorescence mode. The measurements were conducted at the P65 beamline at Petra III (DESY, Hamburg). X-ray beam flux was ~$10^{11}\frac{ph}{s}$ with the beam spot of 0.3 x 1 mm. The signal was detected with the PIPS diode in RT. The estimated experimental resolution around the Co K-edge was 1 eV. The radical was generated by 2 h illumination with a Xenon lamp 330 nm longpass filter, upon visual change of the solution's color to purple from yellow, and in accordance with previous successful attempts of the radical generation. A separate bath of each complex was used to evaluate the radiation damage process, and the measurement conditions were adjusted to avoid this effect in the final measurements.

Detailed pre-edge transition analysis for $[Co(ImP^{NMe2})_2]^+$ is presented in Table S7 together with the transition assignments in Fig. S31. The HOMO-LUMO gap in the complex is estimated to be 3.37 eV. The first transition in TDDFT calculation is to LUMO+2 MO (σ) and has a mixed character with 53.5% $3d_{x2-y2}$ character. The second mixed-type transition (11 in TDDFT calculation, see Table SXX) is to LUMO+8 and LUMO+10 with $3d_{z2}$ character (σ*) of 33.7% and 9.7%, respectively. Transitions 60-64 at approx. 7711 eV involves orbitals with a strong contribution of the benzene

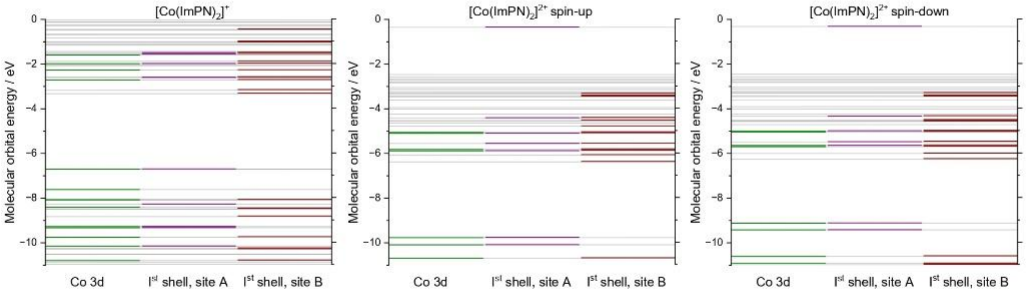

Figure S30: Molecular orbital energies around the energy gap. Grey color indicates all MOs in the calculations. Three types of MOs were included in the analysis and are marked by distinct colors: > 5% Co 3d contributions (green), >5% 2p contributions from first coordination shell ligands in the main molecular axis (violet, "I^{st} shell, site A"), and >5% 2p contributions from first coordination shell ligands perpendicular to the main molecular axis (red, "I^{st} shell, site B").

group's π* systems in the main molecular axis, and they reproduce the experimental spectrum particularly well. The energy distance between the $3d_{x2-y2}$ and $3d_{z2}$ orbitals (0.73 eV) involved in pre-edge transitions indicates significant distortion from ideal octahedral geometry around the Co atom. Despite that, oscillator strengths of pre-edge transitions are very low, which indicates delocalization of the electron density over the molecule. Additionally, there is a strong imbalance in the number of MOs involved in the transitions along the molecular axis and perpendicular to it, as evidenced by analysis of the I^{st} shell ligand contributions.

For $[Co(ImP^{NMe2})_2]^{2+}$, the results are summarized in Table S8 and in Fig. S32. The HOMO-LUMO gap is formed from spin-down MOs and is of 3.34 eV, thus, almost identical to the reference complex. The first TDDFT transition is around 7702 eV to the LUMO with 16% Co 3d contribution (11.2% d_{xz} and 4.8 d_{yz}) and spin-down. Next are two pre-edge transitions, spin-up and spin-down around 7704 eV to LUMO+2 and LUMO+3 MOs, both involved in σ* bonds. First contains 5.0% $3d_{x2-y2}$ + 3.6% $3d_{xz}$ (164α) and 46.0% $3d_{x2-y2}$ (165α). The second one is composed of 44.7% $3d_{x2-y2}$ (164β) and 7.0% $3d_{x2-y2}$ + 4.8% $3d_{xz}$ (165β) contributions, respectively. The energy difference between spin-up MOs with dominating $3d_{x2-y2}$ and 3dz2 (167α, not populated in XAS) is 0.79 eV, while for spin down, it is hard to estimate due to the strong delocalization. Nevertheless, the value for spin-up is similar to the reference complex, indicating, the distortion from the octahedral structure is still present in the radical. States 100-127 of both types reproduce experimental peak at 7711 eV, with a significant fraction of transitions to the benzene π*-system;

however, they are also more delocalized over the molecular backbone. The electronic density delocalization over the molecule is similarly heterogenous in radical, as in the $[Co(ImP^{NMe2})_2]^+$.

While Co K-edge XAS shows no significant differences, it is important to underline, this method locally probes p-projected electronic structure from the Co point of view. Lack of spectral change indicates that the radical unpaired electrons are indeed on the side groups far from the Co center, and changes in the electronic structure around Co have secondary character or are too weak to be experimentally resolved (first pre-edge transitions).

Table S7: Important molecular orbitals contributing to the XAS spectrum of $[Co(ImP^{NMe2})_2]^+$.

1.	164a (98.82%) 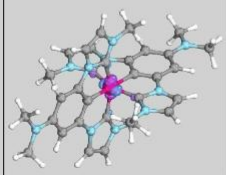		16.	178a (98.41%) 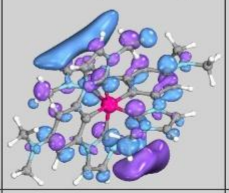	
2	170a (80.55%) 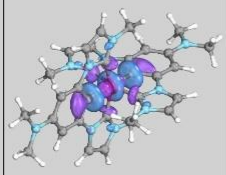	172a (15.98%) 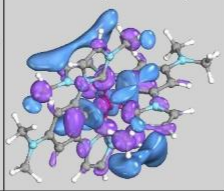	18.	177a (37.74%) 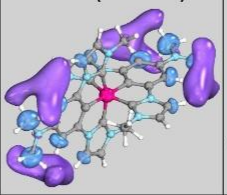	179a (61.12%) 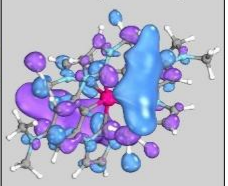
5	165a (90.55%) 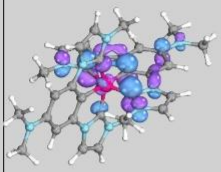	166a (9.12%) 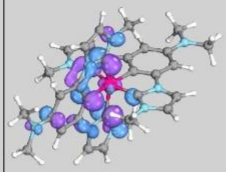	24.	185a (48.78%) 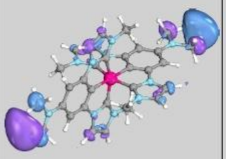	186a (50.73%) 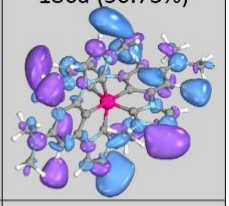
11	170a (16.70%) 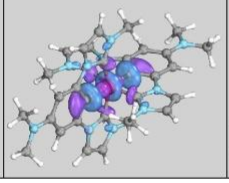	172a (82.67%) 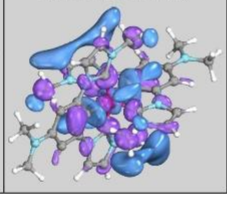	26.	187a (89.92%) 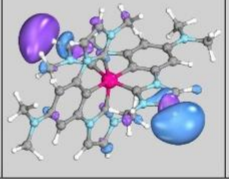	188a (8.53%) 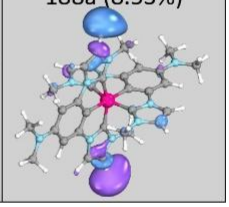

12	173a (98. 84%) 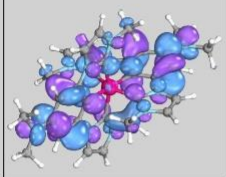		27.	187a (8.67%) 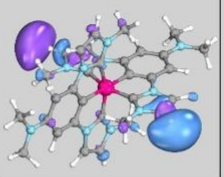	188a (90. 54%) 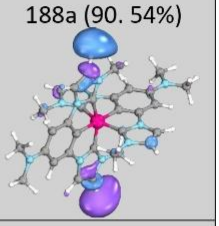
13	174a (98.81%) 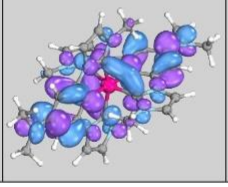		50.	212a (88.51%) 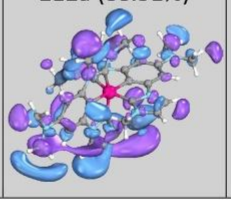	

57.	218a (95.42%) 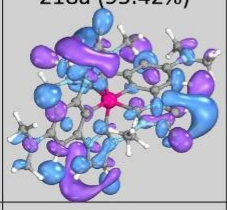		70.	231a (94.03%) 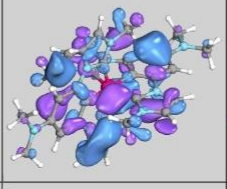	233a (5.86%) 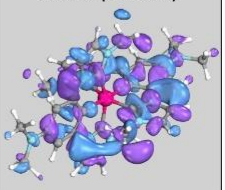
59.	221a (94.03%) 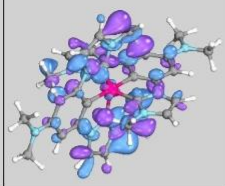		76.	236a (32.29%) 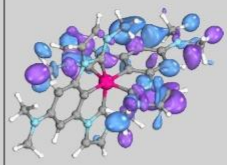	237a (64.45%) 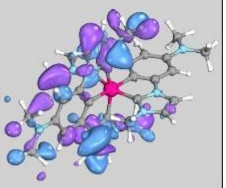
60.	220a (96.35%) 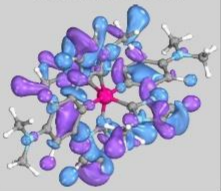		83.	243a (97.24%) 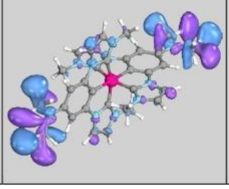	

61.	222a (89.06%) 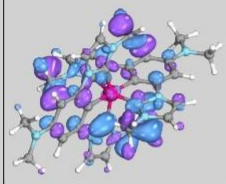		84.	244a (11.32%) 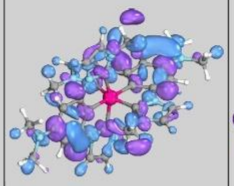	245a (85.64%) 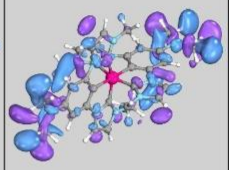
62.	223a (75.78%) 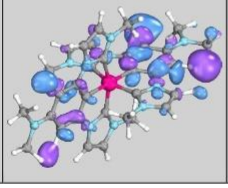	226a (11.76%) 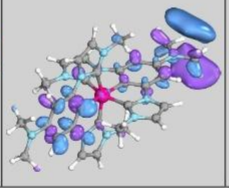			

64.	224a (58.13%) 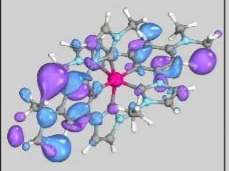	226a (5.77%) 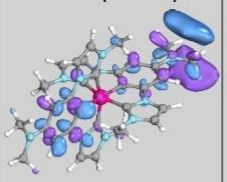			
	228a (9.97%) 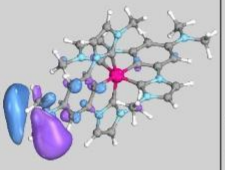	229a (13.42%) 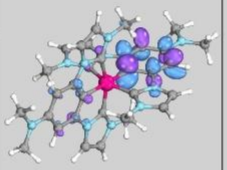			
	230a (5.07%) 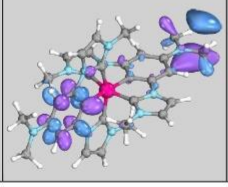				

S41

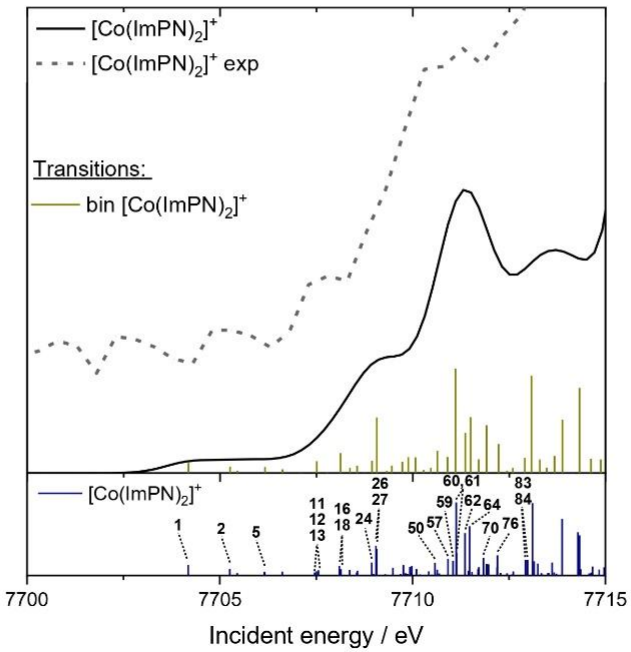

Figure S31: Assignment of the transitions from Table S7.

Table S8. Important spin-down molecular orbitals contributing to the XAS spectrum of $[Co(ImP^{NMe2})_2]^{2+}$.

1.	161b (98.60%) 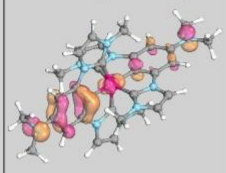		51.	187b (97.85%) 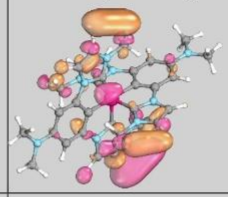	
3.	164b (85.33%) 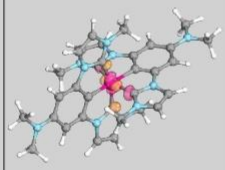	165b (13.06%) 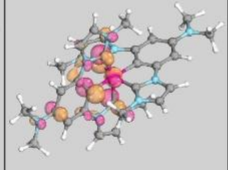	55.	188b (98.41%) 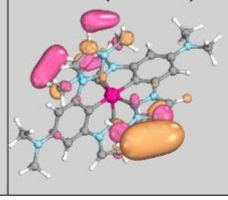	

35.	178b (79.49%) 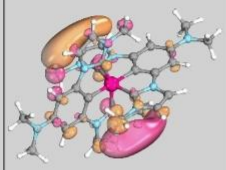	180b (16.85%) 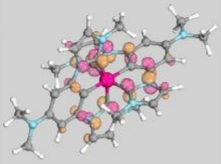	77.	195b (10.37%) 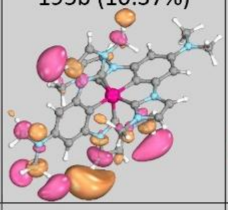	197b (35.33%) 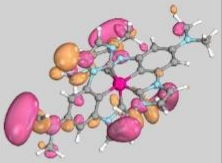
39.	179b (57.69%) 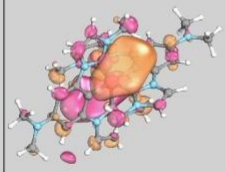	180b (30.25%) 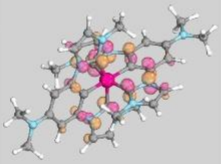		198b (29.98%) 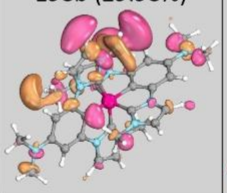	199b (16.57%) 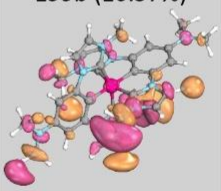
	182b (7.15%) 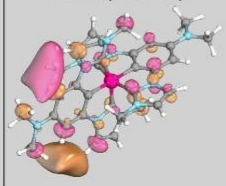		81.	200b (14.46%) 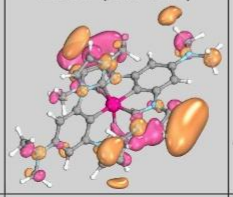	201b (48.03%) 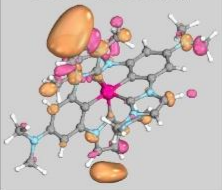
49.	185b (94.07%) 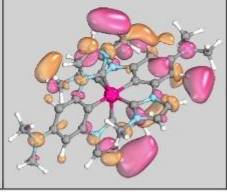			202b (28.36%) 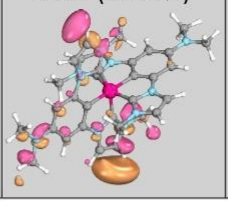	

83.	200b (16.05%) 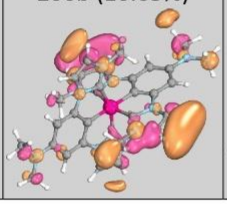	201b (13.44%) 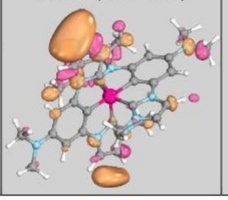	157.	238b (8.61%) 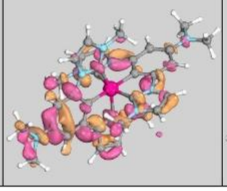	239b (87.35%) 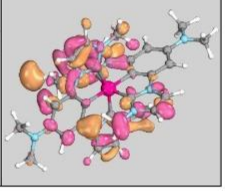

S43

	202b (62.77%) 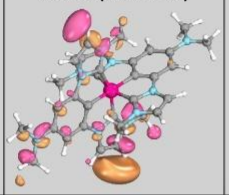				
100.	210b (5.30%) 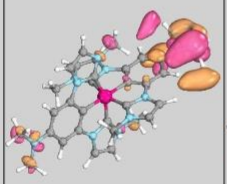	211b (87.27%) 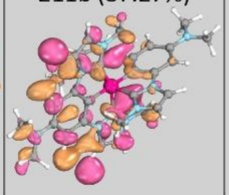			
119.	220b (59.93%) 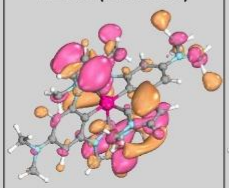	221b (35.18%) 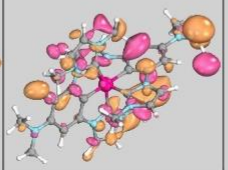			
123.	222b (83.42%) 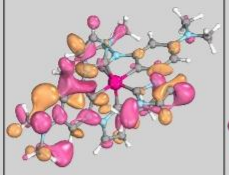	223b (11.36%) 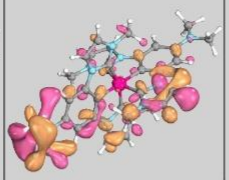			
127.	224b (98.24%) 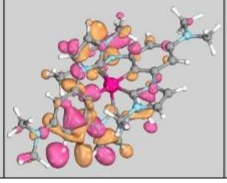				

S44

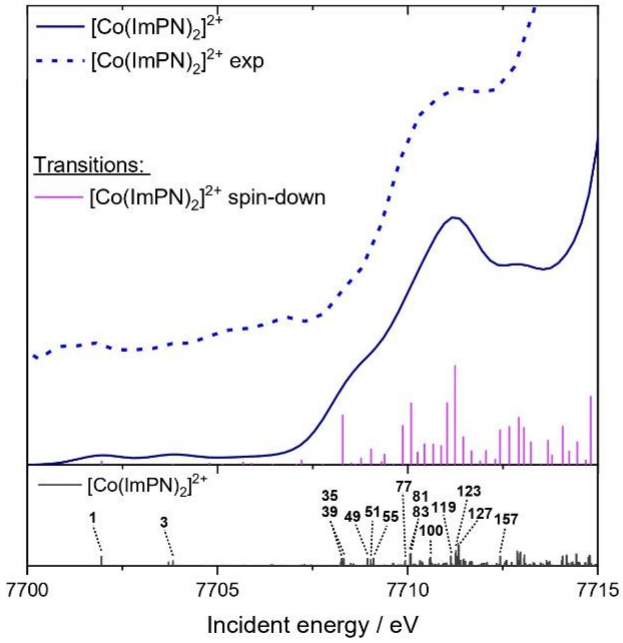

Figure S32: Assignment of the spin-down transitions from Table S8.

Table S9. Important spin-up molecular orbitals contributing to the XAS spectrum of $[Co(ImP^{NMe2})_2]^{2+}$.

2.	164a (9.90%) 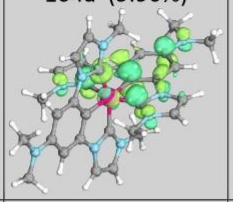	165a (88.92%) 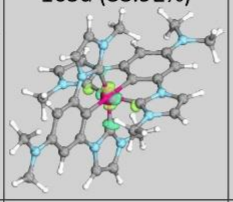	54.	188a (98.34%) 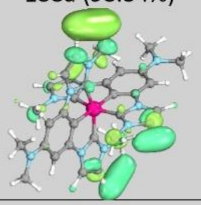	
36.	178a (47.22%) 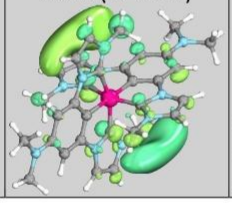	179a (22.34%) 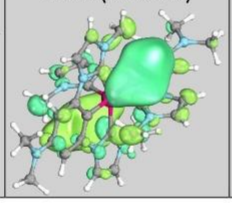	75.	195a (11.56%) 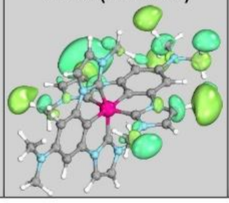	197a (25.83%) 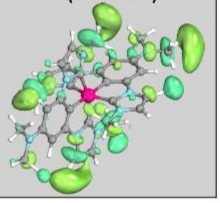

	180a (27.76%) 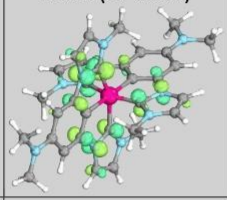			198a (39.59%) 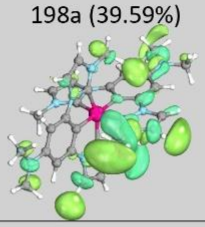	199a (16.57%) 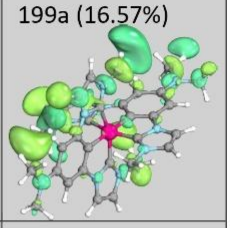
38.	179a (69.72%) 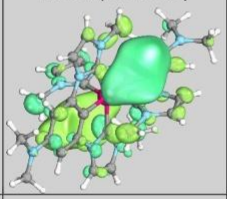	180a (21.80%) 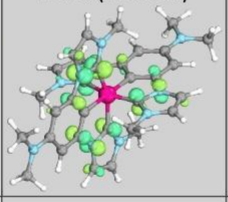	82.	200a (29.13%) 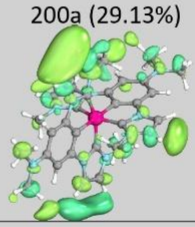	201a (29.06%) 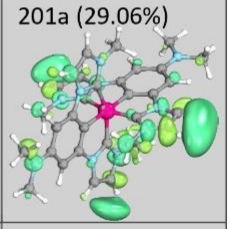
48.	185a (93.86%) 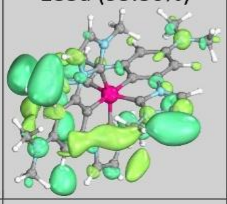	186a (5.32%) 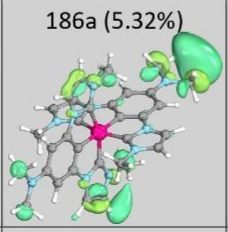		202a (31.80%) 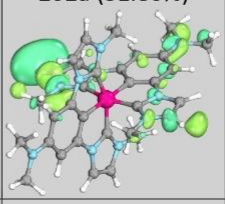	
50.	187a (97.26%) 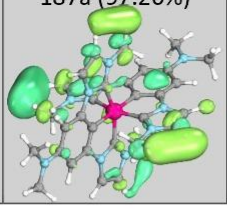		-		

98.	2 10a (25.45%) 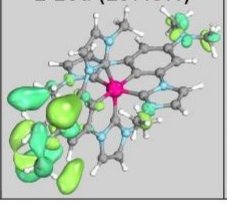	211a (54.07%) 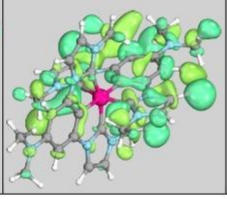			

	212a (16.35%) 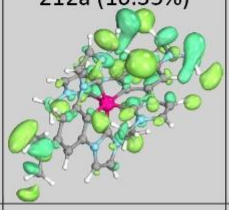				
118.	220a (21.93%) 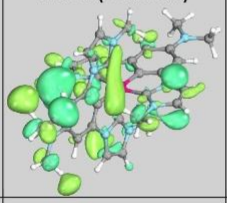	221a (74.66%) 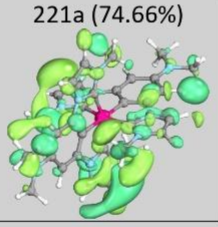			
122.	222a (83.32%) 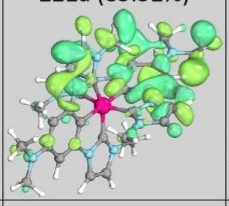	223a (11.08%) 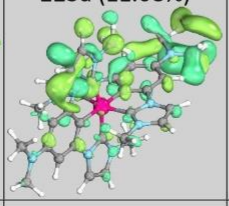			
126.	224a (93.87%) 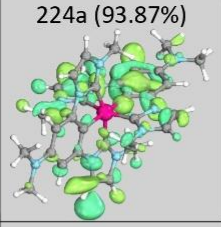				
156.	239a (94.65%) 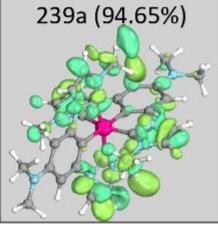				

S47

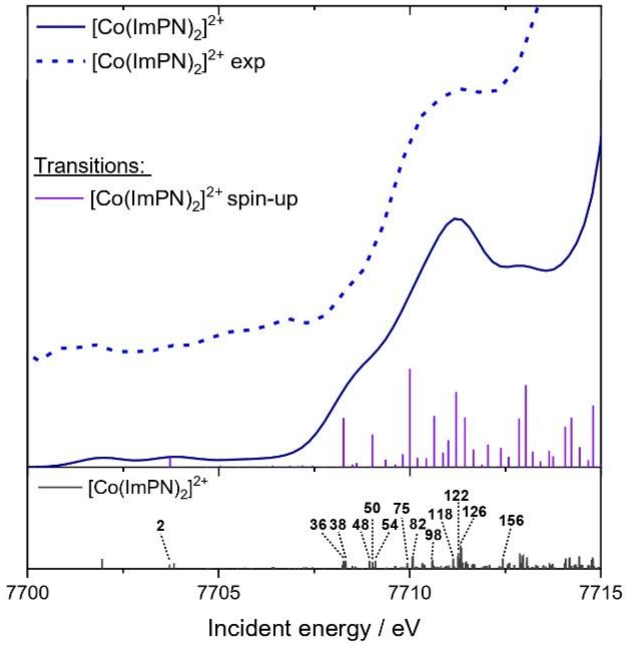

Figure S33: Assignment of the spin-up transitions from Table S9.

Transient Absorption

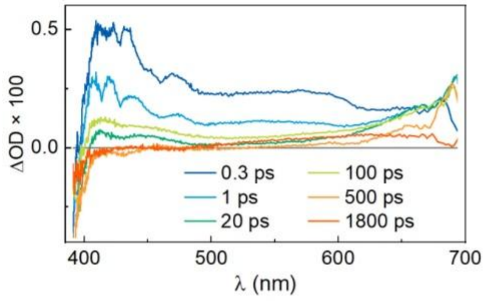

Figure S34: Transient absorption spectra in DCM.

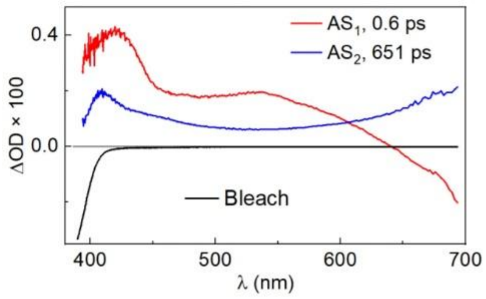

Figure S35: DAAS spectrum in DCM.

Photooxidation

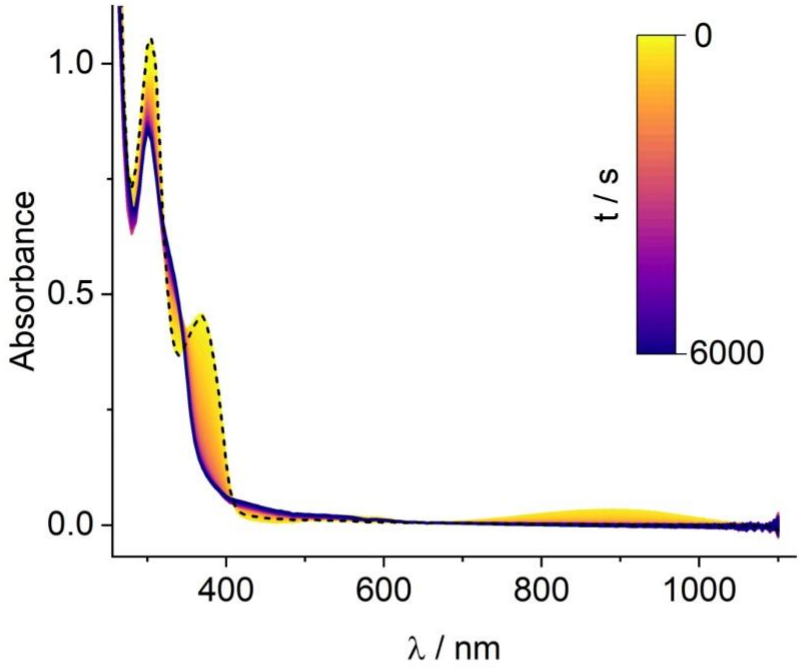

Figure S36: 3 mL of 0.5 mM solution of $[Co(ImP^{NMe2})_2][BF_4]$ in TeCA was irradiated using a Xenon lamp equipped with a longpass 330 nm filter, and UV-Vis absorption spectra were simultaneously recorded every 10 s for 6000 s.

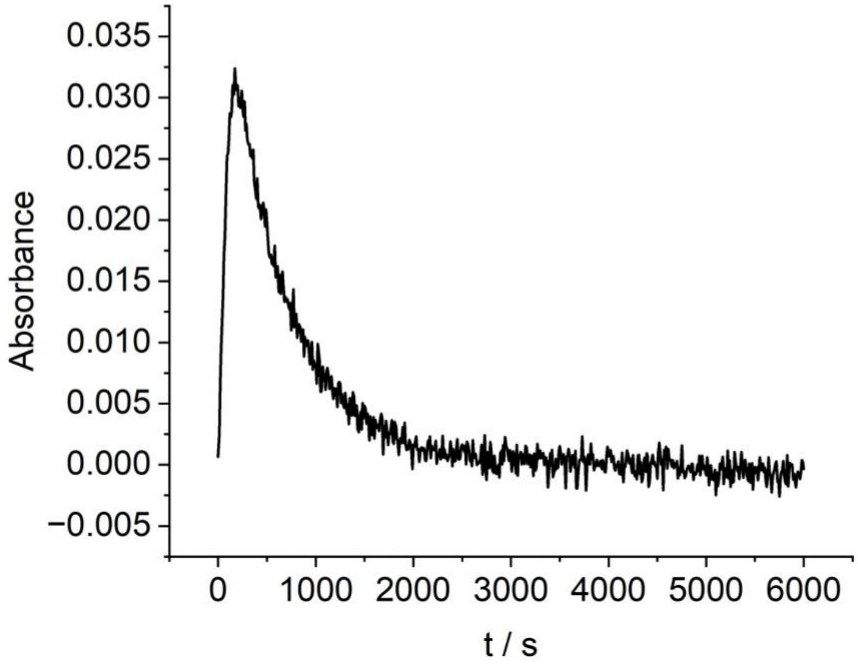

Figure S37: Absorbance over time graph for the absorption band at 900 nm for Fig. S36 in pure TeCA @ 900 nm.

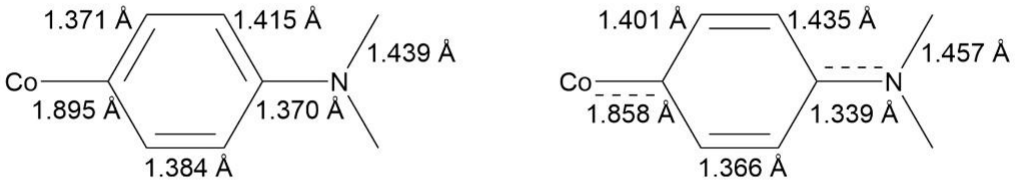

Figure S38: Bond lengths within the phenyl-unit of $[Co(ImP^{NMe2})_2]^+$ (left) and the radical ligand of $[Co(ImP^{NMe2})_2]^{2+}$ (right) indicating the transition towards a semi-quinon like structure.

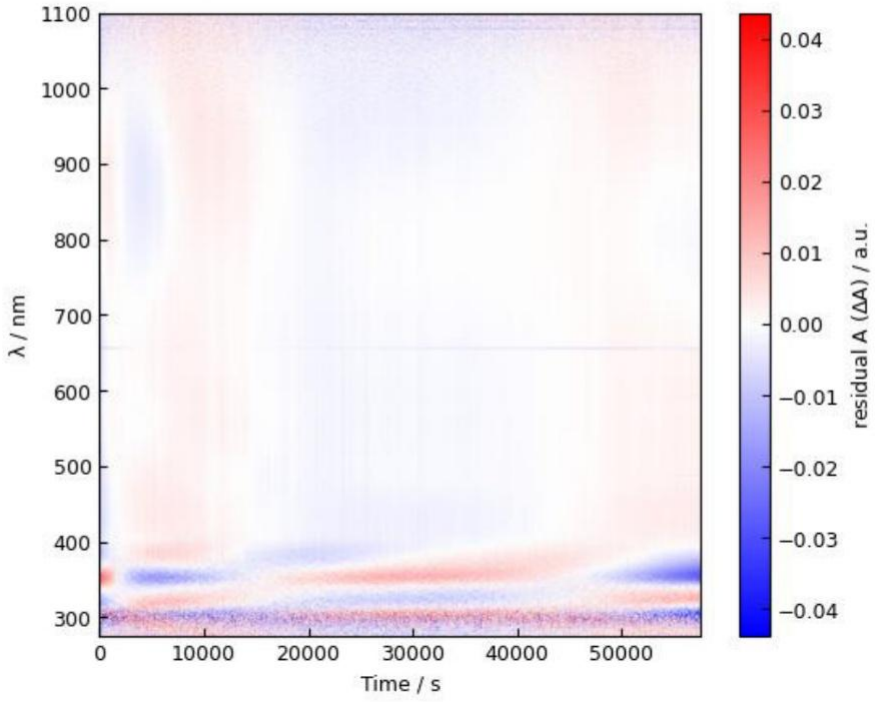

Figure S39: Residuals of the fit provided in Figure 7. The larges deviations of the fit are found between 300 and 400 nm and can likely be attributed to the fitting approach fitting, which utilized three ligand spectra instead of 5 species spectra. Nevertheless,fitting without this approximation did not result in sensible spectras and tested post-corrections did not lower the residuals significantly.

Reactivity

Reactivity towards TEMPO

$[Co(ImP^{NMe2})_2][BF4]$ (4.52 mg, 0.006 mmol) and TEMPO (10 mg ,0.063 mmol) were added to deuterated $C_2D_2Cl_4$ and irradiated with soft UV-light overnight. 1H NMR was recorded at 0h, 1h, and 2h to monitor the formation of the product at 1 ppm.

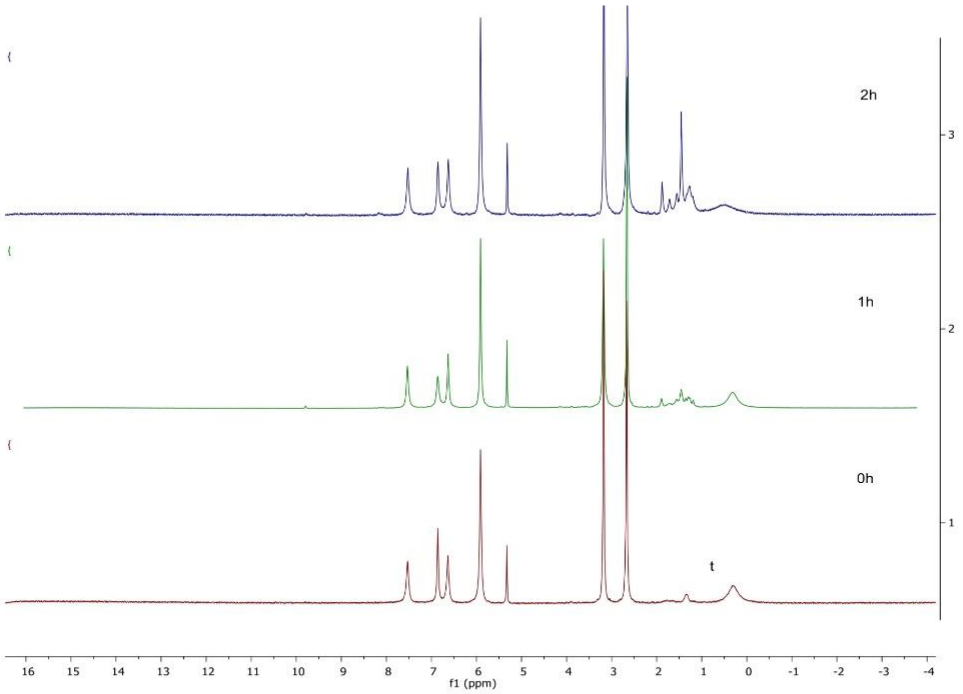

Figure S40: ^1H NMR of TEMPO at 0h (bottom), 1h (middle), and 2h (top) 1 day upon reaction with 0.1 eq of $[Co(ImP^{NMe2})_2][BF_4]$ in $C_2D_2Cl_4$.

Reactivity towards Ascorbic Acid

$[Co(ImP^{NMe2})_2][BF4]$ (4.52 mg ,0.006 mmol) and ascorbic acid (11.2 mg, 0.063 mmol) were dissolved in $C_2D_2Cl_4$ was added to deuterated water $C_2D_2Cl_4$ and irradiated with soft UV-light overnight. ^1H NMR of the deuterated water phase was recorded after 1 day to confirm the production of dehydroascorbic acid.

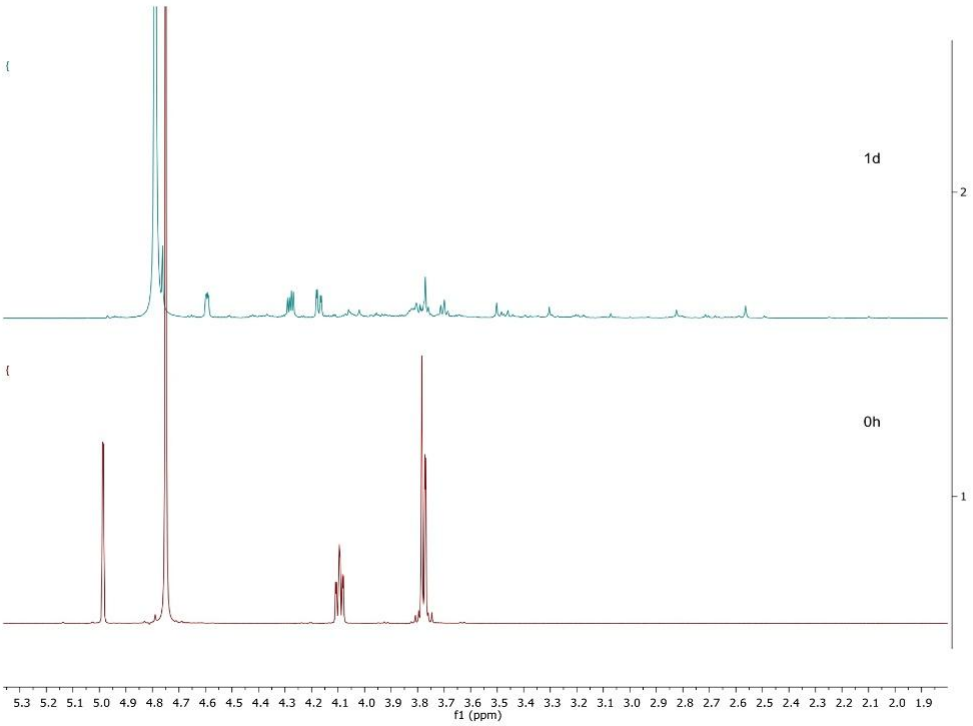

Figure S41: ^{1}H NMR of ascorbic acid (bottom) and ^{1}H NMR of ascorbic acid after 1 day upon reaction with 0.1 eq of $[Co(ImP^{NMe2})_2][BF_4]$ in D_20.

Reactivity towards Bu_3SnH

$[Co(ImP^{NMe2})_2][BF4]$ (4.52 mg, 0.006 mmol) was dissolved in CD_2Cl_2 and irradiated for 3 hours to get the intermediate radical complex. The solvent was then distilled off, and a green solid was obtained. 2.05 µL (0.0076 mmol) of Bu_3SnH was added to 2 mL of isopropanol. ^{119}Sn NMR was recorded in $CDCl_3$ after 20 mins to confirm the production of Bu_6Sn_2. A blank of the Bu_3SnH and isopropanol in $CDCl_3$ to confirm the product formation.

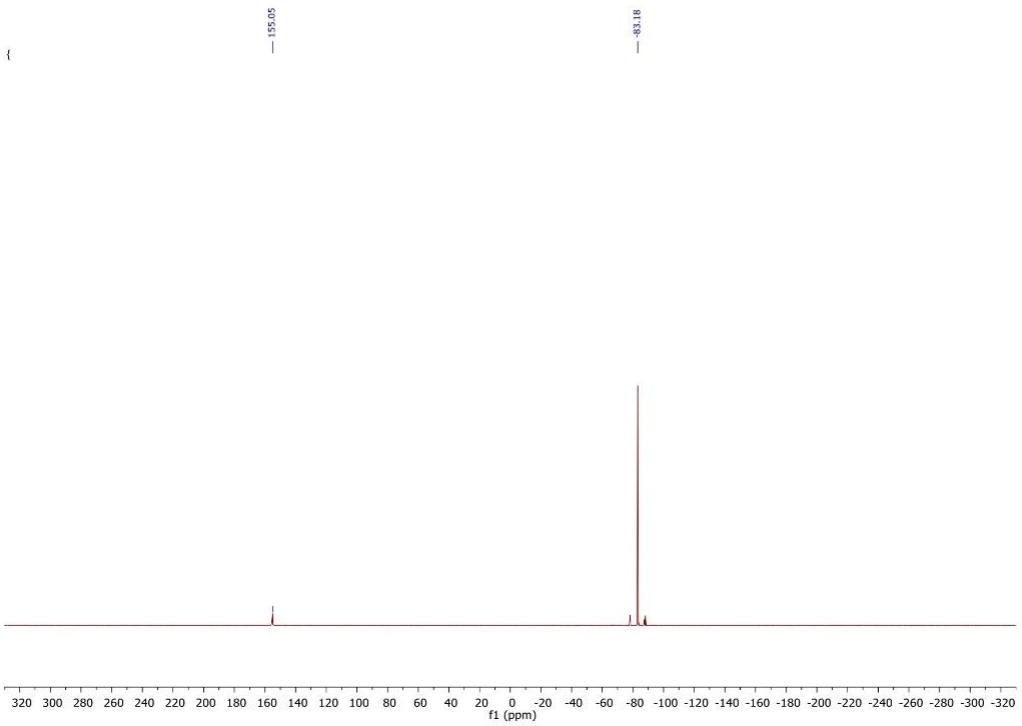

Figure S42: ^{119}Sn-NMR spectrum of Bu_3SnH in CD_3Cl.

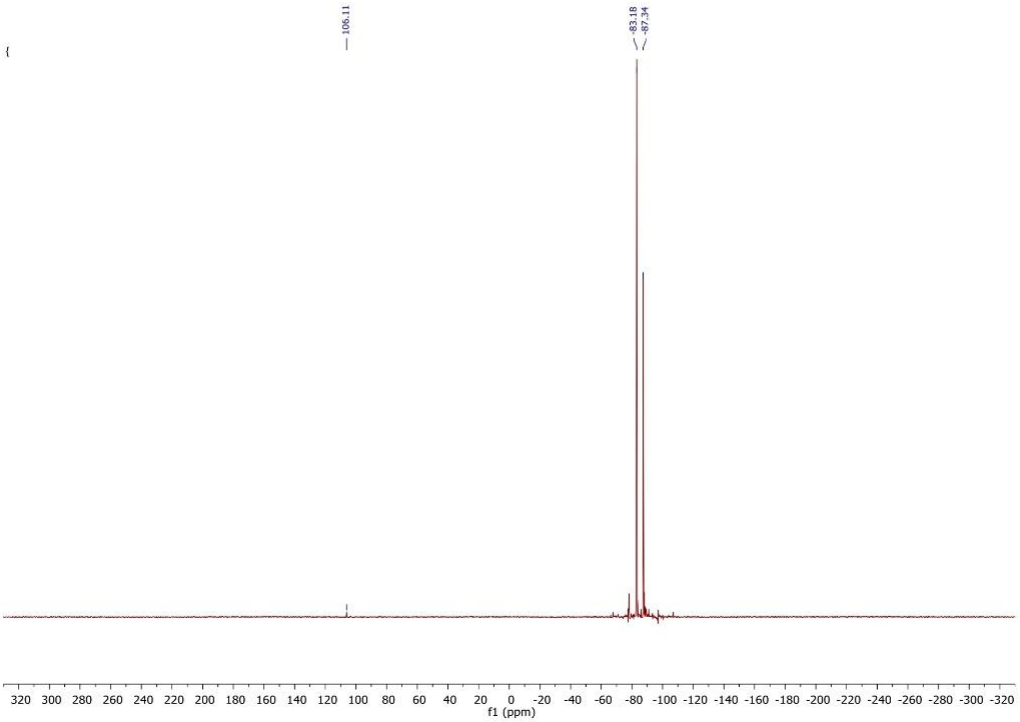

Figure S43: ^{119}Sn-NMR spectrum of ^{119}Sn-NMR spectrum of Bu_6Sn_2 in CD_3Cl after $[Co(ImPN^{Me2})_2]^{2+}$ was added.

S55

XAS Analysis for Bu_3SnH and Bu_6Sn_2

A **dimerization reaction with sacrificial hydrogen donor tributyltin complex (Bu_3SnH) was used**

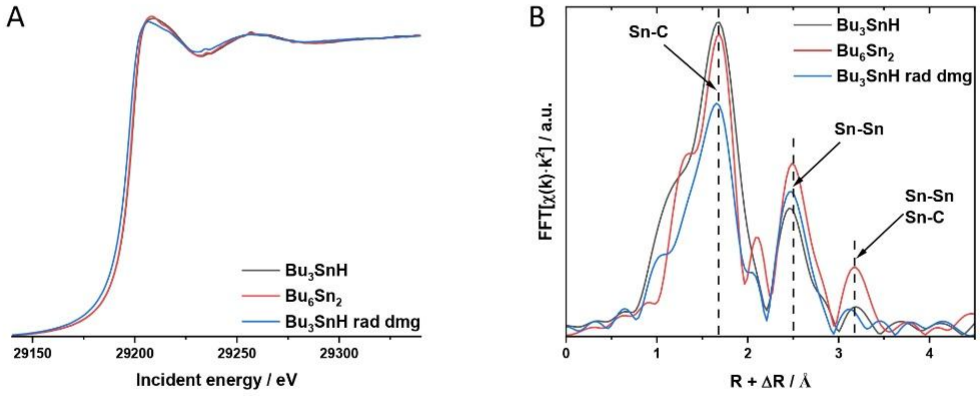

Figure S44: A) XAS spectrum of Bu_3SnH and Bu_6Sn_2. B) Respective fourier transforms.

Tracking the reactivity of the radical species using EXAFS at Sn K-edge.

The measurement conditions were the same as for the complex characterization (see "X-ray Absorption spectroscopy" section above), except that no illumination was applied. Fig. S44 A shows absorption edges of the Bu_3SnH (black), Bu_6Sn_2 (red), and Bu_3SnH radiation-damaged (blue). The Sn K-edge is affected by large core-hole broadening of ~6 eV [30], thus edges are relatively featureless. The radiation damage was mitigated by repeating the same measurements several times in MeCN solution. For clarity, we report the spectrum of the beam-damaged Bu_3SnH, indicating its pronounced -1.2 eV absorption shift. Fig. S44 B) presents the Fourier transforms of the respective species. Interestingly, the radiation damage is the most pronounced in the Ist coordination shell, most likely indicating Sn-C bond cleavage; thus, it was easy to differentiate it from the other two complexes, and it was not analyzed in detail. Structures required for EXAFS analysis of Bu_3SnH and Bu_6Sn_2 were constructed and optimized in Orca. 5.0.1 using composite approach B97-3c [31], def2-mTZVP basis, and def2-mTZVP/J auxiliary basis set. EXAFS fitting was done in 2.0-12.0 Å^{-1} k-range and 1.2-3.6 Å R-range. Results for Bu_3SnH are shown in Fig. S45 and Table S10, while for Bu_6Sn_2 in Fig. S46 and corresponding Table S11.

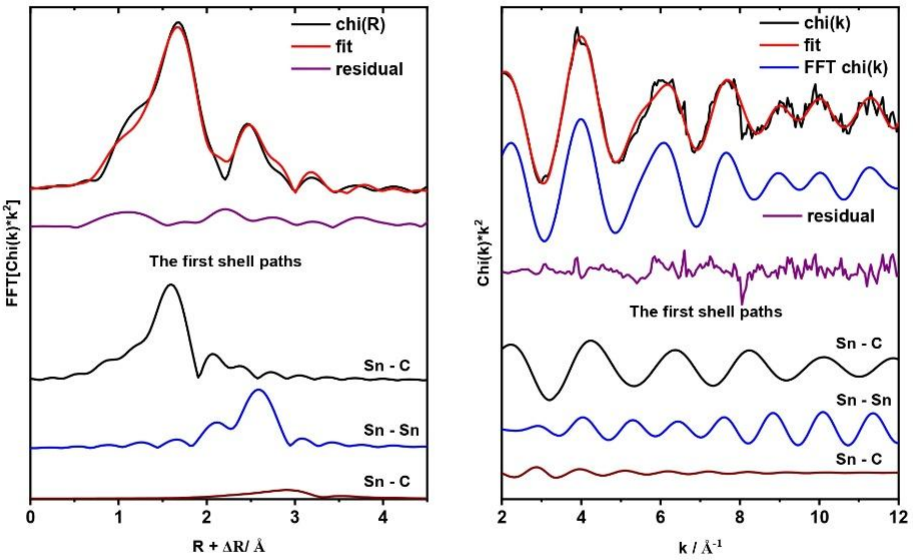

Figure S45: EXAFS fitting results for Bu3SnH. Left: the best fit in R-space along with residuals and important scatters. Right: the best fit in k-space along with the residual function and important scatters.

Table S10: EXAFS fitting results for Bu_3SnH.

Scatter	N	σ^2 / Å^2	R + ΔR / Å
Sn-C	1.0(1)	0.0020(3)	2.096(32)
Sn-C	2.0(1)	0.0020(3)	2.233(18)
Sn-Sn	0.5(1)	0.0042(14)	2.795(15)
Sn-C	1.3(7)	0.0108(15)	3.623(86)
Sn-C	1.1(9)	0.0049(16)	3.998(110)

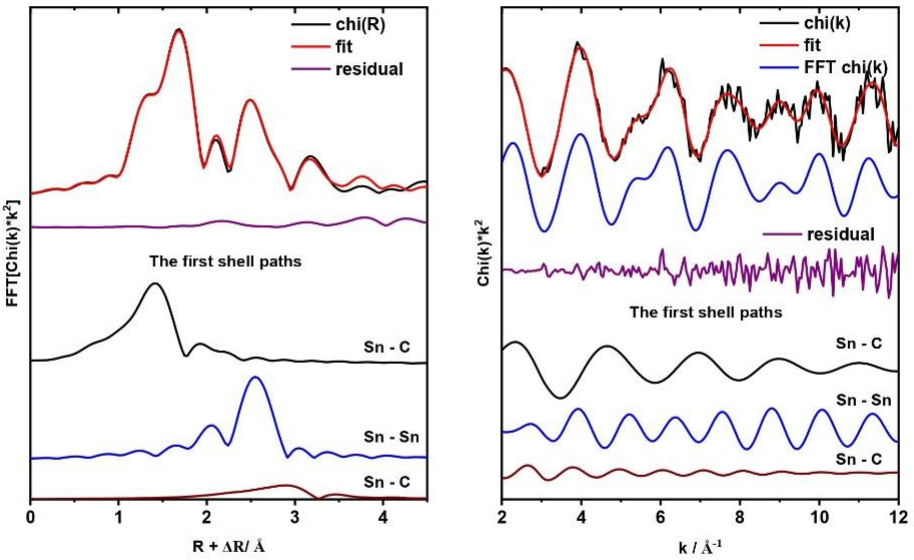

Figure S46: EXAFS fitting results for Bu_6Sn_2. Left: the best fit in R-space along with residuals and important scatters. Right: the best fit in k-space along with the residual function and important scatters.

Table S11: EXAFS fitting results for Bu_6Sn_2.

Scatter	N	σ^2 / Å^2	R + ΔR / Å
Sn-C	0.9(1)	0.0047(4)	1.943(26)
Sn-C	1.9(4)	0.0029(6)	2.155(15)
Sn-Sn	1.0(1)	0.0065(12)	2.785(16)
Sn-C	2.7(1)	0.0097(30)	3.639(81)
Sn-C	3.1(4)	0.0022(10)	3.973(37)

In both fits, the first coordination shell consists of 3 C atoms and Sn-Sn contribution at ~2.8 Å, and a further shell consisting of Sn-C scatters. Additionally, both complexes are reproduced by the same set of scatters, but for Bu_6Sn_2, coordination numbers in the further shells are increased. The presence of Sn-Sn scatter in the EXAFS signal can be explained by the fact that the reaction had already started before the first measurement could be finished. However, in Bu_3SnH, the Sn-Sn has a coordination number of 0.5(1) while in the dimer, it is 1.0(1), thus it is doubled. With the increase in the coordination numbers of the last Sn-C scatters in total from 2 to 6, the EXAFS analysis indicates a dimerization process.

Gas MS

Head space analysis of test reaction with Tributyl tin-hydride and polymethylhydrosiloxane (PMHS) was done with the help of Gas MS. Blanks with the complex (5mg, 7 µmol of $[Co(ImP^{NMe2})_2][BF_4]$) and reagents (0.1 mL, [0.37mmol] Bu_3SnH and 0.1 mL, [0.15 mmol] PMHS) in 3 mL solution mixture of 1:1 TeCA / isopropanol were recorded after 10 minutes of preparation while monitoring hydrogen, argon, nitrogen, oxygen, water and isopropanol in reaction vials pre irradiation and then monitored after 10 mins of irradiation to confirm hydrogen production in both the reactions.

Single Crystal X-ray diffractometry

$C_{32}H_{36}N_{10}Co$, BF_4, 2(0.4(CH_2Cl_2)), M_r = 774.39 Da, yellow block, size 0.14 x 0.18 x 0.20 mm³, orthorhombic space group *Fdd2* (43) with Z=8, a=15.7632(16), b=15.8895(16) Å, c=27.802(4) Å, V=6963.6(14) Å³, D_c=1.477 g/cm³, µ=0.678 mm^{-1}, F(000)=3197, θ_{max}=33.305°, reflections collected: 237154, independent reflections: 6697, R_{int}=0.0810, refinement converged at R1=0.0449 [I>2σ(I)], wR2=0.1356 [all data], min./max. ΔF: -0.48 eÅ³ (0.97 Å from H1B) / 0.60 eÅ³ (0.55 Å from F11), **CCDC No.: 2473170.**

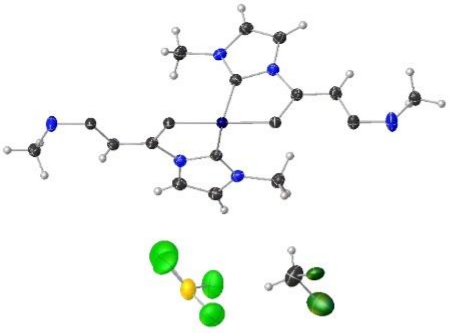

Figure S47: Asymmetric unit of $[Co(ImP^{NMe2})_2][BF_4]$.

molecule, one BF_4 anion is present, of which the B atom is also located on (another) 2-fold axis (Wyckoff letter 8a). The four F atoms of the anion are disordered over two positions (SOF: 0.6). In addition, one dichloromethane molecule with a reduced site occupation factor of 0.8 is present in the structure, which is completely disordered over two

The yellow, block-shaped crystal was obtained from gas phase diffusion of pentane in a dichloromethane solution of $[Co(ImPN)_2][BF_4]$. The Co atom, as well as the center atoms of the two ligands (N13, C17, C18, and N23, C27, C28), are located on a special position – a 2-fold axis, Wyckoff letter 8a – resulting in the description of one half of each ligand. To compensate for the positive charge of the complex

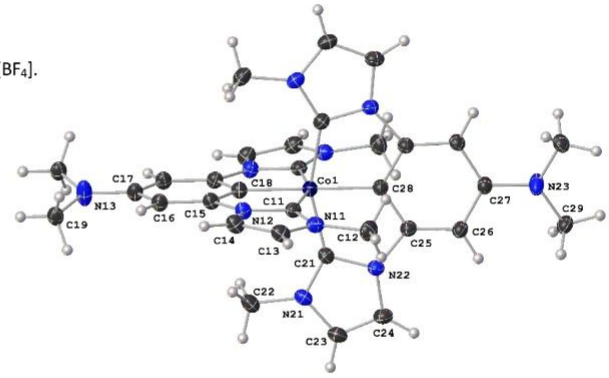

Figure S48: Crystal structure of $[Co(ImP^{NMe2})_2][BF_4]$ with anisotropic displacement ellipsoids drawn on a 50% probability level.

positions, its center of gravity located on a 2-fold axis (Wyckoff letter 8a). The structure was refined as a 2-component inversion twin (BASF 0.107(17)).

All non-hydrogen atoms were refined anisotropically, while the aromatic hydrogen atom positions were refined at idealized positions riding on the carbon atoms with isotropic displacement parameters U_{iso}(H)=1.2 U_{eq}(C) and C-H bond lengths of 0.950 Å. The methyl groups are idealized with tetrahedral angles in a combined rotating and rigid group refinement with the 1.5-fold isotropic displacement parameters of the equivalent Uij of the corresponding carbon atom at a distance of d(C-H)=0.98 Å.

Nonadiabatic dynamics simulations

Trajectory Surface Hopping Setup

Trajectory surface hopping was performed using the Linear Vibronic Coupling (LVC) Hamiltonian. 500 initial conditions were generated around the optimized geometry using a harmonic Wigner distribution. These initial conditions were transfered to excited states within an energy window of 0.5 eV (3.4–3.9 eV), centered around the optical excitation energy corresponding to a wavelength of 345 nm (3.59 eV). The 200 independent trajectories were chosen based on the excitation energies and oscillator strengths propagated for 1 ps, all of which started in the adiabatic singlet ^{1}MLCT manifold (9 in S7, 16 in S8, 45 in S_9, 28 in S_{10}, 50 in S_{11}, 45 in S_{12}, and 7 in S_{13}). Nuclear and electronic propagations were performed with time steps of 0.5 fs and 0.005 fs, respectively. Gradients of all electronic states were computed in the adiabatic/diabatic basis and subsequently transformed into a diagonal representation. During this transformation, corrections for nonadiabatic couplings were applied to ensure consistency. To account for decoherence effects, we employed the energy-based decoherence correction scheme,[32] using a decoherence parameter of 0.1 a.u. During the surface hops, the kinetic energy was adjusted by rescaling the velocity vectors. Surface hopping probabilities were approximated using the wave function overlaps. To identify the dominant nuclear motion, Cartesian displacements were projected onto the ground-state normal modes relative to the FC geometry. The dimensionless mass-frequency weighted normal mode coordinates q(t) were obtained by $q(t)=D^T \Delta r(t)$, where $\Delta r(t)$ represents the Cartesian displacements from the trajectories, and D is a transformation matrix obtained by diagonalizing the mass-weighted Hessian. To quantify the total nuclear motion for each normal mode, the normal mode activity was calculated by evaluating the standard deviation:

$$\sigma_i = \left(\frac{1}{N_{\text{traj}} N_{\text{step}}} \sum_{j=1}^{N_{\text{traj}}} \sum_{k=1}^{N_{\text{step}}} q_{i,j}^2(k\Delta t) - \left(\frac{1}{N_{\text{traj}} N_{\text{step}}} \sum_{j=1}^{N_{\text{traj}}} \sum_{k=1}^{N_{\text{step}}} q_{i,j}(k\Delta t) \right)^2 \right)^{\frac{1}{2}}$$

Here, N_{traj} and N_{step} denote the number of trajectories and time steps, respectively.[33]

Linear Vibronic Coupling

The LVC Hamiltonian for $Co(ImP^{NMe2})_2^+$ complex was computed using the first twenty singlet states, including the ground state S_0 and excited states (S_1–S_{19}), and the first ten triplet states (T_1–T_{10}). By applying an energy threshold of 0.0003 eV to filter out negligible contributions, the resulting LVC Hamiltonian includes a total of 2173 $\kappa_n^{(i)}$ terms, 22722 $\lambda_n^{(i,j)}$ terms, and 1200 spin-orbit coupling (SOC) terms. These terms respectively represent the linear coupling of vibrational modes to individual electronic states, inter-state vibronic couplings, and spin-orbit interactions between states. Fig. S49 illustrates the distribution of these LVC parameters. As shown, most of the coupling elements are relatively small in magnitude, indicating that strong couplings are limited to a subset of specific vibrational modes and state pairs. This distribution of coupling parameters is typical for transition-metal complexes and highlights the importance of identifying only the most relevant modes for accurate nonadiabatic dynamics simulations.

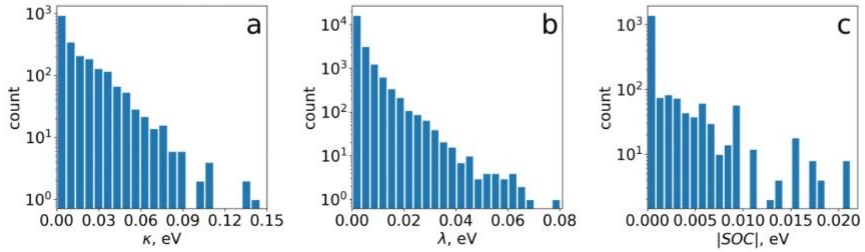

Figure S49: Distribution of coupling parameters in the LVC and SOC Hamiltonians: (a) $\boldsymbol{\kappa} = |\boldsymbol{\kappa_n^{(i)}}|$ representing state-specific vibronic couplings, (b) $\lambda = |\boldsymbol{\lambda_n^{(i,j)}}|$ indicating inter-state vibronic couplings, and (c) |SOC| = $|\boldsymbol{V_{mn}^{(SOC)}}|$ denoting spin-orbit coupling strengths between electronic states.

Absorption spectrum

The experimental absorption spectrum of the $Co(ImP^{NMe2})_2^+$ complex can be divided into three distinct regions: the first region at $\lambda > 325$nm, the second at $275\text{nm} < \lambda < 325\text{nm}$, and the third at $\lambda < 275$nm. The calculated spectrum exhibits a good agreement with the experimental UV-Vis data (Fig. S50). The TDDFT (empirically broadened) and Wigner-based absorption spectra are similar, with the TDDFT spectrum showing a slight blue shift of approximately 25 nm relative to the LVC spectrum. Both methods have identical excitation energies and oscillator strengths at the Franck–Condon point ($q_i = 0$). The observed shift can be attributed to effects beyond the LVC model, quadratic vibronic coupling terms and anharmonicities in the potential energy surfaces.[34]

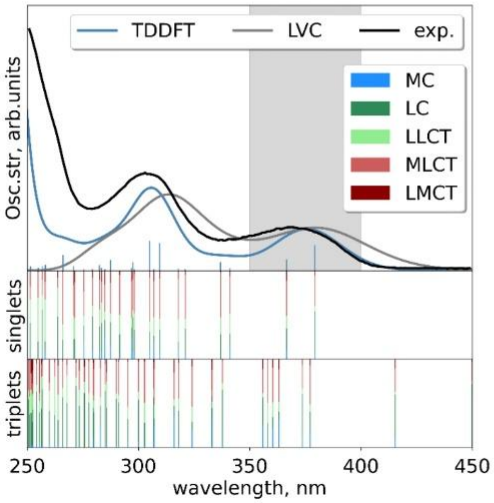

Figure S50: Overlay of the simulated optical absorption spectrum for $Co(ImP^{NMe2})_2^+$ in dichloromethane (blue line) and the experimental spectrum (grey line). Gray shadowed ared shows the excitation window for the simulations (see below). The lower two panels show the density-matrix analysis of the corresponding excited states.

Metal-to-ligand charge-transfer (MLCT) transitions dominate the low-energy region (above 325 nm). These transitions correspond to the excitation of electrons from singly and doubly occupied Co(III) d-orbitals to the π^*-orbitals of the ligand, which are extended over the methyl imidazole-phenylene moieties. The mid-energy region (275 to 325 nm) is characterized by a mixture of transitions, including ligand-to-ligand charge-transfer (LLCT) transitions, which occur between the π-orbitals of one methyl imidazole-phenylene group and the π^*-orbitals of another. This region also features contributions from ligand-to-metal charge-transfer (LMCT) transitions, which involve electron transfer from the π-orbitals of the ligand to Co(III) d-orbitals, as well as ligand-centered (LC) transitions, arising from the covalent bonding of the Co(III) center with the methyl imidazole-phenylene groups. Finally, the high-energy region below 275 nm is primarily dominated by LC transitions. As only the 20 lowest singlet and 10 triplet states were included in further dynamical simulations, their character is discussed in detail below. The S_1 state is of LC character, while S_2-S_{20} are dominated by MLCT contribution. In the triplet manifold, T_1, T_2, and T_9 primarily have LC character, while the other triplet states have a larger MLCT contribution. To emphasize is the strongly mixed character of all lowest excited states.

TSH results

To thoroughly investigate the ultrafast deactivation mechanism, we performed trajectory surface hopping (TSH) simulations based on the LVC model. Fig. S51a presents a state-resolved population

map showing the dynamic evolution of diabatic state populations for both singlet and triplet states throughout the deactivation process. Complementarily, Fig. S51b displays the total diabatic populations, grouped by state character. The initially populated ^{1}MLCT states undergo a rapid decay within approximately 200 fs, primarily driven by intersystem crossing (ISC) into the ^{3}MLCT state. Concurrently, a significant portion of the ^{1}MLCT population undergoes internal conversion (IC) to the ^{1}LC state. As illustrated in Fig. S51a), the ^{3}MLCT states are also populated indirectly from the ^{1}LC state via ISC, which becomes noticeable after about 500 fs. This transition explains the observed decrease in the ^{1}LC population from 500 fs onward. Further analysis of the population dynamics reveals two distinct components in the behavior of the ^{3}MLCT state. A substantial portion of the population rapidly converts into the triplet ^{3}LC state within roughly 200 fs. The resulting ^{3}LC population then decays more slowly on the picosecond timescale. Meanwhile, a fraction of the ^{3}MLCT population persists throughout the simulation, indicating a relatively stable triplet configuration or a slower deactivation channel. The dotted lines in Fig. S51b represent biexponential fits to the population dynamics for each electronic character. The initial fast decay within the first ~500 fs is primarily due to artificial conditions arising from the instantaneous vertical excitation and subsequent ultrafast relaxation. Our focus, however, lies in the slower time constant, which more accurately captures the intrinsic ISC and IC processes. The fitted slower time constants are as follows: 1.8 ps for the ^{1}MLCT state, 620 fs for the ^{1}LC state, 2.6 ps for the ^{3}MLCT state, and 25.0 ps for the ^{3}LC state. Overall, the relaxation pathway can be summarized as: ^{1}MLCT → ^{3}MLCT → ^{3}LC, with intermediate population transfer via the ^{1}LC state. The dashed line in Fig. S51c) represents biexponential fits of the total population of singlet states. Almost 80% of the population undergoes ISC to the triplet manifold in about 280 fs, while the remaining 20% decays through IC to the ground state in about 2.2 ps.

Fig. S51d shows the normal mode activity along the TSH trajectories. The dominant modes are expected to influence ISC most, particularly those involving the metal center, where SOC effects are more important. In general, the lower-frequency normal modes tend to exhibit the most significant deviations.[35] Overall, we observe that a few modes clearly stand out from an otherwise relatively constant background, indicating high activity. The dominant modes are antisymmetric Co–C stretching (ν_7 = 109 cm^{-1}, coupling mode within the LVC model) and symmetric Co–C stretching (ν_{10} = 121 cm^{-1} and ν_{18} = 197 cm^{-1}, tuning modes).

Fig. S52 illustrates the potential energy surfaces (PESs) as a function of the three dominant vibrational modes: ν_7, ν_{10}, and ν_{18}. Our results indicate that these modes are crucial for facilitating electronic relaxation by mediating the coupling between the singlet and triplet manifolds. Specifically, they enable efficient vibronic coupling among the ^{1}LC, ^{1}MLCT, ^{3}LC, and ^{3}MLCT states. Motion along the two tuning modes reduces the energy gaps between these states, leading to regions of near-degeneracy or even direct crossings. This observation supports a mechanism where vibrational motion promotes both ISC and IC between the various excited-state surfaces. This mechanism contrasts sharply with the well-established dynamics in octahedral Fe(II)

complexes, where molecular symmetry imposes more stringent restrictions on the relaxation pathways. For instance, the totally symmetric breathing modes are known to connect the triplet and quintet states.[36] However, because the totally symmetric breathing modes preserve octahedral symmetry, they cannot induce mixing between singlet and triplet MC components. In Fe(II) systems, only antisymmetric modes distorting the symmetry and activating Fe–N stretching can lift the degeneracy, and allow for excited-state surface splitting and state intersection, thereby enabling efficient ISC and IC via the MC PESs. In the $Co(ImP^{NMe2})_2^+$ system, the ν_7, ν_{10}, and particularly the ν_{18} modes involve Co–C bond distortions that breaks the symmetry. This symmetry-breaking action promotes strong vibronic coupling between the LC and MLCT states. Crucially, these breathing modes do not preserve octahedral symmetry, allowing the excited-state PESs of different spin multiplicities and characters to approach avoided crossing regions. As depicted in Fig. S52, all three modes lead to energy splitting that facilitates state mixing without involving MC states, reflecting a fundamentally different and more ligand-centric relaxation landscape for the $Co(ImP^{NMe2})_2^+$ complex.

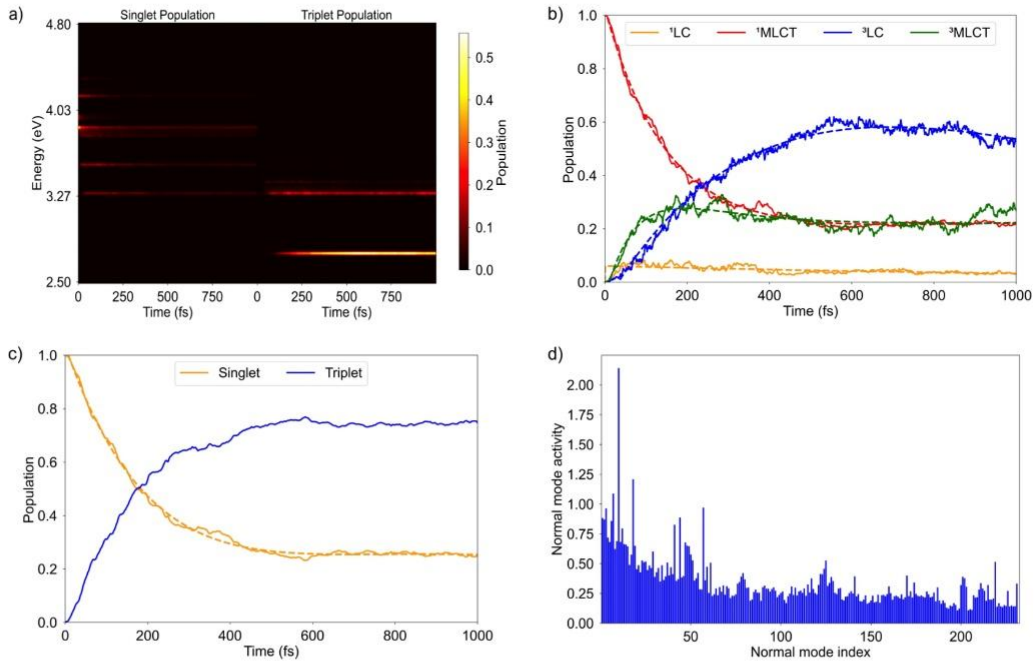

Figure S51. a) Time evolution of the diabatic populations with respect to their energies, b) Time evolution of the sum of ^{1}MLCT, ^{1}LC, ^{3}MLCT and ^{3}LC population fitted with a biexponential decay function, c) Time evolution of the sum of singlet and triplet population fitted with a biexponential decay function, d) Dynamic normal-mode activity of the vibrational motion along the TSH trajectories, and e-g) Illustration of three dominant Co-C stretching modes ν_7, ν_{10}, and ν_{18}.

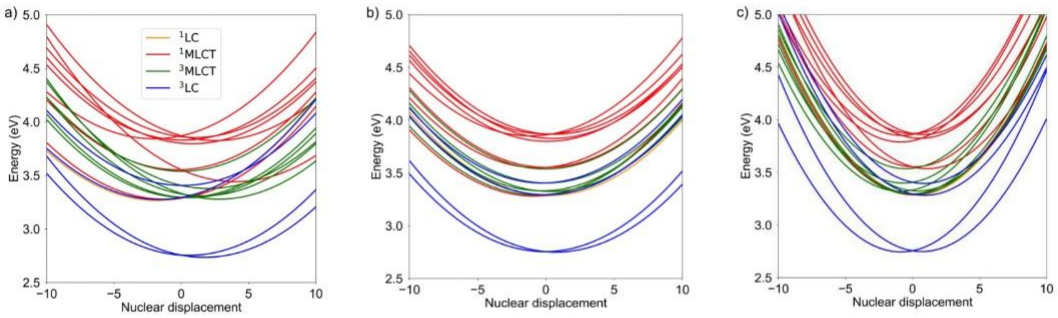

Figure S52. One-dimensional cuts of the adiabatic PESs along (a) ν_7 (b) ν_{10}, and (c) ν_{18}. Nuclear displacements are given in dimensionless mass-frequency-scaled normal coordinates. Coloring is based on the adiabatic character of states.

Fig. S53 depicts the time-resolved evolution of the averaged Co–C bond lengths following photoexcitation. Two distinct types of Co–C bonds are present: equatorial (Co–C_{Im}), where C_{Im} refers to the carbon atom of the methylimidazole ligand, and axial (Co–C_{Cm}), where C_{Cm} refers to the carbon atom of the phenylene ligand bonded to the cobalt center. All equivalent bonds were included in the analysis (four for Co–C_{Im} and two for Co–C_{Cm}). The color bar indicates the trajectory density, derived via Gaussian convolution. Initially, Co–C_{Im} and Co–C_{Cm} are centered at 1.93 Å and 1.91 Å, respectively. For the Co–C_{Cm} bond, a relatively modest elongation is observed, ranging from approximately 1.88 to 2.00 Å during the dynamics. In contrast, the Co–C_{Im} bond undergoes a more rapid and pronounced elongation, reaching 1.90–2.10 Å within the first 200 fs. This elongation then slightly decreases, settling within a range of approximately 1.90–2.04 Å at later times. The early elongation of the axial Co–C_{Cm} bond is consistent with prior studies showing that structural distortions along the axial direction can initiate ISC. Hu et al.[37] demonstrated that axial ligand dynamics in cobalt complexes significantly impact excited-state evolution by modulating metal-ligand orbital interactions, particularly involving the d_z^2 orbital. Similarly, Ito et al.[38] described how axial bond weakening reduces ligand field strength, stabilizing ^{3}MLCT and ^{3}MC states and narrowing the singlet–triplet energy gap. Thus, even though the axial bond elongation is relatively small, it likely serves as a fast, mechanistically critical coordinate to promote ISC. On the other hand, the equatorial Co–C_{Im} bond elongates more substantially and continues evolving beyond the initial sub-picosecond time window. This larger and more persistent distortion suggests a significant structural reorganization associated with the stabilization of longer-lived states, such as ^{3}LC. The timescale of this motion corresponds to the slower component of the biexponential fits, reflecting late-stage excited-state relaxation. Kim et al.[39] emphasized that coherent nuclear motion can persist after ISC and shape the geometry of the relaxed triplet state. This observation aligns with the behavior observed here, where equatorial reorganization appears to dominate the final stages of excited-state decay. Taken together, these observations support a two-step relaxation mechanism: an initial, fast axial distortion (Co–C_{Cm}) facilitates electronic transition and ISC, while a slower, more extensive equatorial rearrangement (Co–C_{Im})

governs the structural stabilization of the long-lived excited state. This finding highlights the anisotropic nature of the excited-state dynamics in $Co(ImP^{NMe2})_2^+$ and illustrates how different ligand environments contribute distinctively to the relaxation process.

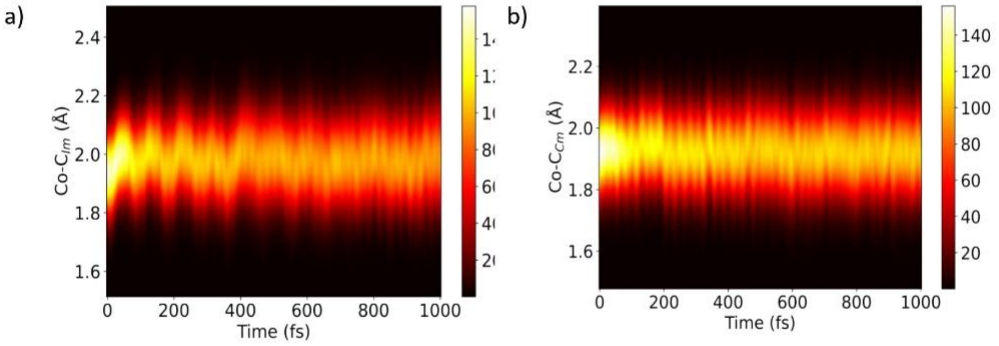

Figure S53. Temporal evolution of bond lengths following excitation: a) Co–C_{Im}, and b) Co–C_{Cm}. The plots were generated from trajectory analysis using Gaussian convolution with a full width at half maximum (FWHM) of 0.01 Å.

References

(1) Nicholson, R. S.; Shain, I. Theory of Stationary Electrode Polarography. Single Scan and Cyclic Methods Applied to Reversible, Irreversible, and Kinetic Systems. *Anal. Chem.* **1964**, *36* (4), 706–723. DOI: 10.1021/ac60210a007.

(2) Heinze, J. Cyclic Voltammetry—"Electrochemical Spectroscopy". New Analytical Methods (25). *Angew. Chem. Int. Ed. Engl.* **1984**, *23* (11), 831–847. DOI: 10.1002/anie.198408313.

(3) Randles, J. E. B. A cathode ray polarograph. Part II.—The current-voltage curves. *Trans. Faraday Soc.* **1948**, *44* (0), 327–338. DOI: 10.1039/TF9484400327.

(4) Scholz, F.; Bond, A. M.; Compton, R. G.; Fiedler, D. A.; Inzelt, G.; Kahlert, H.; Komorsky-Lovrić, Š.; Lohse, H.; Lovrić, M.; Marken, F.; Neudeck, A.; Retter, U.; Scholz, F.; Stojek, Z. *Electroanalytical Methods*; Springer Berlin Heidelberg, 2010. DOI: 10.1007/978-3-642-02915-8.

(5) Päpcke, A.; Friedrich, A.; Lochbrunner, S. Revealing the initial steps in homogeneous photocatalysis by time-resolved spectroscopy. *Journal of physics. Condensed matter : an Institute of Physics journal* **2020**, *32* (15), 153001. DOI: 10.1088/1361-648X/ab5ed1.

(6) Krause, L.; Herbst-Irmer, R.; Sheldrick, G. M.; Stalke, D. Comparison of silver and molybdenum microfocus X-ray sources for single-crystal structure determination. *Journal of applied crystallography* **2015**, *48* (Pt 1), 3–10. DOI: 10.1107/S1600576714022985. Published Online: Jan. 30, 2015.

(7) Sheldrick, G. M. SHELXT - integrated space-group and crystal-structure determination. *Acta crystallographica. Section A, Foundations and advances* **2015**, *71* (Pt 1), 3–8. DOI: 10.1107/S2053273314026370. Published Online: Jan. 1, 2015.

(8) Neese, F.; Wennmohs, F.; Becker, U.; Riplinger, C. The ORCA quantum chemistry program package. *The Journal of Chemical Physics* **2020**, *152* (22), 224108. DOI: 10.1063/5.0004608.
(9) Neese, F. The ORCA program system. *WIREs Comput Mol Sci* **2012**, *2* (1), 73–78. DOI: 10.1002/wcms.81.
(10) Neese, F. Software update: the ORCA program system, version 4.0. *WIREs Comput Mol Sci* **2018**, *8* (1). DOI: 10.1002/wcms.1327.
(11) Grimme, S.; Brandenburg, J. G.; Bannwarth, C.; Hansen, A. Consistent structures and interactions by density functional theory with small atomic orbital basis sets. *The Journal of Chemical Physics* **2015**, *143* (5), 54107. DOI: 10.1063/1.4927476.
(12) Furness, J. W.; Kaplan, A. D.; Ning, J.; Perdew, J. P.; Sun, J. Accurate and Numerically Efficient r2SCAN Meta-Generalized Gradient Approximation. *The journal of physical chemistry letters* **2020**, *11* (19), 8208–8215. DOI: 10.1021/acs.jpclett.0c02405. Published Online: Sep. 16, 2020.
(13) Schäfer, A.; Horn, H.; Ahlrichs, R. Fully optimized contracted Gaussian basis sets for atoms Li to Kr. *The Journal of Chemical Physics* **1992**, *97* (4), 2571–2577. DOI: 10.1063/1.463096.
(14) Kruse, H.; Grimme, S. A geometrical correction for the inter- and intra-molecular basis set superposition error in Hartree-Fock and density functional theory calculations for large systems. *The Journal of Chemical Physics* **2012**, *136* (15), 154101. DOI: 10.1063/1.3700154.
(15) Grimme, S.; Ehrlich, S.; Goerigk, L. Effect of the damping function in dispersion corrected density functional theory. *Journal of computational chemistry* **2011**, *32* (7), 1456–1465. DOI: 10.1002/jcc.21759. Published Online: Mar. 1, 2011.
(16) Grimme, S.; Antony, J.; Ehrlich, S.; Krieg, H. A consistent and accurate ab initio parametrization of density functional dispersion correction (DFT-D) for the 94 elements H-Pu. *The Journal of Chemical Physics* **2010**, *132* (15), 154104. DOI: 10.1063/1.3382344.
(17) Weigend, F. Accurate Coulomb-fitting basis sets for H to Rn. *Physical chemistry chemical physics : PCCP* **2006**, *8* (9), 1057–1065. DOI: 10.1039/B515623H. Published Online: Jan. 3, 2006.
(18) Jensen, K. P. Bioinorganic chemistry modeled with the TPSSh density functional. *Inorganic chemistry* **2008**, *47* (22), 10357–10365. DOI: 10.1021/ic800841t. Published Online: Oct. 15, 2008.
(19) Caldeweyher, E.; Bannwarth, C.; Grimme, S. Extension of the D3 dispersion coefficient model. *The Journal of Chemical Physics* **2017**, *147* (3), 34112. DOI: 10.1063/1.4993215.
(20) Caldeweyher, E.; Ehlert, S.; Hansen, A.; Neugebauer, H.; Spicher, S.; Bannwarth, C.; Grimme, S. A generally applicable atomic-charge dependent London dispersion correction. *The Journal of Chemical Physics* **2019**, *150* (15), 154122. DOI: 10.1063/1.5090222.
(21) Weigend, F.; Ahlrichs, R. Balanced basis sets of split valence, triple zeta valence and quadruple zeta valence quality for H to Rn: Design and assessment of accuracy. *Physical chemistry chemical physics : PCCP* **2005**, *7* (18), 3297–3305. DOI: 10.1039/b508541a. Published Online: Aug. 4, 2005.
(22) Cossi, M.; Rega, N.; Scalmani, G.; Barone, V. Energies, structures, and electronic properties of molecules in solution with the C-PCM solvation model. *Journal of computational chemistry* **2003**, *24* (6), 669–681. DOI: 10.1002/jcc.10189.
(23) Neese, F.; Wennmohs, F.; Hansen, A.; Becker, U. Efficient, approximate and parallel Hartree–Fock and hybrid DFT calculations. A 'chain-of-spheres' algorithm for the Hartree–Fock exchange. *Chemical Physics* **2009**, *356* (1-3), 98–109. DOI: 10.1016/j.chemphys.2008.10.036.
(24) Iikura, H.; Tsuneda, T.; Yanai, T.; Hirao, K. A long-range correction scheme for generalized-gradient-approximation exchange functionals. *The Journal of Chemical Physics* **2001**, *115* (8), 3540–3544. DOI: 10.1063/1.1383587.

(25) Livshits, E.; Baer, R. A density functional theory for symmetric radical cations from bonding to dissociation. *The journal of physical chemistry. A* **2008**, *112* (50), 12789–12791. DOI: 10.1021/jp803606n.
(26) Stein, T.; Kronik, L.; Baer, R. Reliable prediction of charge transfer excitations in molecular complexes using time-dependent density functional theory. *J. Am. Chem. Soc.* **2009**, *131* (8), 2818–2820. DOI: 10.1021/ja8087482.
(27) Stein, T.; Kronik, L.; Baer, R. Prediction of charge-transfer excitations in coumarin-based dyes using a range-separated functional tuned from first principles. *The Journal of Chemical Physics* **2009**, *131* (24), 244119. DOI: 10.1063/1.3269029.
(28) Richter, M.; Marquetand, P.; González-Vázquez, J.; Sola, I.; González, L. SHARC: ab Initio Molecular Dynamics with Surface Hopping in the Adiabatic Representation Including Arbitrary Couplings. *Journal of chemical theory and computation* **2011**, *7* (5), 1253–1258. DOI: 10.1021/ct1007394. Published Online: Mar. 29, 2011.
(29) Stoll, S.; Schweiger, A. EasySpin, a comprehensive software package for spectral simulation and analysis in EPR. *Journal of magnetic resonance (San Diego, Calif. : 1997)* **2006**, *178* (1), 42–55. DOI: 10.1016/j.jmr.2005.08.013. Published Online: Sep. 26, 2005.
(30) Farges, F.; Linnen, R. L.; Brown, G. E. REDOX AND SPECIATION OF TIN IN HYDROUS SILICATE GLASSES: A COMPARISON WITH Nb, Ta, Mo AND W. *The Canadian Mineralogist* **2006**, *44* (3), 795–810. DOI: 10.2113/gscanmin.44.3.795.
(31) Brandenburg, J. G.; Bannwarth, C.; Hansen, A.; Grimme, S. B97-3c: A revised low-cost variant of the B97-D density functional method. *The Journal of Chemical Physics* **2018**, *148* (6), 64104. DOI: 10.1063/1.5012601.
(32) Granucci, G.; Persico, M.; Zoccante, A. Including quantum decoherence in surface hopping. *The Journal of Chemical Physics* **2010**, *133* (13), 134111. DOI: 10.1063/1.3489004.
(33) Pápai, M. Photoinduced Low-Spin → High-Spin Mechanism of an Octahedral Fe(II) Complex Revealed by Synergistic Spin-Vibronic Dynamics. *Inorg. Chem.* **2021**, *60* (18), 13950–13954. DOI: 10.1021/acs.inorgchem.1c01838. Published Online: Sep. 9, 2021.
(34) Farkhutdinova, D.; Polonius, S.; Karrer, P.; Mai, S.; González, L. Parametrization of Linear Vibronic Coupling Models for Degenerate Electronic States. *The journal of physical chemistry. A* **2025**, *129* (10), 2655–2666. DOI: 10.1021/acs.jpca.4c07472. Published Online: Mar. 4, 2025.
(35) Pápai, M. Toward Simulation of Fe(II) Low-Spin → High-Spin Photoswitching by Synergistic Spin-Vibronic Dynamics. *Journal of chemical theory and computation* **2022**, *18* (3), 1329–1339. DOI: 10.1021/acs.jctc.1c01184. Published Online: Feb. 24, 2022.
(36) Bokareva, O. S.; Baig, O.; Al-Marri, M. J.; Kühn, O.; González, L. The effect of N-heterocyclic carbene units on the absorption spectra of Fe(II) complexes: a challenge for theory. *Physical chemistry chemical physics : PCCP* **2020**, *22* (47), 27605–27616. DOI: 10.1039/D0CP04781C.
(37) Hu, W.; Wang, D.; Ma, Q.; Reinhart, B. J.; Zhang, X.; Huang, J. The Impact of Axial Ligation on the Excited State Dynamics of Cobalt(II) Phthalocyanine. *Journal of Photochemistry and Photobiology* **2022**, *11*, 100132. DOI: 10.1016/j.jpap.2022.100132.
(38) Ito, A.; Iwamura, M.; Sakuda, E. Excited-state dynamics of luminescent transition metal complexes with metallophilic and donor–acceptor interactions. *Coordination Chemistry Reviews* **2022**, *467*, 214610. DOI: 10.1016/j.ccr.2022.214610.
(39) Kim, P.; Valentine, A. J. S.; Roy, S.; Mills, A. W.; Castellano, F. N.; Li, X.; Chen, L. X. Ultrafast branching in intersystem crossing dynamics revealed by coherent vibrational wavepacket motions in a bimetallic Pt(II) complex. *Faraday discussions* **2022**, *237* (0), 259–273. DOI: 10.1039/D2FD00009A. Published Online: Sep. 15, 2022.

References

(1) Cohen, J.; Agel, L.; Barlow, M.; Garfinkel, C. I.; White, I. Linking Arctic variability and change with extreme winter weather in the United States. *Science (New York, N.Y.)* **2021**, *373* (6559), 1116–1121. DOI: 10.1126/science.abi9167. Published Online: Sep. 1, 2021.

(2) Perkins-Kirkpatrick, S. E.; Lewis, S. C. Increasing trends in regional heatwaves. *Nature communications* **2020**, *11* (1), 3357. DOI: 10.1038/s41467-020-16970-7. Published Online: Jul. 3, 2020.

(3) Pfleiderer, P.; Schleussner, C.-F.; Kornhuber, K.; Coumou, D. Summer weather becomes more persistent in a 2 °C world. *Nat. Clim. Chang.* **2019**, *9* (9), 666–671. DOI: 10.1038/s41558-019-0555-0.

(4) Fischer, E. M.; Knutti, R. Anthropogenic contribution to global occurrence of heavy-precipitation and high-temperature extremes. *Nat. Clim. Chang.* **2015**, *5* (6), 560–564. DOI: 10.1038/nclimate2617.

(5) Pfahl, S.; O'Gorman, P. A.; Fischer, E. M. Understanding the regional pattern of projected future changes in extreme precipitation. *Nat. Clim. Chang.* **2017**, *7* (6), 423–427. DOI: 10.1038/nclimate3287.

(6) Khan, R.; Liu, J. Coordinate to combat Pakistan's climate-driven disasters. *Nature* **2025**, *645* (8081), 592. DOI: 10.1038/d41586-025-03004-9.

(7) Ayugi, B.; Eresanya, E. O.; Onyango, A. O.; Ogou, F. K.; Okoro, E. C.; Okoye, C. O.; Anoruo, C. M.; Dike, V. N.; Ashiru, O. R.; Daramola, M. T.; Mumo, R.; Ongoma, V. Review of Meteorological Drought in Africa: Historical Trends, Impacts, Mitigation Measures, and Prospects. *Pure and applied geophysics* **2022**, *179* (4), 1365–1386. DOI: 10.1007/s00024-022-02988-z. Published Online: Mar. 14, 2022.

(8) Waqas, M. A. Pakistan's floods flow from climate injustice. *Science (New York, N.Y.)* **2022**, *378* (6619), 482. DOI: 10.1126/science.ade8490. Published Online: Nov. 3, 2022.

(9) Liu, Q.; Fu, C.; Xu, Z.; Ding, A. Global warming intensifies extreme day-to-day temperature changes in mid–low latitudes. *Nat. Clim. Chang.* **2025.** DOI: 10.1038/s41558-025-02486-9.

(10) Grochala, W. First there was hydrogen. *Nature chemistry* **2015**, *7* (3), 264. DOI: 10.1038/nchem.2186.

(11) Amouyal, E. Photochemical production of hydrogen and oxygen from water: A review and state of the art. *Solar Energy Materials and Solar Cells* **1995**, *38* (1-4), 249–276. DOI: 10.1016/0927-0248(95)00003-8.

(12) Møller, K. T.; Jensen, T. R.; Akiba, E.; Li, H. Hydrogen - A sustainable energy carrier. *Progress in Natural Science: Materials International* **2017**, *27* (1), 34–40. DOI: 10.1016/j.pnsc.2016.12.014.

(13) Holleman, A. F.; Wiberg, E.; Wiberg, N. *Lehrbuch der anorganischen Chemie Holleman-Wiberg. Begr. von A. F. Holleman. Fortgef. von Egon und Nils Wiberg*, 102., stark umgearbeitete und verb. Aufl.; de Gruyter, 2007.

(14) Kumar, M. S.; Srinivasan, S. A.; Vichitra, M.; C, A. S.; Beemkumar, N.; Singh, R. P.; K, K. P. Green, blue, and turquoise hydrogen: A review of production technologies and sustainability. *Results in Engineering* **2025**, *27*, 106238. DOI: 10.1016/j.rineng.2025.106238.
(15) Weisenburger, P. 50 shades of hydrogen: A perspective on definitions in science and public communication. *Energy Research & Social Science* **2025**, *129*, 104346. DOI: 10.1016/j.erss.2025.104346.
(16) Singla, M. K.; Gupta, J.; Beryozkina, S.; Safaraliev, M.; Singh, M. The colorful economics of hydrogen: Assessing the costs and viability of different hydrogen production methods - A review. *International Journal of Hydrogen Energy* **2024**, *61*, 664–677. DOI: 10.1016/j.ijhydene.2024.02.255.
(17) Hermesmann, M.; Müller, T. E. Green, Turquoise, Blue, or Grey? Environmentally friendly Hydrogen Production in Transforming Energy Systems. *Progress in Energy and Combustion Science* **2022**, *90*, 100996. DOI: 10.1016/j.pecs.2022.100996.
(18) Kusoglu, A. (Re)Defining Clean Hydrogen: From Colors to Emissions. *Electrochem. Soc. Interface* **2022**, *31* (4), 47–52. DOI: 10.1149/2.F08224IF.
(19) Arcos, J. M. M.; Santos, D. M. F. The Hydrogen Color Spectrum: Techno-Economic Analysis of the Available Technologies for Hydrogen Production. *Gases* **2023**, *3* (1), 25–46. DOI: 10.3390/gases3010002.
(20) Howarth, R. W.; Jacobson, M. Z. How green is blue hydrogen? *Energy Science & Engineering* **2021**, *9* (10), 1676–1687. DOI: 10.1002/ese3.956.
(21) Shiva Kumar, S.; Lim, H. An overview of water electrolysis technologies for green hydrogen production. *Energy Reports* **2022**, *8*, 13793–13813. DOI: 10.1016/j.egyr.2022.10.127.
(22) AlHumaidan, F. S.; Absi Halabi, M.; Rana, M. S.; Vinoba, M. Blue hydrogen: Current status and future technologies. *Energy Conversion and Management* **2023**, *283*, 116840. DOI: 10.1016/j.enconman.2023.116840.
(23) Dubey, A.; Arora, A. Advancements in carbon capture technologies: A review. *Journal of Cleaner Production* **2022**, *373*, 133932. DOI: 10.1016/j.jclepro.2022.133932.
(24) Wilberforce, T.; Olabi, A. G.; Sayed, E. T.; Elsaid, K.; Abdelkareem, M. A. Progress in carbon capture technologies. *The Science of the total environment* **2021**, *761*, 143203. DOI: 10.1016/j.scitotenv.2020.143203. Published Online: Nov. 11, 2020.
(25) Schneider, S.; Bajohr, S.; Graf, F.; Kolb, T. Verfahrensübersicht zur Erzeugung von Wasserstoff durch Erdgas-Pyrolyse. *Chemie Ingenieur Technik* **2020**, *92* (8), 1023–1032. DOI: 10.1002/cite.202000021.
(26) Incer-Valverde, J.; Korayem, A.; Tsatsaronis, G.; Morosuk, T. “Colors” of hydrogen: Definitions and carbon intensity. *Energy Conversion and Management* **2023**, *291*, 117294. DOI: 10.1016/j.enconman.2023.117294.
(27) Kusoglu, A. Chalkboard 1 - The Many Colors of Hydrogen. *Electrochem. Soc. Interface* **2021**, *30* (4), 44–48. DOI: 10.1149/2.F12214IF.
(28) Ocenic, E.-L.; Tanţău, A. Redefining the Hydrogen “Colours” based on Carbon Dioxide Emissions: A New Evidence-Based Colour Code. *Proceedings of the International*

Conference on Business Excellence **2023**, *17* (1), 111–121. DOI: 10.2478/picbe-2023-0013.
(29) Buffi, M.; Prussi, M.; Scarlat, N. Energy and environmental assessment of hydrogen from biomass sources: Challenges and perspectives. *Biomass and Bioenergy* **2022**, *165*, 106556. DOI: 10.1016/j.biombioe.2022.106556.
(30) Barber, J. Photosynthetic energy conversion: natural and artificial. *Chemical Society Reviews* **2009**, *38* (1), 185–196. DOI: 10.1039/B802262N. Published Online: Nov. 10, 2008.
(31) Nocera, D. G. The artificial leaf. *Accounts of chemical research* **2012**, *45* (5), 767–776. DOI: 10.1021/ar2003013. Published Online: Apr. 4, 2012.
(32) Hoffert, M. I.; Caldeira, K.; Benford, G.; Criswell, D. R.; Green, C.; Herzog, H.; Jain, A. K.; Kheshgi, H. S.; Lackner, K. S.; Lewis, J. S.; Lightfoot, H. D.; Manheimer, W.; Mankins, J. C.; Mauel, M. E.; Perkins, L. J.; Schlesinger, M. E.; Volk, T.; Wigley, T. M. L. Advanced technology paths to global climate stability: energy for a greenhouse planet. *Science (New York, N.Y.)* **2002**, *298* (5595), 981–987. DOI: 10.1126/science.1072357.
(33) Lewis, N. S.; Nocera, D. G. Powering the planet: chemical challenges in solar energy utilization. *Proceedings of the National Academy of Sciences of the United States of America* **2006**, *103* (43), 15729–15735. DOI: 10.1073/pnas.0603395103. Published Online: Oct. 16, 2006.
(34) Blankenship, R. E.; Tiede, D. M.; Barber, J.; Brudvig, G. W.; Fleming, G.; Ghirardi, M.; Gunner, M. R.; Junge, W.; Kramer, D. M.; Melis, A.; Moore, T. A.; Moser, C. C.; Nocera, D. G.; Nozik, A. J.; Ort, D. R.; Parson, W. W.; Prince, R. C.; Sayre, R. T. Comparing photosynthetic and photovoltaic efficiencies and recognizing the potential for improvement. *Science (New York, N.Y.)* **2011**, *332* (6031), 805–809. DOI: 10.1126/science.1200165.
(35) National Academy of Engineering. *America's energy future*:*Technology and transformation*; America's energy future series; National Academies Press, 2009.
(36) Chu, S.; Majumdar, A. Opportunities and challenges for a sustainable energy future. *Nature* **2012**, *488* (7411), 294–303. DOI: 10.1038/nature11475.
(37) Zhang, H. L.; Baeyens, J.; Degrève, J.; Cacères, G. Concentrated solar power plants: Review and design methodology. *Renewable and Sustainable Energy Reviews* **2013**, *22*, 466–481. DOI: 10.1016/j.rser.2013.01.032.
(38) Ciamician, G. THE PHOTOCHEMISTRY OF THE FUTURE. *Science (New York, N.Y.)* **1912**, *36* (926), 385–394. DOI: 10.1126/science.36.926.385.
(39) Hisatomi, T.; Kubota, J.; Domen, K. Recent advances in semiconductors for photocatalytic and photoelectrochemical water splitting. *Chemical Society Reviews* **2014**, *43* (22), 7520–7535. DOI: 10.1039/C3CS60378D.
(40) Chen, X.; Shen, S.; Guo, L.; Mao, S. S. Semiconductor-based photocatalytic hydrogen generation. *Chemical reviews* **2010**, *110* (11), 6503–6570. DOI: 10.1021/cr1001645.
(41) Darwent, J. R.; Douglas, P.; Harriman, A.; Porter, G.; Richoux, M.-C. Metal phthalocyanines and porphyrins as photosensitizers for reduction of water to hydrogen.

Coordination Chemistry Reviews **1982**, *44* (1), 83–126. DOI: 10.1016/S0010-8545(00)80518-4.
(42) Gärtner, F.; Boddien, A.; Barsch, E.; Fumino, K.; Losse, S.; Junge, H.; Hollmann, D.; Brückner, A.; Ludwig, R.; Beller, M. Photocatalytic hydrogen generation from water with iron carbonyl phosphine complexes: improved water reduction catalysts and mechanistic insights. *Chemistry (Weinheim an der Bergstrasse, Germany)* **2011**, *17* (23), 6425–6436. DOI: 10.1002/chem.201003564. Published Online: Apr. 19, 2011.
(43) Goldsmith, J. I.; Hudson, W. R.; Lowry, M. S.; Anderson, T. H.; Bernhard, S. Discovery and high-throughput screening of heteroleptic iridium complexes for photoinduced hydrogen production. *Journal of the American Chemical Society* **2005**, *127* (20), 7502–7510. DOI: 10.1021/ja0427101.
(44) Ozawa, H.; Sakai, K. Photo-hydrogen-evolving molecular devices driving visible-light-induced water reduction into molecular hydrogen: structure-activity relationship and reaction mechanism. *Chemical communications (Cambridge, England)* **2011**, *47* (8), 2227–2242. DOI: 10.1039/C0CC04708B. Published Online: Jan. 8, 2011.
(45) Tinker, L. L.; Bernhard, S. Photon-driven catalytic proton reduction with a robust homoleptic iridium(III) 6-phenyl-2,2'-bipyridine complex (Ir(C--N--N)(2)(+)). *Inorganic chemistry* **2009**, *48* (22), 10507–10511. DOI: 10.1021/ic900777g.
(46) Wang, M.; Na, Y.; Gorlov, M.; Sun, L. Light-driven hydrogen production catalysed by transition metal complexes in homogeneous systems. *Dalton transactions (Cambridge, England : 2003)* **2009** (33), 6458–6467. DOI: 10.1039/b903809d. Published Online: May. 29, 2009.
(47) Whang, D. R.; Sakai, K.; Park, S. Y. Highly efficient photocatalytic water reduction with robust iridium(III) photosensitizers containing arylsilyl substituents. *Angewandte Chemie (International ed. in English)* **2013**, *52* (44), 11612–11615. DOI: 10.1002/anie.201305684. Published Online: Sep. 11, 2013.
(48) Lazarides, T.; McCormick, T.; Du, P.; Luo, G.; Lindley, B.; Eisenberg, R. Making hydrogen from water using a homogeneous system without noble metals. *Journal of the American Chemical Society* **2009**, *131* (26), 9192–9194. DOI: 10.1021/ja903044n.
(49) Grätzel, M. *Heterogeneous photochemical electron transfer*; CRC Press, 1989.
(50) Kalyanasundaram, K. Photophysics, photochemistry and solar energy conversion with tris(bipyridyl)ruthenium(II) and its analogues. *Coordination Chemistry Reviews* **1982**, *46*, 159–244. DOI: 10.1016/0010-8545(82)85003-0.
(51) Juris, A.; Balzani, V.; Barigelletti, F.; Campagna, S.; Belser, P.; Zelewsky, A. von. Ru(II) polypyridine complexes: photophysics, photochemistry, eletrochemistry, and chemiluminescence. *Coordination Chemistry Reviews* **1988**, *84*, 85–277. DOI: 10.1016/0010-8545(88)80032-8.
(52) Crutchley, R. J.; Lever, A. B. P. Ruthenium(II) tris(bipyrazyl) dication - a new photocatalyst. *Journal of the American Chemical Society* **1980**, *102* (23), 7128–7129. DOI: 10.1021/ja00543a053.

(53) Neshvad, G.; Hoffman, M. Z. Reductive quenching of the luminescent excited state of tris(2,2'-bipyrazine)ruthenium(2+) ion in aqueous solution. *J. Phys. Chem.* **1989**, *93* (6), 2445–2452. DOI: 10.1021/j100343a044.
(54) Lakowicz, J. R. *Principles of fluorescence spectroscopy*, 3rd ed.; Springer, 2006. DOI: 10.1007/978-0-387-46312-4.
(55) *Photosensibilized Reduction of Water in Dye Solutions-Model of Bacterial Photosyntesis*, 1977.
(56) *CHEMICAL STORAGE OF LIGHT ENERGY CATALYTIC GENERATION OF HYDROGEN BY VISIBLE LIGHT OR SUNLIGHT. IRRADIATION OF NEUTRAL …*, 1977.
(57) Okura, I.; Kim-Thuan, N. Hydrogen generation by visible light with zinc(II) tetraphenylporphyrin in aqueous micellar solutions. *Journal of Molecular Catalysis* **1979**, *6* (3), 227–230. DOI: 10.1016/0304-5102(79)85004-X.
(58) Kalyanasundaram, K.; Kiwi, J.; Grätzel, M. Hydrogen Evolution from Water by Visible Light, a Homogeneous Three Component Test System for Redox Catalysis. *Helvetica Chimica Acta* **1978**, *61* (7), 2720–2730. DOI: 10.1002/hlca.19780610740.
(59) Miranda, M. A.; Garcia, H. 2,4,6-Triphenylpyrylium Tetrafluoroborate as an Electron-Transfer Photosensitizer. *Chem. Rev.* **1994**, *94* (4), 1063–1089. DOI: 10.1021/cr00028a009.
(60) Leung, C.-F.; Lau, T.-C. Organic Photosensitizers for Catalytic Solar Fuel Generation. *Energy Fuels* **2021**, *35* (23), 18888–18899. DOI: 10.1021/acs.energyfuels.1c02675.
(61) Detty, M. R.; Merkel, P. B. Chalcogenapyrylium dyes as potential photochemotherapeutic agents. Solution studies of heavy atom effects on triplet yields, quantum efficiencies of singlet oxygen generation, rates of reaction with singlet oxygen, and emission quantum yields. *J. Am. Chem. Soc.* **1990**, *112* (10), 3845–3855. DOI: 10.1021/ja00166a019.
(62) Zhang, X.-F.; Zhang, I.; Liu, L. Photophysics of halogenated fluoresceins: involvement of both intramolecular electron transfer and heavy atom effect in the deactivation of excited states. *Photochemistry and photobiology* **2010**, *86* (3), 492–498. DOI: 10.1111/j.1751-1097.2010.00706.x.
(63) Han, Z.; McNamara, W. R.; Eum, M.-S.; Holland, P. L.; Eisenberg, R. A nickel thiolate catalyst for the long-lived photocatalytic production of hydrogen in a noble-metal-free system. *Angewandte Chemie (International ed. in English)* **2012**, *51* (7), 1667–1670. DOI: 10.1002/anie.201107329. Published Online: Jan. 11, 2012.
(64) Han, Z.; Shen, L.; Brennessel, W. W.; Holland, P. L.; Eisenberg, R. Nickel pyridinethiolate complexes as catalysts for the light-driven production of hydrogen from aqueous solutions in noble-metal-free systems. *Journal of the American Chemical Society* **2013**, *135* (39), 14659–14669. DOI: 10.1021/ja405257s. Published Online: Sep. 18, 2013.
(65) Islam, S. D.-M.; Konishi, T.; Fujitsuka, M.; Ito, O.; Nakamura, Y.; Usui, Y. Photosensitized Reduction of Methyl Viologen Using Eosin-Y in Presence of a Sacrificial Electron Donor in Water-Alcohol Mixture. *Photochemistry and photobiology* **2000**, *71* (6), 675–680. DOI: 10.1562/0031-8655(2000)0710675PROMVU2.0.CO2.

(66) Misawa, H.; Sakuragi, H.; Usui, Y.; Tokumaru, K. PHOTOSENSITIZING ACTION OF EOSIN Y FOR VISIBLE LIGHT INDUCED HYDROGEN EVOLUTION FROM WATER. *Chemistry Letters* **1983**, *12* (7), 1021–1024. DOI: 10.1246/cl.1983.1021.
(67) McLaughlin, M. P.; McCormick, T. M.; Eisenberg, R.; Holland, P. L. A stable molecular nickel catalyst for the homogeneous photogeneration of hydrogen in aqueous solution. *Chemical communications (Cambridge, England)* **2011**, *47* (28), 7989–7991. DOI: 10.1039/C1CC12347E. Published Online: Jun. 17, 2011.
(68) Zhang, P.; Wang, M.; Dong, J.; Li, X.; Wang, F.; Wu, L.; Sun, L. Photocatalytic Hydrogen Production from Water by Noble-Metal-Free Molecular Catalyst Systems Containing Rose Bengal and the Cobaloximes of BF x -Bridged Oxime Ligands. *J. Phys. Chem. C* **2010**, *114* (37), 15868–15874. DOI: 10.1021/jp106512a.
(69) Lambert, C. R.; Kochevar, I. E. Electron transfer quenching of the rose bengal triplet state. *Photochemistry and photobiology* **1997**, *66* (1), 15–25. DOI: 10.1111/j.1751-1097.1997.tb03133.x.
(70) Chmyrov, A.; Arden-Jacob, J.; Zilles, A.; Drexhage, K.-H.; Widengren, J. Characterization of new fluorescent labels for ultra-high resolution microscopy. *Photochemical & photobiological sciences : Official journal of the European Photochemistry Association and the European Society for Photobiology* **2008**, *7* (11), 1378–1385. DOI: 10.1039/b810991p. Published Online: Sep. 30, 2008.
(71) Zhang, X.; Jin, Z.; Li, Y.; Li, S.; Lu, G. Efficient Photocatalytic Hydrogen Evolution from Water without an Electron Mediator over Pt−Rose Bengal Catalysts. *J. Phys. Chem. C* **2009**, *113* (6), 2630–2635. DOI: 10.1021/jp8085717.
(72) Abdelrahman, A. H.; Abdelrahman, M. A.; Elbadawy, M. K. Possibility of using the beet dyes as a laser gain medium. *NS* **2013**, *05* (11), 1183–1188. DOI: 10.4236/ns.2013.511144.
(73) Ahmed, S. A.; Gergely, J. S.; Infante, D. Energy transfer organic dye mixture lasers. *The Journal of Chemical Physics* **1974**, *61* (4), 1584–1585. DOI: 10.1063/1.1682111.
(74) Fukuzumi, S.; Kotani, H.; Ohkubo, K.; Ogo, S.; Tkachenko, N. V.; Lemmetyinen, H. Electron-transfer state of 9-mesityl-10-methylacridinium ion with a much longer lifetime and higher energy than that of the natural photosynthetic reaction center. *J. Am. Chem. Soc.* **2004**, *126* (6), 1600–1601. DOI: 10.1021/ja038656q.
(75) Fukuzumi, S.; Ohkubo, K.; Suenobu, T. Long-lived charge separation and applications in artificial photosynthesis. *Accounts of chemical research* **2014**, *47* (5), 1455–1464. DOI: 10.1021/ar400200u. Published Online: May. 5, 2014.
(76) Tsudaka, T.; Kotani, H.; Ohkubo, K.; Nakagawa, T.; Tkachenko, N. V.; Lemmetyinen, H.; Fukuzumi, S. Photoinduced Electron Transfer in 9-Substituted 10-Methylacridinium Ions. *Chemistry (Weinheim an der Bergstrasse, Germany)* **2017**, *23* (6), 1306–1317. DOI: 10.1002/chem.201604527. Published Online: Dec. 14, 2016.
(77) Bassan, E.; Gualandi, A.; Cozzi, P. G.; Ceroni, P. Design of BODIPY dyes as triplet photosensitizers: electronic properties tailored for solar energy conversion, photoredox catalysis and photodynamic therapy. *Chemical science* **2021**, *12* (19), 6607–6628. DOI: 10.1039/D1SC00732G. Published Online: Apr. 14, 2021.

(78) Sasikumar, D.; John, A. T.; Sunny, J.; Hariharan, M. Access to the triplet excited states of organic chromophores. *Chemical Society Reviews* **2020**, *49* (17), 6122–6140. DOI: 10.1039/D0CS00484G.

(79) Marian, C. M. Understanding and Controlling Intersystem Crossing in Molecules. *Annual review of physical chemistry* **2021**, *72*, 617–640. DOI: 10.1146/annurev-physchem-061020-053433. Published Online: Feb. 19, 2021.

(80) Förster, C.; Heinze, K. Photophysics and photochemistry with Earth-abundant metals - fundamentals and concepts. *Chemical Society Reviews* **2020**, *49* (4), 1057–1070. DOI: 10.1039/c9cs00573k.

(81) Crosby, G. A.; Demas, J. N. Quantum efficiencies on transition metal complexes. II. Charge-transfer luminescence. *Journal of the American Chemical Society* **1971**, *93* (12), 2841–2847. DOI: 10.1021/ja00741a003.

(82) Ishida, H.; Tobita, S.; Hasegawa, Y.; Katoh, R.; Nozaki, K. Recent advances in instrumentation for absolute emission quantum yield measurements. *Coordination Chemistry Reviews* **2010**, *254* (21-22), 2449–2458. DOI: 10.1016/j.ccr.2010.04.006.

(83) Kim, Y.; Ma, R.; Lee, J.; Harich, J.; Nam, D.; Kim, S.; Kim, M.; Ochmann, M.; Eom, I.; Huse, N.; Lee, J. H.; Kim, T. K. Ligand-Field Effects in a Ruthenium(II) Polypyridyl Complex Probed by Femtosecond X-ray Absorption Spectroscopy. *The journal of physical chemistry letters* **2021**, *12* (51), 12165–12172. DOI: 10.1021/acs.jpclett.1c02400. Published Online: Dec. 16, 2021.

(84) Amini, A.; Harriman, A.; Mayeux, A. The triplet excited state of ruthenium(ii) bis(2,2′:6′,2″-terpyridine): Comparison between experiment and theory. *Phys. Chem. Chem. Phys.* **2004**, *6* (6), 1157–1164. DOI: 10.1039/B313526H.

(85) McCusker, J. K. Electronic structure in the transition metal block and its implications for light harvesting. *Science (New York, N.Y.)* **2019**, *363* (6426), 484–488. DOI: 10.1126/science.aav9104. Published Online: Jan. 31, 2019.

(86) Wenger, O. S. Is Iron the New Ruthenium? *Chemistry (Weinheim an der Bergstrasse, Germany)* **2019**, *25* (24), 6043–6052. DOI: 10.1002/chem.201806148. Published Online: Feb. 18, 2019.

(87) Wenger, O. S. Photoactive Complexes with Earth-Abundant Metals. *Journal of the American Chemical Society* **2018**, *140* (42), 13522–13533. DOI: 10.1021/jacs.8b08822. Published Online: Oct. 11, 2018.

(88) Pyykkö, P. Dirac-Fock One-Centre Calculations Part 8. The 1 Σ States of ScH, YH, LaH, AcH, TmH, LuH and LrH. *Phys. Scr.* **1979**, *20* (5-6), 647–651. DOI: 10.1088/0031-8949/20/5-6/016.

(89) Kaupp, M. The role of radial nodes of atomic orbitals for chemical bonding and the periodic table. *Journal of computational chemistry* **2007**, *28* (1), 320–325. DOI: 10.1002/jcc.20522.

(90) Jamula, L. L.; Brown, A. M.; Guo, D.; McCusker, J. K. Synthesis and characterization of a high-symmetry ferrous polypyridyl complex: approaching the 5T2/3T1 crossing point for Fe(II.). *Inorganic chemistry* **2014**, *53* (1), 15–17. DOI: 10.1021/ic402407k. Published Online: Dec. 17, 2013.

(91) Mengel, A. K. C.; Förster, C.; Breivogel, A.; Mack, K.; Ochsmann, J. R.; Laquai, F.; Ksenofontov, V.; Heinze, K. A heteroleptic push-pull substituted iron(II) bis(tridentate) complex with low-energy charge-transfer states. *Chemistry (Weinheim an der Bergstrasse, Germany)* **2015**, *21* (2), 704–714. DOI: 10.1002/chem.201404955. Published Online: Nov. 13, 2014.

(92) Jakubikova, E.; Bowman, D. N. Fe(II)-Polypyridines as Chromophores in Dye-Sensitized Solar Cells: A Computational Perspective. *Accounts of chemical research* **2015**, *48* (5), 1441–1449. DOI: 10.1021/ar500428t. Published Online: Apr. 28, 2015.

(93) Steube, J.; Kruse, A.; Bokareva, O. S.; Reuter, T.; Demeshko, S.; Schoch, R.; Argüello Cordero, M. A.; Krishna, A.; Hohloch, S.; Meyer, F.; Heinze, K.; Kühn, O.; Lochbrunner, S.; Bauer, M. Janus-type emission from a cyclometalated iron(III) complex. *Nature chemistry* **2023**, *15* (4), 468–474. DOI: 10.1038/s41557-023-01137-w. Published Online: Feb. 27, 2023.

(94) Liu, Y.; Persson, P.; Sundström, V.; Wärnmark, K. Fe N-Heterocyclic Carbene Complexes as Promising Photosensitizers. *Accounts of chemical research* **2016**, *49* (8), 1477–1485. DOI: 10.1021/acs.accounts.6b00186. Published Online: Jul. 25, 2016.

(95) Liu, Y.; Harlang, T.; Canton, S. E.; Chábera, P.; Suárez-Alcántara, K.; Fleckhaus, A.; Vithanage, D. A.; Göransson, E.; Corani, A.; Lomoth, R.; Sundström, V.; Wärnmark, K. Towards longer-lived metal-to-ligand charge transfer states of iron(II) complexes: an N-heterocyclic carbene approach. *Chemical communications (Cambridge, England)* **2013**, *49* (57), 6412–6414. DOI: 10.1039/c3cc43833c.

(96) Duchanois, T.; Etienne, T.; Cebrián, C.; Liu, L.; Monari, A.; Beley, M.; Assfeld, X.; Haacke, S.; Gros, P. C. An Iron-Based Photosensitizer with Extended Excited-State Lifetime: Photophysical and Photovoltaic Properties. *Eur J Inorg Chem* **2015**, *2015* (14), 2469–2477. DOI: 10.1002/ejic.201500142.

(97) Harlang, T. C. B.; Liu, Y.; Gordivska, O.; Fredin, L. A.; Ponseca, C. S.; Huang, P.; Chábera, P.; Kjaer, K. S.; Mateos, H.; Uhlig, J.; Lomoth, R.; Wallenberg, R.; Styring, S.; Persson, P.; Sundström, V.; Wärnmark, K. Iron sensitizer converts light to electrons with 92% yield. *Nature chemistry* **2015**, *7* (11), 883–889. DOI: 10.1038/nchem.2365. Published Online: Oct. 12, 2015.

(98) Zimmer, P.; Burkhardt, L.; Friedrich, A.; Steube, J.; Neuba, A.; Schepper, R.; Müller, P.; Flörke, U.; Huber, M.; Lochbrunner, S.; Bauer, M. The Connection between NHC Ligand Count and Photophysical Properties in Fe(II) Photosensitizers: An Experimental Study. *Inorganic chemistry* **2018**, *57* (1), 360–373. DOI: 10.1021/acs.inorgchem.7b02624. Published Online: Dec. 13, 2017.

(99) Fredin, L. A.; Pápai, M.; Rozsályi, E.; Vankó, G.; Wärnmark, K.; Sundström, V.; Persson, P. Exceptional Excited-State Lifetime of an Iron(II)-N-Heterocyclic Carbene Complex Explained. *The journal of physical chemistry letters* **2014**, *5* (12), 2066–2071. DOI: 10.1021/jz500829w. Published Online: May. 29, 2014.

(100) Liu, L.; Duchanois, T.; Etienne, T.; Monari, A.; Beley, M.; Assfeld, X.; Haacke, S.; Gros, P. C. A new record excited state (3)MLCT lifetime for metalorganic iron(ii)

complexes. *Phys. Chem. Chem. Phys.* **2016**, *18* (18), 12550–12556. DOI: 10.1039/c6cp01418f. Published Online: Apr. 18, 2016.

(101) Huber-Gedert, M.; Nowakowski, M.; Kertmen, A.; Burkhardt, L.; Lindner, N.; Schoch, R.; Herbst-Irmer, R.; Neuba, A.; Schmitz, L.; Choi, T.-K.; Kubicki, J.; Gawelda, W.; Bauer, M. Fundamental Characterization, Photophysics and Photocatalysis of a Base Metal Iron(II)-Cobalt(III) Dyad. *Chemistry (Weinheim an der Bergstrasse, Germany)* **2021**, *27* (38), 9905–9918. DOI: 10.1002/chem.202100766. Published Online: Jun. 1, 2021.

(102) Chábera, P.; Kjaer, K. S.; Prakash, O.; Honarfar, A.; Liu, Y.; Fredin, L. A.; Harlang, T. C. B.; Lidin, S.; Uhlig, J.; Sundström, V.; Lomoth, R.; Persson, P.; Wärnmark, K. FeII Hexa N-Heterocyclic Carbene Complex with a 528 ps Metal-to-Ligand Charge-Transfer Excited-State Lifetime. *The journal of physical chemistry letters* **2018**, *9* (3), 459–463. DOI: 10.1021/acs.jpclett.7b02962. Published Online: Jan. 11, 2018.

(103) Nolan, S. P., Ed. *N-heterocyclic carbenes*:*Effective tools for organometallic synthesis*; WILEY-VCH Verlag GmbH & Co. KGaA, 2014.

(104) Mukherjee, S.; Bowman, D. N.; Jakubikova, E. Cyclometalated Fe(II) complexes as sensitizers in dye-sensitized solar cells. *Inorganic chemistry* **2015**, *54* (2), 560–569. DOI: 10.1021/ic502438g. Published Online: Dec. 22, 2014.

(105) Kisserwan, H.; Kamar, A.; Shoker, T.; Ghaddar, T. H. Photophysical properties of new cyclometalated ruthenium complexes and their use in dye sensitized solar cells. *Dalton transactions (Cambridge, England : 2003)* **2012**, *41* (35), 10643–10651. DOI: 10.1039/c2dt30482a. Published Online: Jul. 27, 2012.

(106) Bomben, P. G.; Robson, K. C. D.; Sedach, P. A.; Berlinguette, C. P. On the viability of cyclometalated Ru(II) complexes for light-harvesting applications. *Inorganic chemistry* **2009**, *48* (20), 9631–9643. DOI: 10.1021/ic900653q.

(107) Flamigni, L.; Barbieri, A.; Sabatini, C.; Ventura, B.; Barigelletti, F. Photochemistry and Photophysics of Coordination Compounds: Iridium. In *Photochemistry and Photophysics of Coordination Compounds II*; Balzani, V., Campagna, S., Eds.; Topics in Current Chemistry, Vol. 281; Springer Berlin Heidelberg, 2007; pp 143–203. DOI: 10.1007/128_2007_131.

(108) Dixon, I. M.; Alary, F.; Boggio-Pasqua, M.; Heully, J.-L. Reversing the relative 3MLCT-3MC order in Fe(ii) complexes using cyclometallating ligands: a computational study aiming at luminescent Fe(ii) complexes. *Dalton transactions (Cambridge, England : 2003)* **2015**, *44* (30), 13498–13503. DOI: 10.1039/C5DT01214G.

(109) Leis, W.; Argüello Cordero, M. A.; Lochbrunner, S.; Schubert, H.; Berkefeld, A. A Photoreactive Iron(II) Complex Luminophore. *Journal of the American Chemical Society* **2022**, *144* (3), 1169–1173. DOI: 10.1021/jacs.1c13083. Published Online: Jan. 13, 2022.

(110) Wegeberg, C.; Wenger, O. S. Luminescent First-Row Transition Metal Complexes. *JACS Au* **2021**, *1* (11), 1860–1876. DOI: 10.1021/jacsau.1c00353. Published Online: Sep. 24, 2021.

(111) Morselli, G.; Reber, C.; Wenger, O. S. Molecular Design Principles for Photoactive Transition Metal Complexes: A Guide for "Photo-Motivated" Chemists. *Journal of the*

American Chemical Society **2025**, *147* (14), 11608–11624. DOI: 10.1021/jacs.5c02096. Published Online: Mar. 27, 2025.

(112) Hockin, B. M.; Li, C.; Robertson, N.; Zysman-Colman, E. Photoredox catalysts based on earth-abundant metal complexes. *Catal. Sci. Technol.* **2019**, *9* (4), 889–915. DOI: 10.1039/C8CY02336K.

(113) Li, Q. Y.; Gockel, S. N.; Lutovsky, G. A.; DeGlopper, K. S.; Baldwin, N. J.; Bundesmann, M. W.; Tucker, J. W.; Bagley, S. W.; Yoon, T. P. Decarboxylative cross-nucleophile coupling via ligand-to-metal charge transfer photoexcitation of Cu(II) carboxylates. *Nature chemistry* **2022**, *14* (1), 94–99. DOI: 10.1038/s41557-021-00834-8. Published Online: Jan. 5, 2022.

(114) Chábera, P.; Liu, Y.; Prakash, O.; Thyrhaug, E.; Nahhas, A. E.; Honarfar, A.; Essén, S.; Fredin, L. A.; Harlang, T. C. B.; Kjær, K. S.; Handrup, K.; Ericson, F.; Tatsuno, H.; Morgan, K.; Schnadt, J.; Häggström, L.; Ericsson, T.; Sobkowiak, A.; Lidin, S.; Huang, P.; Styring, S.; Uhlig, J.; Bendix, J.; Lomoth, R.; Sundström, V.; Persson, P.; Wärnmark, K. A low-spin Fe(iii) complex with 100-ps ligand-to-metal charge transfer photoluminescence. *Nature* **2017**, *543* (7647), 695–699. DOI: 10.1038/nature21430.

(115) Gygi, D.; Gonzalez, M. I.; Hwang, S. J.; Xia, K. T.; Qin, Y.; Johnson, E. J.; Gygi, F.; Chen, Y.-S.; Nocera, D. G. Capturing the Complete Reaction Profile of a C-H Bond Activation. *Journal of the American Chemical Society* **2021**, *143* (16), 6060–6064. DOI: 10.1021/jacs.1c02630. Published Online: Apr. 16, 2021.

(116) Kainz, Q. M.; Matier, C. D.; Bartoszewicz, A.; Zultanski, S. L.; Peters, J. C.; Fu, G. C. Asymmetric copper-catalyzed C-N cross-couplings induced by visible light. *Science (New York, N.Y.)* **2016**, *351* (6274), 681–684. DOI: 10.1126/science.aad8313.

(117) Paulus, B. C.; Adelman, S. L.; Jamula, L. L.; McCusker, J. K. Leveraging excited-state coherence for synthetic control of ultrafast dynamics. *Nature* **2020**, *582* (7811), 214–218. DOI: 10.1038/s41586-020-2353-2. Published Online: Jun. 11, 2020.

(118) Sinha, N.; Wenger, O. S. Photoactive Metal-to-Ligand Charge Transfer Excited States in 3d6 Complexes with Cr0, MnI, FeII, and CoIII. *Journal of the American Chemical Society* **2023**, *145* (9), 4903–4920. DOI: 10.1021/jacs.2c13432. Published Online: Feb. 21, 2023.

(119) Chan, A. Y.; Ghosh, A.; Yarranton, J. T.; Twilton, J.; Jin, J.; Arias-Rotondo, D. M.; Sakai, H. A.; McCusker, J. K.; MacMillan, D. W. C. Exploiting the Marcus inverted region for first-row transition metal-based photoredox catalysis. *Science (New York, N.Y.)* **2023**, *382* (6667), 191–197. DOI: 10.1126/science.adj0612. Published Online: Oct. 12, 2023.

(120) Kaufhold, S.; Rosemann, N. W.; Chábera, P.; Lindh, L.; Bolaño Losada, I.; Uhlig, J.; Pascher, T.; Strand, D.; Wärnmark, K.; Yartsev, A.; Persson, P. Microsecond Photoluminescence and Photoreactivity of a Metal-Centered Excited State in a Hexacarbene-Co(III) Complex. *Journal of the American Chemical Society* **2021**, *143* (3), 1307–1312. DOI: 10.1021/jacs.0c12151. Published Online: Jan. 15, 2021.

(121) Sinha, N.; Pfund, B.; Wegeberg, C.; Prescimone, A.; Wenger, O. S. Cobalt(III) Carbene Complex with an Electronic Excited-State Structure Similar to Cyclometalated Iridium(III)

Compounds. *Journal of the American Chemical Society* **2022**, *144* (22), 9859–9873. DOI: 10.1021/jacs.2c02592. Published Online: May. 27, 2022.
(122) Pal, A. K.; Li, C.; Hanan, G. S.; Zysman-Colman, E. Blue-Emissive Cobalt(III) Complexes and Their Use in the Photocatalytic Trifluoromethylation of Polycyclic Aromatic Hydrocarbons. *Angewandte Chemie (International ed. in English)* **2018**, *57* (27), 8027–8031. DOI: 10.1002/anie.201802532. Published Online: Jun. 4, 2018.
(123) Burton, S. T.; Lee, G.; Moore, C. E.; Sevov, C. S.; Turro, C. Cyclometallated Co(III) Complexes with Lowest-Energy Charge Transfer Excited States Accessible with Visible Light. *Journal of the American Chemical Society* **2025**, *147* (16), 13315–13327. DOI: 10.1021/jacs.4c18299. Published Online: Apr. 10, 2025.
(124) Barbara, P. F.; Meyer, T. J.; Ratner, M. A. Contemporary Issues in Electron Transfer Research. *J. Phys. Chem.* **1996**, *100* (31), 13148–13168. DOI: 10.1021/jp9605663.
(125) Marcus, R. A.; Sutin, N. Electron transfers in chemistry and biology. *Biochimica et Biophysica Acta (BBA) - Reviews on Bioenergetics* **1985**, *811* (3), 265–322. DOI: 10.1016/0304-4173(85)90014-x.
(126) Marcus, R. A. Theoretical relations among rate constants, barriers, and Broensted slopes of chemical reactions. *J. Phys. Chem.* **1968**, *72* (3), 891–899. DOI: 10.1021/j100849a019.
(127) Marcus, R. A. Theoretical relations among rate constants, barriers, and Broensted slopes of chemical reactions. *J. Phys. Chem.* **1968**, *72* (3), 891–899. DOI: 10.1021/j100849a019.
(128) Miller, J. R.; Calcaterra, L. T.; Closs, G. L. Intramolecular long-distance electron transfer in radical anions. The effects of free energy and solvent on the reaction rates. *J. Am. Chem. Soc.* **1984**, *106* (10), 3047–3049. DOI: 10.1021/ja00322a058.
(129) Closs, G. L.; Miller, J. R. Intramolecular long-distance electron transfer in organic molecules. *Science (New York, N.Y.)* **1988**, *240* (4851), 440–447. DOI: 10.1126/science.240.4851.440.
(130) Hicks, R. G. *Stable Radicals*; Wiley, 2010. DOI: 10.1002/9780470666975.
(131) Büttner, T.; Geier, J.; Frison, G.; Harmer, J.; Calle, C.; Schweiger, A.; Schönberg, H.; Grützmacher, H. A stable aminyl radical metal complex. *Science (New York, N.Y.)* **2005**, *307* (5707), 235–238. DOI: 10.1126/science.1106070.
(132) Rodríguez-Lugo, R. E.; Bruin, B. de; Trincado, M.; Grützmacher, H. A Stable Aminyl Radical Coordinated to Cobalt. *Chemistry (Weinheim an der Bergstrasse, Germany)* **2017**, *23* (28), 6795–6802. DOI: 10.1002/chem.201605624. Published Online: Mar. 6, 2017.
(133) Pierpont, C. G.; Lange, C. W. The Chemistry of Transition Metal Complexes Containing Catechol and Semiquinone Ligands. In *Progress in Inorganic Chemistry*; Karlin, K. D., Ed.; Progress in Inorganic Chemistry; Wiley, 1994; pp 331–442. DOI: 10.1002/9780470166420.ch5.
(134) Chaudhuri, P.; Wieghardt, K. Phenoxyl Radical Complexes. In *Progress in Inorganic Chemistry*; Karlin, K. D., Ed.; Progress in Inorganic Chemistry; Wiley, 1994; pp 151–216. DOI: 10.1002/0471227110.ch2.
(135) Alfassi, Z. B. *N-centered radicals*; The chemistry of free radicals; Wiley, 1998.

(136) Donati, N.; Stein, D.; Büttner, T.; Schönberg, H.; Harmer, J.; Anadaram, S.; Grützmacher, H. Rhodium and Iridium Amino, Amido, and Aminyl Radical Complexes. *Eur J Inorg Chem* **2008**, *2008* (30), 4691–4703. DOI: 10.1002/ejic.200800702.
(137) Yao, C.-J.; Zheng, R.-H.; Shi, Q.; Zhong, Y.-W.; Yao, J. 1,4-Benzene-bridged covalent hybrid of triarylamine and cyclometalated ruthenium: a new type of organic-inorganic mixed-valent system. *Chemical communications (Cambridge, England)* **2012**, *48* (45), 5680–5682. DOI: 10.1039/c2cc32471g. Published Online: May. 1, 2012.
(138) Yao, C.-J.; Yao, J.; Zhong, Y.-W. Electronic communication between two amine redox centers bridged by a bis(terpyridine)ruthenium(II) complex. *Inorganic chemistry* **2011**, *50* (15), 6847–6849. DOI: 10.1021/ic200701j. Published Online: Jul. 7, 2011.
(139) Yao, C.-J.; Zheng, R.-H.; Nie, H.-J.; Cui, B.-B.; Shi, Q.; Yao, J.; Zhong, Y.-W. A combined experimental and computational study of linear ruthenium(II) coordination oligomers with end-capping organic redox sites: insight into the light absorption and charge delocalization. *Chemistry (Weinheim an der Bergstrasse, Germany)* **2013**, *19* (37), 12376–12387. DOI: 10.1002/chem.201301319. Published Online: Aug. 6, 2013.
(140) Nie, H.-J.; Yao, C.-J.; Sun, M.-J.; Zhong, Y.-W.; Yao, J. Ruthenium- bis -terpyridine Complex with Two Redox-Asymmetric Amine Substituents: Potential-Controlled Reversal of the Direction of Charge-Transfer. *Organometallics* **2014**, *33* (21), 6223–6231. DOI: 10.1021/om500904k.
(141) Cui, B.-B.; Zhong, Y.-W.; Yao, J. Three-state near-infrared electrochromism at the molecular scale. *Journal of the American Chemical Society* **2015**, *137* (12), 4058–4061. DOI: 10.1021/jacs.5b00586. Published Online: Mar. 17, 2015.
(142) Cui, B.-B.; Yao, C.-J.; Yao, J.; Zhong, Y.-W. Electropolymerized films as a molecular platform for volatile memory devices with two near-infrared outputs and long retention time. *Chemical science* **2014**, *5* (3), 932–941. DOI: 10.1039/C3SC52815D.
(143) Schmitz, L.; Argüello Cordero, M. A.; Al-Marri, M. J.; Schoch, R.; Egold, H.; Neuba, A.; Steube, J.; Bracht, B.; Bokareva, O. S.; Lochbrunner, S.; Bauer, M. Chromophore Induced Effects in Iron(III) Complexes. *Inorganic chemistry* **2025**, *64* (28), 14101–14117. DOI: 10.1021/acs.inorgchem.5c00526. Published Online: Jul. 8, 2025.
(144) Steube, J.; Fritsch, L.; Kruse, A.; Bokareva, O. S.; Demeshko, S.; Elgabarty, H.; Schoch, R.; Alaraby, M.; Egold, H.; Bracht, B.; Schmitz, L.; Hohloch, S.; Kühne, T. D.; Meyer, F.; Kühn, O.; Lochbrunner, S.; Bauer, M. Isostructural Series of a Cyclometalated Iron Complex in Three Oxidation States. *Inorganic chemistry* **2024**, *63* (37), 16964–16980. DOI: 10.1021/acs.inorgchem.4c02576. Published Online: Sep. 2, 2024.
(145) Reilly, S. W.; Webster, C. E.; Hollis, T. K.; Valle, H. U. Transmetallation from CCC-NHC pincer Zr complexes in the synthesis of air-stable CCC-NHC pincer Co(iii) complexes and initial hydroboration trials. *Dalton transactions (Cambridge, England : 2003)* **2016**, *45* (7), 2823–2828. DOI: 10.1039/C5DT04752H. Published Online: Jan. 27, 2016.
(146) Rubio, R. J.; Andavan, G. T. S.; Bauer, E. B.; Hollis, T. K.; Cho, J.; Tham, F. S.; Donnadieu, B. Toward a general method for CCC N-heterocyclic carbene pincer synthesis: Metallation and transmetallation strategies for concurrent activation of three

C–H bonds. *Journal of Organometallic Chemistry* **2005**, *690* (23), 5353–5364. DOI: 10.1016/j.jorganchem.2005.05.007.
(147) Fulmer, G. R.; Miller, A. J. M.; Sherden, N. H.; Gottlieb, H. E.; Nudelman, A.; Stoltz, B. M.; Bercaw, J. E.; Goldberg, K. I. NMR Chemical Shifts of Trace Impurities: Common Laboratory Solvents, Organics, and Gases in Deuterated Solvents Relevant to the Organometallic Chemist. *Organometallics* **2010**, *29* (9), 2176–2179. DOI: 10.1021/om100106e.
(148) Scholz, F.; Bond, A. M. *Electroanalytical methods*:*Guide to experiments and applications*, 2nd, rev. and extended ed.; Springer, 2010.
(149) Randles, J. E. B. A cathode ray polarograph. Part II.—The current-voltage curves. *Trans. Faraday Soc.* **1948**, *44* (0), 327–338. DOI: 10.1039/TF9484400327.
(150) Nicholson, R. S.; Shain, I. Theory of Stationary Electrode Polarography. Single Scan and Cyclic Methods Applied to Reversible, Irreversible, and Kinetic Systems. *Anal. Chem.* **1964**, *36* (4), 706–723. DOI: 10.1021/ac60210a007.
(151) Heinze, J. Cyclovoltammetrie — die „Spektroskopie" des Elektrochemikers. *Angewandte Chemie* **1984**, *96* (11), 823–840. DOI: 10.1002/ange.19840961104.